Microstructure control and property enhancement of NiTi-stainless steel dissimilar joints

by

Kaiping Zhang

A thesis
presented to the University of Waterloo
in the fulfillment of the
thesis requirement for the degree of
Doctor of Philosophy
in
Mechanical and Mechatronics Engineering

Waterloo, Ontario, Canada, 2025
© Kaiping Zhang 2025

Examining Committee Membership:

The following served on the Examining Committee for this thesis. The decision of the Examining Committee is by majority vote.

External Examiner:	Zhenzhen Yu Associate Professor, Dept. of Metallurgical and Materials Engineering, Colorado School of Mines
Supervisor:	Y. Norman Zhou Professor, Dept. of Mechanical and Mechatronics Engineering, University of Waterloo
Supervisor:	Peng Peng Assistant Professor, Dept. of Mechanical and Mechatronics Engineering, University of Waterloo
Internal Member	Ehsan Toyserkani Professor, Dept. of Mechanical and Mechatronics Engineering, University of Waterloo
Internal Member	Adrian Gerlich Professor, Dept. of Mechanical and Mechatronics Engineering, University of Waterloo
Internal-external Member	Boxin Zhao Professor, Dept. of Chemical Engineering, University of Waterloo

Author’s Declaration

This thesis consists of material all of which I authored or co-authored: see Statement of Contributions included in the thesis. This is a true copy of the thesis, including any required final revisions, as accepted by my examiners.

I understand that my thesis may be made electronically available to the public.

Statement of Contributions

This thesis consists of six chapters. Chapter 1 and Chapter 2 are background introduction and literature review, respectively. Chapters 3-5 include published or submitted manuscripts by the candidate. These manuscripts have been modified to fit the style of this thesis. The candidate is the primary author of all the manuscripts. The following co-authors have contributed to the work as outlined below:

Prof. Norman Zhou and Prof. Peng Peng supervised the research progress, advised the research direction, provided technical discussions, and reviewed manuscripts.

Chapter 3:

K. Zhang, P. Peng, Y.N. Zhou, Laser welding-brazing of NiTi/304 stainless steel wires with beam defocus and large offset, Mater. Sci. Eng. A. 835 (2022) 142660.

K. Zhang, F. Liu, C. Tan, Y.N. Zhou, P. Peng, Effect of heat input modes on microstructure , mechanical properties and porosity of laser welded NiTi-316L joints : A comparative study, Mater. Sci. Eng. A. 848 (2022) 143426.

F. Liu and C. Tan supported software and finite volume modeling (FVM) in the flow field simulation.

Chapter 4:

K. Zhang, A. Shamsolhodaei, A. Ghatei-Kalashami, J.P. Oliveira, C. Zang, N. Schell, J. Li, A.R.H. Midawi, J.G. Lopes, J. Yan, P.E.J. Rivera-Díaz-del-Castillo, P. Peng, Y.N. Zhou, Revealing microstructural evolution and mechanical properties of resistance spot welded NiTi-stainless steel with Ni or Nb interlayer, J. Mater. Sci. Technol. 180 (2024) 160–173.

A. Shamsolhodaei helped with the design of resistance spot welding experiments and reviewed the manuscript. A. Ghatei-Kalashami supported resistance spot welding experiments. J.P. Oliveira, N. Schell and J.G. Lopes supported the synchrotron X-ray diffraction (SXRD). C. Zang and P.E.J. Rivera-Díaz-del-Castillo provided thermo-calc software. A.R.H. Midawi helped with the mechanical testing. J. Li and J. Yan provided technical discussions and reviewed the manuscript.

Chapter 5:

K. Zhang, J. Li, A. Anousheh, J. Li, C. Zang, Y.N. Zhou, P. Peng, Interfacial liquid control to realize superior comprehensive properties of microwelded NiTi-stainless steel joints for multifunctional biomedical device fabrication, J. Mater. Sci. Technol. Submitted.

J. Li (the second author) supported the Ni ion release testing. A. Anousheh helped with the micro-XRD characterization. J. Li (the fourth author) provided discussions on cyclic tensile testing and reviewed the manuscript. C. Zang provided thermo-calc software.

Abstract

Dissimilar joining between Nickel-Titanium (NiTi) and stainless steel (SS) is of significance in many areas especially biomedical applications, however, achieving reliable NiTi-SS joints is highly challenging due to the formation of brittle intermetallic compounds (IMCs) in the fusion zone (FZ) or the interface. Two strategies can be summarized to address this issue: *(1)* restricting the mixing of molten metals and *(2)* replacing the most harmful Laves $(Fe,Cr)_2Ti$ with ductile phases. The former one poses large processing complexity and may lead to NiTi plastic deformation degrading the functional properties. The latter struggles to eliminate brittle IMCs entirely in the FZ and may introduce toxic elements. This research investigated both aspects to control the microstructure and properties of NiTi-SS joints by leveraging the flexibility of laser beam and the thermomechanical process of resistance welding.

The combination of laser beam defocus and large offset enabled the laser weld-brazing of NiTi and SS wires. This approach successfully eliminated the IMCs network in the FZ, shifting the conventional and complex FZ brittleness issue to a focus on controlling the brazed interface. Additionally, laser welding mode significantly influenced the macrosegregation and porosity in the FZ of NiTi-SS joints. Low laser power density and long welding time mitigated the macrosegregation and porosity by weakening the laser keyhole effect and prolonging the molten pool duration. In NiTi-SS laser weld FZ, large pores were caused by the instability or collapse of the laser keyhole, while small pores originated from the Ni vaporization.

Both IMCs control strategies were investigated in resistance spot welding (RSW) of NiTi and SS for the first time. The use of Nb interlayer resulted in a unique sandwich-structured joint, where two FZs were separated by solid-state Nb, suppressing the mixing of dissimilar molten metals. Nb-containing eutectics formed at both interfaces, enhancing the joint strength with a 38% increase in fracture load and a remarkable 460% increase in energy absorption. In another approach, increasing Ni concentration via a melted Ni interlayer effectively replaced Fe_2Ti with relatively ductile Ni_3Ti in the FZ. However, high Ni content also induced large pores and cracks, limiting the effectiveness of this strategy in NiTi-SS RSW.

A novel processing approach leveraging interfacial liquid control was proposed, achieving a solid-state joined interface in NiTi-SS fusion welding (e.g., resistance microwelding) without any additional interlayers. The produced NiTi-SS joints showed superior strength, superelasticity and corrosion resistance compared to NiTi joints or base metal. The ultrathin reaction layer at the solid-state joined interface contributed to a strong metallurgical bonding, while Joule heating effects and interfacial reactions enhanced superelasticity and corrosion resistance of the joint. Notably, a face-centered-cubic

(FCC) reorientated layer (ROL) was found between SS and IMC layer at the controlled ultrathin interface. The formation of this ROL was uncovered based on an epitaxial growth model. This ROL introduced a strong crystallographic mismatch with the textured SS, resulting in the fracture at this interface. These phenomenal findings offer valuable insights for studying material interface and controlling dissimilar-metal welding process.

Keywords: NiTi, stainless steel, dissimilar welding, intermetallic compounds, material interface, microstructure, mechanical properties.

Acknowledgements

I am deeply thankful to my supervisors, Prof. Y. Norman Zhou and Prof. Peng Peng, for the tremendous support and the academic freedom they provided throughout my research. Their guidance and insights have been invaluable, profoundly influencing both my research work and personal development.

I would also like to extend my thanks to my collaborators, whose contributions have been helpful to my research. I am grateful to the funding agencies and industrial partners for their support in making this work possible. My appreciation also goes to the Waterloo Advanced Technology Laboratory (WATLab) and the Canadian Centre for Electron Microscopy (CCEM) for their support in material characterizations. Special thanks to all my friends and colleagues in University of Waterloo and Center for Advanced Materials Joining (CAMJ).

Finally, I want to express my deepest love to my parents for their unconditional love and unwavering belief in me, which have been the cornerstone of my success throughout this journey.

Dedication

To my family

Table of Contents

Author's Declaration ..... **iii**

Statement of Contributions ..... **iv**

Abstract ..... **vi**

Acknowledgements ..... **viii**

Dedication ..... **ix**

List of Figures ..... **xiii**

List of Tables ..... **xxiii**

Chapter 1 Introduction **1**

1.1 Background 1

1.2 Objectives 2

1.3 Thesis outline 2

Chapter 2 Literature review **4**

2.1 Introduction of NiTi and SS 4

2.1.1 Physical metallurgy of NiTi 4

2.1.2 Superelasticity and shape memory effect of NiTi 8

2.1.3 Metallurgy and weldability of austenitic SS 10

2.2 Laser welding and resistance welding of dissimilar metals 12

2.3 Recent progress on NiTi-SS dissimilar welding 16

2.3.1 Typical microstructure and properties of NiTi-SS dissimilar joints 16

2.3.2 IMCs control strategies for NiTi-SS welding 20

2.3.2.1 Adding interlayers 20

2.3.2.2 Post-weld heat treatment 22

2.3.2.3 Laser beam or assembly designs 23

2.3.2.4 Solid-state welding 24

2.3.3 Other problems related to NiTi-SS welding 26

2.4 Summary 29

Chapter 3 Control of IMCs, macrosegregation and porosity in laser welded NiTi-SS joints 31

3.1 Overview 31
3.2 Methodology 31
3.3 Elimination of IMCs network in the fusion zone by laser weld-brazing 34
3.4 Control of macrosegregation and porosity by modifying the heat input mode 44
3.5 Summary 57

Chapter 4 Mixing restriction and brittle phase replacement in resistance spot welded NiTi-SS joints 58

4.1 Overview 58
4.2 Methodology 58
4.3 Effect of Nb interlayer on the microstructure 60
4.4 Effect of Ni interlayer on the microstructure 67
4.5 Mechanical properties and fractography 72
4.6 Joining and failure mechanisms 75
4.7 Summary 79

Chapter 5 Interfacial liquid control and the reaction layer of resistance microwelded NiTi-SS joints 80

5.1 Overview 80
5.2 Methodology 80
5.3 Process window for the interfacial liquid control 84
5.4 Microstructure and mechanical properties of joints 87
5.5 Superelasticity and corrosion resistance of joints 93
5.6 Ultrathin multi-phase reaction layer at the RMWed NiTi-SS interface 103
5.7 Summary 109

Chapter 6 Conclusions and future work 110

6.1 Conclusions 110

6.2 Future work 111

References 113

Appendix A: FVM simulation setup of NiTi-SS laser welding in Chapter 3 121

Appendix B: Supporting information of NiTi-SS RSW in Chapter 4 122

Appendix C: Supporting information of NiTi-SS RMW in Chapter 5 126

Appendix D: List of copyright permissions 134

List of Figures

Fig. 2.1 The development history and biomedical applications of NiTi SMAs [6,25]. 5
Fig. 2.2 Ni-Ti binary phase diagram [2]. 6
Fig. 2.3 Crystal structures of austenite and martensite of NiTi [26]. 6
Fig. 2.4 (a, b) NiTi austenite observed in optical microscopy (OM) image [27] and TEM image [28], respectively; (c, d) NiTi martensite observed in OM image [29] and TEM image [30], respectively. 7
Fig. 2.5 Schematic martensitic transformations by different routes [31]. 8
Fig. 2.6 NiTi loading-unloading and heating-cooling curves showing SE and SME [32]. 9
Fig. 2.7 (a) Schematic diagram representing the influence of Ni content on Ms temperature (concluded from [33]); (b) Schematic diagram representing the influence of stress and temperature on SE, SME and slip (concluded from [34]); (c) loading-unloading curves of the Ni-rich NiTi tested at different temperatures [35]; (d) influence of microstructure on NiTi SE [36]. 10
Fig. 2.8 Microstructures of (a) 316L and (b) 304 SS [40,41]; (c) XRD pattern of γ-Fe [40]. 11
Fig. 2.9 Austenitic SS welding problems: (a) schematic solidification modes of austenitic SS (type A: complete austenite, type AE: primary austenite with eutectic, type FE: primary ferrite with eutectic, type F: complete ferrite) [45]; (b) crack along the weld centerline of austenitic SS [46]; (c) TEM observation of $Cr_{23}C_6$ precipitate; (d) the related diffraction pattern of (c), in which the formation of diffraction rings was due to the presence of $Cr_{23}C_6$ [47]; (e, f) σ phase in austenitic SS [48]; (g-i) typical stress corrosion crack in austenitic SS [49]. 12
Fig. 2.10 (a) Fish bone diagram for factors in laser welding that can influence the weld quality [51]; (b) schematic diagram presenting the RSW mechanism [54]. 14
Fig. 2.11 (a) Schematic of Al-steel laser weld-brazing; (b) cross section of laser weld-brazed joint revealing the FZ at only Al side; (c) temperature field simulation proving that interfacial peak temperature is lower than steel melting point; (d) interfacial IMCs reaction layer [64]; (e) cross section of Mg/Al-Si coated steel RSWed joint with FZ at Mg side; (f) schematic of Mg-steel RSW mechanism indicating the squeezing-out of brittle Mg-Al eutectics; (g) the observation of squeezing-out zone at Mg-steel weld border region [65]. 15
Fig. 2.12 (a) Schematic of 3D chemical analysis method based on layer-by-layer FIB, SEM and EDS; (b) ternary composition histogram (FZ near to NiTi side) superimposed on a 1000 ^{o}C isothermal section of Ni-Ti-Fe phase diagram; (c) the 3D reconstruction of the whole analyzed volume: Region 1: original

NiTi base metal, Region 2: (Fe,Ni)Ti dendrites, Region 3: Ni_3Ti formed in eutectic, Region 4: a possible mixture of phases, Region 5: Fe_2Ti dendrites, Region 6: eutectic of γ-(Fe,Ni) in yellow and Fe_2Ti in red [17]; (d, e) SXRD and hardness testing results of NiTi-SS laser welded joint, respectively [16]..... 17
Fig. 2.13 (a) EBSD phase map indicating the formation of γ and IMCs in the FZ; (b) The typical IMCs network of Fe_2Ti and Ni_3Ti in the FZ; (c,d) The SEM and EBSD images showing the microcrack propagation in Fe_2Ti and Ni_3Ti network [18]; (e) EBSD phase map of the region in FZ adjacent to the NiTi side; (f) TEM diffraction pattern revealing the formation of Fe_2Ti in FZ (lattice parameters of a=0.4734 and c=0.7717); Thermodynamic calculated (g) phases fraction and (h) element fraction in liquid with the concentration of 35.7% Ni-31.6% Ti-30.6% Fe-1.4% Cr (at.%) [72]; (i-l) OM/SEM images of the overall FZ of NiTi-SS weld, with obvious macrosegregations in both butt [73,75,76] and lap [74] joints 18
Fig. 2.14 (a) Typical stress-strain curves of NiTi-SS and NiTi-NiTi laser welded joints during tensile testing [77]; (b,c) fracture path of NiTi-SS joint located at FZ centerline [77,78]; (d,e) fracture path of NiTi-SS joint located at FZ near to NiTi side [73,79]; (f) fracture surface of NiTi-SS laser welded wire joint [16]; (g) in-situ tensile testing results of NiTi-SS laser welded wire joint [75]. 19
Fig. 2.15 (a, b) EBSD phase maps of Ni and FeNi interlayered electron beam welded NiTi-SS FZ, respectively; (c-e) hardness distributions of electron beam welded NiTi-SS FZs without interlayer, with Ni interlayer and with FeNi interlayer, respectively; (f, g) EBSD phase maps of NiTi-SS FZ obtained with Ni interlayer and FeNi interlayer, respectively (microcrack is marked by arrows) [18]; (h) SXRD results of NiTi-SS laser welded joint with Ni interlayer [16]; (i) tensile testing results of NiTi-SS joint with different interlayers [18]; (j) EBSD phase map of the FZ of NiTi-SS laser welded joint with the addition of 50% Ni powder. (k) hardness distributions of NiTi-SS laser welded joints by adding different concentrations of Ni powder [81]. 21
Fig. 2.16 (a) XRD pattern of NiTi-SS weld zone with different Cu interlayer thicknesses [84]; (b) XRD pattern of NiTi-SS weld zone with different Co interlayer thicknesses [85]; (c, d) FZ microstructure and hardness distribution of NiTi-SS joints with Ta interlayers, respectively [78]; (e, f) XRD pattern and hardness distribution of NiTi-SS joint with and without CoCrFeNiMn interlayer, respectively [86]. 22
Fig. 2.17 (a) XRD patterns of the NiTi-SS laser welded FZ obtained with different PWHT temperatures; FZ microstructure of NiTi-SS laser welded joints (b) without PWHT and after PWHT temperature of (c) 650 ^oC and (d) 850 ^oC, respectively; (e) hardness distribution of NiTi-SS joints with and without PWHT [79]; (f) polarization curves of NiTi-SS laser welded joints with PWHT at different temperatures [87]. 23

Fig. 2.18 (a-f) EDS mappings of laser welded NiTi-SS joints without and with laser beam offset, respectively [16]; (g) schematic and cross section of laser welded NiTi-SS joint with Nb+Cu interlayers; (h) the tensile test curves of the joints welded with and without Nb+Cu interlayers, respectively [90]..... 24
Fig. 2.19 (a) EDS mapping and (b) cyclic loading-unloading testing results of NiTi-SS impact welded joint [94]; (c) interfacial microstructure and (d) XRD patterns of friction welded NiTi-steel joint [21]; (e) schematic and (f) interface morphology of ultrasonic welded NiTi-SS joint [20]; (g) schematic, (h) interfacial IMCs layer and (i) tensile testing results of resistance welded NiTi-SS wire-tube joint [19]. 26
Fig. 2.20 (a, b) Simulated stress distribution in laser welded NiTi joint at 5% strain, with the radial and hoop components of the stress tensor, respectively [75]; (c) cross section of NiTi-SS laser welded joint, showing obvious macrosegregation [82]; (d) the pore in laser welded NiTi-SS joint [82]; (f) EBSD result of high-power laser welded B2-NiTi joint [100]. 27
Fig. 2.21 (a) Potentiodynamic polarization curves for NiTi, SS and FSWed NiTi-SS [91]; (b) stress recorded during stress corrosion testing of NiTi wire [101]; (c) AC-SECM images of laser welded NiTi-SS joint, in which brighter regions represent higher local electrochemical activity [102]; (d,e) fracture surfaces of as-received and after-hydrogen-charging NiTi wires, respectively; (f) stress-strain curves of NiTi wires after hydrogen charging with different current densities [104]; (g) schematic of in vivo biocompatibility testing of 3D-printed NiTi [105]. 28
Fig. 3.1 The schematic of laser welding of NiTi-SS wires. 33
Fig. 3.2 Weld appearances and cross sections of NiTi-SS joints obtained with various beam offsets: (a, a1) -0.4; (b, b1) -0.2; (c, c1) 0; (d, d1) +0.2; (e, e1) +0.4. 35
Fig. 3.3 The EDS mapping of the joint welded with (a) -0.4, (b) 0 or (c) +0.4 beam offset, respectively. 36
Fig. 3.4 (a) Weld appearance and (b) cross section of NiTi-SS joint welded using focused laser beam with -0.4 offset. 37
Fig. 3.5 SEM morphologies of the joint welded with -0.4-mm beam offset: (a) cross section of the joint; (b) the corresponding region marked in Fig. 3.5a; (c) the enlarged view of the region marked in Fig. 3.5b; (d, e) the corresponding region marked in Fig. 3.5a; (f)EDS line scanning result along the direction marked in Fig. 3.5b. 38
Fig. 3.6 SEM morphologies of the joint welded with +0.4-mm beam offset: (a) cross section of the joint; (b) the corresponding region marked in Fig. 3.6a; (c) the enlarged view of the region marked in Fig.

3.6b; (d, e) the corresponding region marked in Fig. 3.6a; (f) EDS line scanning result along the direction marked in Fig. 3.6b. 39
Fig. 3.7 SEM morphologies of the joint welded without beam offset: (a) cross section of the joint; (b-g) the corresponding regions marked in Fig. 3.7a; (h, i) EDS line scanning result along the direction marked in Fig. 3.7b and 3.7g respectively. 40
Fig. 3.8 (a) Microhardness line distribution across joints welded with various beam offsets; Microhardness mappings for joints welded with (b) -0.4, (c) 0 and (d) +0.4 beam offset, respectively.. 41
Fig. 3.9 (a) The tensile strength and (b) load-displacement curve of NiTi-SS joints welded with different laser beam offsets. 42
Fig. 3.10 Fracture morphologies of (a) -0.4, (b) 0 and (c) +0.4 offset; the overall SS side fracture surface of the joints welded with (a1) -0.4, (b1) 0 and (c1) +0.4 offset; (a2, a3) the corresponding regions marked at Fig. 3.10a1; (b2, b3) the corresponding regions marked at Fig. 3.10b1; (c2, c3) the corresponding regions marked at Fig. 3.10c1. 43
Fig. 3.11 Schematics of NiTi-SS welding and fracture mechanisms with different beam offsets (not to scale). 44
Fig. 3.12 Weld appearances of laser welded NiTi-SS joints obtained with defocus distance of (a) -1 mm, (b) -0.5 mm, (c) 0 mm, (d) +10 mm, (e) +20 mm, (f) +30 mm; (g) the relationship between defocus distance and laser power density or the selected welding time; (h) average FZ width obtained with different defocus distance. 45
Fig. 3.13 The pore distribution in NiTi-SS weld cross sections obtained with different defocus distances: (a-a2) -1 mm; (b-b2) -0.5 mm; (c-c2) 0 mm; (d-d2) +10 mm; (e-e2) +20 mm; (f-f2) +30 mm. 46
Fig. 3.14 SEM images showing morphologies of the HPD_S joint: (a) cross section of the joint; (b-h) the corresponding regions marked in Fig. 3.14a; (i) EDS line scanning result along the direction marked in Fig. 3.14c. 47
Fig. 3.15 The EDS mapping results of the γ-Fe macrosegregation as shown in Fig. 3.14d. 48
Fig. 3.16 SEM images showing morphologies of the LPD_L joint: (a) cross section of the joint; (b, d and e) the corresponding regions marked in Fig. 3.16a; (c) the corresponding regions marked in Fig. 3.16b; (f) EDS line scanning result along the direction marked in Fig. 3.16b. 49
Fig. 3.17 FVM results of (a) cross sections-melting fields and (b) flow fields of HPD_S and LPD_L modes, respectively. 50

Fig. 3.18 (a) Microhardness line distribution and (b, c) microhardness mappings in joints welded with HPD_S and LPD_L modes, respectively. 51
Fig. 3.19 (a) The tensile strength and (b) load-displacement curves of NiTi-SS joints welded with different welding parameters. 52
Fig. 3.20 (a) Fracture position of LPD_L joint; (b, c) the fracture surface morphologies of LPD_L joint observed from the edge and center regions, respectively; (d) Fracture position of HPD_S joint; (e, f) two types of fracture surface morphologies of HPD_S joint; (g) the large pore observed at the fracture surface of HPD_S joint; (h, i) the corresponding regions marked at Fig. 3.20g. 53
Fig. 3.21 (a) Pore number and average diameter in NiTi-SS joints welded with different parameters; (b) $R\text{-}LCC_{total}$ of pores in NiTi-SS joints welded with different parameters. 54
Fig. 3.22 SEM morphologies of pores in the HPD_S joint with different diameters: (a) 17.4 μm; (b) 46.7 μm; (a) 64.0 μm; (d) 122.1 μm. 55
Fig. 3.23 EPMA analysis of pores with diameters of (a) 100.3 μm, (b) 64.0 μm and (c) 19.1 μm; (d) the corresponding EMPA results marked in Figs. 3.23a-c. 56
Fig. 4.1 XRD results of (a) NiTi and (b) 316L SS BMs; (c) schematic RSW configuration; (d) dynamic resistance curves during the RSW process. 59
Fig. 4.2 Weld appearances and EDS mappings of NiTi-SS RSWed joints: (a, d) without interlayer, (b, e) with Ni interlayer, and (c, f) with Nb interlayer. 61
Fig. 4.3 (a) SEM image of the cross section of Nb-interlayered joint; (b) morphology of the SS BM/SS FZ interface; (c) morphology of the SS FZ; (d) morphology Nb-rich segregation; (e) morphology of the Nb-SS TZ/Nb interface; (f) unmolten Nb interlayer; (g) morphology of the Nb/Nb-NiTi TZ; (h) morphology of the NiTi FZ; (i) morphology of the NiTi FZ/NiTi BM interface; (j) EDS line scanning result according to the direction marked in Fig. 4.3a. 63
Fig. 4.4 SXRD results of the Nb-interlayered NiTi-SS RSWed joint: (a) the overall scanning result and the main phases at the WZ; (b-d) the detailed phase identification at SS BM, WZ and NiTi BM respectively; (e) the calculated microstrain along the joint. 64
Fig. 4.5 (a) HAADF image of the Nb/SS interface region; (b) EDS mappings of square regions marked in Fig. 4.5a; (c) HRTEM image of a dislocation pile-up region in Nb; (d) SAD pattern from the region marked in Fig. 4.5a at Nb; (e) TEM image and SAD pattern from the marked Nb-rich region, as also marked in Fig. 4.5a; (f) HAADF image and SAD pattern from the marked Nb-Fe mixed region, as also marked in Fig. 4.5a (the insert shows the HRSTEM image of a interface between eutectic phases). 66

Fig. 4.6 (a) HAADF image of the detailed Nb/SS interface showing an interfacial layer between Nb and Nb-SS TZ; (b) EDS mappings the region of Fig. 4.6a; (c) HRSTEM image (with averaging filter) of the interfacial region and the SAD pattern from the interfacial layer marked in Fig. 4.6a. (d) HRSTEM image of the interfacial layer/Nb interface; (e) HRSTEM image (with averaging filter) of the interfacial layer/Nb-SS TZ interface. 67
Fig. 4.7 (a-c) SEM images of different regions from the cross section of a directly welded sample; (d) microstructure in weld nugget center; (e, f) morphologies of SS/weld nugget interface and weld nugget/NiTi interface, respectively; (g) EDS line scanning result according to the direction marked in Fig. 4.7a. 68
Fig. 4.8 (a) SEM image of the cross section of Ni-interlayered joint; (b) morphology of the SS/weld nugget interface; (c) weld nugget microstructure near SS side; (d) weld nugget microstructure near the NiTi side; (e) morphology of the weld nugget/NiTi interface; (f) shrinkage cavities in the weld nugget; (g, h) morphologies of cracks in the weld nugget; (i) microstructure near cracks in the weld nugget center region; (j) EDS line scanning result according to the direction marked in Fig. 4.8a. 70
Fig. 4.9 For the composition of 29.1 at.% Ni, 32.4 at. Ti, 30.8 at.% Fe, 7.7 at.% Cr: the calculated equilibrium phase fractions with (a) TCFE10 database and (b) SSOL6 database, respectively; Scheil calculation results with (c) TCFE10 database and (d) SSOL6 database, respectively. For the composition of 51.2 at.% Ni, 19.7 at. Ti, 23.4 at.% Fe, 5.7 at.% Cr: the calculated equilibrium phase fractions with (e) TCFE10 database and (f) SSOL6 database, respectively; Scheil calculation results with (g) TCFE10 database and (h) SSOL6 database, respectively. 71
Fig. 4.10 (a) Microhardness distributions, (b) tensile-shear strength and energy absorption, (c) load-displacement curves and (d) shear/tensile stress-displacement curves of the RSWed joints without interlayer, with Ni interlayer and with Nb interlayer, respectively. 73
Fig. 4.11 Micro-scale indentation results of (a) the BMs and (b) NiTi FZ. 73
Fig. 4.12 SEM images of fracture surfaces from (a1-a4) directly welded joint, (b1-b4) Ni-interlayered joint and (c1-c4) Nb-interlayered joint. 74
Fig. 4.13 EBSD results of the Nb-interlayered joint characterized by (a) IPF map (with grain boundaries), (b) KAM map, and (c) PF maps; (d-f) the joint formation mechanisms of Nb-interlayered joint, directly welded joint and Ni-interlayered joint, respectively. 77

Fig. 4.14 (a) Simulated residual stress distribution in the weld zone of Nb-interlayered joint; (b, c) corresponding residual stress along the line directions marked in Fig. 4.14a; (d) the dynamic residual stress distributions at different temperatures during the cooling. 78
Fig. 5.1 (a, b) μXRD of NiTi and 316L SS BMs, respectively; (c) SEM image of NiTi BM (the inserted EDS line scanning result is according to the region labelled by the blue arrow); (d) EBSD IPF and PF maps of SS; (e) schematic of RMW configuration; (f) schematics of tensile-shear test and superelasticity test for the NiTi-SS joint. (the inserted schematics in Fig. 5.1c, d and e represent observing directions for NiTi and SS cross sections, respectively) 82
Fig. 5.2 (a) Welding current-electrode force process window, (b) the curve of tensile-shear load versus electrode force with the fixed welding current of 0.55 kA; (c) the curve of tensile-shear load versus welding current with the fixed electrode force of 5.3 kgf (corresponding cross sections are inserted); (d) OM images showing the microstructure and interfacial hardness of low-electrode-force and high-welding-current samples; influence of (e) electrode force and (f) welding current on the joint hardness distribution, respectively. 86
Fig. 5.3 (a) Cross-sectional SEM image and (b) the hardness mapping of the optimized joint; (c) EBSD IPF-X map of the interface; (d) EBSD GND density map and its distribution frequency of the interface; (e) EBSD PF maps of interfacial SS and NiTi, respectively; (f) SEM image of the interface between SS and NiTi; (g) EDS line scanning result for the region labelled in Fig. 5.3f; (h) SEM image of NiTi HAZ; (i) SEM image of NiTi HAZ/BM boundary. 88
Fig. 5.4 (a) SEM image and (b) EDS mapping of the squeezed-out zone; (c) EDS line scanning result for the region labelled in Fig. 5.4a; the thermodynamic calculation results of phase formation at (d) Fe-rich region, (e) mixed region and (f) NiTi-rich region considering both equilibrium solidification and Scheil simulation (atomic percentages of Fe and Ti are labelled; microstructural images are inserted in the Scheil simulation figures, with the 2-μm scale bar). 89
Fig. 5.5 (a) TEM image of NiTi-SS interface; (b) deformation twin in the SS side; (c) HRTEM image of the deformation twin boundary; (d) FFT pattern obtained from SS deformation twin boundary; (e) SAD pattern obtained from the main phase of the reaction layer; (f) SAD pattern obtained within one grain of the recrystallized NiTi HAZ. 90
Fig. 5.6 (a) Three typical load-displacement curves and the related deformation images of RMWed NiTi-SS joints during tensile-shear testing (BF sample and low-strength IF sample were welded with

0.55 kA-0.5 kgf and 0.4 kA-5.3 kgf, respectively); (b) simple demos showing the deformation and superelasticity capacities from NiTi-SS RMWed joints. 91
Fig. 5.7 SEM images of fracture surfaces of BF samples welded with (a) low electrode force and (b) high welding current, respectively; (c) SEM images of fracture surfaces of the typical IF sample welded with low welding current; (d) fracture surfaces of the optimized sample (LSCM image of NiTi side with height value; SEM images of SS side); (d1) height profile along a line across NiTi-side fracture surface; (d2) SEM image of SS-side fracture surface (EDS results of all marked positions in Table C3). 93
Fig. 5.8 Load-strain curves obtained from the cyclic loading-unloading test of (a) welded NiTi and (b) NiTi BM, respectively; evolution of (c) residual strain and (d) superelasticity plateau level (at 5.0% strain) during the cyclic test, respectively; nanoindentation load-depth curves of (e) NiTi HAZ of welded joint and (f) NiTi BM, respectively (different colors represent different height in HAZ, while they represent random test points in BM; dashed curve in Fig. 5.8f was from the test on SS showing a typical elastoplastic behavior as a reference). 96
Fig. 5.9 (a) Schematics of hydrogen charging and the subsequent tensile-shear test of NiTi-SS RMWed joints (not to scale); (b,c) load-displacement curves of joints hydrogen charged with different current densities and durations, respectively; (d) joint appearances after hydrogen charging; (e) morphologies of as-received NiTi BM surface and NiTi surfaces/fracture surfaces from welded joint after hydrogen charging and tensile-shear testing. 98
Fig. 5.10 (a) Schematics of Ni ion release experiment and fluorescent characterization (not to scale); (b) fluorescent images and intensity line distributions of the extracted solutions from the Ni ion release test of NiTi BM and welded NiTi with different current application durations. 100
Fig. 5.11 (a) OCP curves of NiTi BM and welded NiTi; (b) PDP curves of NiTi BM and welded NiTi; (c-e) SEM images of NiTi BM after polarization; (f-h) SEM images of welded NiTi after polarization; (i) SS surface morphology after polarization; (j,k) morphologies of squeezed-out zone after polarization (the inserts in Fig. 5.11 c and f were processed by contrast threshold control to indicate the pit densities; EDS results of spots 1, 2 and 3 are shown in Fig. C8). 102
Fig. 5.12 (a) STEM HAADF image of the reaction layer and the related EDS mappings; (b) EDS line scanning according to the direction marked in Fig. 5.12a; (c) HRTEM image and the related FFT pattern of layer Ⅰ; (d) HAADF image and the FFT pattern from layer Ⅰ and inclusions (FFT was obtained from the same region but in a TEM image); (e) SAD pattern from layer Ⅱ, as marked in Fig. 5.12a; (f)

HRTEM image of layer III and TZ, with FFT pattern from layer III; (g-j) HRTEM image and the related atomic-scale EDS mappings or line scanning. 104
Fig. 5.13 (a) HRTEM image of SS/τ interface with ZA aligned for τ phase; (b-c) FFT patterns obtained from the whole region, the SS side, and the ROL, respectively; (e) HRTEM image of SS/τ interface showing the CR between ROL and τ; (f) HRTEM image of SS/τ interface with ZA aligned for SS; (g-i) FFT patterns obtained from the SS side, τ, and the ROL, respectively; (j) HRTEM image of SS/τ interface showing the CR between ROL and SS. 106
Fig. 5.14 (a) Schematics of epitaxial growth of ROL on τ substrate; (b) h_c-f curves plotted from equation (5.1); (c,d) HRTEM IFFT of the SS/ROL/τ interfaces with masks on $(1\mathbf{1}1)_{ROL}$//$(1\mathbf{4}1)_{\tau}$ and $(0\mathbf{2}0)_{ROL}$//$(33\mathbf{2})_{\tau}$, respectively; (e, f) HRTEM IFFT of the SS/ROL/τ interfaces with masks on $(1\mathbf{1}1)_{ROL}$-$(002)_{SS}$ and $(0\mathbf{2}2)_{ROL}$-$(220)_{SS}$, respectively. 108
Fig. A1 The mesh for FVM simulation of NiTi-SS wires laser welding. 121
Fig. B1 (a) Selected region for the FIB and TEM (SEM high current mode, corresponding to the region in Fig. 4.3e); (b-f) FIB thinning process. 122
Fig. B2 Meshing and dimensions for the simulated region. 123
Fig. B3 Interface constraint and boundary conditions used in the modeling. 124
Fig. B4 OM morphologies of the hardness indents and the related average hardness for (a) Ni foil and (b) Nb foil, respectively. 125
Fig. B5 Tensile curves of (a) SS BM and (b) NiTi BM. 125
Fig. C1 (a) SEM image of the optimized NiTi-SS interface; (b) the region of interest for FIB TEM sample preparation; (c-f) FIB sample thinning process. 126
Fig. C2 SEM image of interfacial residual IMCs and the related EDS mapping results. 126
Fig. C3 SEM image of IMCs penetration and the related EDS mapping results. 127
Fig. C4 SEM images of the optimized joint observed by placing (a) SS and (b) NiTi on the top, respectively; (c) SEM images and EDS mappings for the overall cross section and squeezed-out zone, respectively. 128
Fig. C5 (a) EBSD band contrast map, (b) EBSD IPF-X map and (c) EDS mapping results of the NiTi-SS RMWed interface (the reaction layer was difficult to be indexed by EBSD, due to its ultrafine thickness and grain size that are beyond the capacity of SEM). 129
Fig. C6 (a,b) SEM images of fracture surface observed from SS side; (c-f) EDS mapping results. 129

Fig. C7 Fitting results of PDP curves of (a) NiTi BM and (b) welded NiTi using Tafel extrapolation tool in Origin software. 130
Fig. C8 (a-c) EDS results for spot 1, 2 and 3 as marked in Fig. 5.11d, e and h, respectively; (d) SEM image and EDS results of the selected NiTi area without deep pits after polarization. 131
Fig. C9 Some other typical SEM images of particles with pits in NiTi BM after polarization. 131
Fig. C10 Schematics showing joining formation of NiTi-SS during RMW and tensile-shear test of the joint, with SEM images showing NiTi HAZ and BM microstructures. 132
Fig. C11 STEM HAADF image of the NiTi-SS RMWed interface, with EDS mapping and SAD results. 132

List of Tables

Table 2.1 Some properties of B2 NiTi and 316L SS [66–71] (note that these properties may vary depending on different temperatures and material processing statuses). 15
Table 2.2 Summary of NiTi-SS dissimilar welding research progress (D: diameter and T: thickness) 30
Table 3.1 Welding parameters in Section 3.3. 33
Table 3.2 Welding parameters used in Section 3.4. 34
Table 3.3 EDS analysis (at.%) of different positions marked in Fig. 3.5. 38
Table 3.4 EDS analysis (at.%) of different positions marked in Fig. 3.6. 39
Table 3.5 EDS analysis (at.%) of different positions marked in Fig. 3.7. 40
Table 3.6 EDS analysis (at.%) of different positions marked in Fig. 3.10. 43
Table 3.7 EDS analysis (at.%) of different positions marked in Figs. 3.14 and 3.16. 49
Table 4.1 EDS analysis (at.%) of different positions marked in Fig. 4.12. 75
Table 5.1 Interfacial phases from SS to NiTi 105
Table C1 EDS analysis (at.%) of different positions (Z1-Z4) marked in Fig. C4. 128
Table C2 Phase mole fraction (%) of squeezed-out zone from thermodynamic calculation (300 K). 129
Table C3 EDS analysis (at.%) of different positions marked in Fig. 5.7. 130
Table C4 Data of NiTi BM and welded NiTi from OCP (Fig. 5.11a) and PDP curves (Fig. 5.11b) using Tafel extrapolation method. 131
Table C5 Related physical properties of the ROL layer for the h_c-f equation. 133

Chapter 1 Introduction

1.1 Background

Driven by rising disease prevalence, extending life expectancy and aging population, global medical device manufacturing market is growing rapidly and estimated to increase from USD 65.9 billion in 2021 to USD 113.3 billion in 2026 by an annual grow rate of 11.5% [1]. The COVID-19 pandemic was also accelerating the expansion and upgradation of the medical device industry. Since its discovery in the 1960s at the United States Navy Ordnance Laboratory (NOL), Nickel-Titanium (NiTi, also known as Nitinol) has been considered as one of the most promising biomedical materials for fabrication of biomedical devices, thanks to its excellent functional properties of shape memory effect (SME) and superelasticity (SE), mechanical properties and biocompatibility [2–5]. Nowadays, the applications of NiTi as an implantable material or in medical devices span nearly the entire human body. These include uses such as dental arch wires, heart stents, and foot bone fixation, demonstrating its versatility and significance in modern medicine [6]. As a conventional biomedical material, stainless steel (SS) has already been widely used, especially in some circumstances requiring high corrosion resistance and good formability [7–9].

The development of the medical industry promotes the demand for multifunctional biomedical devices that combine various materials to take advantage of their unique functional or mechanical properties. Dissimilar welding of NiTi to SS is of significant prospect since it can expand application of both materials and contributes to the successful fabrication of multifunctional devices for medical diagnosis and therapy. For instance, in a NiTi-SS hybrid orthodontic device, the corrective force on abnormal teeth is provided by superelastic NiTi wires, meanwhile SS wires can be designed to tailor the whole structure by a better formability and make the device more anticorrosive in oral cavity [10,11]. The joining of NiTi and SS has been applied for the designs of many advanced biomedical device prototypes, such as the multi-functional active catheter with joined SS and NiTi coils [12] and the flexible steerable cannula based on several SS segments connected by NiTi [13]. Besides, NiTi-steel welding is also widely used in aerospace, automobile, sensor, robotics and other industries. For instance, Boeing has developed a variable geometry chevron on the jet engine, which may require the joining between NiTi-based shape memory alloy and steel sheets [14]. The advanced automobile designs of active louver, grab handle and air dam are made of NiTi sheet, which need to be welded to steel structures [14]. Some robotic prototypes also call for the joining of NiTi-SS strips [15].

Achieving reliable dissimilar joining between NiTi and SS while ensuring the desired joint properties is a critical key in the fabrication of these devices or structures. Various welding/joining techniques (e.g., laser welding [16,17], electron beam welding [18], resistance welding [19], ultrasonic welding [20], friction welding [21], etc.) have been adopted for this objective, however, NiTi-SS dissimilar welding is still highly challenging as the welded joint is usually extremely brittle due to the formation of many types of intermetallic compounds (IMCs) in the weld zone. Some typical dissimilar welding defects exist in NiTi-SS joint. The degradation of NiTi or SS mechanical/functional properties after welding is also an issue. The biocompatibility and corrosion resistance of NiTi-SS joints also need to meet the requirements for practical and specific applications. All these joint properties are related to the microstructure of NiTi-SS weld. Therefore, understanding and controlling the microstructure in NiTi-SS welds are crucial to enhance the comprehensive properties of the joints.

1.2 Objectives

The goal of this study is to achieve the reliable dissimilar welding between NiTi and SS. To promote the achievement of this goal and to deepen the understanding of dissimilar welding in a multiple-alloying-element system and material interface, the detailed objectives can be as follows:

I. Understand the metallurgy of the Ni-Ti-Fe-Cr system and control the formation of IMCs and weld defects in the NiTi-SS fusion zone (FZ) with the flexibility of laser beam.
II. Investigate the effects of two IMCs control strategies, i.e., mixing restriction and brittle phase reduction in resistance spot welding (RSW) of NiTi-SS, based on the thermomechanical processing.
III. Built upon the better understanding of the mixing and interface between NiTi and SS, propose a new approach to realize superior comprehensive properties in NiTi-SS joint and explore the nature of dissimilar material interface.

1.3 Thesis outline

Chapter 1 introduces the research background and objectives.

Chapter 2 briefly overviews the material science of NiTi and SS base materials. Fundamentals and some case studies of laser welding and resistance welding are then introduced. The recent progress on NiTi-SS dissimilar welding is reviewed, hence the related welding problems and the strategies are summarized.

Chapter 3 corresponds to objective I. This chapter focuses on the influence of different heat input modes (combinations of laser power density, welding time and beam offset) on microstructural evolution and mechanical properties of laser welded NiTi-SS joints. The weld-brazing mode is achieved where the FZ IMCs network can be eliminated. Formation mechanisms and mitigation strategy of macrosegregation and porosity are also discussed.

Chapter 4 corresponds to objective II. This chapter investigates for the first time, the feasibility of the two IMCs control strategies in NiTi-SS RSW. The joining and failure mechanisms of RSWed joints are uncovered. Some new insights are provided when combining the RSW thermomechanical processing and the IMCs control strategies for NiTi-SS joining.

Chapter 5 corresponds to objective III. This chapter presents a novel approach during resistance microwelding, integrating the advantages of both fusion and solid-state welding methods. The process window, microstructure, and comprehensive properties of welded joints are studied. The ultrathin NiTi/SS interface with some new phenomena is investigated.

Chapter 6 summarizes the key conclusions of this thesis and offers recommendations for future research directions in this field.

Chapter 2 Literature review

2.1 Introduction of NiTi and SS

In this section, the base materials for welding, namely NiTi and SS are introduced, with a focus on their chemical compositions, crystal structures, microstructures, phase transformations, mechanical and functional properties, and weldability. Special emphasis is placed on NiTi, as its performance is often more critical, and many welding challenges in NiTi-SS joints typically arise from the NiTi side. It should be noted that the introduction of these two materials in this section is brief, always with a primary focus on welding-related aspects.

2.1.1 Physical metallurgy of NiTi

NiTi shape memory alloys (SMAs) are a group of equiatomic or near-equiatomic Ni-Ti binary alloys known for their unique functional properties, including shape memory effect (SME) and superelasticity (SE). Although SME was first discovered in Au-Cd and In-Tl alloys in the 1950s [22,23], it gained widespread attention after NiTi was identified by Buehler et al. in NOL in 1963 (Ni+Ti+NOL=Nitinol) [24], thanks to its better mechanical properties offering enhanced potential for practical applications. Fig. 2.1a exhibits the development history of NiTi SMAs [6]. Nowadays, NiTi is commercially used in various industries, particularly in biomedical device fabrication [25] (Fig. 2.1b). As the demand for specialized applications grows, further processing of NiTi, including welding, is playing a critical role in meeting specific industrial requirements.

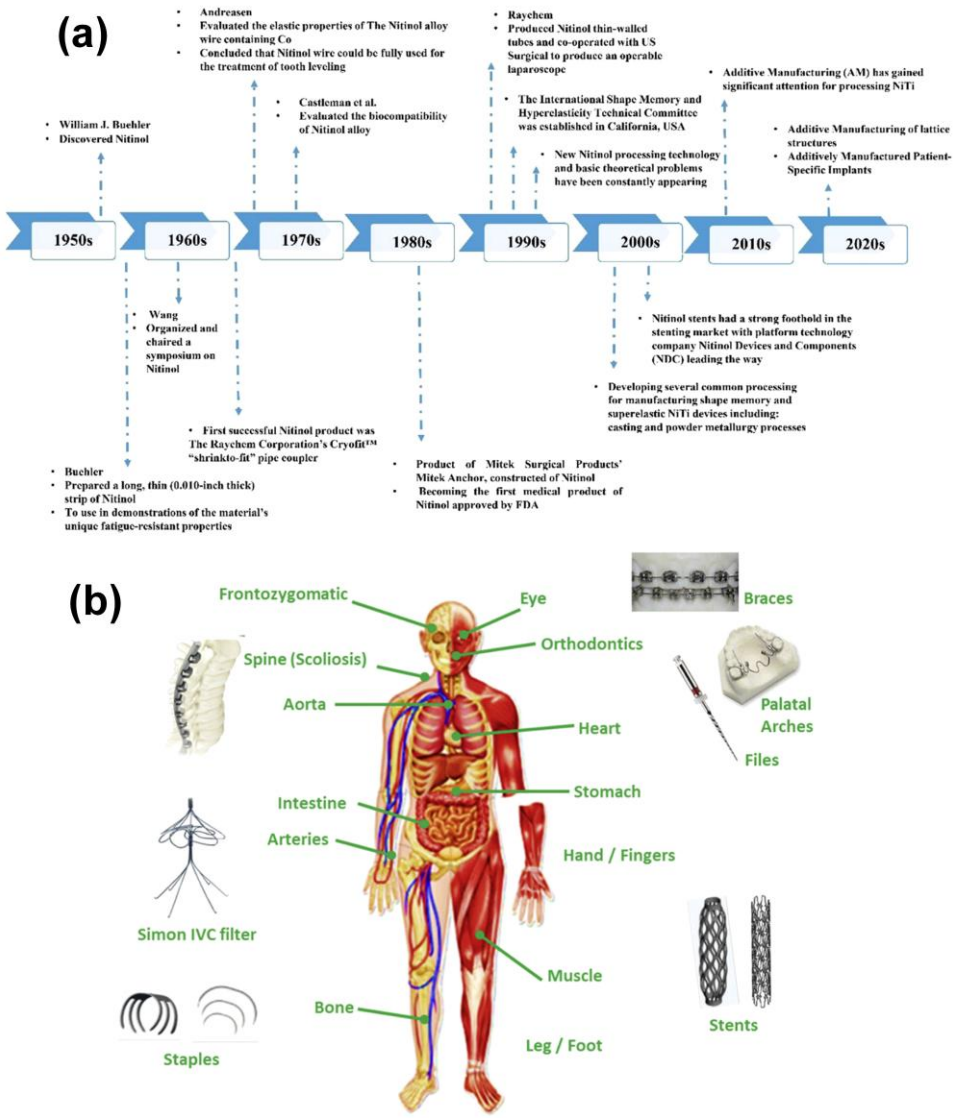


Fig. 2.1 The development history and biomedical applications of NiTi SMAs [6,25].

Fig. 2.2 presents the Ni-Ti binary phase diagram [2]. The NiTi region is located around 50 at.% Ni. Within this region NiTi has mainly two stable or metastable phases, i.e., austenite and martensite. The crystal structures of these two phases are shown in Fig. 2.3 [26]. Like the concepts in steel, austenite is the high-temperature phase of NiTi with a B2 CsCl-type ordered structure (which can be considered as two interpenetrating simple cubes), and the lattice parameter is $a \approx 0.3015$ nm. NiTi martensite is the low-temperature phase with a B19' monoclinic structure. The lattice parameters are $a \approx 0.2889$, $b \approx 0.4120$, $c \approx 0.4622$ (nm), $\beta \approx 96.8^{o}$ [2]. It is necessary to mention that the NiTi B19' martensite consists of twinned and self-accommodated 24 variants. The twinned martensite can undergo a detwinning process by externally applied stress. R-phase is the intermediate phase that sometimes forms in the case that the

maximum strain cannot accommodate the B2-B19’ transformation without macroscopic plastic deformation. R-phase is influenced by dislocation, secondary-phase precipitation and nanostructure. It has a trigonal crystal structure, as it usually originates from the B2 {111} plane stretching [2].

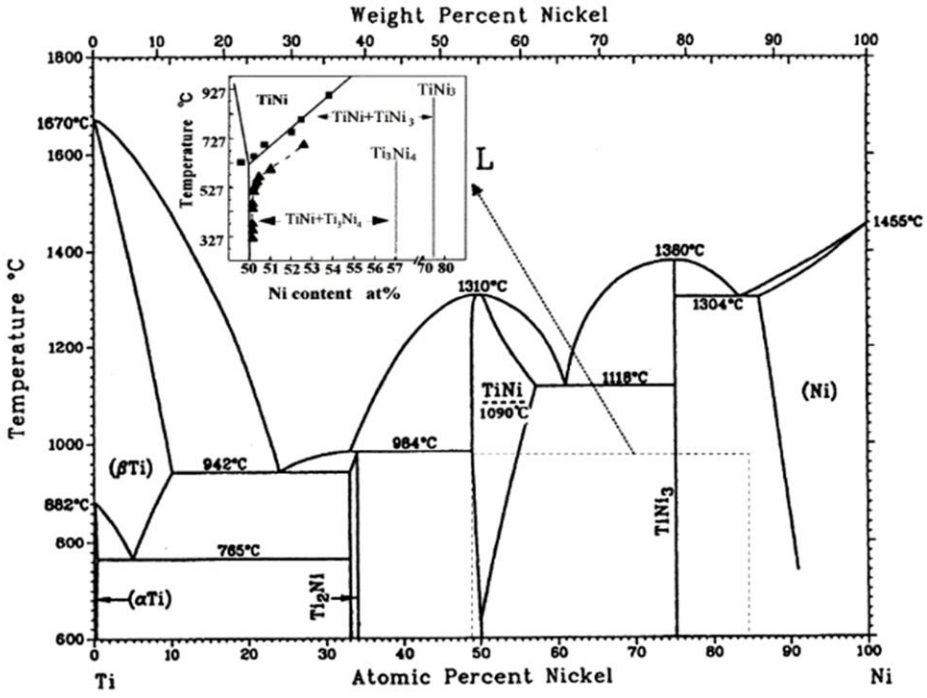


Fig. 2.2 Ni-Ti binary phase diagram [2].

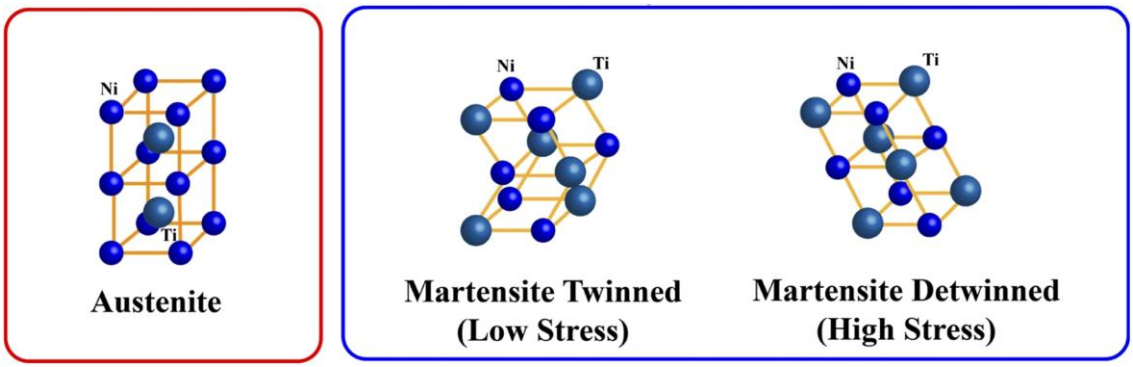


Fig. 2.3 Crystal structures of austenite and martensite of NiTi [26].

Fig. 2.4 shows the experimentally observed NiTi austenite and martensite in different scales. Annealed austenite usually exhibited a morphology of equiaxed grains. Obviously twinned microstructure could be observed in NiTi martensite by transmission electron microscope (TEM), and the corresponding selected area diffraction (SAD) in Fig. 2.4d indicated a <001> type II twins.

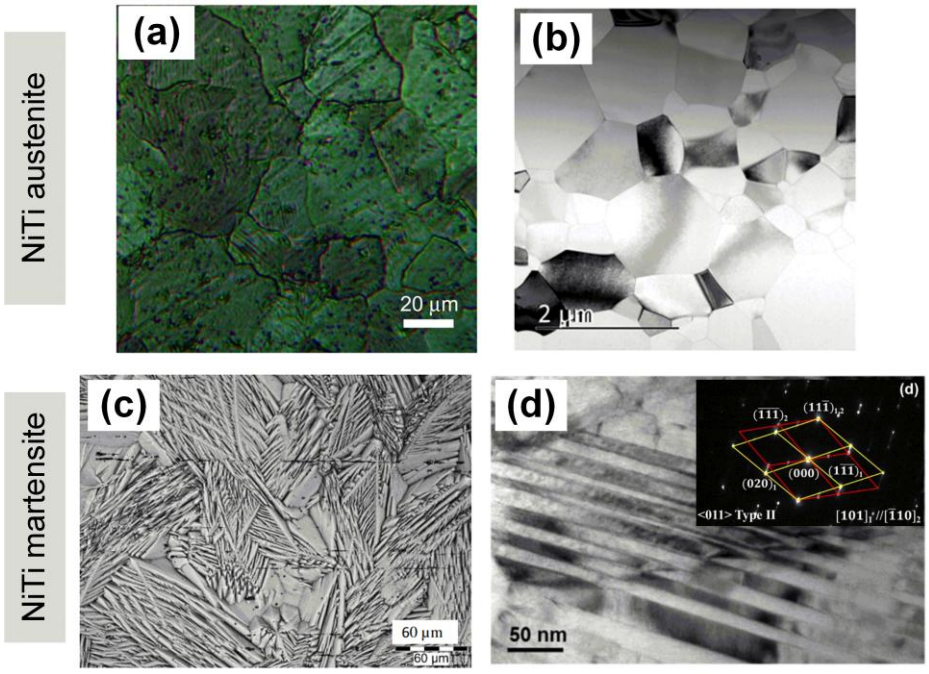


Fig. 2.4 (a, b) NiTi austenite observed in optical microscopy (OM) image [27] and TEM image [28], respectively; (c, d) NiTi martensite observed in OM image [29] and TEM image [30], respectively.

NiTi martensitic transformations are a series of diffusionless phase transformations between NiTi austenite and martensite, including B2-B19', B2-R-B19', etc. Here, the most significant one, namely the B2-B19' transformation is detailed, as it is the main driving force for several well-known NiTi functional properties. NiTi martensitic transformation can be induced by either temperature change or externally applied stress, and it is self-recoverable in some cases. Fig. 2.5 illustrates the schematic diagram of NiTi martensitic transformation from austenite to martensite by different routes [31]. By cooling NiTi down to M_s, austenite starts to transform into twinned martensite, and the NiTi consists of entirely twinned martensite when the temperature is lower than M_f. The twinned martensite variants can self-accommodate, resulting in negligible macroscopic deformation during this temperature-controlled A-M (austenite to martensite, conversely M-A) transformation. Further application of external stress on this twinned martensite enables the detwinning process and causes macroscopic deformation of the material. In another case, the external stress applied to the austenite can lead to direct transformation into detwinned martensite with macroscopic deformation. Heating either twinned martensite or detwinned martensite up to A_s can initiate the reverse transformation to austenite, and this M-A transformation is completed when the temperature is higher than A_f.

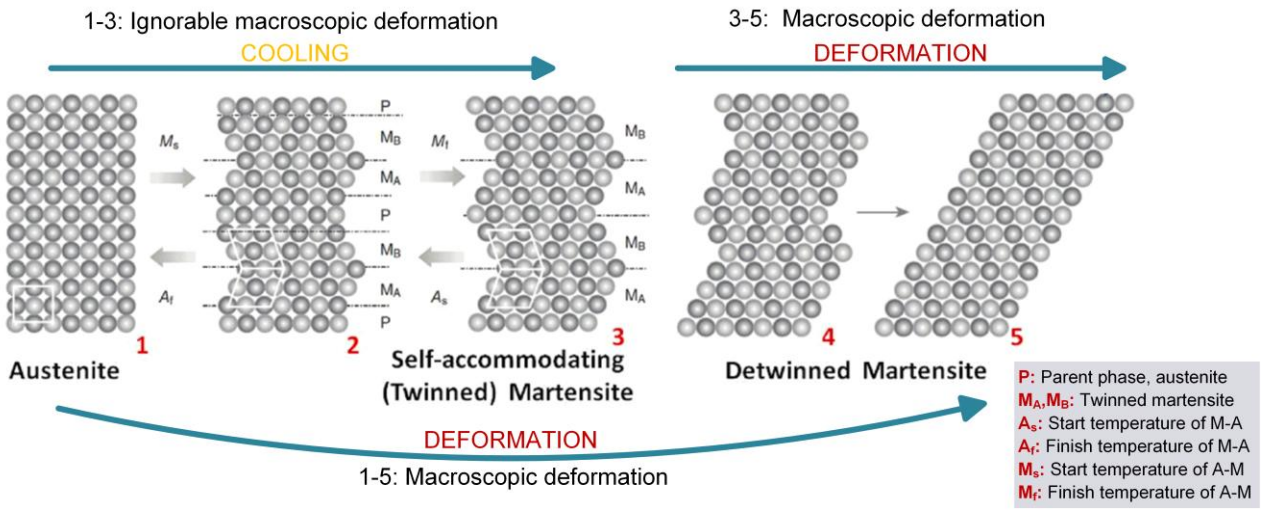


Fig. 2.5 Schematic martensitic transformations by different routes [31].

2.1.2 Superelasticity and shape memory effect of NiTi

Superelasticity (SE) and shape memory effect (SME) are the most well-known NiTi functional properties, and they are both based on the NiTi martensitic transformations. Fig. 2.6 presents the NiTi loading-unloading and heating-cooling curves, in which SE and SME are described [32]. Superelasticity is realized with the original state of NiTi austenite. After the linear elastic stage of the austenite, continued external stress results in a stress-induced transformation of NiTi austenite to detwinned martensite, with an almost constant stress level. The strain can be fully recovered when unloaded within this A-M transformation period, because the detwinned martensite can spontaneously transform back to austenite. The reversible curve is nonlinear and exhibits a different route compared to that in the loading stage, with an extremely large recoverable strain (can reach up to 10%). Therefore, this property is named superelasticity or pseudoelasticity. The shape memory effect occurs when NiTi is in the twinned martensite phase during a loading-unloading-heating-cooling cycle. Applying external stress to the twinned martensite leads to detwinning with nearly constant stress, resulting in significant macroscopic deformation. This strain/deformation is retained after unloading. Heating this detwinned martensite up to A_f completes the M-A transformation and the resultant shape recovery. Subsequently, the A-M transformation occurs by cooling the austenite down to M_f, restoring the original shape of the NiTi twinned martensite.

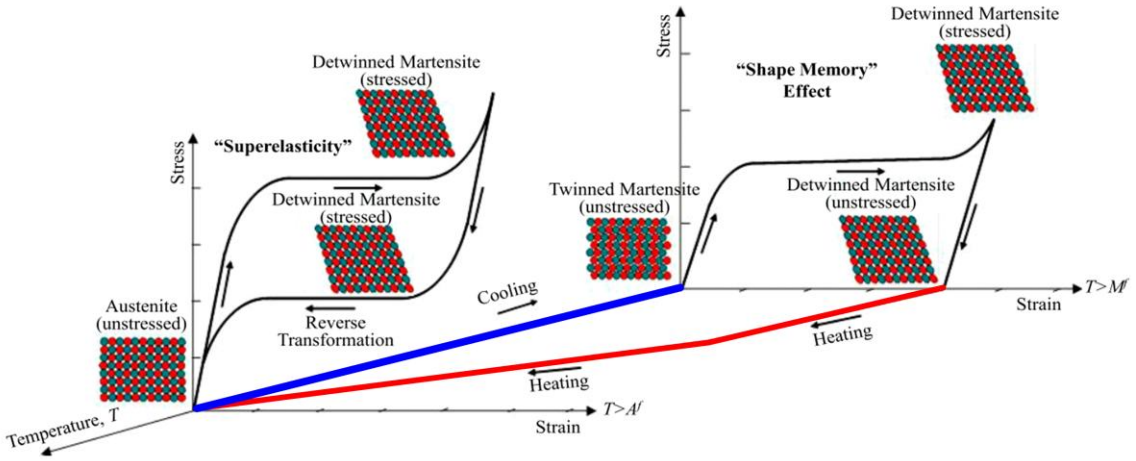


Fig. 2.6 NiTi loading-unloading and heating-cooling curves showing SE and SME [32].

The original phase determines whether the NiTi is superelastic or shape-memory, and it is very susceptible to temperature, chemical composition, and microstructure. As shown in Fig. 2.7a [33], Ni:Ti ratio affects the M_s temperature significantly even with a 0.1 at.% change. Higher Ni content decreases the M_s temperature and thus contributes to the stability of austenite and SE at room temperature. In contrast, Ti-rich NiTi is usually used for its SME at room temperature. Simply put, there is a "competition" between martensitic transformation and slip. Fig. 2.7b describes the occurrence of SME and SE under different temperatures and stresses [34]. It is generally believed that transformation-based SE and SME are both limited by slips (line A and line B). Some experimental results demonstrated the "competition" between phase transformation and dislocation slip, as seen in Fig. 2.7c [35]. Microstructural factors, including dislocations, secondary particles/phases, grain size, significantly influence the SME or SE behavior of NiTi. The loading-unloading curves of cold-rolled (CR), gradient-structured (GS) and coarse-grained (CG, usually through complete annealing to obtain the coarse equiaxed grains) NiTis are shown in Fig. 2.7d [36]. CR and GS samples, especially the CR sample, were not typically superelastic because of the formation of deformation texture, refined grains and high-density defects (as revealed in the TEM observation). These cold-worked structures might promote the slip instead of the martensitic transformation. Therefore, the influence of any material processing (e.g., welding) on the modification of composition and microstructure of NiTi should be taken into account, to preserve or even enhance the functional properties.

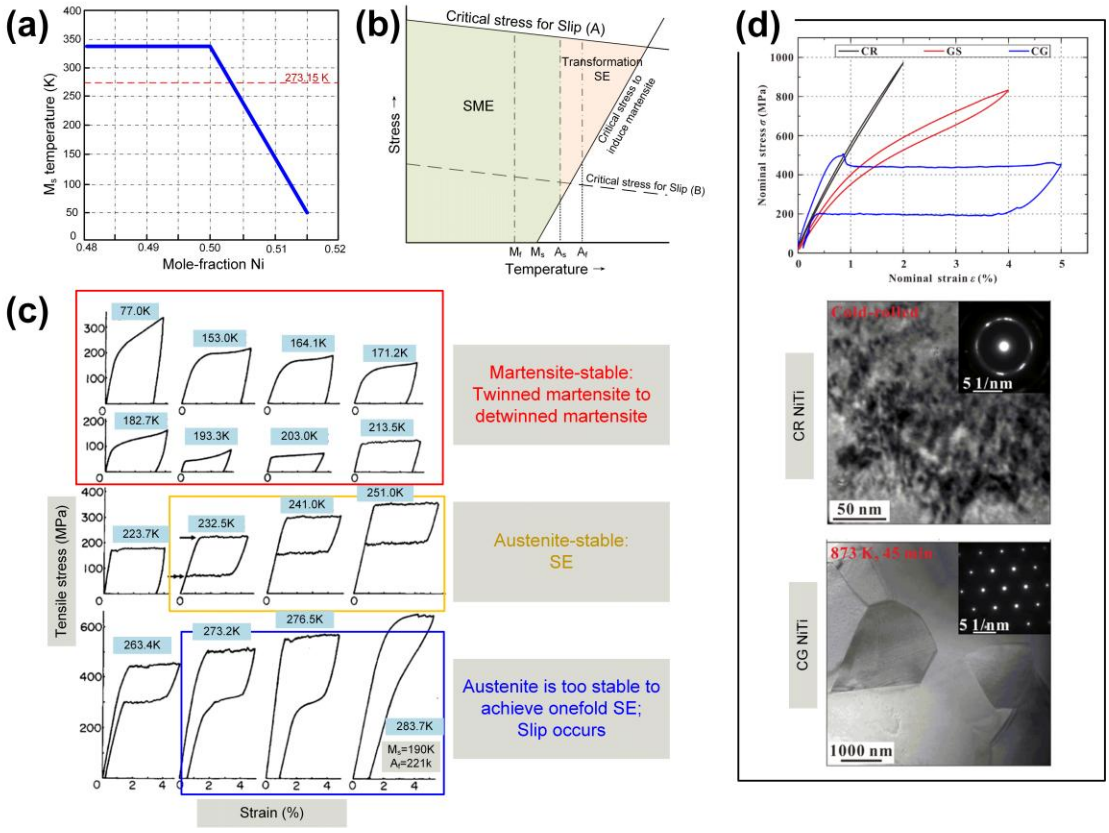


Fig. 2.7 (a) Schematic diagram representing the influence of Ni content on Ms temperature (concluded from [33]); (b) Schematic diagram representing the influence of stress and temperature on SE, SME and slip (concluded from [34]); (c) loading-unloading curves of the Ni-rich NiTi tested at different temperatures [35]; (d) influence of microstructure on NiTi SE [36].

2.1.3 Metallurgy and weldability of austenitic SS

Steel is essentially an iron-based alloy with some other elements acting as the “solute”. Nowadays, stainless steel (SS) is one of the most indispensable materials. SS is a traditional biomedical material; the application of SS as a bone implant was reported as early as the 1920s [9]. The term "stainless" refers to the material's ability to resist staining, rusting, and corrosion. To achieve this "stainlessness," at least 11 wt.% chromium (Cr) should be added to the iron matrix. Cr forms a compact, self-healing oxide layer on the surface of the steel, which prevents harmful reactions between iron and its surrounding environment [37]. In addition to Cr, modern stainless steel usually consists of various trace alloying elements to enhance specific properties [9,37–39]. Ni, as an austenite-stabilizing element, is added to SS to enhance the corrosion resistance and obtain non-magnetic austenitic steel at room temperature with good toughness, formability and wear resistance. Unlike in NiTi, the concept of “austenite” in steel refers to the high-

temperature phase with a face-centered cubic (FCC) crystal structure, also known as γ-Fe. Various grades of austenitic stainless steel are classified based on their composition or intended applications, with 316L, 304, 302, and 321 SS being widely used in biomedical device manufacturing [38]. Adding a small amount of molybdenum (Mo, typically ~2 wt.%, as in 316L SS) can help improve corrosion resistance to chlorides, which are commonly found in seawater and the human body. Therefore, mainly Fe, Ni and Cr (over 10 wt.%) from the SS side can actively contribute to the formation of the metallurgical system during NiTi-SS welding. Fig. 2.8 presents the typical annealed microstructures of 316L and 304 SS [40,41], two of the most commonly used medical-grade stainless steels. Both materials primarily consist of equiaxed austenitic grains with some annealing twins. Additionally, a small amount of residual ferrite is observed in 304 SS. A typical X-ray diffraction (XRD) pattern of austenite is presented in Fig. 2.8c, in which FCC γ-Fe was detected.

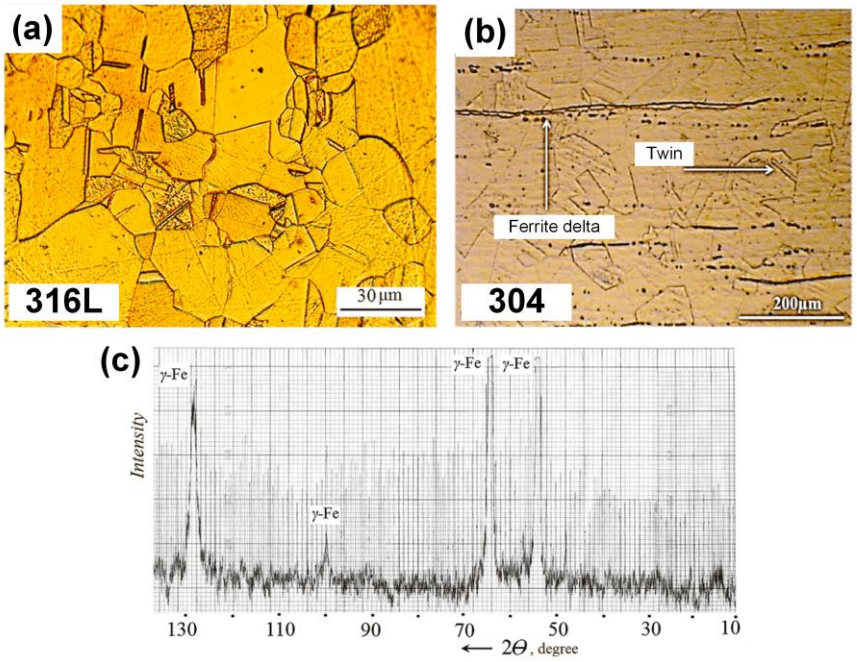


Fig. 2.8 Microstructures of (a) 316L and (b) 304 SS [40,41]; (c) XRD pattern of γ-Fe [40].

Compared to NiTi, the SS side encounters fewer challenges during NiTi-SS dissimilar welding. Austenitic SS is generally regarded as the most weldable type of steel because there is no significant phase transformation at high temperatures [41,42]. It is still necessary to understand the weldability of austenitic SS to ensure the preservation of its desired properties in the dissimilar joint. Austenitic SS has a high susceptibility to solidification cracking [43,44], especially during a welding process with high heating and cooling rates and nonequilibrium solidification. In Fig. 2.9a and b [45,46], a solidification crack formed

along the weld centerline of austenitic SS, due to changes in solidification behavior and compositional segregation which promoted complex austenite-ferrite or their eutectic structures. Another issue in SS welding is the weakening of corrosion resistance caused by Cr-rich precipitates in the weld zone. As a highly Cr-concentrated precipitate (Fig. 2.9c and d [47]), $Cr_{23}C_6$ easily forms at austenite grain boundaries during high-temperature exposure. Additionally, other issues such as Fe-Cr brittle IMC (σ phase) precipitation (Fig. 2.9e and f [48]) and stress corrosion cracking (Fig. 2.9g-i [49]), also need to be considered during austenitic SS welding.

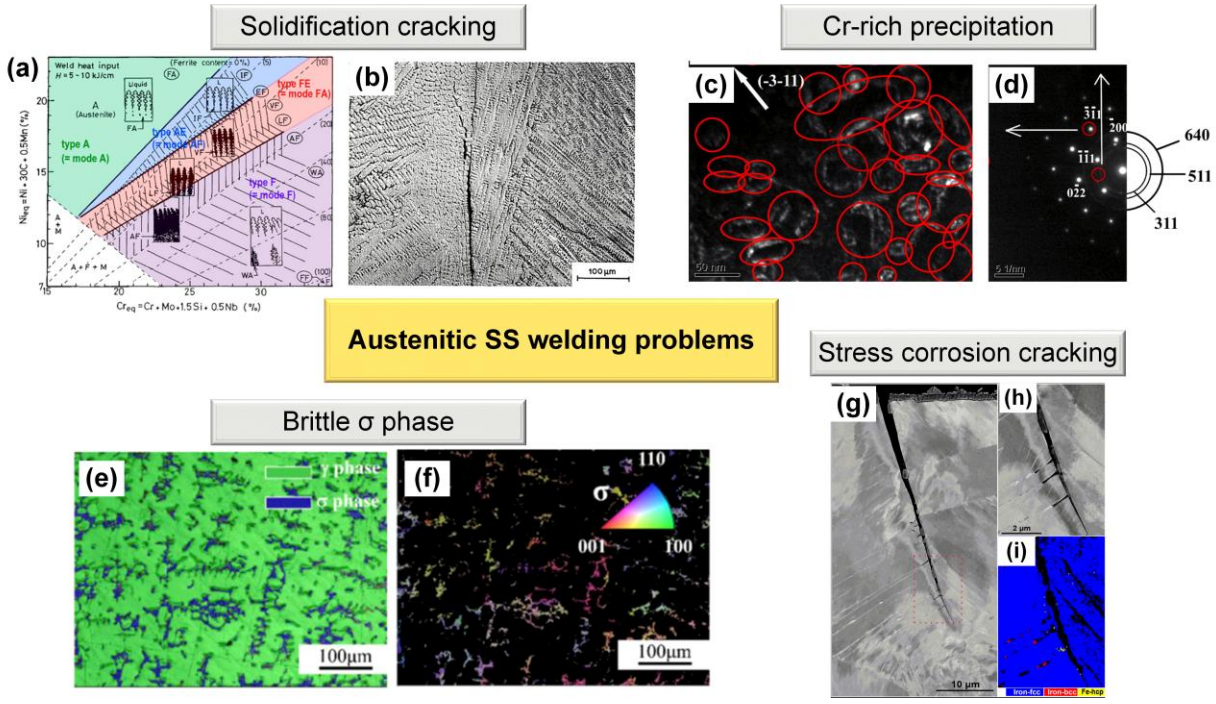


Fig. 2.9 Austenitic SS welding problems: (a) schematic solidification modes of austenitic SS (type A: complete austenite, type AE: primary austenite with eutectic, type FE: primary ferrite with eutectic, type F: complete ferrite) [45]; (b) crack along the weld centerline of austenitic SS [46]; (c) TEM observation of $Cr_{23}C_6$ precipitate; (d) the related diffraction pattern of (c), in which the formation of diffraction rings was due to the presence of $Cr_{23}C_6$ [47]; (e, f) σ phase in austenitic SS [48]; (g-i) typical stress corrosion crack in austenitic SS [49].

2.2 Laser welding and resistance welding of dissimilar metals

Laser welding and resistance welding are effective techniques for dissimilar-metal joining. Their unique advantages in NiTi-SS welding have been attracting researchers' attention, and this thesis work was conducted using these two welding methods. Therefore, laser welding, resistance welding, and typical case studies on dissimilar-metal welding are briefly introduced in this section.

Laser welding is achieved by the energy from a laser beam with high power density (can be over 10^6 W/cm^2). This method is highly flexible and precise, making it particularly suitable for small-scale joining of a wide range of materials. This is especially true for NiTi, which is often used in thin sheets or submillimeter wires [50–52]. Due to its non-contact nature, laser welding offers high efficiency and low cost, eliminating the need for consumable accessories. Lasers are categorized into continuous wave (CW) lasers and pulse wave (PW) lasers, each with various wavelengths. Key parameters in laser welding include laser power, welding speed, beam diameter, and pulse shape. As illustrated in Fig. 2.10a, a fishbone diagram lists the factors in laser welding that influence weld quality [51]. Different combinations of these parameters significantly influence microstructure and properties of the weld zone.

Resistance welding is widely used in unitized vehicle construction. A typical body-in-white constructed contains as many as 6000 resistance spot welds [53]. As seen in Fig. 2.10b [54], the mechanism of resistance spot welding (RSW) is described as follow. After assembly and positioning, the electrodes approach the assembled materials. Subsequently, the base materials are squeezed by electrode force. The welding current is passed through the tightly contacted materials; hence the heat is generated mainly at the interface of metals due to the existence of surface contaminations and asperities, but further heat generation is determined by the bulk resistance, namely the resistance of the whole material system, according to the Joule's law:

$$Q=\int_{t1}^{t2} I^2(t)R(t)\,dt \tag{2.1}$$

where Q is the energy delivered into the materials in Joule, $t1$ and $t2$ respectively denote the beginning and terminating time of the electrical current, $I(t)$ is the welding current, $R(t)$ is the dynamic resistance. For an alternative current RSW machine, I for Joule's law is the root mean square value:

$$I = I_{RMS} = \sqrt{\frac{\int_{t1}^{t2} I_{max}^2 dt}{t2-t1}} \tag{2.2}$$

where I_{max} is the peak value of the sine wave. The weld nugget formation is realized by all the resistance heat. RSW is a typical thermomechanical processing for materials. The flexibility of resistance welding can be achieved by designing electrodes with various tip geometries and dimensions.

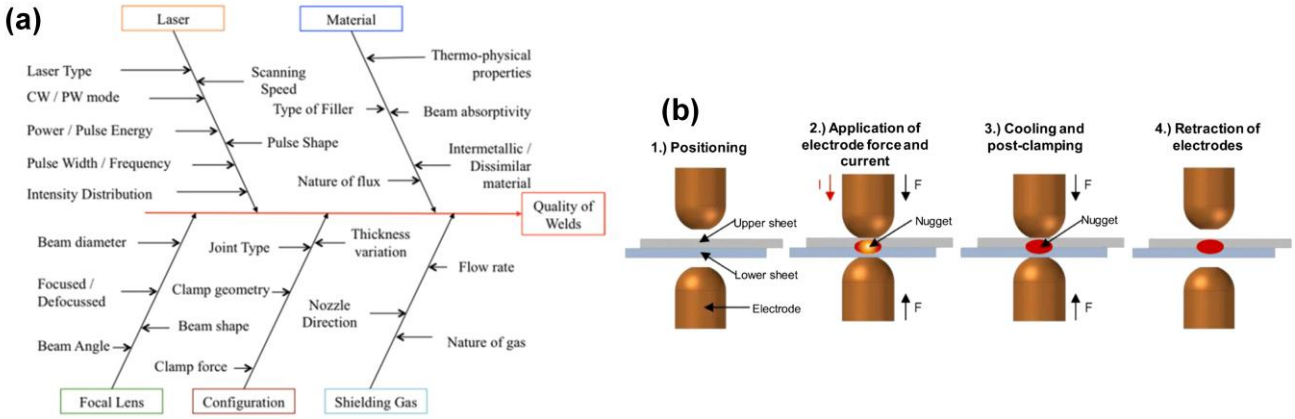


Fig. 2.10 (a) Fish bone diagram for factors in laser welding that can influence the weld quality [51]; (b) schematic diagram presenting the RSW mechanism [54].

It is necessary to classify dissimilar welding cases according to two material combinations. If the dissimilar metals are nonreactive and immiscible (such as Mg-steel [55–57] and Mg-Ti [58,59]), there is usually a weak crystallographic bonding between phases from base metals (BMs). Therefore, the first task is to realize the good metallurgical bonding between BMs, which is typically facilitated by the addition of alloying elements. Once this is achieved, further optimization of the interfacial reaction layer should be performed. Secondly, if the dissimilar materials are reactive or miscible, there is either an interfacial reaction layer (usually a layer consisting of IMCs) between BMs (e.g., Al-steel [60,61] and Al-Cu [62], which have significantly different melting points), or a complex FZ formed by the highly mixed dissimilar molten metals (such as NiTi-SS [17,50] and Inconel-steel [63], which have similar melting points). The main challenge for the second type of dissimilar welding is controlling the formation of brittle IMCs in either the interfacial layer or the entire FZ. A metallurgical system containing multiple alloying elements serves as the foundation for the formation of various IMCs in FZ or interface, especially considering the nonequilibrium solidification in welding process. Laser welding and resistance welding are effective to control this metallurgical system and the resultant microstructure, benefiting from the highly controllable laser beam and thermomechanical processing, respectively. For instance, laser weld-brazing mode could be realized in Al-steel welding where the FZ only formed at Al side because of its lower melting point (Fig. 2.11a-d) [64]. In this case, the mixing of dissimilar molten metals and the IMCs formation were suppressed; IMCs layers at the brazed interface need to be further optimized to improve the joint properties. Fig. 2.11e shows that the FZ only formed at Mg side during the RSW of Mg to Al-Si coated steel, because of different dynamic resistances, thermal conductivities and melting points between Mg and steel [65]. It was also worth noting that bulk and brittle Mg-Al eutectics were squeezed out of the interface by electrode

force, which ensured the clean contact between molten Mg and solid-state steel (Fig. 2.11f and g). Both the laser weld-brazing mode and the thermomechanical processing of resistance welding are inspirational for NiTi-SS welding. However, based on similar melting points, thermal conductivities and electrical resistivities (Table 2.1 [66–71]), the welding between these two materials is expected to be challenging and some special designs should be performed.

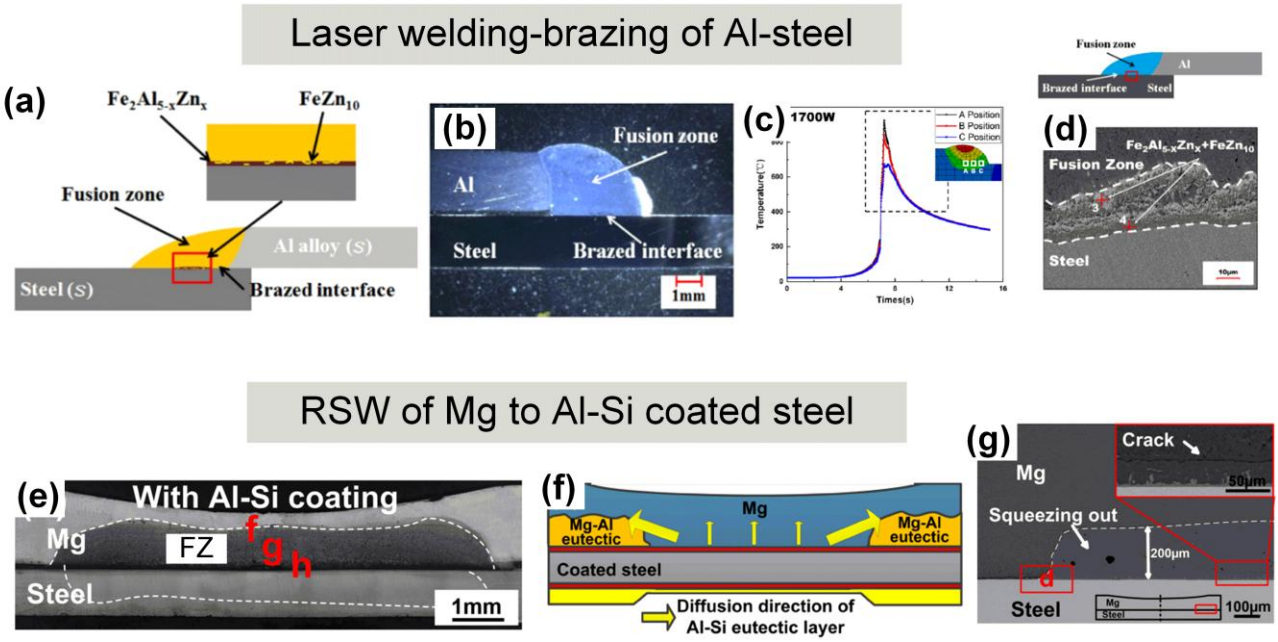


Fig. 2.11 (a) Schematic of Al-steel laser weld-brazing; (b) cross section of laser weld-brazed joint revealing the FZ at only Al side; (c) temperature field simulation proving that interfacial peak temperature is lower than steel melting point; (d) interfacial IMCs reaction layer [64]; (e) cross section of Mg/Al-Si coated steel RSWed joint with FZ at Mg side; (f) schematic of Mg-steel RSW mechanism indicating the squeezing-out of brittle Mg-Al eutectics; (g) the observation of squeezing-out zone at Mg-steel weld border region [65].

Table 2.1 Some properties of B2 NiTi and 316L SS [66–71] (note that these properties may vary depending on different temperatures and material processing statuses).

Properties	**NiTi (B2)**	**316L SS**
Melting temperature (K)	1584	1648-1673
Boiling temperature (K)	3560	3090
Thermal conductivity (W/mK)	18	16.2 (at 373K)
Young's modulus (GPa)	83	193
Coefficient of thermal expansion (1/K)	$11*10^{-6}$	$18.4*10^{-6}$
Electrical resistivity (Ωcm)	$86.5*10^{-6}$	$74*10^{-6}$

2.3 Recent progress on NiTi-SS dissimilar welding

2.3.1 Typical microstructure and properties of NiTi-SS dissimilar joints

Most studies on NiTi-SS welding selected superelastic (i.e., B2 austenite) NiTi as the base material. Fig. 2.12a-c present the 3D chemical analysis of a region at FZ near to NiTi side of NiTi-SS laser weld, which was realized by the layer-by-layer focused ion beam (FIB) etching, scanning electron microscope (SEM) and energy-dispersive X-ray spectrometry (EDS) (Fig. 2.12a) [17]. Ternary composition histogram was plotted on the Ni-Ti-Fe phase diagram by counting the stacked Ni, Ti and Fe compositions on EDS mappings (Fig. 2.12b). As a result, the 3D reconstruction of the whole analyzed volume is presented in Fig2.12c. It was obvious that the FZ was not composed of single dominant phase, but rather an IMCs network filled with various IMCs as indexed by regions from 1 to 6b, in which Fe_2Ti and Ni_3Ti were detected as the primary IMCs in this FZ. To confirm phase formation with higher accuracy, synchrotron X-ray diffraction (SXRD) was utilized, leveraging its shorter X-ray wavelength for higher diffraction density and spatial resolution. The SXRD analysis was conducted in a step-by-step scanning mode across the weld zone and base metal to provide detailed microstructural evolution. The SXRD results for a NiTi-SS laser-welded joint are shown in Fig. 2.12d [16], revealing a variety of IMCs, including Fe_2Ti, Ni_3Ti Cr_2Ti, etc. within the FZ. The hardness results in Fig. 2.12e indicated that this FZ were extremely harder than both NiTi and SS BMs, suggesting the brittleness of the whole FZ.

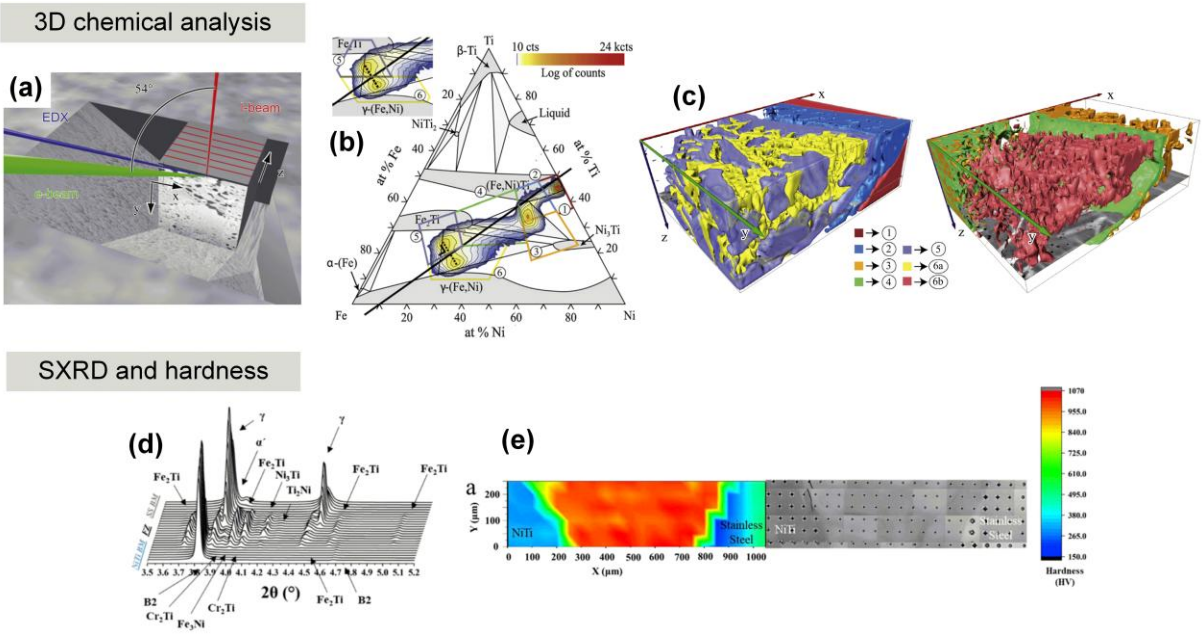


Fig. 2.12 (a) Schematic of 3D chemical analysis method based on layer-by-layer FIB, SEM and EDS; (b) ternary composition histogram (FZ near to NiTi side) superimposed on a 1000 ^{o}C isothermal section of Ni-Ti-Fe phase diagram; (c) the 3D reconstruction of the whole analyzed volume: Region 1: original NiTi base metal, Region 2: (Fe,Ni)Ti dendrites, Region 3: Ni_3Ti formed in eutectic, Region 4: a possible mixture of phases, Region 5: Fe_2Ti dendrites, Region 6: eutectic of γ-(Fe,Ni) in yellow and Fe_2Ti in red [17]; (d, e) SXRD and hardness testing results of NiTi-SS laser welded joint, respectively [16].

Electron backscattered diffraction (EBSD) combined with EDS was also used for investigating the phase distribution in the NiTi-SS FZ. Fig. 2.13a, b and d illustrate that the FZ of the electron beam welded NiTi-SS joint is dominated by an IMC network primarily composed of Fe_2Ti and Ni_3Ti [18]. Fig. 2.13c and d exhibit the presence of microcrack in this IMCs network, highlighting the high brittleness and the possible residual stress in the NiTi-SS FZ. Crack was more likely to propagate inside Fe_2Ti due to its low deformability compared to other IMCs or solid solutions. The lower solubility of Fe-Ti melt usually results in the formation of brittle Fe_2Ti IMCs. Fe_2Ti, Cr_2Ti, and/or $(Fe,Cr)_2Ti$, known as C14-Laves phase with a topologically close-packed (TCP) structure, are usually considered as one of the most harmful phases in NiTi-SS fusion welded joint, owing to its high modulus and low slip or plastic deformation capacity [11]. EBSD analysis of another study on NiTi-SS laser welded joint also indicated the complicated phase formation in the FZ, as seen in Fig. 2.13e [72]. In this work, the region near to NiTi side mainly consisted of C14-Laves phase (i.e., $(Fe,Cr)_2Ti$), and the TEM diffraction (Fig. 2.13f) proved the formation of the this phase in the FZ. Thermodynamic calculation on the Fe-Ni-Ti-Cr system was conducted. As shown in

Fig. 2.13 g and h, the calculation from a typical composition (35.7% Ni-31.6% Ti-30.6% Fe-1.4% Cr, at.%) suggested that Fe_2Ti and Ni_3Ti are primary phases, and some other phases such as γ-(Fe,Ni) and B2-NiTi could also form in the FZ. Macroscopic morphology of the NiTi-SS weld could be observed by optical microscope (OM) or SEM (Fig. 2.13 i-l) [73–76]. The FZ was often nonuniform, exhibiting macrosegregations, due to the strong convection or Marangoni effect (also can be verified in Fig. 2.13a) during welding, which could further localize brittleness in Fe-Ti-rich regions due to the bulk precipitation of Laves IMCs.

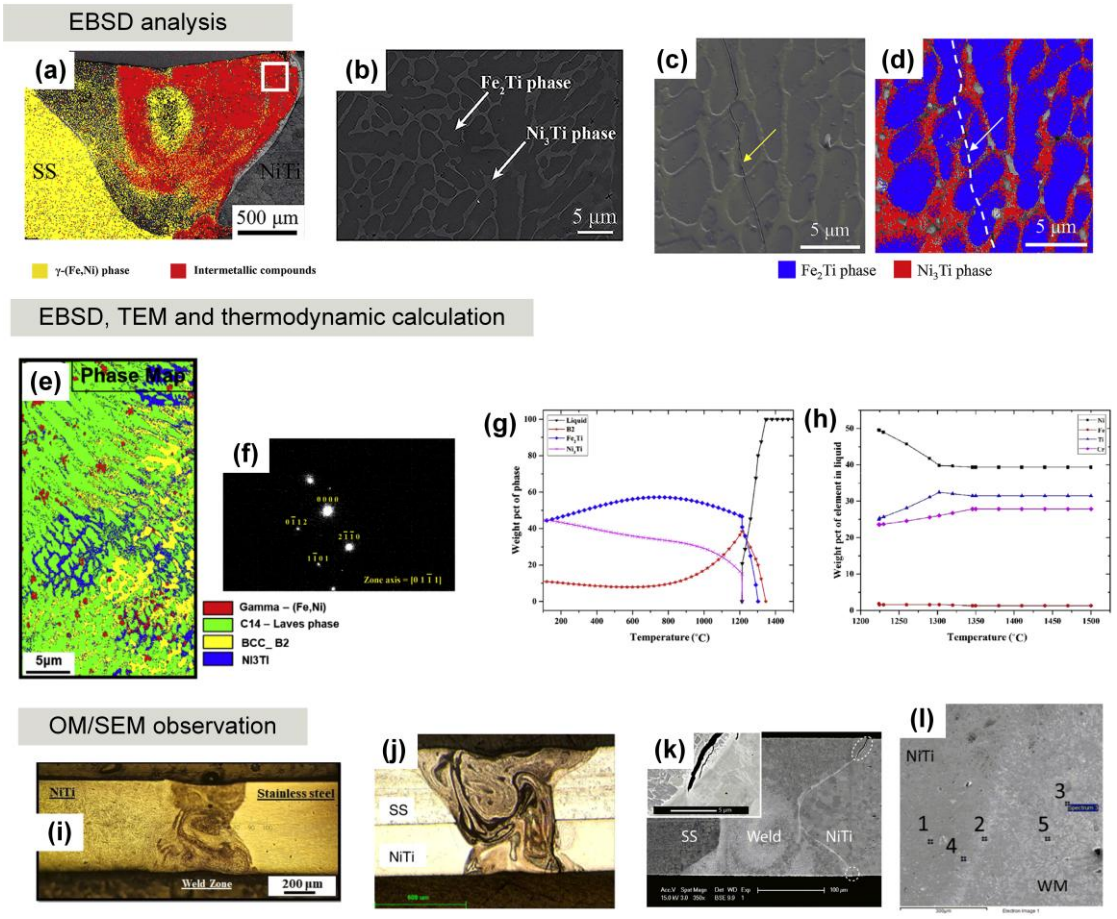


Fig. 2.13 (a) EBSD phase map indicating the formation of γ and IMCs in the FZ; (b) The typical IMCs network of Fe_2Ti and Ni_3Ti in the FZ; (c,d) The SEM and EBSD images showing the microcrack propagation in Fe_2Ti and Ni_3Ti network [18]; (e) EBSD phase map of the region in FZ adjacent to the NiTi side; (f) TEM diffraction pattern revealing the formation of Fe_2Ti in FZ (lattice parameters of a=0.4734 and c=0.7717); Thermodynamic calculated (g) phases fraction and (h) element fraction in liquid with the concentration of 35.7% Ni-31.6% Ti-30.6% Fe-1.4% Cr (at.%) [72]; (i-l) OM/SEM images of the overall FZ of NiTi-SS weld, with obvious macrosegregations in both butt [73,75,76] and lap [74] joints .

Due to the overall brittleness of FZ, the NiTi-SS joint typically fractured during the early elasticity stage with low ultimate strength (Fig. 2.14a) [77] in the mechanical testing. Compared to NiTi BM or NiTi-NiTi welded joint, achieving the critical stress for NiTi superelasticity in NiTi-SS joints is highly challenging. Some studies have reported that the joint fracture occurred along the FZ centerline (Fig. 2.14b and c) [77,78], while other work observed the fracture location within the FZ but near the NiTi side (Fig. 2.14d and e) [73,79], indicating potential influences from macrosegregation, residual stress and even the surface geometry of the weld zone. The fracture surfaces exhibited typical brittle characteristics, with large, sharp cleavage facets clearly visible (Fig. 2.14e and f) [16,79]. The in-situ tensile testing of NiTi-SS laser welded joint found that the crack initiated from welded wire's surface and then propagated over the peripheral perimeter of the weld, as seen in Fig. 2.14g [75]. In this testing the joint could achieve the NiTi superelasticity stage; it should be mentioned that samples in this work were wire-rotation welded and centerless ground after welding (the diameter was reduced by 1/3) to remove surface defects. Another case study also achieved the NiTi superelasticity in the NiTi-SS joint [80], however, the BM wires used in this work had a thinner diameter of only 0.1 mm, compared to the more commonly used range of 0.3–1 mm in other studies. The reduced diameter of wires may significantly mitigate the brittleness issue.

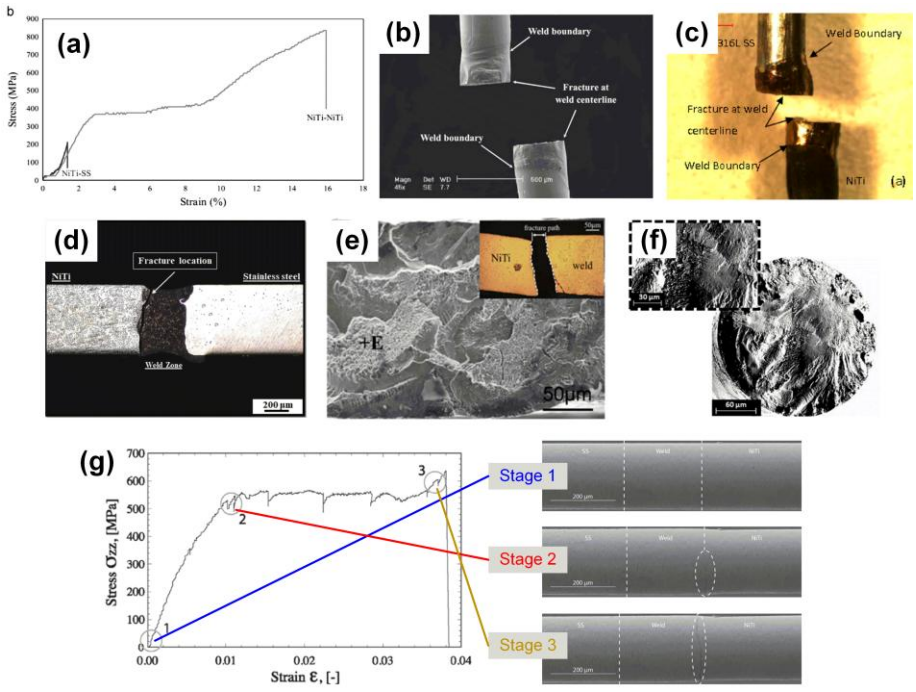


Fig. 2.14 (a) Typical stress-strain curves of NiTi-SS and NiTi-NiTi laser welded joints during tensile testing [77]; (b,c) fracture path of NiTi-SS joint located at FZ centerline [77,78]; (d,e) fracture path of NiTi-SS joint located at FZ near to NiTi side [73,79]; (f) fracture surface of NiTi-SS laser welded wire joint [16]; (g) in-situ tensile testing results of NiTi-SS laser welded wire joint [75].

2.3.2 IMCs control strategies for NiTi-SS welding

2.3.2.1 Adding interlayers

In recent years, various strategies have been explored to control the microstructure and to improve the properties of NiTi-SS joints. One of the approaches involves introducing alloying elements into the Ni-Ti-Fe-Cr system to modify phase formation in the FZ. Methods for introducing these elements ranged from using foils to powders, with additions including Ni [11,16,18,81,82], Cu [83,84], Co [85], Ta [78], etc.

Adding pre-existing alloying elements (i.e., Ni, Ti, Fe or Cr) to NiTi-SS welding is a more feasible approach as it minimizes potential biocompatibility issues. Using Ni foil or Ni powder as an intermediate layer between NiTi and SS BMs has proven effective in suppressing the formation of brittle Fe-Ti IMCs by promoting the formation of Ni_3Ti or Fe-Ni phases instead. Compared to the results shown in Fig. 2.13a-d, Ni-interlayered NiTi-SS FZ exhibited an increase in γ-phase and Ni_3Ti content with significantly lower hardness (Fig. 2.15a, c, d, and f) [18]. The SXRD results also confirmed the formation of more Ni_3Ti and Fe_3Ni phases in FZ when inserting a Ni foil for NiTi-SS laser welding [16] (as seen in Fig. 2.15h, in comparison with no interlayer condition in Fig. 2.12d). Adding Ni powder is more effective for Ni atom dispersion and diffusion in the FZ. The EBSD phase map revealed the dominant phase in the FZ near the NiTi side was changed from Fe_2Ti+Ni_3Ti IMCs network into γ-(Fe,Ni) and Ni_3Ti phases, which exhibited lower hardness and improved toughness (Fig. 2.15j and k) [81]. Moreover, FeNi foil with 50 wt.%-Ni was selected as an interlayer in NiTi-SS electron beam welding [18]. It improved the fraction of γ-(Fe,Ni) in the FZ, but there was still an IMCs-rich layer in the FZ/NiTi interface (Fig. 2.15b, e and g) due to the higher concentration of Ti here. The tensile testing results indicated that the NiTi-SS joint strength was significantly enhanced by adding Ni or FeNi into the FZ, but all the welded joints could not exhibit obviously enhanced ductility or NiTi SE (Fig. 2.15i), compared to NiTi BM.

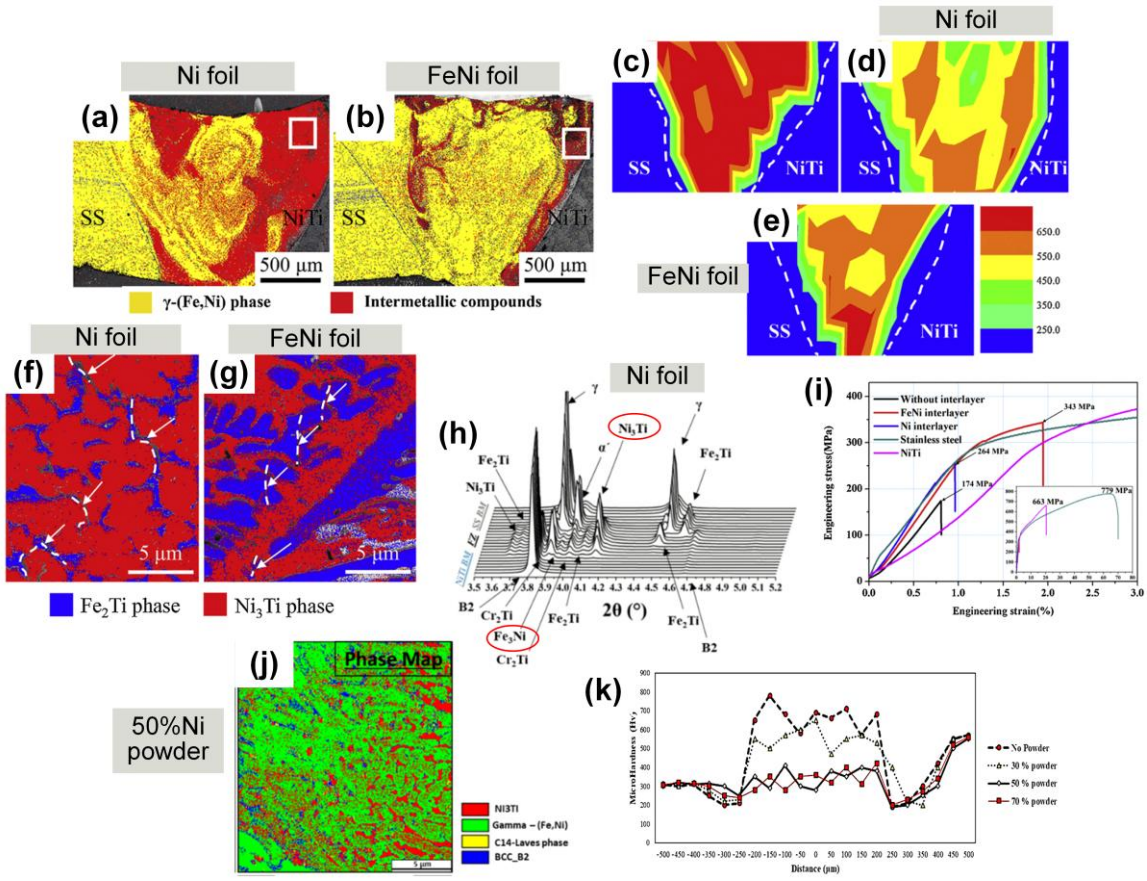


Fig. 2.15 (a, b) EBSD phase maps of Ni and FeNi interlayered electron beam welded NiTi-SS FZ, respectively; (c-e) hardness distributions of electron beam welded NiTi-SS FZs without interlayer, with Ni interlayer and with FeNi interlayer, respectively; (f, g) EBSD phase maps of NiTi-SS FZ obtained with Ni interlayer and FeNi interlayer, respectively (microcrack is marked by arrows) [18]; (h) SXRD results of NiTi-SS laser welded joint with Ni interlayer [16]; (i) tensile testing results of NiTi-SS joint with different interlayers [18]; (j) EBSD phase map of the FZ of NiTi-SS laser welded joint with the addition of 50% Ni powder. (k) hardness distributions of NiTi-SS laser welded joints by adding different concentrations of Ni powder [81].

Adding Cu by the interlayer for NiTi-SS laser welding could reduce brittle IMCs by promoting the formation of Cu solid solutions in FZ (Cu phase indexed in the XRD pattern in Fig. 2.16a) [83,84]. However, excessive Cu could lead to the formation of Ni_3Ti and Cu-Ti IMCs, which, in turn, decreased joint strength. Similarly, Co interlayer could modify the microstructure by replacing brittle Fe-Ti IMCs with some Ti-Co IMCs (Fig. 2.16b) [85]. The addition of Co content should also be controlled, as excessive formation of new IMCs increased the susceptibility to cracking. In contrast, the addition of a Ta interlayer showed minimal impact on optimizing the FZ microstructure or improving joint strength. This was evident in the similar IMC network (Fig. 2.16c) and hardness profile (Fig. 2.16d), compared to

directly welded NiTi-SS joints [78]. The limited effect was reasonable, given that XRD analysis detected no Ta-Ti or Ta-Fe phases, only Ta-Ni and Ta-Cr in the FZ. More recently, researchers employed equiatomic CoCrFeNiMn high-entropy alloy (HEA) as an interlayer, achieving a strength increase from ~30 N to 175 N in the NiTi-SS laser welded joints [86]. The addition of CoCrFeNiMn HEA promoted the formation of γ-(Fe,Ni) (or FCC HEA phase) meanwhile restricted the precipitation of brittle Fe-Ti phase (Fig. 2.16e and f). It is also noteworthy that none of the interlayered joints demonstrated significant superelasticity during tensile testing. All joints exhibited either brittle or mixed fracture modes.

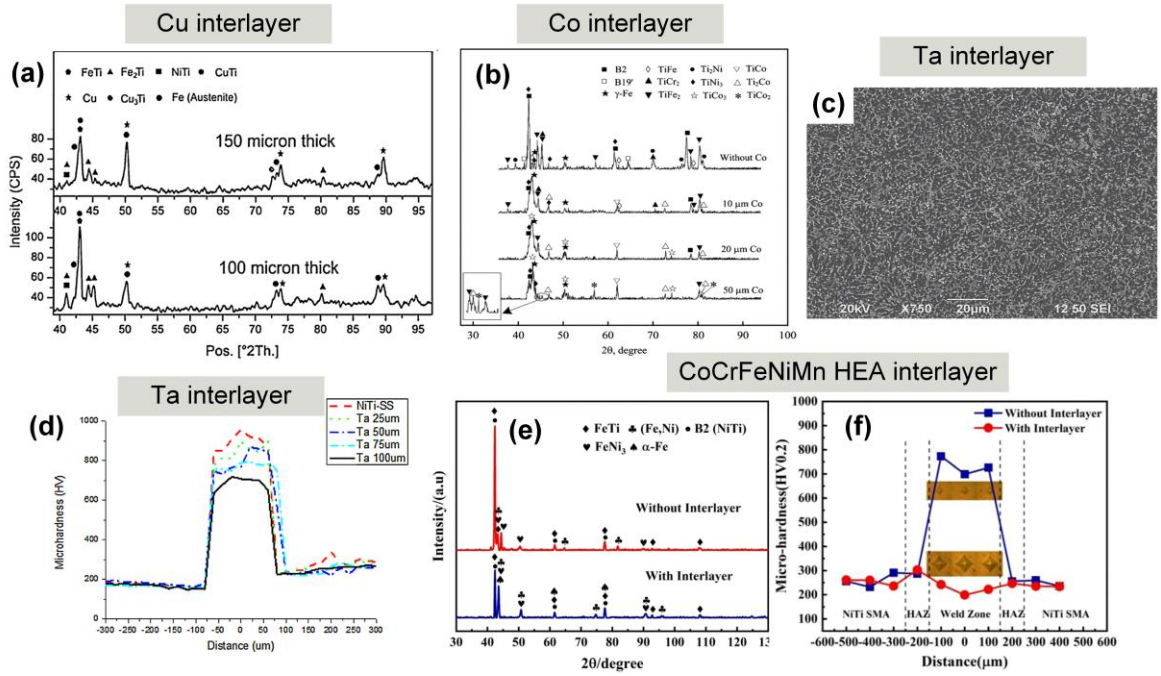


Fig. 2.16 (a) XRD pattern of NiTi-SS weld zone with different Cu interlayer thicknesses [84]; (b) XRD pattern of NiTi-SS weld zone with different Co interlayer thicknesses [85]; (c, d) FZ microstructure and hardness distribution of NiTi-SS joints with Ta interlayers, respectively [78]; (e, f) XRD pattern and hardness distribution of NiTi-SS joint with and without CoCrFeNiMn interlayer, respectively [86].

2.3.2.2 Post-weld heat treatment

Post-weld heat treatment (PWHT), particularly post-weld annealing, has been shown to significantly improve the strength of NiTi-SS joints [73,79,87] by releasing residual stress. Moreover, when an appropriate annealing temperature (850 °C) and a duration (3600 s) were combined with the addition of a Ni interlayer, the strength of the post-treated NiTi-SS laser welded joint increased to 2.12 times that of the as-welded joint [79]. XRD and SEM analysis clarified that more Ni_3Ti particles precipitated in the PWHTed FZ that strengthened the joint, and the FZ hardness was also significantly decreased after PWHT

(Fig. 2.17a-e). The homogenization of the FZ microstructure due to PWHT also contributed to the enhancement of joint strength. In addition to mechanical properties, the impact of PWHT on the electrochemical corrosion of NiTi-SS joints was also studied [87]. Polarization curve analysis showed that PWHT at 200 °C slightly improved the joint's corrosion resistance. However, a higher PWHT temperature of 400 °C severely reduced the corrosion resistance, likely due to the disruption of tangled dislocations, which could limit the feasibility of PWHT for NiTi-SS welding (Fig. 2.17f).

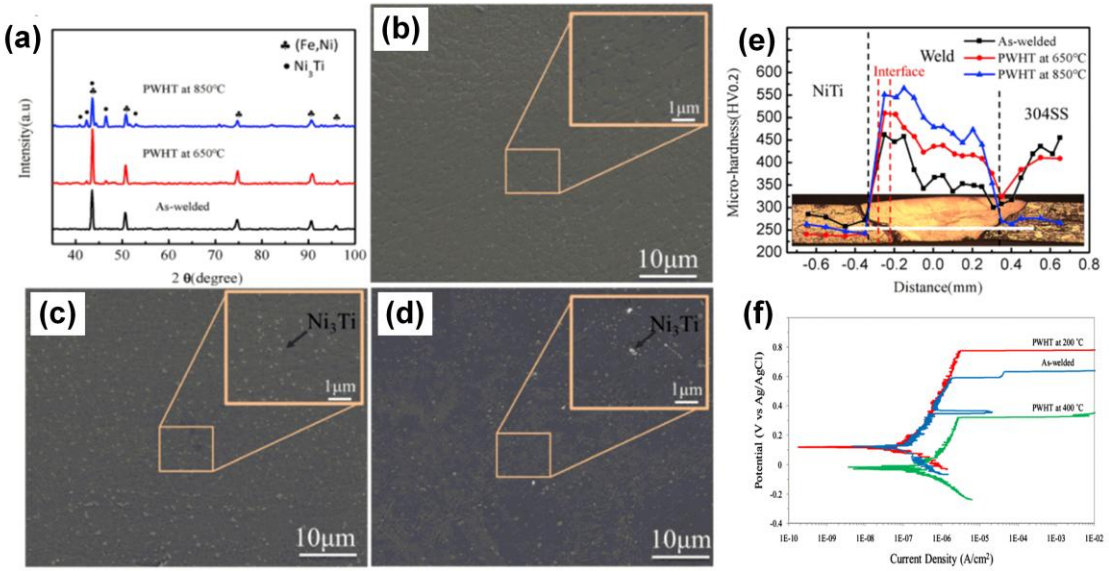


Fig. 2.17 (a) XRD patterns of the NiTi-SS laser welded FZ obtained with different PWHT temperatures; FZ microstructure of NiTi-SS laser welded joints (b) without PWHT and after PWHT temperature of (c) 650 ^{o}C and (d) 850 ^{o}C, respectively; (e) hardness distribution of NiTi-SS joints with and without PWHT [79]; (f) polarization curves of NiTi-SS laser welded joints with PWHT at different temperatures [87].

2.3.2.3 Laser beam or assembly designs

Specialized laser beam configurations and specimen assembly strategies can effectively control the melting and mixing behavior of dissimilar metals. In laser welded NiTi-SS lap joints, placing SS above NiTi has been shown to be a better configuration, as Ni enrichment in the FZ improved the anti-crack capacity of the joint [74]. Laser beam offset could be used to restrict the mixing of dissimilar molten metals [16,88,89]. Compared with directly welded joint, the laser offset towards SS side could significantly reduce the NiTi melting and Ti diffusion, resulting in less brittle Fe-Ti IMCs formation (Fig. 2.18a-f). A joint welded with a 0.1 mm offset towards the SS side achieved strength comparable to that of Ni-interlayered joints [16], but there were still obvious IMCs and macrosegregation in the FZ. A complex assembly involving laser beam offsetting-scanning, wire rotation and a cup-cone butt geometry was

designed for NiTi-SS welding [89]. In this case the mixed region could be narrowed to approximately 30-μm width. A recent study used multiple interlayers and carefully controlled laser beam positioning (Fig. 2.18g and h) [90]. Due to different melting points between Nb, Cu and BMs, two thick reaction layer zones formed at both sides, without overall melting of NiTi and SS. The Nb/Cu interface was regarded as the weakest position due to the formation of micro-cracks. Cu is commonly considered as the toxic element in biomedical applications, limiting suitability for NiTi-SS welding. Despite these advancements, these welding designs or PWHT was also difficult to produce a NiTi-SS joint exhibiting the significant ductility and NiTi functional properties.

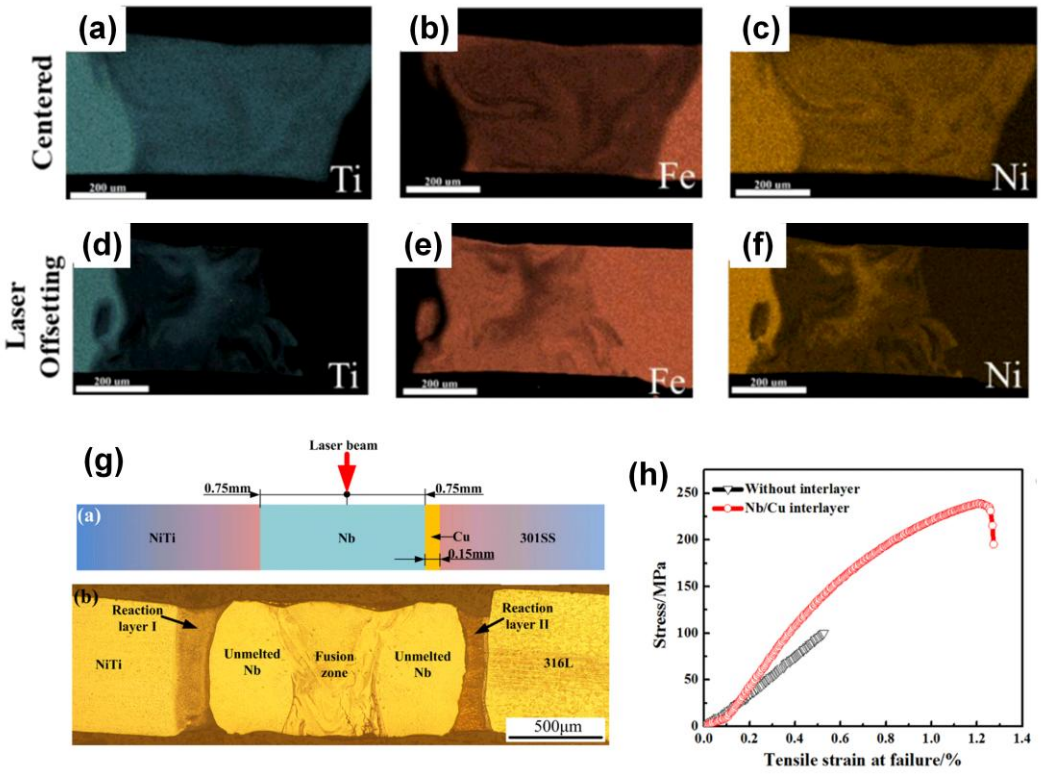


Fig. 2.18 (a-f) EDS mappings of laser welded NiTi-SS joints without and with laser beam offset, respectively [16]; (g) schematic and cross section of laser welded NiTi-SS joint with Nb+Cu interlayers; (h) the tensile test curves of the joints welded with and without Nb+Cu interlayers, respectively [90].

2.3.2.4 Solid-state welding

Due to the absence of significant macro-melting of BMs, solid-state welding nearly eliminates the mixing of dissimilar molten metals, enabling some NiTi-SS joints to retain NiTi SE [19,91–94]. For instance, impact welding of lapped NiTi and SS wires was achieved using a vaporizing foil actuator that generates pressure through metal vaporization. EDS mapping of the interface region confirmed the

absence of overall mixing of dissimilar molten metals (Fig. 2.19a), and the resulting ductile joint preserved NiTi SE (Fig. 2.19b) [94]. Further characterizations indicated localized melting and the formation of amorphous phases in some interfacial areas; however, weld defects, including an unwelded center region and shear cracks, were observed [92]. Large plastic deformation likely contributed to the formation of these weld defects, as well as the microstructural change of NiTi that degraded the SE behaviors. In recent years, friction welding of bulk NiTi and steel samples has shown promise for improving joint properties due to the absence of excessive melting and metallurgical reactions. An ultrathin IMCs layer was observed at the interface (Fig. 2.19c) [21], and this thin layer was generally considered non-detrimental to joint performance. However, XRD detected the transformation from original NiTi austenite to martensite near the interface (Fig. 2.19d) caused by the high pressure and deformation, indicating potential damage to NiTi SE. Ultrasonic welding of NiTi and SS was performed with a Cu interlayer, which flowed toward the weld border during welding (Fig. 2.19e) [20]. Similarly, resistance butt welding of NiTi and SS wires was achieved using a relatively complex setup (Fig. 2.19g), creating two distinct interfaces: the NiTi/SS interface and the base metals/SS tube interface [19]. A reaction layer of IMCs, approximately 10 μm thick, formed at the NiTi/SS interface (Fig. 2.19h). The resistance-welded joint maintained the NiTi SE plateau (Fig. 2.19i), however, the SE curves were significantly modified by the welding process. Current results indicate that solid-state welding techniques usually rely on complex configurations with limited flexibility and are constrained by BM dimensions and joint types. NiTi SE is highly susceptible to degradation during the solid-state welding process due to work-hardening or significant plastic deformation. This is evidenced by the formation of the B19' phase, amorphous phases, and alterations to cyclic curves [50,94,95], which challenged the capacity of NiTi to provide corrective force or to mimic bone deformation behavior, as a biomedical material [96,97].

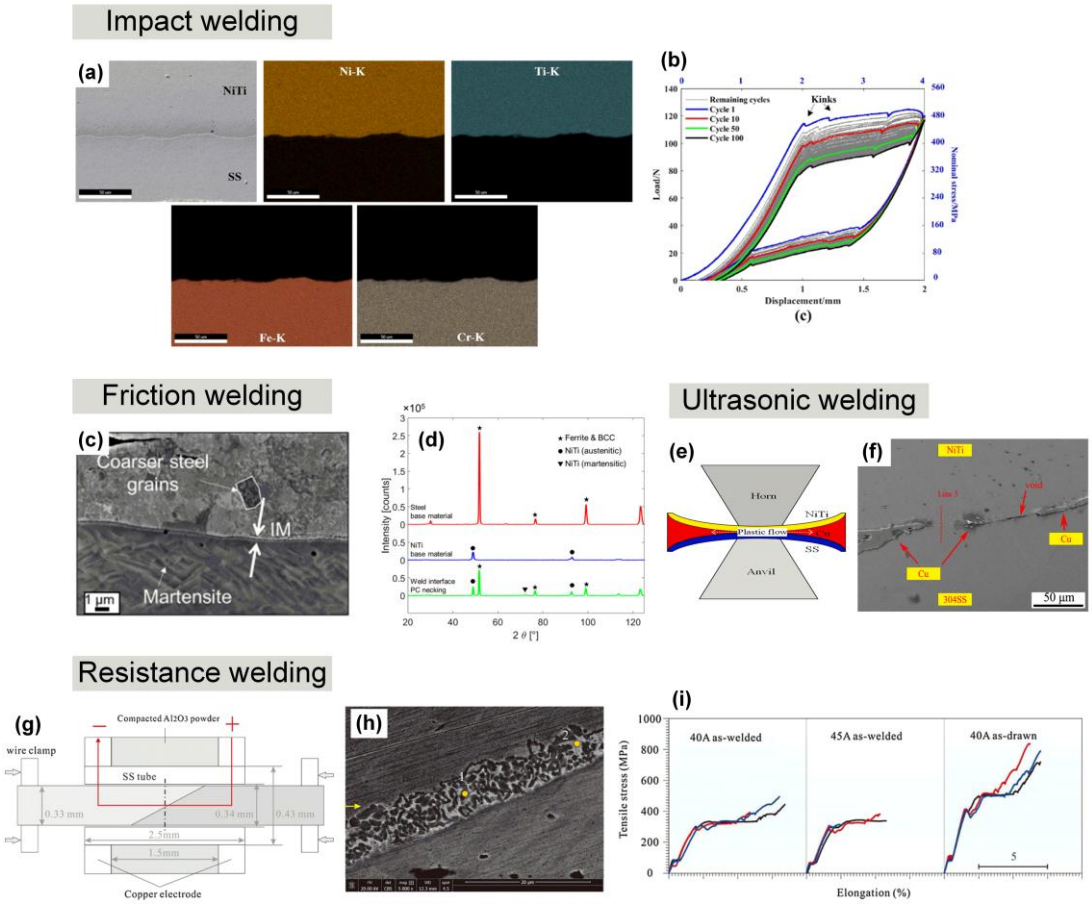


Fig. 2.19 (a) EDS mapping and (b) cyclic loading-unloading testing results of NiTi-SS impact welded joint [94]; (c) interfacial microstructure and (d) XRD patterns of friction welded NiTi-steel joint [21]; (e) schematic and (f) interface morphology of ultrasonic welded NiTi-SS joint [20]; (g) schematic, (h) interfacial IMCs layer and (i) tensile testing results of resistance welded NiTi-SS wire-tube joint [19].

2.3.3 Other problems related to NiTi-SS welding

As mentioned in Section 1.1, some typical dissimilar welding defects also exist in the NiTi-SS combination, especially on the NiTi side of the joint. The different thermophysical properties between NiTi and SS resulted in significant residual stress in the welded joint (Fig. 2.20a and b) [75,98], which usually led to microcracks in the low-ductility IMCs network [99]. Macrosegregation, caused by strong convection or Marangoni effect in the complex melt, poses another issue in NiTi-SS fusion welding. This phenomenon, as illustrated in Fig. 2.20c [82], could cause FZ inhomogeneity and localized brittle Fe-Ti segregation, which significantly weakened the joint. Porosity in NiTi-SS joints has drawn researchers' attention (Fig. 2.20d) [82,98], and a previous work reported a correlation between Ni content and pore susceptibility [82], though further studies are needed to understand the mechanisms of pore formation and

mitigation strategies. Because of the high equilibrium vapor pressure of Ni, Ni loss has been considered as a serious issue during NiTi welding and NiTi additive manufacturing. A slight variation in Ni content would result in obvious change of NiTi phase transformation temperature. For instance, in the high-power laser welded B2 NiTi joint, some unindexed EBSD regions suggested the formation of B19' phase at room temperature (Fig. 2.20e) [100]. Moreover, as discussed earlier, NiTi functional properties are highly sensitive to its microstructure. Therefore, preserving these properties in NiTi-SS dissimilar joints is critical and warrants thorough evaluation.

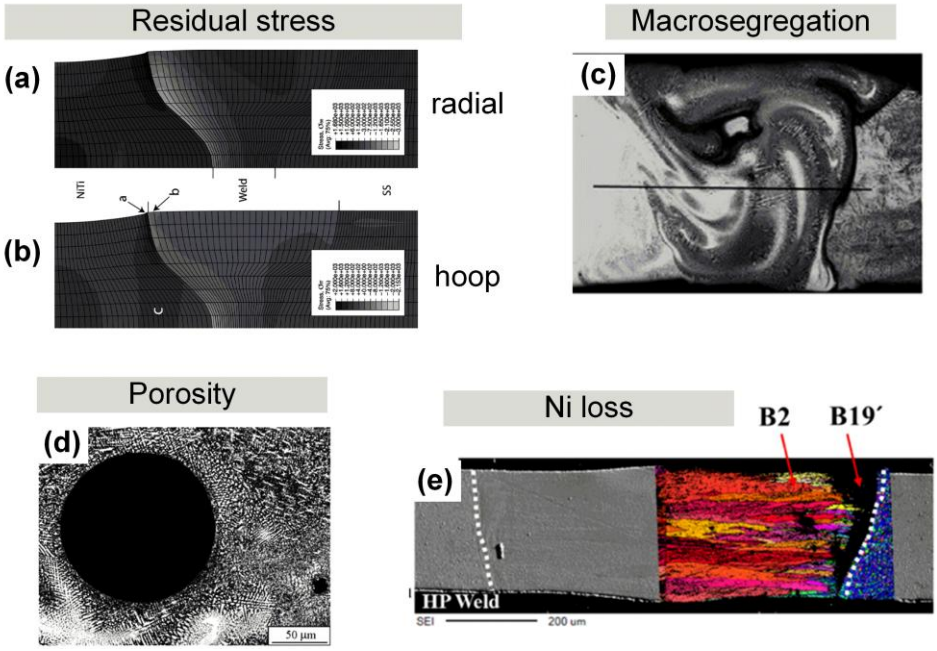


Fig. 2.20 (a, b) Simulated stress distribution in laser welded NiTi joint at 5% strain, with the radial and hoop components of the stress tensor, respectively [75]; (c) cross section of NiTi-SS laser welded joint, showing obvious macrosegregation [82]; (d) the pore in laser welded NiTi-SS joint [82]; (f) EBSD result of high-power laser welded B2-NiTi joint [100].

For practical applications of NiTi-SS joints in biomedical devices, corrosion and biocompatibility testing should be conducted. While some studies have highlighted biocompatibility concerns in NiTi-SS welds, research in this area remains limited. It is reasonable to expect that existing biocompatibility issues associated with NiTi or SS may also arise or even be exacerbated in the NiTi-SS weld zone. Electrochemical corrosion testing in a NaCl solution revealed that the NiTi-SS friction stir welded joint exhibited lower corrosion resistance compared to the BMs (NiTi and SS) (Fig. 2.21a) [91]. The authors considered that this reduction was attributed to the replacement of the original thin passive surface film by an inhomogeneous layer with reduced protective capabilities. Stress curve recordings of NiTi wire

during potentiostatic polarization in a mixed NaCl and NaF solution confirmed its susceptibility to stress corrosion (Fig. 2.21b) [101], but whether the NiTi-SS weld zone is more susceptible to stress corrosion remains unclear. Alternating current scanning electrochemical microscopy (AC-SECM) was used to detect the local electrochemical behavior and Ni ion release of NiTi-SS laser welded joint in a simulated human-body environment [102]. The results in Fig. 2.21c suggest that the weld zone (encircled region) exhibited a lower local electrochemical activity, improved passivation, and reduced Ni ion release, likely due to the combined presence of Ti and Cr. However, conclusions regarding the electrochemical behavior of NiTi-SS welds remain inconsistent across studies [103]. The absorption of hydrogen easily takes place in a bio-environment, especially in oral cavities, where galvanic currents in saliva facilitate hydrogen charging. As seen in Fig. 2.21d-f, the NiTi wire showed severe embrittlement after hydrogen charging testing in a NaCl solution [104]. It would be meaningful to conduct the hydrogen charging testing for NiTi-SS joints in a simulated bio-environment, to evaluate the hydrogen embrittlement of the weld zone. In addition, in vivo or in vitro biocompatibility testing for medical NiTi and SS has been performed (Fig. 2.21g), thus subjecting NiTi-SS joints to these in vivo or in vitro evaluations could provide a more direct assessment of their biocompatibility [105].

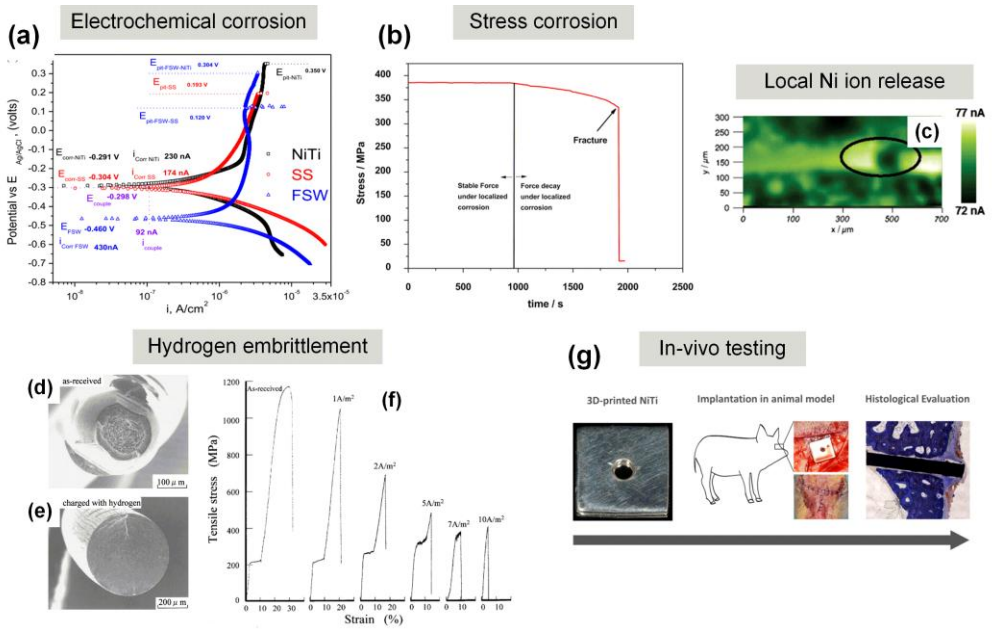


Fig. 2.21 (a) Potentiodynamic polarization curves for NiTi, SS and FSWed NiTi-SS [91]; (b) stress recorded during stress corrosion testing of NiTi wire [101]; (c) AC-SECM images of laser welded NiTi-SS joint, in which brighter regions represent higher local electrochemical activity [102]; (d,e) fracture surfaces of as-received and after-hydrogen-charging NiTi wires, respectively; (f) stress-strain curves of NiTi wires after hydrogen charging with different current densities [104]; (g) schematic of in vivo biocompatibility testing of 3D-printed NiTi [105].

2.4 Summary

Chapter 2 provides an overview of metallurgy and properties of NiTi and SS that should be considered during NiTi-SS welding. Then laser welding and resistance welding are introduced, which show unique advantages in NiTi-SS welding and are therefore selected as the welding techniques in this research. The typical microstructure of NiTi-SS joints is an IMCs network (mainly Fe_2Ti and Ni_3Ti) in the FZ. The NiTi-SS joint usually fractures at the elastic stage with low strength during mechanical testing. Table 2.2 lists different NiTi-SS welding studies from the literature, and it shows that the reliable joining is highly challenging. Two main strategies can be summarized as reducing IMCs and minimizing the brittleness of the joint:

The first strategy is to limit the scale of Ni-Ti-Fe-Cr mixture by restricting the melting and mixing of BMs in the joint, which can be realized by laser beam or assembly designs, or by solid-state welding methods. However, the limited laser beam or assembly designs cannot eliminate IMCs in the FZ. In the case of solid-state welding, a thin reaction layer forms at the interface, which, in turn, can lead to a high-strength joint that retains NiTi SE. However, the complex configurations required for assembly design and solid-state welding limit their applications, especially when BMs have small dimensions. The desirable functional properties of BMs are easily degraded due to the increased work hardening or plastic deformation during welding process.

The second strategy is to replace the brittle Laves $(Fe,Cr)_2Ti$ with ductile phases (e.g., Ni_3Ti, γ-(Fe,Ni), Cu-Ti, etc.) in the FZ of the joints, which can be achieved by inserting interlayers (Ni, Cu, HEA, etc.) and PWHT. Although these joints exhibit enhanced strength and ductility, eliminating harmful IMCs and achieving NiTi SE are still challenging, especially considering typical defects in fusion welding such as macrosegregation and porosity. Moreover, the addition of toxic elements in the FZ (e.g., Cu, Ni and Co) is usually not acceptable in biomedical device manufacturing [106,107].

The development of highly efficient and flexible NiTi-SS dissimilar welding techniques that achieve superior joint properties remains a critical requirement. Some fundamental issues, including the FZ microstructure, the dissimilar-metal interface, material dynamics under processing, and joint deformation and failure behaviors, should also be addressed.

Table 2.2 Summary of NiTi-SS dissimilar welding research progress (D: diameter and T: thickness)

Strategy	Joint strength	Method & configuration	Base metal dimension	Microstructure	If showing SE	Reference
Direct welding	~200MPa	Laser welding; butt	D=360μm wire	Overall IMCs network	No	[77]
Direct welding	~200MPa	Laser welding; butt	D=400μm wire	Overall IMCs network	No	[16]
Direct welding	27N	Laser welding; lap	T=200μm sheet	Overall IMCs network(crack)	No	[86]
Direct welding	174MPa	Electron beam welding; butt	T=1.6mm sheet	Overall IMCs network	No	[18]
Direct welding	420MPa	Plasma welding; lap	D=200μm wire	Overall IMCs network (crack)	No	[108]
Ni interlayer	~400MPa	Laser welding; butt	D=400 or 480μm wire	Ni_3Ti-rich IMCs network	No	[16,82]
Ni interlayer	264MPa	Electron beam welding; butt	T=1.6mm sheet	Ni_3Ti-rich IMCs network	No	[18]
Cu interlayer	521MPa	Laser welding; butt	D=480μm wire	Ni_3Ti-rich IMCs and Ti-Cu phase	No	[83,84]
Co interlayer	347MPa	Laser welding; butt	D=480μm wire	Co-Ti rich IMCs	No	[85]
Ta interlayer	251MPa	Laser welding; butt	D=1mm wire	IMCs network+ Ni_3Ta and $TaCr_2$	No	[78]
FeNi interlayer	343MPa	Electron beam welding; butt	T=1.6mm sheet	γ-(Fe,Ni) dominated	No	[18]
Ni powder	~300MPa	Laser welding; butt	431.8*635 μm rectangular	More Ni_3Ti and γ-(Fe,Ni)	No	[11,81]
CoCrFeNiMn interlayer	175N	Laser welding; lap	T=200μm sheet	More (Fe,Ni) solid solution	No	[86]
PWHT	~350-400MPa	Laser welding; butt	D= 360μm wire	Overall IMCs network	No	[73,87]
PWHT+Ni	643MPa	Laser welding; butt	T=200μm sheet	More uniform FZ+Ni_3Ti precipitates	No	[79]
Laser beam offset	~400MPa	Laser welding; butt	Wire or sheet	Less brittle Fe-Ti IMCs	No	[16,88]
Laser beam offset	623MPa	Laser welding; butt	D= 100μm wire	--	Yes (low speed testing)	[80]
Offset scanning and wire rotation	~340MPa	Laser welding; butt	D= 762μm wire	30-μm mixed region	No	[89]
CuNbCu+laser positioning	240MPa	Laser welding; butt	T=800μm sheet	Cu-rich reaction layer	No	[90]
Multiple laser pulses	Over 600MPa	Laser welding; butt; wire-rotation	D= 300μm wire	IMCs network	Yes (reduced diameter and in-situ testing)	[75]
Impact welding	~300N; 522MPa	Lap or butt	500*500μm square; D= 330μm wire	Solid-bonded interface	Yes	[92–94]
Friction welding	Over 600MPa; over 400MPa	Butt	D= ~12mm bar; T= 2mm sheet;	Interfacial reaction layer; Stir zone	Yes	[21,91,109]
Resistance welding	830MPa	Butt, specially designed	D= 330μm wire	Interfacial reaction layer	Yes	[19]
Ultrasonic welding	~690N	Lap	T= 150μm sheet	Interfacial reaction layer	No	[20]

Chapter 3 Control of IMCs, macrosegregation and porosity in laser welded NiTi-SS joints

3.1 Overview

Many efforts have been applied to reduce IMCs and to improve laser welded NiTi-SS joint properties. However, complex assembly and post-processing are high-cost and low-efficiency; additional alloying elements are usually unacceptable in biomedical application. Therefore, the achievement of one-step direct laser welding of NiT-SS wires is of great significance.

Weld-brazing, as introduced in Section 2.2, shows great advantages in dissimilar alloys joining. It has been used in the joining of Al/steel, Mg/steel, Mg/Ti, e.g. [110–112] where a FZ forms on one BM side with low melting point. The joint strength is mainly determined by the brazed interface between the FZ and another solid-state BM. However, given the similar melting points of NiTi and SS, achieving a weld-brazing mode in this combination is expected to be challenging. Furthermore, as introduced in Section 2.3.3, macrosegregation and porosity have been observed in the FZ of NiTi-SS joints, but these issues have not yet been thoroughly analyzed.

Different laser heat input modes, namely combinations of power density, welding time, and laser beam offset significantly influence the microstructure and properties of welds [113,114], demonstrating the flexibility of laser welding for dissimilar metals. In Section 3.3, laser weld-brazing between NiTi and SS wires was achieved using laser defocus and a large beam offset. The IMCs network was eliminated in the FZ of weld-brazed NiTi-SS joints. Section 3.4 investigated the influence of different heat input modes, (*1)* high power density with short welding time (HPD_S) and (*2)* low power density with long welding time (LPD_L), on the control of microstructure, porosity, and mechanical properties of laser welded NiTi-SS wires. The mechanisms and mitigation strategies of porosity and macrosegregation in laser welded NiTi-SS joint are investigated.

3.2 Methodology

Commercial B2 NiTi and SS wires with 1-mm diameter were used as base materials. NiTi and SS wires were cleaned in acid to remove any impurities, then their faying surfaces were ground using 2000# SiC paper for tight fit-up. Before welding, all the wires were finally cleaned in acetone with ultrasound for 10 min. A quasi-continuous fiber laser (QCW150, IPG) was employed, with a peak power of maximum

1.5 kW and 1064±10 nm output wavelength. Base metals were assembled in a butt configuration. The confirmation of laser defocus distance and real-time monitoring of welding process was achieved by a coaxial CCD camera (MTV-13V6HC). Pure argon was selected to protect the welding pool with a flow rate of around 10 L/min.

Fig. 3.1 shows the schematic of NiTi-SS laser welding. For Section 3.3, to eliminate the FZ IMCs network by the weld-brazing mode, a defocused laser beam (+15 mm) was chosen to match up with different beam offsets from 0.4 mm in NiTi side (marked as -0.4) to 0.4 mm in SS side (marked as +0.4), as shown in Table 3.1 and Fig. 3.1. For Section 3.4, to understand the nature of NiTi-SS fusion zone and to control the FZ macrosegregation and porosity, laser beam was irradiated in the centerline of NiTi/SS interface, and some welding parameters were constant (output laser waveform: square; pulse width: 10 ms; frequency: 50 Hz). To investigate the effect of heat input modes, output laser varied from a negatively defocused or focused beam to a positively defocused beam. The welding time and peak power were adjusted accordingly (Table 3.2). All the process window of laser parameters were selected after the preliminary experiments, and more details on the necessity of matching laser output modes are given in Sections 3.3 and 3.4.

After welding, samples for metallographic observations were mounted in epoxy, then they were ground and polished by SiC papers and diamond spray, respectively. Sample surfaces were etched for microstructural studies. The overall weld appearance, microstructure and alloying element distribution of joints were characterized by optical microscope (OM, Axio Scope.A1, ZEISS) and scanning electron microscope (SEM, ZEISS-MERLIN Compact) with an energy–dispersive X-ray spectrometer (EDS). Electron probe microanalyzer (EPMA, JXA8230, JEOL) was used for the porosity analysis. Static tensile tests were carried out at room temperature by a universal tester (8801, INSTRON), with the 0.5-mm/min tensile speed and the 30-mm gauge length. Fractographic characterizations were conducted via OM, SEM and EDS. Vickers microhardness measurement was performed through a hardness meter (Falcon 500, INNOVATEST) with 200-g load and 10-s dwell time. The finite volume modeling (FVM) of flow field simulation was performed using *Ansys Fluent*. Detailed information can be found in *Appendix A*.

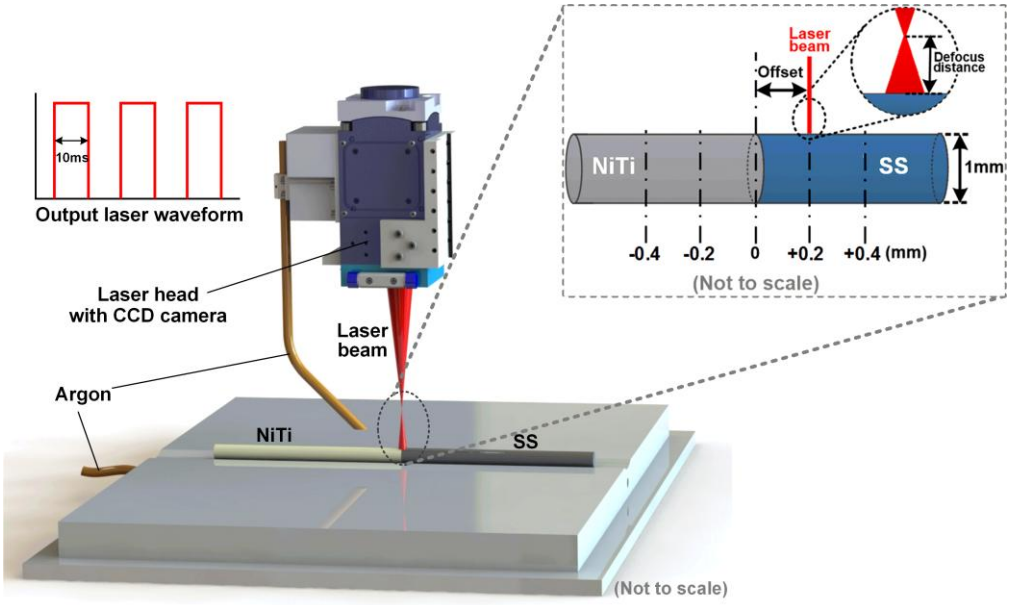


Fig. 3.1 The schematic of laser welding of NiTi-SS wires.

Table 3.1 Welding parameters in Section 3.3.

Welding parameters	Value
Output laser waveform	Square
Pulse width (ms)	10
Frequency (Hz)	50
Peak power (W)	255
Welding time (ms)	150
Defocus distance [a] (mm)	+15
Beam offset [b] (mm)	-0.4, -0.2, 0, +0.2, +0.4

a. the distance from focus point to top surface of wires
b. the distance between beam and NiTi/SS centerline

Table 3.2 Welding parameters used in Section 3.4.

Defocus distance [a] (mm)	Peak power (W)	Welding time (ms)	Heat input mode
-1	200	150	HPD_S
-0.5	213	155	HPD_S
0	225	160	HPD_S
+10	240	180	LPD_L
+20	265	210	LPD_L
+30	285	280	LPD_L

a. the distance from laser focal point to wire top surface: negative refers to a focal position is lower than wire top surface; positive refers to a focal position is higher than wire top surface

3.3 Elimination of IMCs network in the fusion zone by laser weld-brazing

Fig. 3.2 shows the weld appearances and cross sections of NiTi-SS joints welded with various laser beam offsets. Full-penetration NiTi-SS welds without any obvious defects could be realized even in a very large offset (-0.4 or +0.4 mm). The width of FZ obtained using less offset was smaller than that using larger offset, indicating that more heat input was consumed on mixing of molten metals. It was worth noting that a laser weld-brazing mode could be achieved when using -0.4-mm or +0.4-mm large beam offset (Fig. 3.2a1 and Fig. 3.2e1). In this case, the BM at beam-offset side melted while the counter part is still solid or slightly surface-melted, which is a welding mode between fusion welding and brazing, and the interfacial morphologies and phase formations in this work indicated a good agreement with other typical weld-brazing cases [110,112]. The formation of FZ was attributed to a fusion-solidification process of NiTi (-0.4) or SS (+0.4) BM, meanwhile obvious brazed interfaces (Fig. 3.2a1 and Fig. 3.2e1) formed between this FZ and the counterpart base metal. However, smaller or no offset (Fig. 3.2b1-d1) resulted in a typical fusion welding characteristic [76]. Obvious macrosegregation as highlighted in Fig. 3.2b1 and 3.2c1 was usually considered as the verification of immiscibility between molten NiTi and SS due to the Marangoni convection or a swirling effect [16,115]. Some small pores and microcracks appeared in the FZ of the non-offset joint [50,116]. It should be mentioned that the offset over 0.4 mm was ineffective for joining due to a fusion boundary away from NiTi/SS interface (spheroidization of the melt would occur in the offset side).

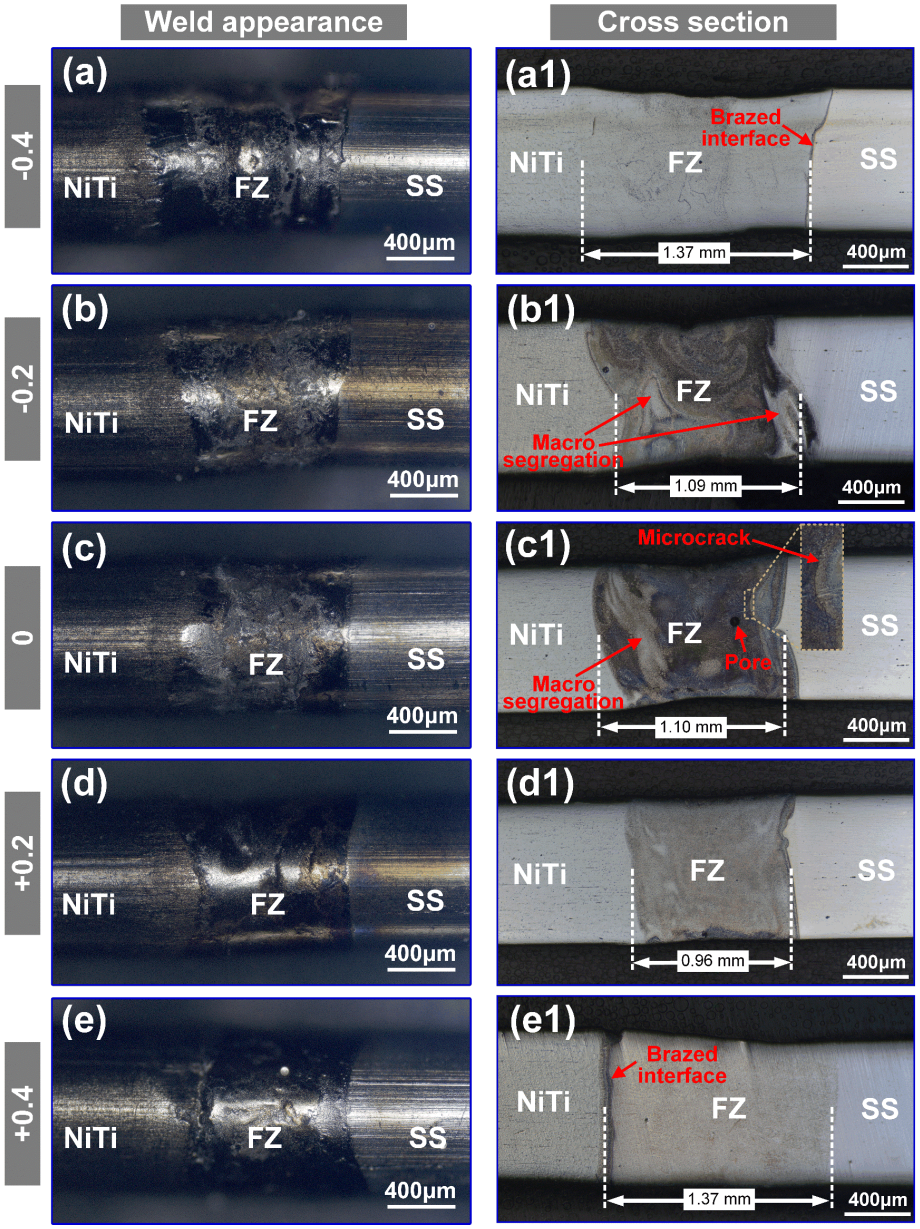


Fig. 3.2 Weld appearances and cross sections of NiTi-SS joints obtained with various beam offsets: (a, a1) -0.4; (b, b1) -0.2; (c, c1) 0; (d, d1) +0.2; (e, e1) +0.4.

To further confirm the weld-brazing mode, EDS mapping of joints with -0.4, 0 and +0.4 beam offsets was presented in Fig. 3.3. In -0.4 joint (Fig. 3.3a), the FZ was mainly composed of Ni and Ti. Fe and Cr are the primary elements in the FZ of +0.4 joint in Fig. 3.3c, indicating the fusion-solidification of SS. Nevertheless, the joint welded without offset exhibited mixed Ni, Ti, Fe and Cr in the FZ, indicated the fusion of both NiTi and SS (Fig. 3.3b). Here, through large beam offset to restrict the melting location, the weld-brazing mode can be introduced into the NiTi-SS combination. The achievement of large offset

was attributed to the use of a defocused laser beam. Fig. 3.4 shows that the reliable NiTi-SS joining was difficult to be realized when a focused laser beam was combined with 0.4-mm offset on NiTi side. A defocused beam with relatively low laser energy density but large effect area could ensure a proper wetting of molten metal on the other metal [117]. The variation ranges of beam offset for a weld-brazing mode should be based on specific materials dimension and welding parameters. The welding time was another important factor that should be carefully controlled to ensure full penetration on BM thickness direction but no excessive melting of the counterpart BM.

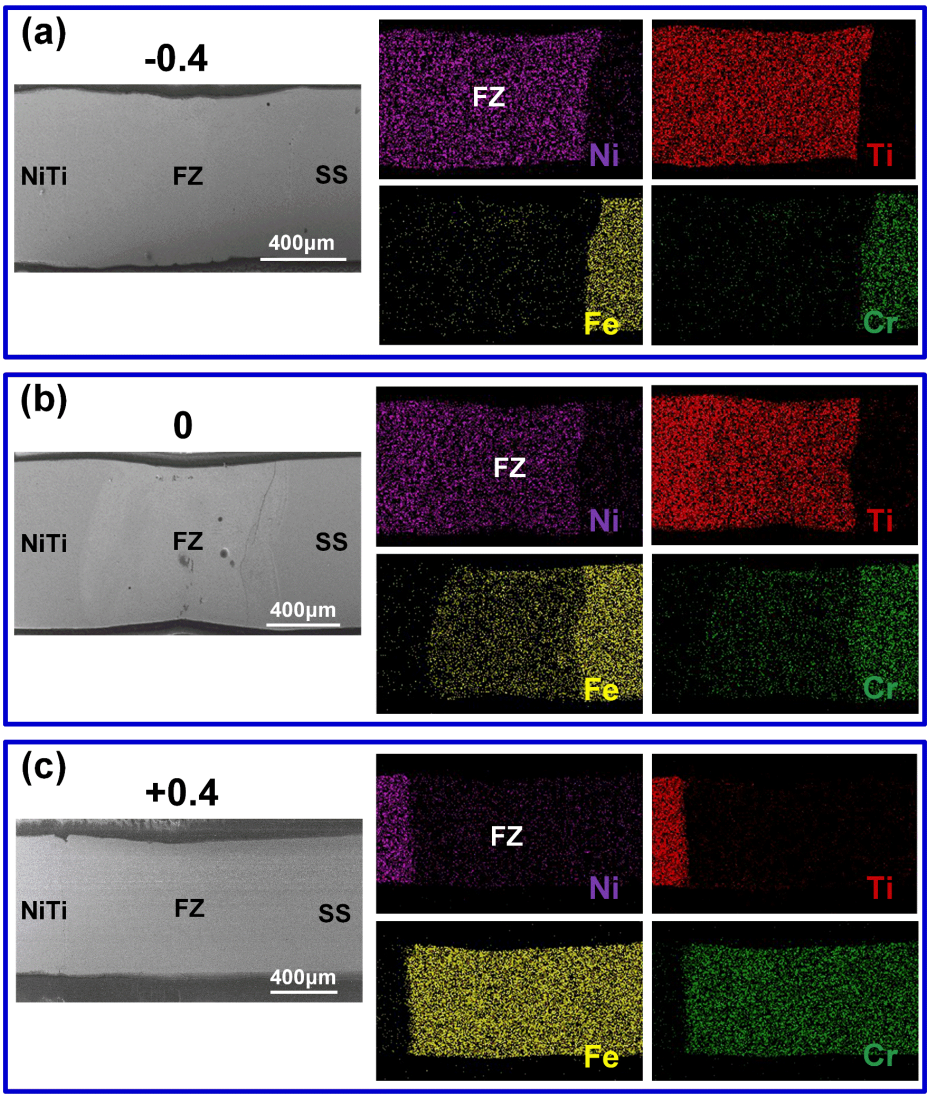


Fig. 3.3 The EDS mapping of the joint welded with (a) -0.4, (b) 0 or (c) +0.4 beam offset, respectively.

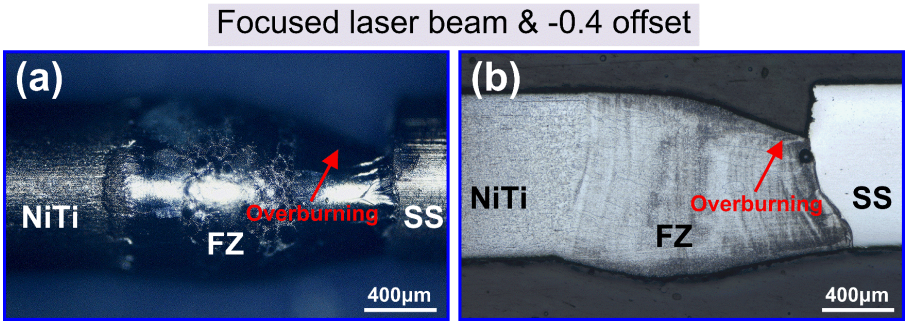


Fig. 3.4 (a) Weld appearance and (b) cross section of NiTi-SS joint welded using focused laser beam with -0.4 offset.

In the weld-brazed joint obtained with -0.4 offset as depicted in Fig. 3.5a-c, a reaction layer could be observed at the brazed interface, which contained three different regions (Fig. 3.5c). From EDS results (Table 3.3), Fe-Ni-Ti phase diagram and other investigations on NiTi-SS microstructural identification [16–18,50], this reaction layer was identified as a possible combination of multilayered structure of γ+Fe_2Ti → Fe_2Ti +Ni_3Ti → B2+ Fe_2Ti+Ni_3Ti, from position 1 to 3 as indicated in Fig. 3.5c. A higher concentration of Ti and Fe usually results in more brittle Fe_2Ti IMCs, which are widely regarded as the main factor for weakening of NiTi-SS joint performance [11,18]. Ti has a severe influence on IMC formation due to its lower solubility than Fe in the Fe-Ni-Ti system. Fe_2Ti usually precipitated with Ni_3Ti, and the complete IMCs-filled layer at position 2 (Fe_2Ti +Ni_3Ti) might be a weak point in this reaction layer zone. Fig. 3.5d and 3.5e present the microstructural evolution from FZ to NiTi heat affect zone (HAZ). NiTi after a fusion-solidification process exhibited a morphology of columnar grains in FZ (Fig. 3.5d), which could be clarified by the classical supercooling theory based on the rapid cooling rate of laser welding [118]. It is revealed that the FZ is composed of NiTi B2 phase (position 4 in Table 3.3) rather than IMCs network. Obvious equiaxed NiTi grains formed at the HAZ due to the grain coarsening. Reaction layer zone could also be identified at the brazed interface through the EDS line scanning result shown in Fig. 3.5f. Since the concentrations of Fe and Cr in FZ were both very low (marked by dotted circle), it suggested a highly mitigated mixing of molten liquids in this weld-brazing mode.

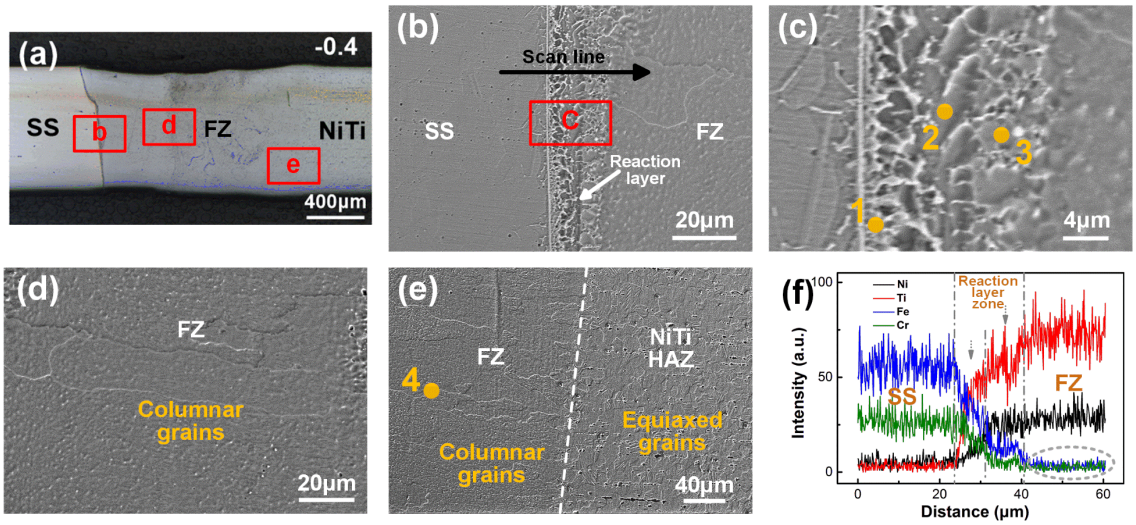


Fig. 3.5 SEM morphologies of the joint welded with -0.4-mm beam offset: (a) cross section of the joint; (b) the corresponding region marked in Fig. 3.5a; (c) the enlarged view of the region marked in Fig. 3.5b; (d, e) the corresponding region marked in Fig. 3.5a; (f)EDS line scanning result along the direction marked in Fig. 3.5b.

Table 3.3 EDS analysis (at.%) of different positions marked in Fig. 3.5.

Position	Ni	Ti	Fe	Cr	Possible phase
1	15.0	15.9	48.9	Bal.	γ+Fe_2Ti
2	18.0	33.7	35.4	Bal.	Fe_2Ti+Ni_3Ti
3	46.1	36.8	13.1	Bal.	B2+ Fe_2Ti+Ni_3Ti
4	50.6	49.2	--	Bal.	B2

Fig. 3.6 presents the microstructure of the NiTi-SS joint welded using +0.4 offset. Similarly, a diffusion-induced reaction layer formed at the brazed interface (Fig. 3.6b and 3.6c). Close to the interface, NiTi HAZ exhibited a morphology of equiaxed grains. As seen in Fig. 3.6c, the reaction layer was also multilayered. Near the SS side (position 1), a thin (~2.5 μm) γ phase layer formed with a small amount of precipitated Fe_2Ti. A layer (position 2 in Fig. 3.6c) characterized as γ matrix with increased Fe_2Ti was possibly formed close to NiTi side. A distinct transition zone (TZ) of approximately 30 μm was found between the reaction layer and NiTi HAZ (TZ, Fig. 3.6b and 3.6c). This TZ consisted of B2 matrix with some precipitated Fe_2Ti+Ni_3Ti, and its relatively high thickness could make it a weak point in the joint. In the FZ, vermicular δ ferrite phases were uniformly distributed in γ austenite matrix (Fig. 3.6d). The formation of δ phase was caused by an incomplete δ-γ transition from SS, due to the high cooling rate of laser welding [119]. No IMCs network was observed in the FZ (Fig. 3.6d and 3.6e), significantly reducing

overall joint brittleness. Compared to the -0.4 mm offset joint, Ti concentration decreased in the reaction layer zone (Fig. 3.6f.) of this joint, suggesting a reduction in Fe-Ti IMCs and an enhancement in reaction layer strength. The concentration of Ti in FZ was very low, confirming a weld-brazing mode, an entirely different welding mechanism compared to previous NiTi-SS studies, including the work using limited beam offset [16].

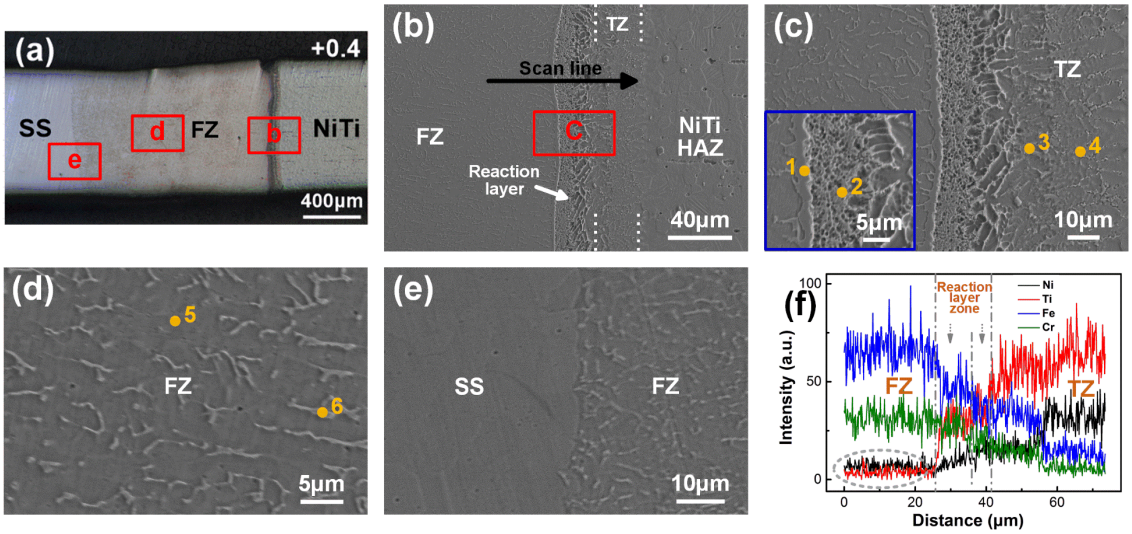


Fig. 3.6 SEM morphologies of the joint welded with +0.4-mm beam offset: (a) cross section of the joint; (b) the corresponding region marked in Fig. 3.6a; (c) the enlarged view of the region marked in Fig. 3.6b; (d, e) the corresponding region marked in Fig. 3.6a; (f) EDS line scanning result along the direction marked in Fig. 3.6b.

Table 3.4 EDS analysis (at.%) of different positions marked in Fig. 3.6.

Position	Ni	Ti	Fe	Cr	Possible phase
1	8.0	10.7	58.5	Bal.	γ+Fe_2Ti
2	13.9	17.1	50.7	Bal.	γ+Fe_2Ti
3	40.1	32.5	20.8	Bal.	B2+ Fe_2Ti+Ni_3Ti
4	49.2	32.6	14.8	Bal.	B2+ Fe_2Ti+Ni_3Ti
5	5.8	0.7	68.7	Bal.	γ
6	8.5	0.6	69.7	Bal.	δ

Fig. 3.7 shows the microstructure of NiTi-SS joint welded without offset. It presents a different morphology without an obvious reaction layer formed at the interface (Fig. 3.7b and 3.7g). As shown in position 1 in Fig. 3.7b, a Fe-rich zone with precipitated Fe_2Ti on γ matrix formed in FZ near to SS side.

Adjacent to this Fe-rich zone, an intermediate region of Fe_2Ti and Ni_3Ti was observed (position 2 in Fig. 3.7c). Some microcrack and pores also existed as shown in Fig. 3.7d and 3.7e. Fig. 3.7f shows that the FZ was filled by a typical IMCs network of Ni_3Ti+Fe_2Ti. Fig. 3.7g depicts that some Fe_2Ti also precipitated on the NiTi B2 matrix in the FZ/NiTi HAZ interface. Ni, Ti, Fe and Cr were all detected in the FZ (Fig. 3.7h and 3.7i) revealing the mixing of molten BMs.

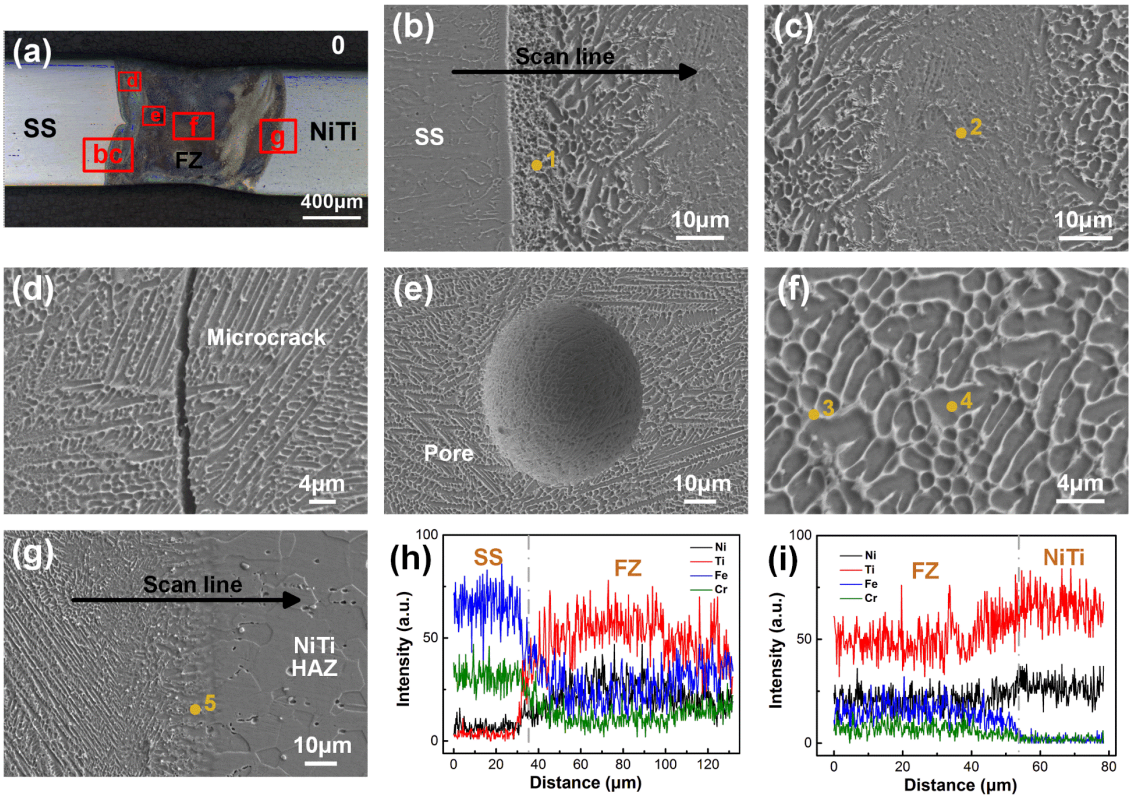


Fig. 3.7 SEM morphologies of the joint welded without beam offset: (a) cross section of the joint; (b-g) the corresponding regions marked in Fig. 3.7a; (h, i) EDS line scanning result along the direction marked in Fig. 3.7b and 3.7g respectively.

Table 3.5 EDS analysis (at.%) of different positions marked in Fig. 3.7.

Position	Ni	Ti	Fe	Cr	Possible phase
1	14.5	22.4	46.1	Bal.	γ+Fe_2Ti
2	28.5	32.3	29.9	Bal.	Fe_2Ti+Ni_3Ti
3	51.0	31.6	13.8	Bal.	Ni_3Ti+Fe_2Ti (Ni_3Ti-rich)
4	25.6	32.4	32.5	Bal.	Fe_2Ti+Ni_3Ti (Fe_2Ti-rich)
5	45.1	41.9	10.8	Bal.	B2+Fe_2Ti

Fig. 3.8a shows the hardness line distribution across the weld. All the joints exhibited similar hardness in BM (~400 HV) and HAZ (~300 HV at NiTi HAZ and ~200 HV at SS HAZ). Due to the elimination of texture and twins, and grain coarsening, the hardness of HAZ was lower than that of BMs. An extremely high hardness of ~1000 HV could be observed in the FZ of the joint welded without beam offset, corresponding to the presence of the IMCs network. Previous research also shows a similar hardness level [16]. With the increase of beam offset, the hardness in FZ gradually decreased to ~700-~900 HV with ±0.2 offsets and then further reduced to ~400 HV (same as NiTi) when using -0.4 offset or ~200 HV (lower than SS) when using +0.4 offset, respectively. The softened FZ in a +0.4 offset joint might be attributed to the precipitation of δ phase and elimination of work hardening after welding (Fig. 3.6d) [120]. The hardness mappings in Fig. 3.8b-d proved consistent results with as-mentioned hardness changes in FZ among different joints, but a more obvious local deviation in the FZ in Fig. 3.8c indicated the macrosegregation in the non-offset joint. It should be mentioned that the reaction layer zone in laser weld-brazed joints might show higher hardness, but it was narrow (<50 μm) and difficult to measure.

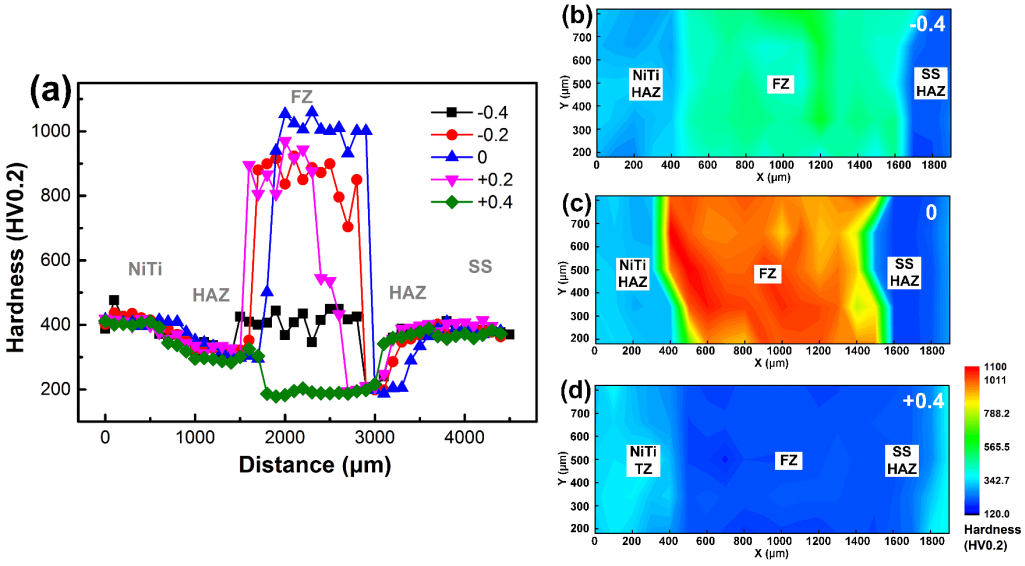


Fig. 3.8 (a) Microhardness line distribution across joints welded with various beam offsets; Microhardness mappings for joints welded with (b) -0.4, (c) 0 and (d) +0.4 beam offset, respectively.

When the offset changed from -0.4 mm on NiTi to +0.4 mm on SS, the tensile strength of NiTi-SS joints firstly decreased from 242 MPa to the lowest of 177 MPa (without offset), and then gradually enhanced to the maximum of 330 MPa (with +0.4 offset) as shown in Fig. 3.9a. It is higher than reported strengths of regular laser welded NiTi-SS wire joints with a range of 150-200 MPa [11,16,73,77]. The joint obtained with +0.4 offset also showed a reasonable elongation increase, despite all the joints fractured

at the elastic stage before the NiTi could exhibit its SE plateau (Fig. 3.9b). The highest strength obtained with +0.4 offset was attributed to the reduced presence of Fe-Ti IMCs in the reaction layer zone. Large laser beam offset could improve the mechanical properties of NiTi-SS joints, because the overall brittleness in FZ was effectively suppressed in a weld-brazing mode.

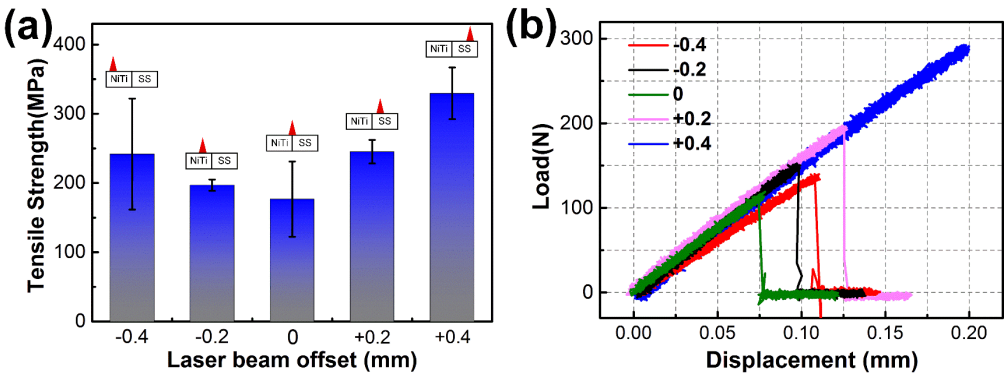


Fig. 3.9 (a) The tensile strength and (b) load-displacement curve of NiTi-SS joints welded with different laser beam offsets.

NiTi-SS joints welded with large beam offset fractured at the brazed interface region, while the joints without offset fractured inside of the FZ (Fig. 3.10a-c). No obvious necking occurred in all joints. The fracture surface of -0.4 joint exhibited the variation of height, indicating the change of crack paths (Fig. 3.10a1). A large crater-like structure formed, and its inner surface should be the primary SS surface (position 1 in Fig. 3.10a1 and Table 3.6). The lower part of the fracture surface was identified as Fe_2Ti+Ni_3Ti (Fig. 3.10a2) with smooth and brittle-fracture feature, corresponding to the position 2 of the reaction layer as previously indicated in Fig. 3.5c. Fig. 3.10a3 shows that the crack propagated inside NiTi with tearing ridges and a few dimples (ductile-brittle quasi-cleavage fracture) [16,18]. Nevertheless, the fracture surface of the joint without beam offset shows an almost flat and smooth surface (Fig. 3.10b1-b3). The crack might initiate from the original microcrack and propagated sharply inside the IMCs network. The fracture surface of +0.4 offset joint also demonstrated different heights (Fig. 3.10c1) suggesting a higher anti-crack ability. The lower region (Fig. 3.10c2) exhibited a typical cleavage feature and corresponded to position 3 or 4 (B2+Fe_2Ti+Ni_3Ti) in TZ as marked in Fig. 3.6c, while the upper region was identified as NiTi BM (Fig. 3.10c3) with tearing ridges and dimples as well.

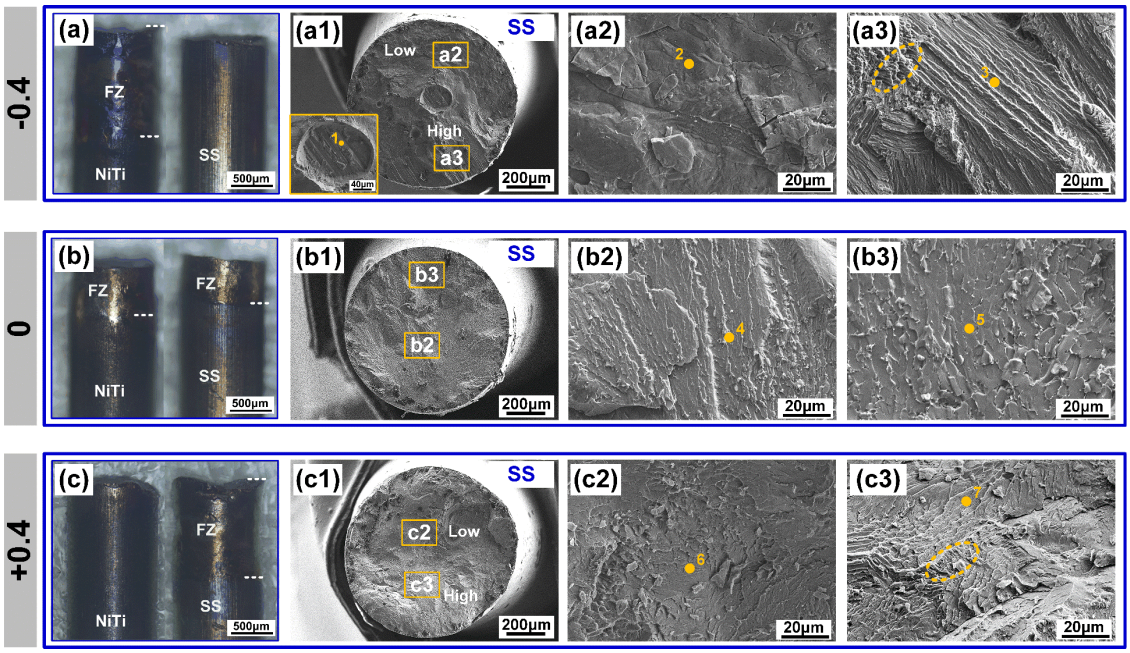


Fig. 3.10 Fracture morphologies of (a) -0.4, (b) 0 and (c) +0.4 offset; the overall SS side fracture surface of the joints welded with (a1) -0.4, (b1) 0 and (c1) +0.4 offset; (a2, a3) the corresponding regions marked at Fig. 3.10a1; (b2, b3) the corresponding regions marked at Fig. 3.10b1; (c2, c3) the corresponding regions marked at Fig. 3.10c1.

Table 3.6 EDS analysis (at.%) of different positions marked in Fig. 3.10.

Position	Ni	Ti	Fe	Cr	Possible phase
1	8.6	0.4	68.5	Bal.	γ
2	16.8	26.6	42.8	Bal.	Fe_2Ti+Ni_3Ti
3	47.5	51.3	0.7	Bal.	B2
4	29.1	32.1	29.8	Bal.	Fe_2Ti+Ni_3Ti
5	26.0	33.7	30.6	Bal.	Fe_2Ti+Ni_3Ti
6	47.9	36.9	12.9	Bal.	$B2+Fe_2Ti+Ni_3Ti$
7	47.3	45.8	5.7	Bal.	B2

Schematics of NiTi-SS welding and fracture mechanisms under different beam offsets are shown in Fig. 3.11. With a large beam offset, melting occurred on only one BM side, followed by the diffusion of molten NiTi or SS toward the interface. In contrast, no beam offset resulted in the mixing of NiTi and SS in the FZ. In the ±0.4-mm offset joints, the FZ (columnar NiTi in the -0.4-mm joint and γ matrix with δ

in the +0.4-mm joint, respectively) was formed by the fusion-solidification of a single BM, meanwhile a diffusion-induced reaction layer zone developed at the brazed interface. In the no-offset joint, the FZ contained a typical IMCs network where cracks propagated sharply.

During tensile testing, crack propagation occurred inside NiTi and the reaction layer in the -0.4-mm joint, while in the +0.4-mm joint, it propagated inside NiTi and the TZ. Therefore, using a defocused laser beam and a large beam offset enabled a weld-brazing mode that effectively suppressed the overall brittleness of the FZ in the NiTi-SS joint. The joint welded with a 0.4-mm offset toward the steel side demonstrated superior properties due to the relatively higher strength and less harmful IMCs at the interfacial region. Since the interfacial region was the weak position in the laser weld-brazed joint, further optimization of this interface or reaction layer is expected to enhance the joint properties and to achieve superelasticity.

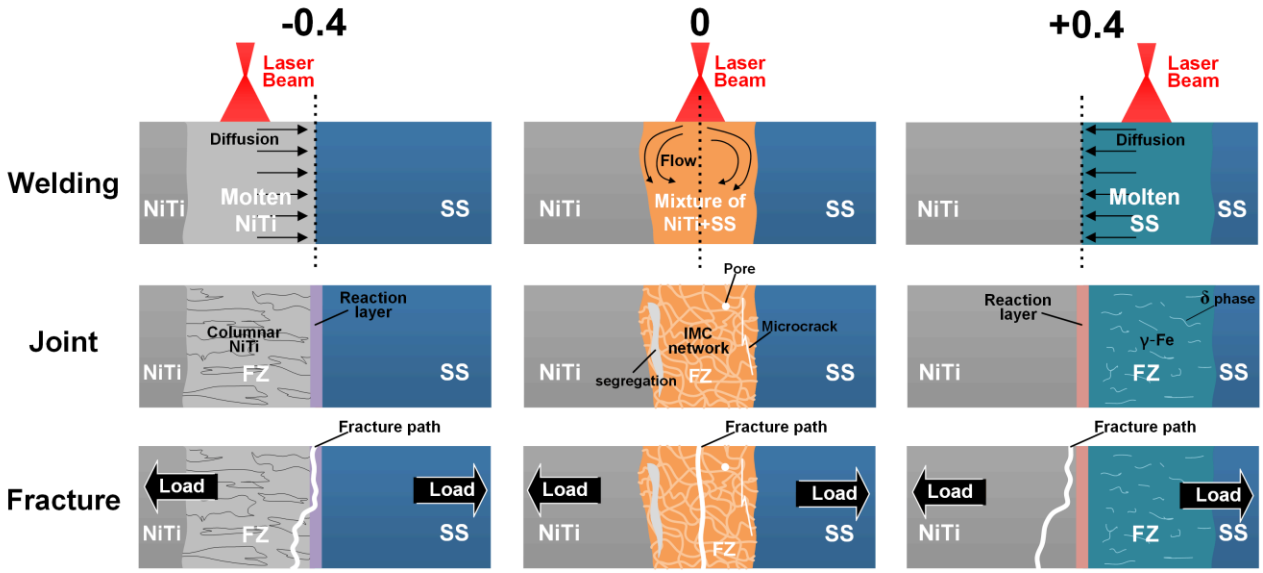


Fig. 3.11 Schematics of NiTi-SS welding and fracture mechanisms with different beam offsets (not to scale).

3.4 Control of macrosegregation and porosity by modifying the heat input mode

This Section focuses on the understanding of Ni-Ti-Fe-Cr melt and the control of macrosegregation and porosity in this melt or FZ. Therefore, all the joints were welded with the laser beam placed at the NiTi/SS centerline (i.e., no offset). Figs. 3.12a-f show appearances of laser welded NiTi-SS joints with different parameters (see Table 3.2). Fully penetrated joints without superficial defects were obtained. Fig. 3.12g illustrates the correspondence between laser power density and defocus distance, which was

calculated using a Gaussian beam. Due to a focal position inside of metals and convergent energy, the negative defocus even shows a much stronger ability on penetration than the surficial-focused beam [121,122]. As the defocus distance increased, the FZ gradually became wider (Fig. 3.12h), indicating a larger laser affect area. In the case of large positive defocus distance, the power density was reduced, thus a fully penetrated and wider NiTi-SS weld was obtained based on the increase of welding time. In a word, the laser keyhole mode tended to convert into a conduction mode when the welding mode was changed from HPD_S to LPD_L.

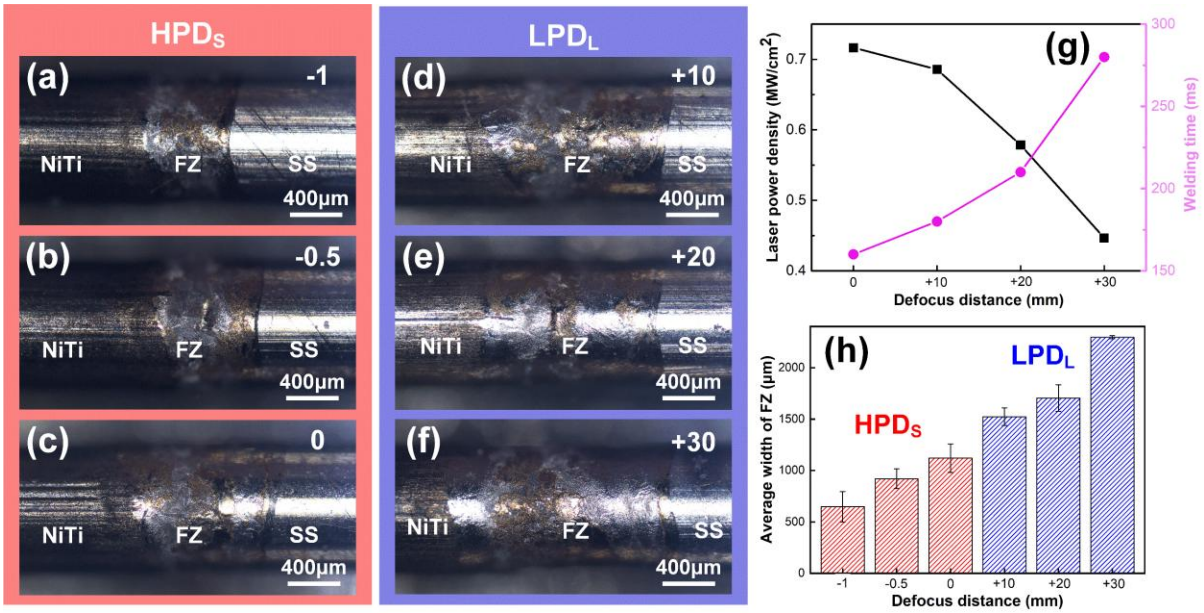


Fig. 3.12 Weld appearances of laser welded NiTi-SS joints obtained with defocus distance of (a) -1 mm, (b) -0.5 mm, (c) 0 mm, (d) +10 mm, (e) +20 mm, (f) +30 mm; (g) the relationship between defocus distance and laser power density or the selected welding time; (h) average FZ width obtained with different defocus distance.

Cross sections of laser welded NiTi-SS joints are presented in Fig. 3.13. To evaluate the pores distribution, an image binarization method was performed by *Matlab*. It is obvious that most pores were located randomly in the FZ of the HPD_S joint, with a spherical shape but in various diameters. The shape of welding pores should be associated with the thermophysical properties of the melted liquid in the FZ and the processing method/parameters. Spherical pores have been observed in laser welding of many types of metals [123–125]. In a normal laser weld, three types of pores were defined: *Uniform*, *Transitional* and *Root* pores [126]. Pores formed in this work could be considered as the *Transitional* pores due to their significant difference in diameter and location. Joints welded with LPD_L mode showed a much lower porosity, particularly with respect to large pores. Therefore, the LPD_L welding mode with low power

density and long welding time was an effective strategy for pore mitigation. The further analysis on porosity will be discussed later. In a few joints, some micro-cracks were observed in the FZ boundary due to a high local residual stress [75].

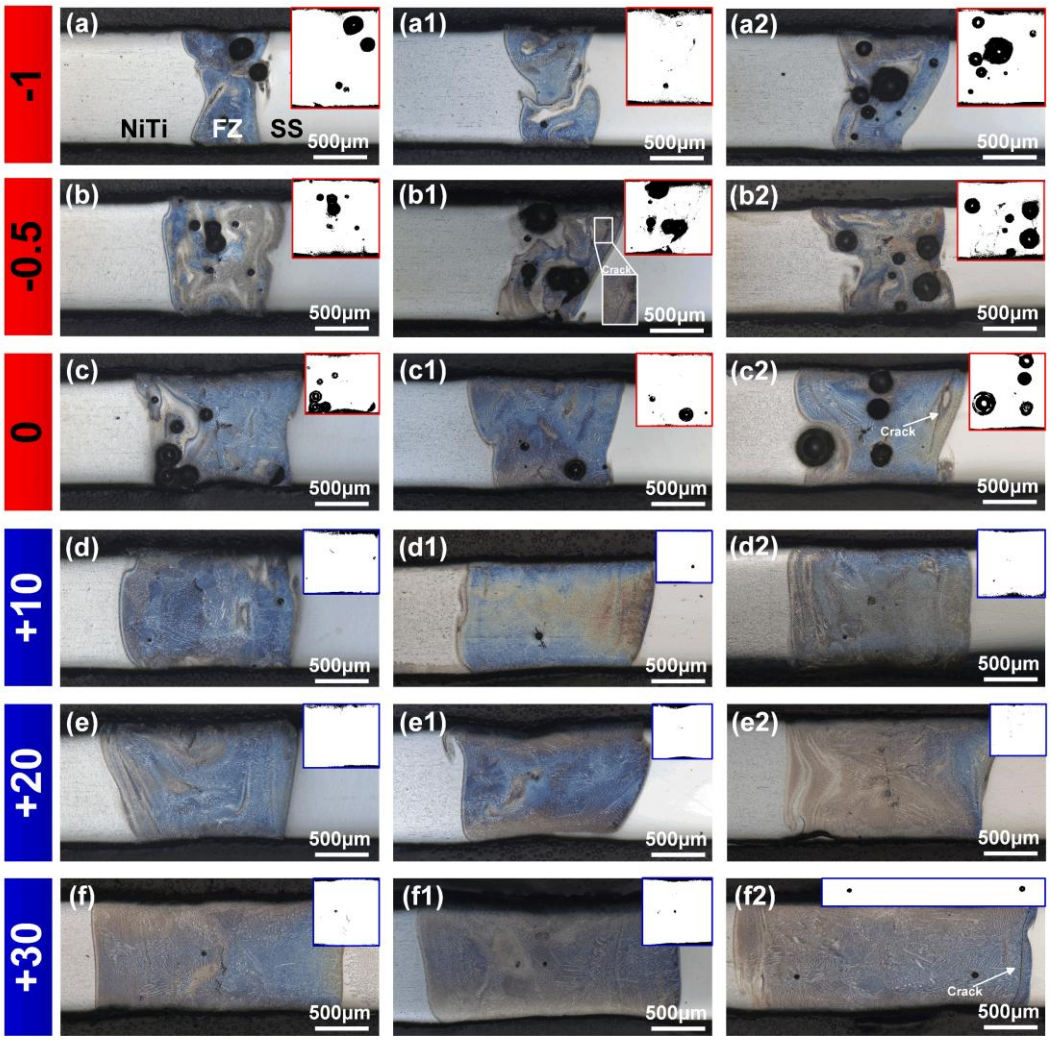


Fig. 3.13 The pore distribution in NiTi-SS weld cross sections obtained with different defocus distances: (a-a2) -1 mm; (b-b2) -0.5 mm; (c-c2) 0 mm; (d-d2) +10 mm; (e-e2) +20 mm; (f-f2) +30 mm.

Fig. 3.14 shows the microstructure of the joint welded with a HPDs mode (-0.5 mm defocus distance) and the corresponding EDS analysis is listed in Table 3.7. Coarse equiaxed grains of B2 NiTi formed in the HAZ (Fig. 3.14b), and a transition zone (Fig. 3.14c) consisting of B2+Ni_3Ti+Fe_2Ti was observed between NiTi HAZ and FZ. The EDS line scanning indicated the formation of transition zone with ~16.5 μm in thickness (Fig. 3.14i). Various microstructures (from *regions d* to *g)* in FZ indicated a non-uniform mixing of dissimilar molten metals. Large and small island-like structures were identified as γ-Fe macrosegregation (Fig. 3.15) and γ matrix with precipitated Fe_2Ti, respectively (Figs. 3.14d and

3.14e). Microstructure in *region f* showed dendrites of γ with Fe_2Ti+Ni_3Ti. *Region g* was composed of a typical Fe_2Ti+Ni_3Ti IMCs network. As indexed by the gradually decreased Fe concentration from *regions d* to *g*, the flow of Fe-rich liquid (molten SS) could be traced (green line in Fig. 3.14a). On the other hand, the formation of other regions was due to the flow of NiTi-rich melt (yellow line in Fig. 3.14a).

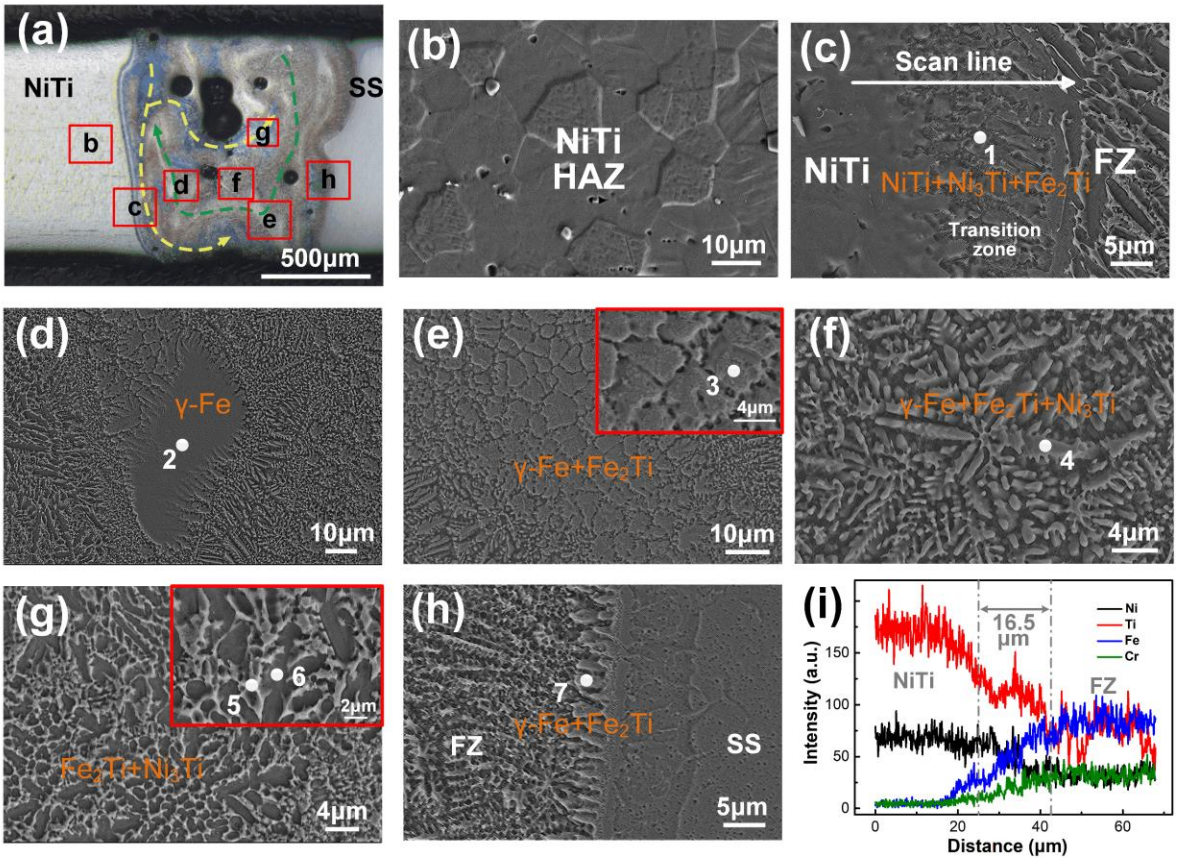


Fig. 3.14 SEM images showing morphologies of the HPDs joint: (a) cross section of the joint; (b-h) the corresponding regions marked in Fig. 3.14a; (i) EDS line scanning result along the direction marked in Fig. 3.14c.

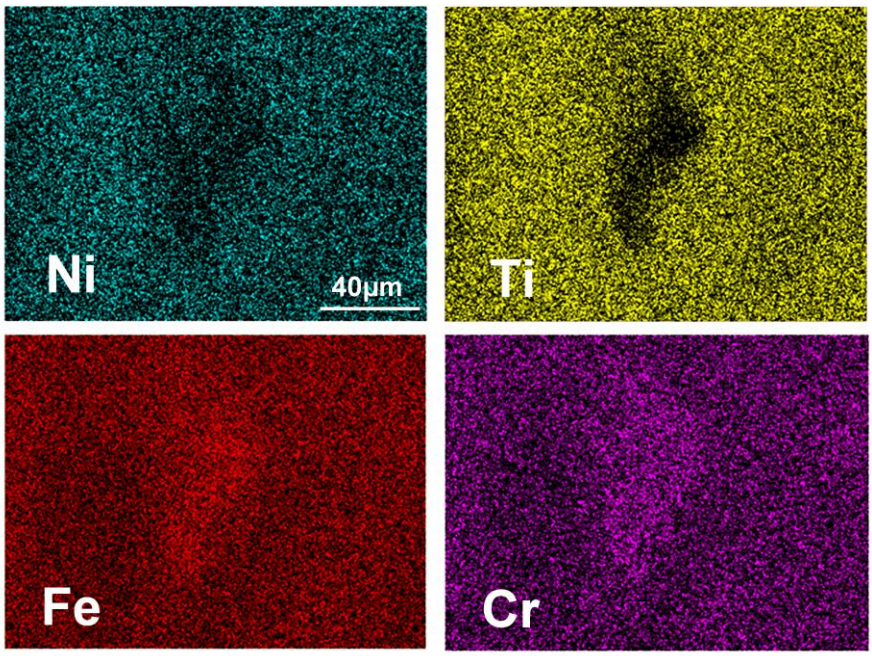


Fig. 3.15 The EDS mapping results of the γ-Fe macrosegregation as shown in Fig. 3.14d.

Fig. 3.16 presents the microstructural evolution in the joint welded with the LPD_L mode (+20 mm defocus distance). A transition zone with the thickness of ~30.3 μm formed in the NiTi HAZ/FZ interface (Figs. 3.16b and 3.16f). Compared to the HPD_S joint (16.5 μm in Fig. 3.14i), the extension of this zone was attributed to more sufficient interfacial reaction due to longer welding time. The microstructure in the FZ was more homogeneous and uniform. It was identified as the typical Fe_2Ti+Ni_3Ti IMCs network (like Fig. 3.14g), with slightly different morphologies: mesh-like (cellular) structure in Fig. 3.16c and lath-like (dendritic) structure in Fig. 3.16d. In both HPD_S and LPD_L joints, a cellular dendritic layer of γ+Fe_2Ti formed in the SS/FZ interface (Figs. 3.14h and 3.16e). In short, the HPD_S welding mode could result in non-uniform microstructures in FZ; while the LPD_L mode with a lower power density but longer welding time promoted the mixing of dissimilar molten metals and the microstructural homogeneity.

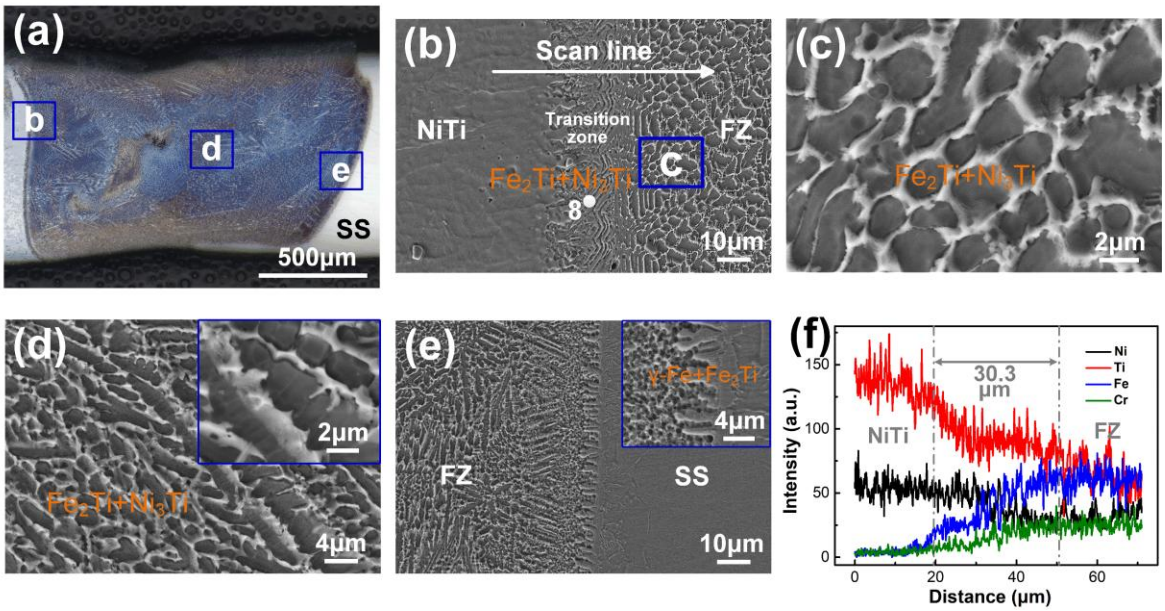


Fig. 3.16 SEM images showing morphologies of the LPD_L joint: (a) cross section of the joint; (b, d and e) the corresponding regions marked in Fig. 3.16a; (c) the corresponding regions marked in Fig. 3.16b; (f) EDS line scanning result along the direction marked in Fig. 3.16b.

Table 3.7 EDS analysis (at.%) of different positions marked in Figs. 3.14 and 3.16.

Position	Ni	Ti	Fe	Cr	Possible phase
1	40.6	34.1	21.1	Bal.	B2+Ni_3Ti+Fe_2Ti
2	9.7	1.3	70.1	Bal.	γ
3	14.2	11.2	56.9	Bal.	γ+Fe_2Ti
4	17.7	16.4	51.0	Bal.	γ+Fe_2Ti+Ni_3Ti
5	35.7	15.0	38.7	Bal.	Fe_2Ti+Ni_3Ti
6	23.3	26.1	40.9	Bal.	Fe_2Ti+Ni_3Ti
7	15.8	7.7	60.2	Bal.	γ+Fe_2Ti
8	29.8	31.6	31.1	Bal.	Fe_2Ti+Ni_3Ti

Fig. 3.17 shows the FVM simulation results in HPD_S (-0.5 mm, 155 ms) and LPD_L (+20 mm, 210 ms) welding modes. Widths at three different heights of FZ (W1, W2, W3) were compared between joint cross section and simulated melting field, and the average errors were 6.67 % and 2.98 % for HPD_S mode and for LPD_L mode respectively, suggesting a good verification of this model. As seen in the melting field, a laser keyhole formed during HPD_S welding process. The width of semi-molten region in HPD_S mode was

narrower than that in LPD_L mode due to a shorter welding duration, which was in good agreement with the analysis for the transition zone thickness (Figs. 3.14i and 3.16f). In the flow field of HPD_S mode (Fig. 3.17b), the NiTi-rich and SS-rich liquids flowed at different regions around the laser keyhole, indicating the inadequate mixing, especially taking the shorter welding time into account. The different flow locations in HPD_S mode were basically consistent with the microstructural distribution in Fig. 3.14a. The liquids in LPD_L mode showed smooth bidirectional flows. It is worth noting that the overall flow velocity in HPD_S mode was higher than that in LPD_L mode, especially in the keyhole surroundings with high recoil force from violent evaporation [127]. The laser keyhole intensified the agitation of molten pool and the instability of the flows.

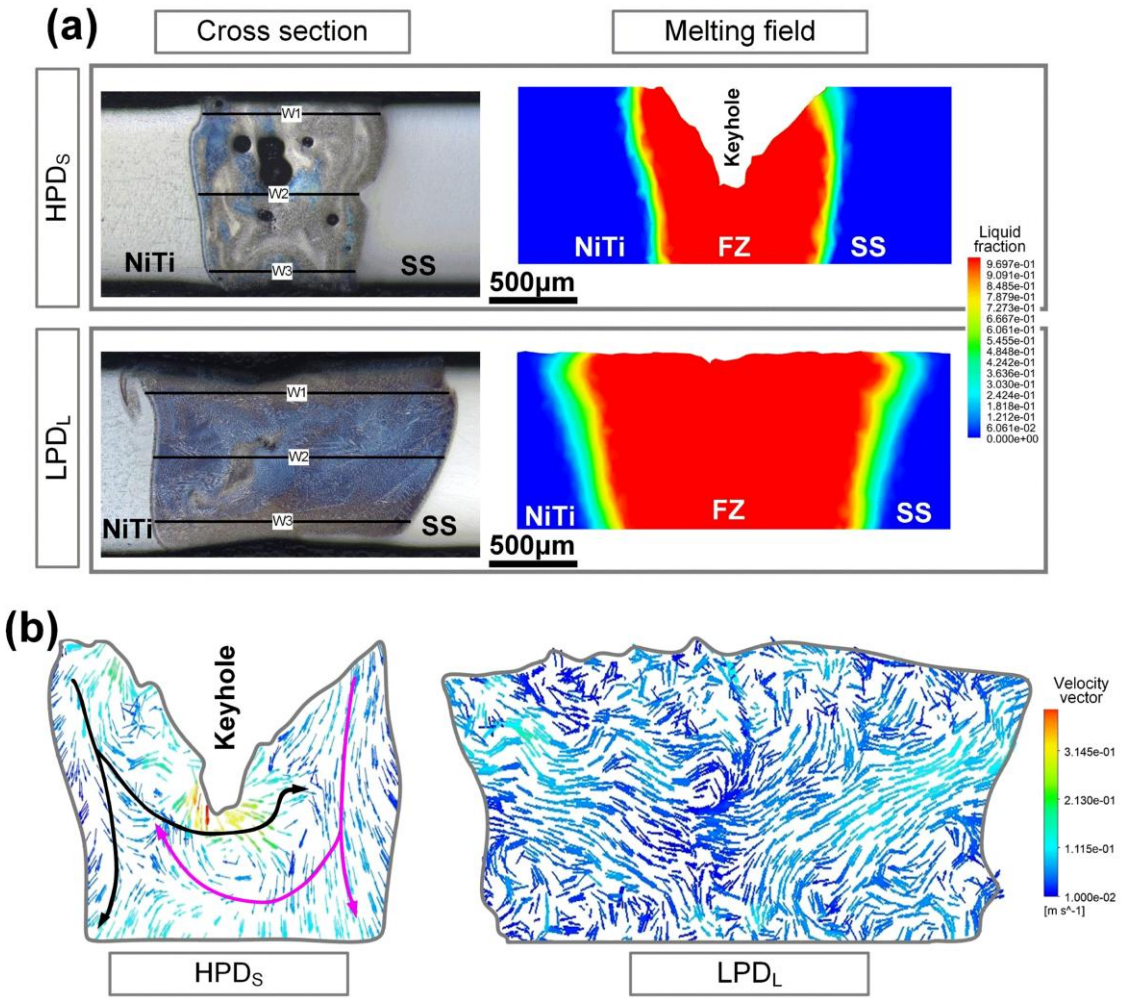


Fig. 3.17 FVM results of (a) cross sections-melting fields and (b) flow fields of HPD_S and LPD_L modes, respectively.

Fig. 3.18a shows the microhardness distribution across the HPD_S (-0.5 mm defocus distance) and LPD_L (+20 mm defocus distance) joints. The hardness in HAZ was lower than that in BMs due to the grain coarsening. Lower HAZ hardness in the LPD_L joint suggested further grain coarsening because of the longer welding time. Hardness in both FZs was much higher because of existence of IMCs network, and it was at a relatively consistent value of ~800 HV in the LPD_L joint. However, a fluctuation from < 800 HV to ~1000 HV could be seen in the FZ of the HPD_S joint. From Fig. 3.18b, the region with high hardness was corresponding to the macro-segregated microstructures as analyzed before, thus high hardness should be attributed to the precipitation of more Fe-Ti-rich Laves IMCs [11,16]. In the LPD_L joint, the uniform FZ microstructure resulted in a relatively uniform hardness in the FZ (Fig. 3.18c).

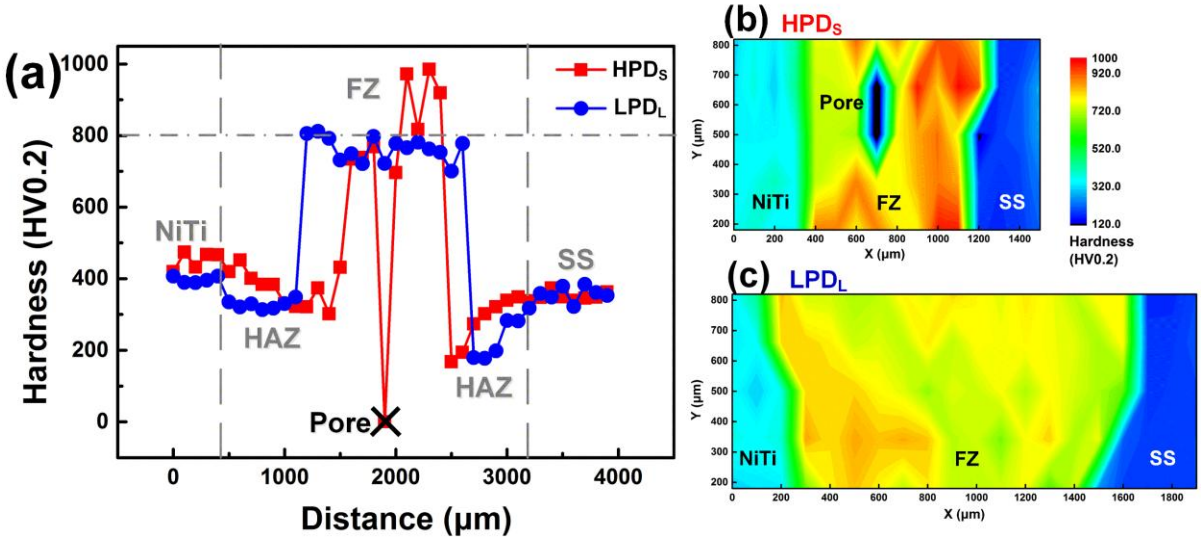


Fig. 3.18 (a) Microhardness line distribution and (b, c) microhardness mappings in joints welded with HPD_S and LPD_L modes, respectively.

The NiTi-SS joints welded with a HPD_S mode exhibited low tensile strength (lower than 186 MPa) as shown in Fig. 3.19a. The joint strength was significantly improved by using the LPD_L mode, and the maximum strength of 290 MPa was obtained when +20-mm defocus distance and 210-ms welding time were used. The joints welded with LPD_L mode also showed better elongation (Fig. 3.19b), but all the joints were fractured at the elastic stage. There is no doubt that the large pores in HPD_S joints reduced the effective joining area of NiTi and SS wires [128]. This should be one of the main reasons for low tensile strength and ductility of HPD_S joints.

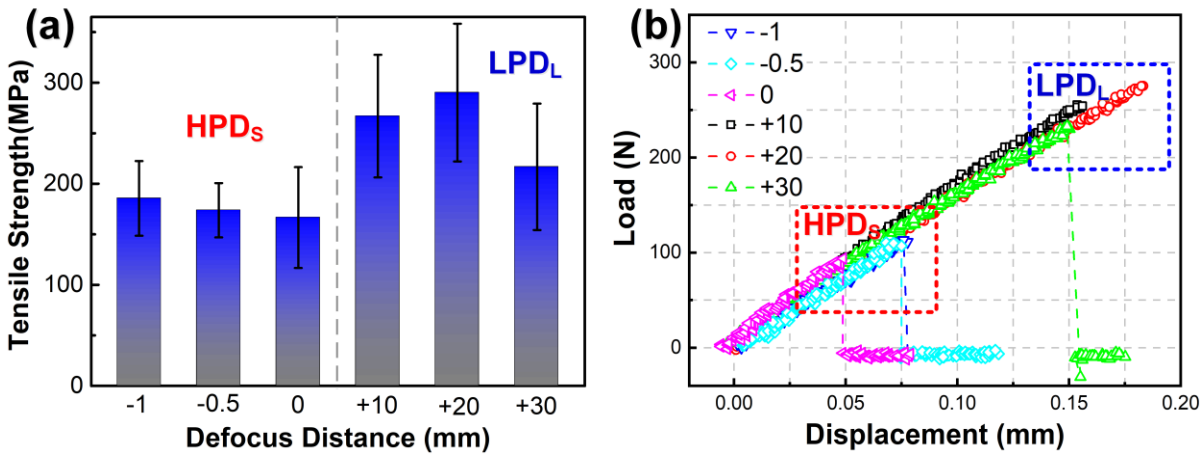


Fig. 3.19 (a) The tensile strength and (b) load-displacement curves of NiTi-SS joints welded with different welding parameters.

Because of brittleness of the overall IMCs network, both HPD_S and LPD_L joints fractured at the FZ, as shown in Fig. 3.20a and 3.20d respectively [77]. Fig. 3.20b presents the edge of the fracture surface of the LPD_L joint (+20 mm defocus distance). Several fine cleavage facets existed, which were caused by crack propagation inside of the fine and uniform IMCs network. The denser striation along the perimeter direction (marked by arrows in Fig. 3.20b) suggested that the crack initiated from the welded wire's surface and then propagated over the peripheral perimeter of the weld. As the final failure region, the fracture surface center also exhibited fine cleavage facets (Fig. 3.20c). Similar crack striation was also observed at the edge of fracture surface of the HPD_S joint (-0.5 mm defocus distance). However, further crack propagation behavior in the HPD_S joint differed from that in LPD_L joint. Fracture surface tended to be the section with high porosity (insert in Fig. 3.20d). Main fracture morphologies were large cleavage facets and flat surface as shown in Fig. 3.20e and Fig. 3.20f, respectively. These fracture surfaces indicated the rapid and dramatic propagation of crack. There were two potential reasons for unstable and fast crack propagation in the HPD_S joint: *a).* Large pores reduced the effective joining area and increased the stress concentration that amplified the instability of crack [129]; *b).* Coarse and bulk Fe_2Ti-rich regions provided path for rapid crack propagation. It has been clarified that the crack is more likely to grow inside brittle Fe_2Ti IMC in the IMCs network of the NiTi-SS joint [18]. Fig. 3.20h and 3.20i display the inner surface of the large pore, with the existence of shrinkage cavities. The shrinkage cavities initiated at columnar grains boundaries and its formation reason will be discussed later.

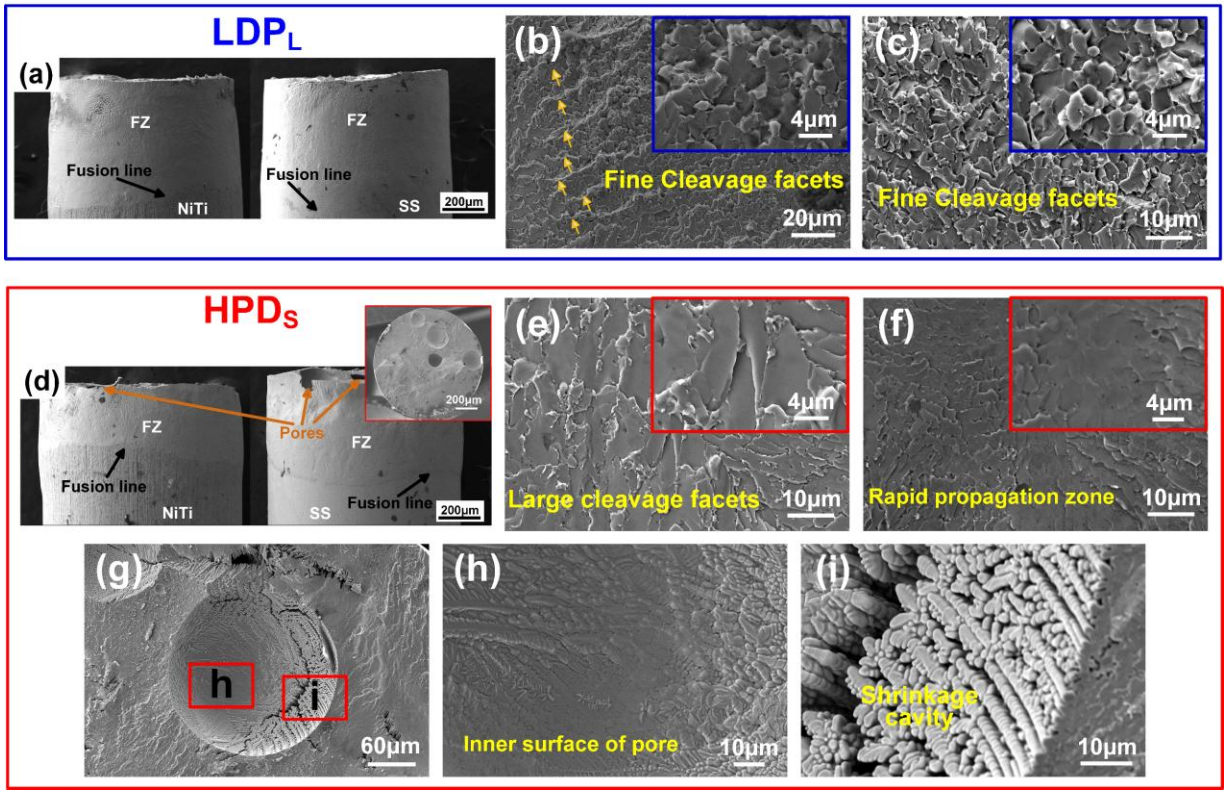


Fig. 3.20 (a) Fracture position of LPD_L joint; (b, c) the fracture surface morphologies of LPD_L joint observed from the edge and center regions, respectively; (d) Fracture position of HPD_S joint; (e, f) two types of fracture surface morphologies of HPD_S joint; (g) the large pore observed at the fracture surface of HPD_S joint; (h, i) the corresponding regions marked at Fig. 3.20g.

Pores formed during the welding process always present different sizes and morphologies, and their influences on welded structures vary. It is necessary to establish some estimations to evaluate their influences on NiTi-SS joint properties. Firstly, the total number and average diameter of pores per joint were counted (Fig. 3.21a). A larger number of pores can be observed in HPD_S joints with a maximum of 13, while the number of pores was less than 4 in LPD_L joints. LPD_L welding mode could also effectively reduce the pore size (from >70 μm in HPD_S joints to <40 μm in LPD_L joints). According to the previous research [130], the resistance to the load-carrying capacity (*R-LCC*$_{total}$) of a weld is introduced here, which provides an evaluation about influences of all the pores on final weld properties:

$$R - LCC_{total} = 2\sum_{1}^{n}\left(\frac{\sigma H_P\left(\frac{W_{max}}{2} - D_p\right)}{\left(2+1.18\left(1-\frac{D_p}{W_{max}}\right)^4\right)}\right) \quad (3.1)$$

Where σ is the applied stress and here it is assumed as 100 MPa [130], H_p and D_p are defined as the height and width of a single pore respectively, W_{max} is the maximum weld width (for spot welding, considering the applied load along the NiTi-SS wires direction, the W_{max} can be the diameter of the wire). The results are shown in Fig. 3.21b. HPD_S joints exhibited higher $R\text{-}LCC_{total}$ value (maximum>23), suggesting that pores seriously decreased the joint load-carrying capacity. LPD_L welding mode showed much less influence from pores on the final joint properties, as indicated by a much lower $R\text{-}LCC_{total}$ (<5). Obviously, the LPD_L mode with low power density and long welding time significantly mitigated the porosity and its negative effects on the NiTi-SS weld.

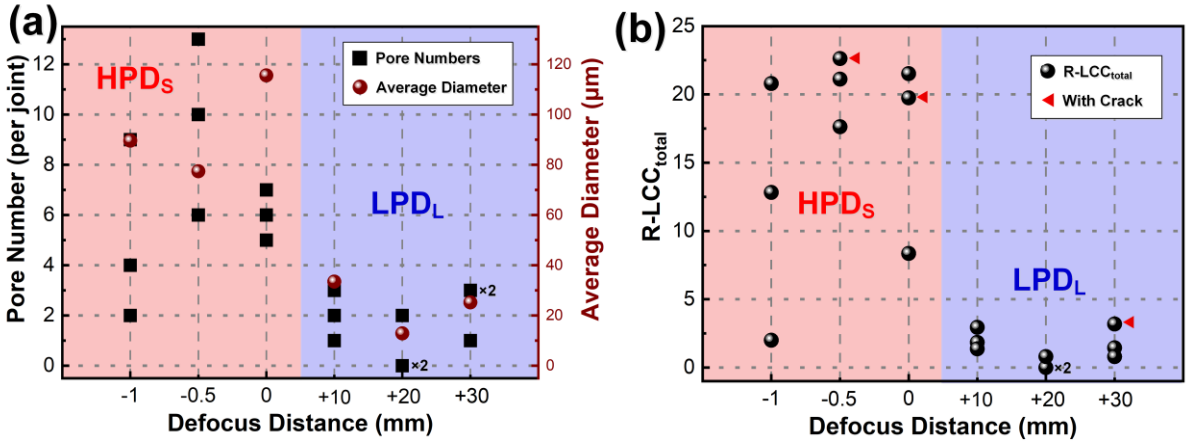


Fig. 3.21 (a) Pore number and average diameter in NiTi-SS joints welded with different parameters; (b) $R\text{-}LCC_{total}$ of pores in NiTi-SS joints welded with different parameters.

There are multiple factors that cause porosity formation, including laser keyhole, alloying element vaporization, microstructure and other inner effects [130]. In similar materials welding the effects of alloying elements and microstructure are usually minor; however, in dissimilar welding of NiTi-SS all of these factors should be taken into account [131,132]. Fig. 3.22 shows the SEM morphologies of different pores in the HPD_S joint. These pores were all spherical with diameters from 17.4 μm to 122.1 μm. The inner surface of a small pore (Fig. 3.22a) was different from its surrounding microstructure, while other large pores illustrated a similar inner microstructure as their surroundings (Figs. 3.22b-d). This suggested their different formation mechanisms. Shrinkage cavities were observed again at the inner surface of the large pore (over 100 μm). Aly J. Castellanos S. et al. established a function to describe the surface tension σ_b of a micro bubble in liquid [133]:

$$\sigma_b = \sigma_\infty \left[\frac{1}{\left(1+\frac{2\delta''}{r}\right)} \right] \tag{3.2}$$

Here, σ_∞ is surface tension of the plane interface, δ'' is determined by the geometrical conformation of the molecules in liquid and will never be negative or infinity, r is the radius of bubble. Equation (3.2) reveals that the increase in surface tension should be expected when a bubble becomes larger in molten metals. The calculated surface tension rose dramatically for a methane bubble when its size was greater than 100 μm in water [133]. In the NiTi-SS joints, the formation of shrinkage cavities might originate from the increase of the surface tension.

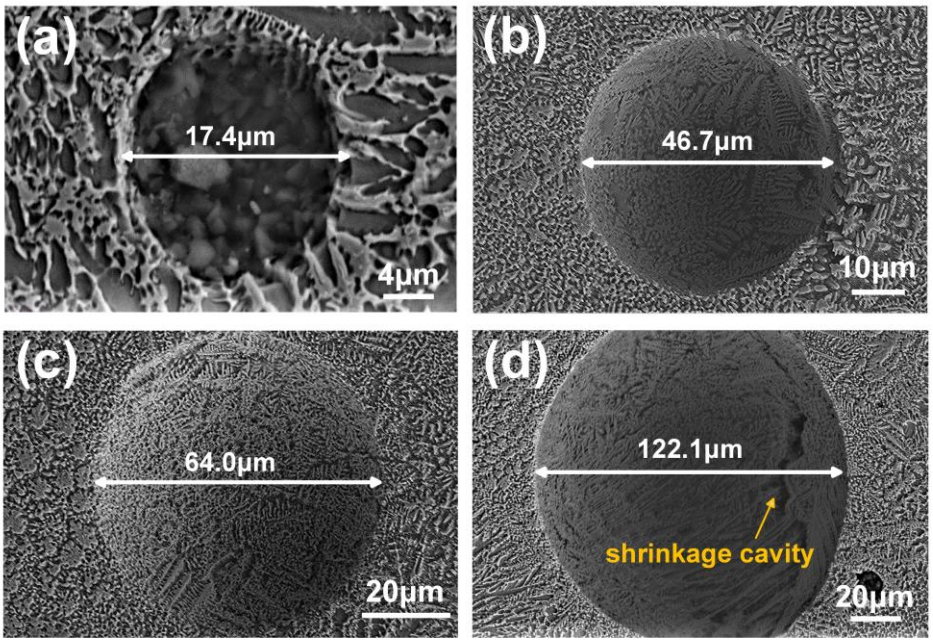
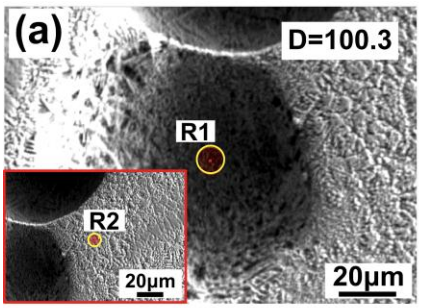


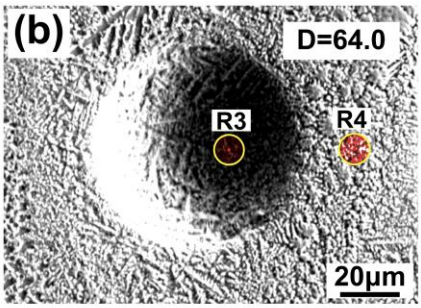
Fig. 3.22 SEM morphologies of pores in the HPD_S joint with different diameters: (a) 17.4 μm; (b) 46.7 μm; (a) 64.0 μm; (d) 122.1 μm.

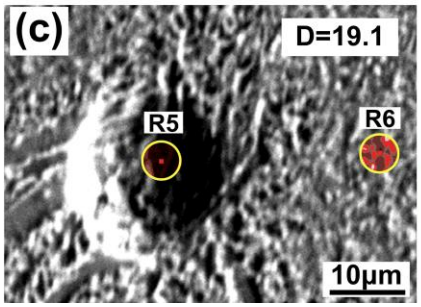
The composition change around pores is helpful for the analysis of pore formation mechanisms [130,134]. EPMA of Ni, Ti, Fe and Cr was performed for pores with different diameters of 100.3 μm, 64.0 μm and 19.1 μm (see Fig. 3.23). The results indicated that there were two main differences between large and small pores. *Firstly*, the total content of Ni, Ti, Fe, Cr inside large pore was less than that outside pore. However, the small 19.1-μm pore had a higher inner total content than its surrounding (Fig. 3.23d). It suggested that some impurities might exist on the inner surface of large pores, such as oxygen, carbon or other elements dissolved in molten metal. Similar phenomenon has been observed in laser hybrid welding of steels although shielding gas was used [130]. The instability of laser keyhole was the reason for large pore formation [135], which is usually associated with evolution and entrapment of impurity gas from air or BM [130,134]. Laser keyhole also provides a channel for the contact between molten metal (or its vapor) and outside gas. This means the observed large pore can be a processing-induced pore. Considering the

laser spot welding used in this work, one possible incentive for large pores is the keyhole collapse after laser was switched off, instead of keyhole moving. By an advanced X-ray imaging technique, the formation of large spherical pores has been directly observed during laser switch-off [136]. Moreover, bubble escaping from the instable keyhole during laser irradiation would be another cause, especially when the mixing of molten metals was non-uniform in the HPD_S mode.

Secondly, Ni concentration inside the small pore is higher than that at surroundings, unlike in large pores. Meanwhile the inside of small pore shows a lower content of Ti (Fig. 3.23d), indicating that the Ni enrichment was from Ni vaporization instead of NiTi segregation. Because of the high equilibrium vapor pressure of Ni, its vaporization is considered as a common issue during NiTi welding or additive manufacturing. Even Ni loss at ~0.3 at.% would result in obvious change of phase transformation temperature [137]. Therefore, the small pore in this study might initiate from the Ni vaporization, and it belongs to a diffusion-induced pore. As Ni diffused from the melt into the initial bubble, the final size of small pore is positively correlated with Ni vapor content and the duration of welding pool [134]. These two factors determine the final diameter of pores. When the molten pool persisted for a longer duration due to the extended welding time employed in LPD_L mode, a few small pores were observed (Fig. 3.21a), which further validates the mechanism. H.M. Li et al. also found that excessive addition of Ni in NiTi-SS laser welding significantly increased weld porosity [82].







(d) EPMA result

	Ni (at.%)	Ti (at.%)	Fe (at.%)	Cr (at.%)	Total mass (%)
R1	18.13	24.41	47.92	9.53	84.70
R2	19.32	14.94	51.42	14.30	92.25
R3	17.94	21.05	51.03	9.98	80.56
R4	18.41	18.09	49.80	13.71	92.75
R5	26.59	18.19	42.08	13.14	95.86
R6	25.57	19.29	43.18	11.95	90.63

Fig. 3.23 EPMA analysis of pores with diameters of (a) 100.3 μm, (b) 64.0 μm and (c) 19.1 μm; (d) the corresponding EMPA results marked in Figs. 3.23a-c.

The HPD_S mode with a high-power density enhanced the laser keyhole effect, leading to the formation of larger pores. The shorter welding time could not provide sufficient time for pore escape. Additionally, the non-uniform FZ microstructure caused by the HPD_S mode contributed to small pore formation due to Ni-rich segregation. In contrast, the LPD_L mode mitigated or even eliminated the laser keyhole effect, allowed more time for pore escape, and uniformized the FZ microstructure, resulting in significant reduction of porosity in the FZ.

3.5 Summary

To achieve weld-brazing of dissimilar NiTi-SS, defocused laser and large beam offset were combined to restrict the fusion location on only NiTi or SS side. Weld-brazing mode decreased FZ hardness from ~1000 HV to ~200 HV due to the reduced IMCs. The joint tensile strength was enhanced significantly from 177 MPa to 330 MPa because of the elimination of overall FZ brittleness and the formation of a reaction layer with fewer harmful IMCs. NiTi-SS weld-brazed joints fractured at the brazed interface region with a mixed ductile-brittle fracture mode. The HPD_S mode with high power density and short welding time resulted in non-uniform microstructure and hardness in the FZ. In contrast, the LPDL mode, with low power density and long welding time, produced a relatively uniform IMC network of Fe_2Ti+Ni_3Ti in the FZ. Two pore formation mechanisms were proposed: large pores were caused by instability or collapse of the laser keyhole, while small pores initiated from the Ni vaporization. The LPD_L welding mode was an effective strategy for porosity mitigation in NiTi-SS laser welding, since it weakened the laser keyhole, increased melting time for pore escaping and uniformized the FZ microstructure.

It should be noted that the tensile strength of the brazed interface was comparable to that of the homogeneous Fe_2Ti+Ni_3Ti IMCs network, as indicated by the joint strengths discussed in Sections 3.3 and 3.4. Laser weld-brazing of NiTi-SS remains significant as it shifts the focus from the conventional and complex issue of FZ brittleness to the control of the brazed interface. Further optimization of the brazed interface—such as introducing Ni at the interface to replace Fe_2Ti with Ni_3Ti or γ-(Fe,Ni) in the reaction layer—is anticipated to enhance joint strength.

Chapter 4 Mixing restriction and brittle phase replacement in resistance spot welded NiTi-SS joints

4.1 Overview

Many engineering applications require the joining of NiTi and SS not only in wire form but also in sheet or strip form [17,74,80,86]. As mentioned earlier, aeronautical and automobile manufacturing calls for the joining of NiTi shape memory alloys to steel sheets [14]. Additionally, some robotic prototypes also demand the joining of NiTi-SS strips [15].

Through thermomechanical processing, RSW exhibits unique capacities in controlling the dynamic behavior of dissimilar metals based on their different melting points, resistivities, thermal conductivities, and hardness. The RSW process is expected to provide new insights into NiTi-SS welding when combined with the two IMC control strategies summarized in Section 2.4. However, even the microstructure and the control of metallurgical reactions in the weld zone of a typical RSWed NiTi-SS joint have yet to be reported. In this chapter, RSW of NiTi-316L SS sheets was conducted. To comprehensively understand both IMCs control strategies (*1.* restricting mixing; *2.* replacing harmful phase), Nb and Ni were selected as the interlayer, respectively. The joint formation and failure mechanisms were uncovered through microstructural characterizations, mechanical testing, thermodynamic calculations and numerical simulations. This study provides first-hand observations on the RSW of NiTi and SS.

4.2 Methodology

Commercially available Ni-rich (50.8 at.%) superelastic NiTi sheet with a thickness of 380 μm and 316L SS with a thickness of 400 μm were used for welding. The X-ray diffraction (XRD, XPERT-PRO diffractometer) pattern of the NiTi base material (BM), detailed in Fig. 4.1a, showed a B2 austenite phase in as-received material, and the undetected (2 0 0) peak was due to the cold-rolling and subsequent annealing process [138]. XRD of 316L SS (Fig. 4.1b) indicated the presence of γ-Fe as the parent phase. Fig. 4.1c depicts the RSW configuration, in which a pair of Cu-Cr water-cooled electrodes with a 4-mm flat tip was adopted. The lap area is a 13×13 mm^2 square, and Nb (melting point: ~2196 K) or Ni (melting point: ~1584 K) interlayer with a thickness of 100 μm was inserted between BMs. RSW was performed by a medium frequency direct current (MFDC) resistance welder. By preliminary experiments (investigation of process window form no joining, to joining to explosion/overburning), the optimized

parameters of electrical current, electrode force and welding time were selected as 4.0 kA, 3.5 kN, and 150 ms, respectively. The detected dynamic resistance for the whole material system is plotted in Fig. 4.1d. The overall profiles with and without Nb or Ni interlayers were similar, showing higher contact resistance at the initial stage and stable bulk resistance during the rest of the RSW process. Compared to those without the interlayer, the contact resistance with Nb or Ni interlayer was relatively higher, which was attributed to more gaps/interfaces between BMs.

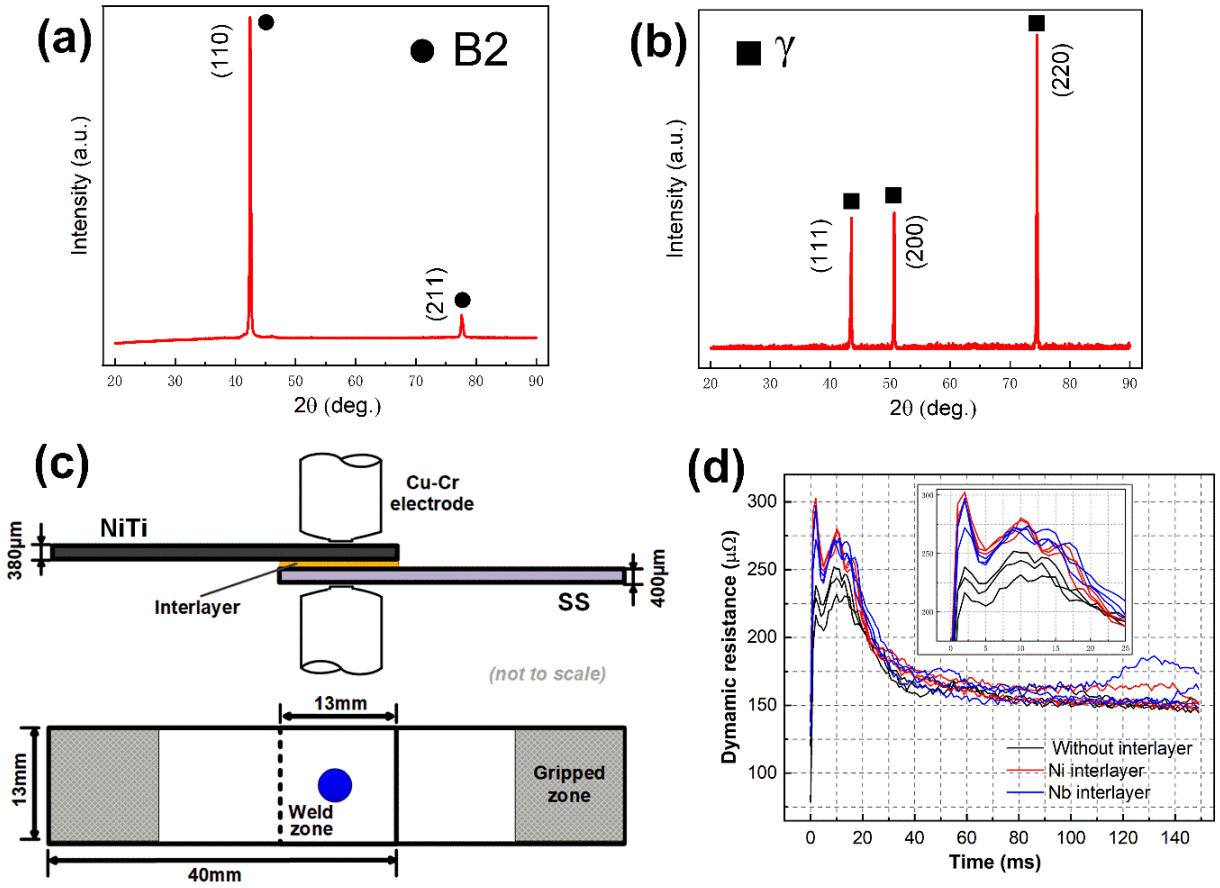


Fig. 4.1 XRD results of (a) NiTi and (b) 316L SS BMs; (c) schematic RSW configuration; (d) dynamic resistance curves during the RSW process.

The cross section of the welded sample was cut along the centerline of the weld zone and then mounted, ground and polished. Weld appearance and microstructure were characterized by optical microscopy (OM, Axio Scope.A1, ZEISS) and field emission scanning electron microscopy (SEM, Zeiss Ultra Plus) equipped with an energy–dispersive X-ray spectrometer (EDS), after etching with Kroll's etchant (HF: HNO_3: H_2O= 2: 3: 45). To understand its unique joint formation mechanism, the Nb-interlayered metallographic sample was further vibratory polished for electron backscattered diffraction

(EBSD) performed using a JEOL 7000F SEM in the Canadian Centre for Electron Microscopy, and the obtained data was post-processed by *HKL channel 5* software. The Nb/SS interface was characterized by scanning transmission electron microscopy (STEM/TEM, ThermoFisher Scientific Spectra Ultra), operated at 200 kV. TEM sample was prepared by the focused ion beam (FIB, *Appendix B*). Thermodynamic calculations of multi-principal alloying elements in FZs of directly welded and Ni-interlayered joints were performed using *Thermo-Calc* software, in which both equilibrium phase fraction and Scheil simulation were calculated. To identify detailed phases in the Nb-interlayered joint, high energy synchrotron XRD (SXRD) was performed with 0.1426 Å-wavelength X-rays (87 keV) at beamline P07 high energy materials science (HEMS) of Helmholtz-Zentrum Geesthacht at PETRA III, DESY. Measurements were performed with a 0.2*0.2 mm beam size and a spacing of 0.2 mm between scans. Microhardness distribution was measured by a CMT Clemex hardness tester with the indent force of 200 g and the dwell time of 10 s. At least 3 welded samples under each condition were used for tensile-shear testing through an MTS frame with the 1 mm/min crosshead speed at room temperature. Gaskets were placed in both gripped zones during the testing (Fig. 4.1c). Fractographic analysis was conducted by SEM and EDS. To evaluate the influence of RSW process on the NiTi superelasticity, micro-scale indentation was performed by an indentation tester (Nanovea-M1) with a spherical indenter, a load control of 5 N and a dwell time of 10 s. Using *Abaqus* package, finite element modelling (FEM) of residual stress distribution on the Nb-interlayered joint was analyzed. Details on modeling are given in *Appendix B*.

4.3 Effect of Nb interlayer on the microstructure

Typical weld nuggets formed in both directly welded (no interlayer) and Ni-interlayered joints, indicating the mixing of molten NiTi and SS (Fig. 4.2a and b). Cracks in these joints were caused by electrode pressure and inherent weld nugget brittleness. A large pore at the boundary of the Ni-interlayered weld nugget that might originate from the Ni vaporization and the original gaps between the materials. The Nb-interlayered joint exhibited a distinct cross section (Fig. 4.2c), in which a FZ could be observed at the NiTi side. Note that Kroll's etchant was ineffective for SS, hence there should be another FZ at SS side considering similar melting points, electrical resistivities and thermal conductivities between NiTi and SS. From Fig. 4.2d and 2e, Ni, Ti, Fe, Cr were all detected in both directly welded and Ni-interlayered joints, supporting mixing of dissimilar molten metals and the resulting formation of IMCs [16]. Addition of Ni from the interlayer could enhance the Ni concentration in the weld nugget to the similar level as that in the NiTi BM, which was expected to promote Ni_3Ti formation and thus reduce the brittle Fe_2Ti. EDS

mapping for Nb-interlayered joint (Fig. 4.2f) verified that the mixing of dissimilar molten metals was significantly limited.

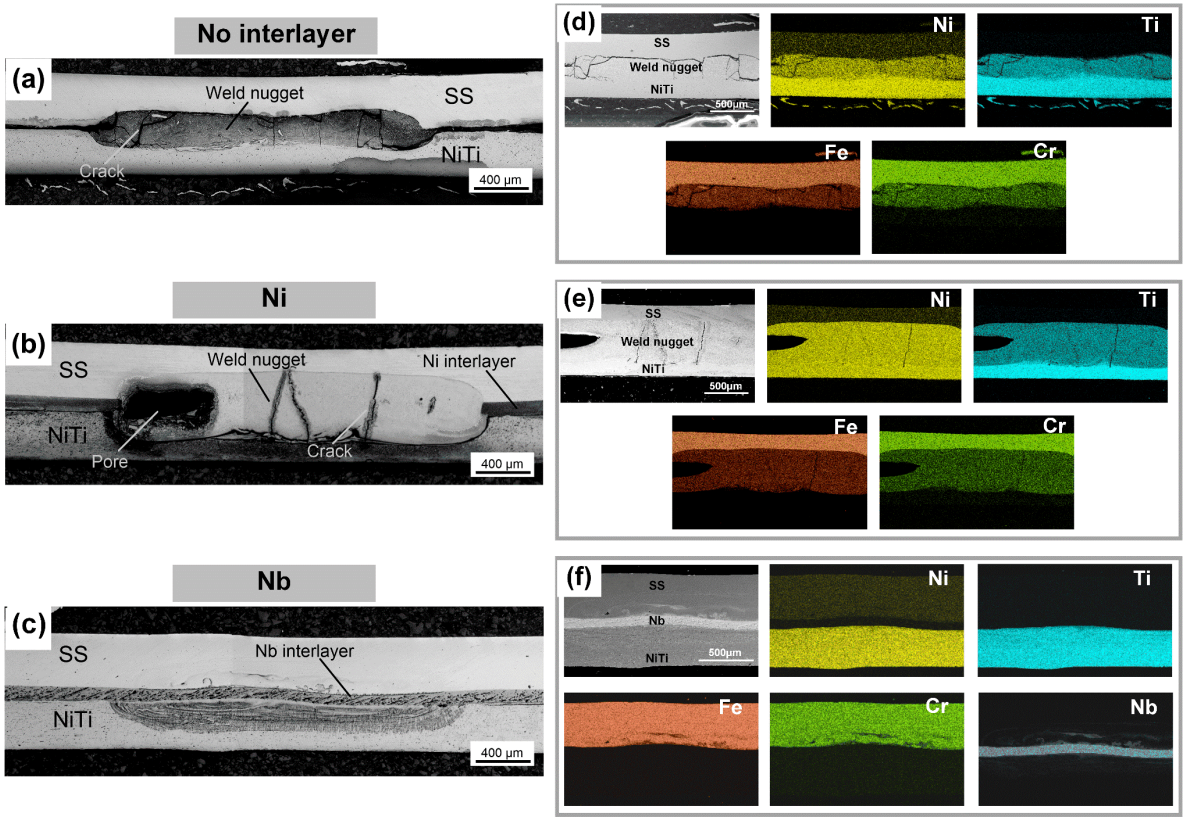


Fig. 4.2 Weld appearances and EDS mappings of NiTi-SS RSWed joints: (a, d) without interlayer, (b, e) with Ni interlayer, and (c, f) with Nb interlayer.

When Nb was used as an interlayer, no obvious defects could be found as shown in Fig. 4.3a. The interface between SS BM and SS FZ could be observed after excessive etching (Fig. 4.3b). Some vermicular phase on γ-Fe matrix at the FZ boundary (Fig. 4.3c) corresponded to residual δ ferrite due to the rapid solidification conditions experienced by the material [119,120], or corresponded to dispersed Fe-Nb phases. The formation of Nb-rich segregation (Fig. 4.3d) in the SS FZ was attributed to the squeezing and the subsequent turbulence of Nb in the molten material [139]. A transition zone (TZ) with some diffused Nb formed adjacent to SS the FZ/Nb interface (Fig. 4.3e). Fig. 4.3f shows the unmolten Nb. Similarly, a TZ was also found between the Nb and NiTi FZ (Fig. 4.3g). The formation of TZs and detailed interfacial microstructure will be discussed later. Columnar NiTi grains formed in the FZ (Fig. 4.3h) due to the supercooling [65,118]. The microstructure changed to equiaxed NiTi in BM (Fig. 4.3i). The EDS line scan of Fig. 4.3j validated all the above observations. It is worth noting that the pure Nb in the interlayer zone indicated that it would remain in a solid state during RSW, because of its high melting

point of ~2196 K. From the SXRD pattern of the Nb-interlayered joint (Fig. 4.4a), γ-Fe-FCC, Nb-BCC and NiTi B2 were mainly detected across the joint. No obvious strong peaks of other phases, indicating fewer IMCs in the Nb-interlayered joint. To clarify the detailed phases, Fig. 4.4b-d display the site-specific diffraction patterns of both BMs and weld zone (WZ). It was possible that there was a small amount of Fe-BCC phase in as received SS due to the manufacturing process. As seen in Fig. 4.4c, beyond the dominated phases including Fe-FCC from SS BM/FZ, Nb-BCC from the interlayer, as well as NiTi-B2 from NiTi BM/FZ, some trace-amount phases were also detected in the WZ. Fe-Nb IMCs formed due to the mixing of Fe and Nb at the narrow TZ in the SS FZ/Nb interface. The formation of the NiTi-B19' martensite might originate from the deformation, nonequilibrium solidification and Ni loss in the NiTi FZ, which was also found in other NiTi welds [140]. Furthermore, to infer on the deformation and residual stress state, Fig. 4.4e exhibits the microstrain evolution from BMs to WZ (calculation details in *Appendix B*). Based on the different thermophysical properties between BMs, three phases showed distinct microstrain evolution tendencies. The microstrain in SS tended to slightly change with proximity to the WZ, suggesting a low compression stress or possibly some released stress after welding. However, NiTi showcased a dramatically increased microstrain in the WZ, indicating the higher tensile residual stress at NiTi WZ. At the Nb interlayer, an overall tendency for the microstrain to slightly increase towards the NiTi side was observed, which also verified a higher stress value in NiTi side.

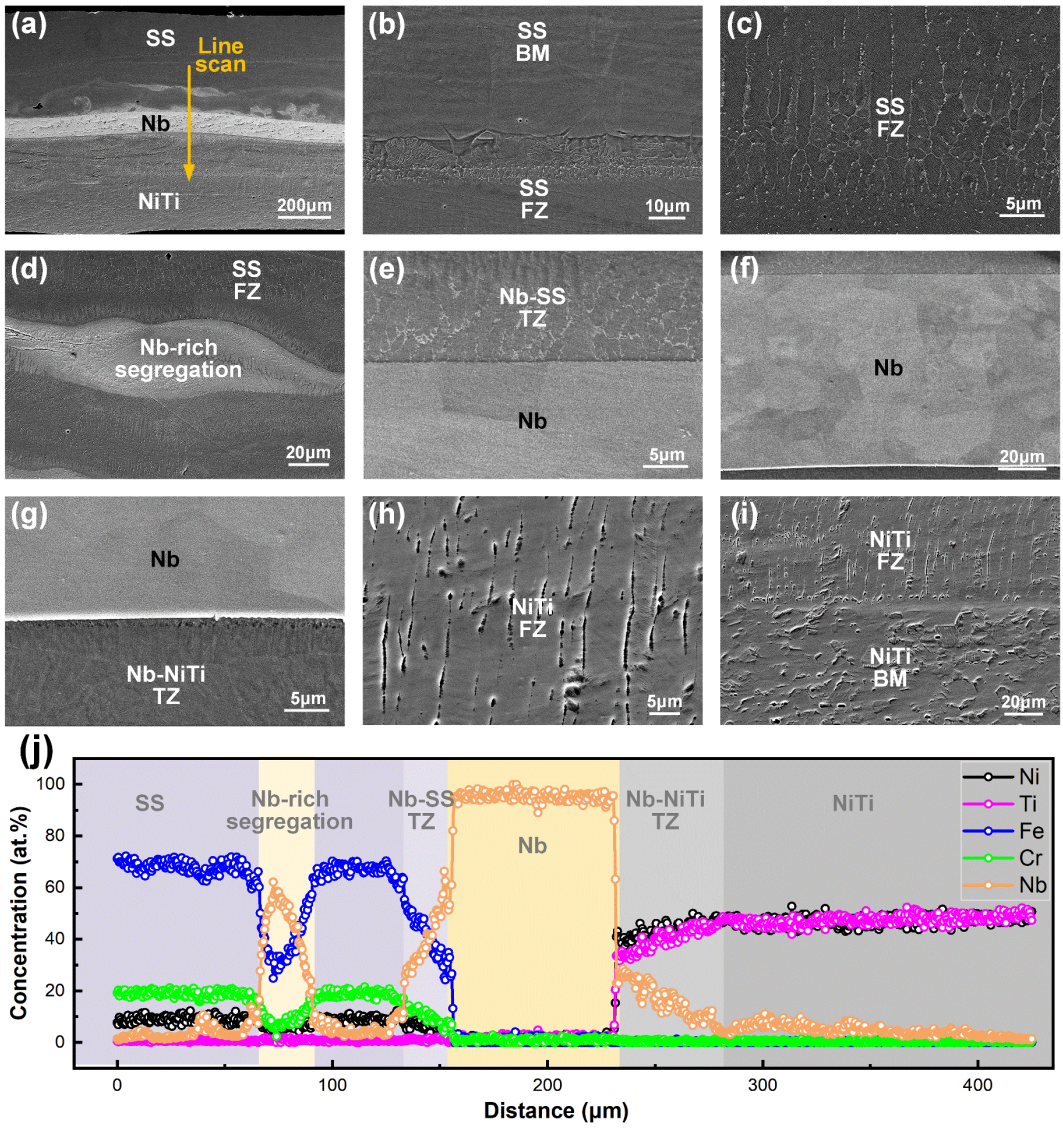


Fig. 4.3 (a) SEM image of the cross section of Nb-interlayered joint; (b) morphology of the SS BM/SS FZ interface; (c) morphology of the SS FZ; (d) morphology Nb-rich segregation; (e) morphology of the Nb-SS TZ/Nb interface; (f) unmolten Nb interlayer; (g) morphology of the Nb/Nb-NiTi TZ; (h) morphology of the NiTi FZ; (i) morphology of the NiTi FZ/NiTi BM interface; (j) EDS line scanning result according to the direction marked in Fig. 4.3a.

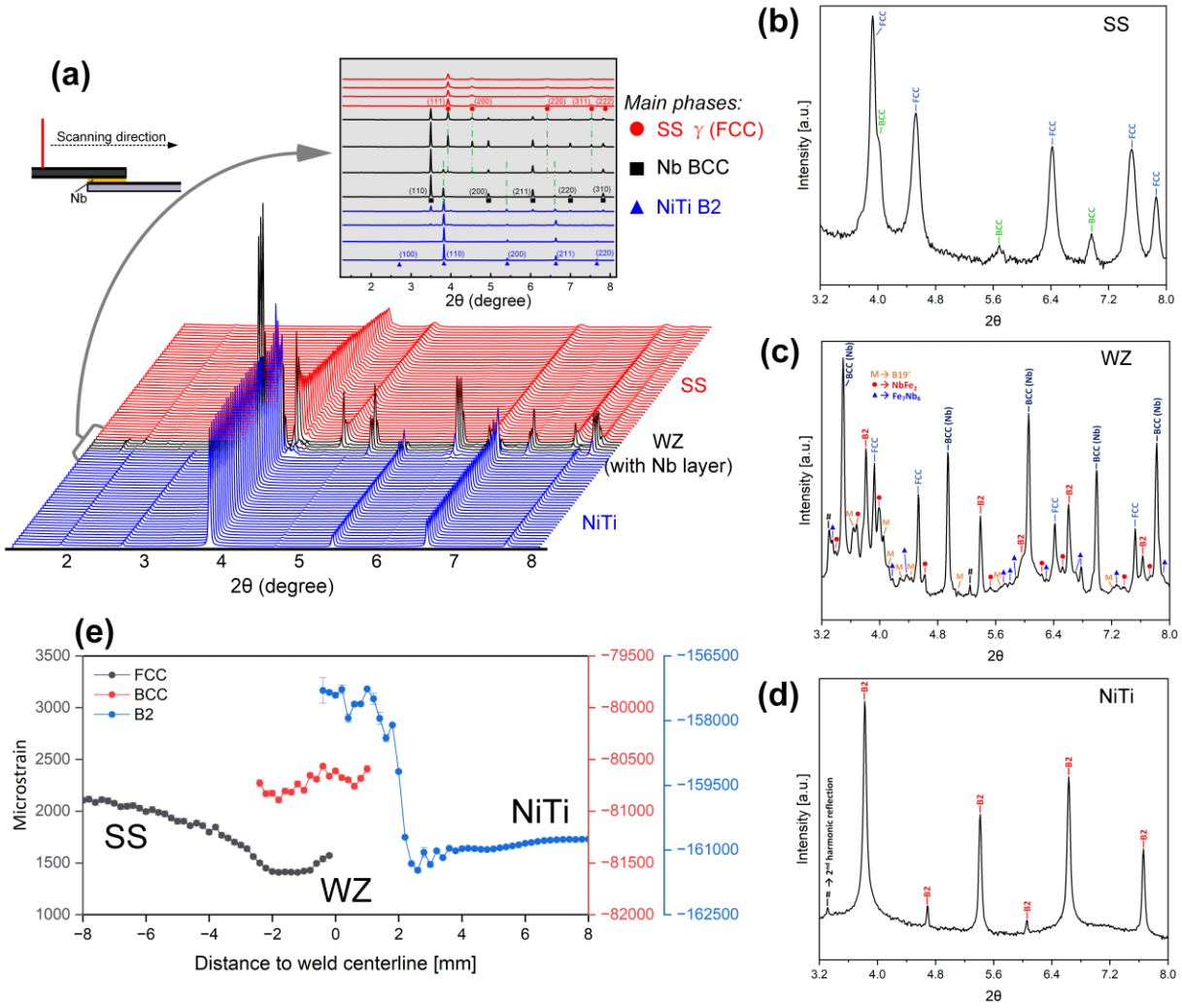


Fig. 4.4 SXRD results of the Nb-interlayered NiTi-SS RSWed joint: (a) the overall scanning result and the main phases at the WZ; (b-d) the detailed phase identification at SS BM, WZ and NiTi BM respectively; (e) the calculated microstrain along the joint.

From the previous work and the NiTi-Nb phase diagram [141], the detailed microstructure on NiTi/unmolten Nb interface has been analyzed. Due to a low eutectic isotherm, two phases of B2 NiTi and BCC Nb were formed in the NiTi-Nb mixed zone, which corresponded to the phases formed at the Nb-NiTi TZ in this work, especially considering that no other Nb-Ni-Ti phases were detected by SXRD. Therefore, an interface between NiTi-Nb eutectics and pure Nb was obtained. There is also published work on Nb-SS welded interface [142], but with a complex mixed zone due to high metal vaporizing pressure. Therefore, TEM analysis on this interface was conducted in this work. Fig. 4.5a and b show the STEM high-angle annular dark-field (HAADF) image of the Nb/Nb-SS TZ interface and the EDS mappings of Nb and Fe from the related regions. It was verified again that the bulk Nb was unmolten since

there was no obvious Fe in the Nb interlayer, and the selected area diffraction (SAD) in this side indicated a Nb-BCC structure (Fig. 4.5d). Note that there were many dislocation pileups inside Nb interlayer, and Fig. 4.5c exhibits the high-resolution TEM (HRTEM) image of a location pile-up region. By the inverse fast Fourier transition (IFFT) of a square region from the dislocation pile-up, high-density dislocations could be observed in Nb (1 1 0) planes (e.g., the marked edge dislocation), which evidenced the severe deformation of Nb interlayer during the welding process. The Nb surface melted during the RSW initial stage and then diffused into the SS FZ, resulting in the formation of the Nb-SS TZ composed of interlaced Nb-rich and Nb-Fe-mixed phases. The SAD verified that the Nb-rich phase was Nb-BCC structure (Fig. 4.5e), while the Nb-Fe-mixed phase was identified as the rhombohedral Fe_7Nb_6 phase (Fig. 4.5f), which was also detected by SXRD. Based on the Nb-Fe phase diagram and the morphologies of these two phases in Fig. 4.5b, it was clear that Nb-Fe_7Nb_6 eutectics formed in the Nb-SS TZ. In Fig. 4.4c, Fe_2Nb was also found by SXRD, but it was not found in the near-interface Nb-SS TZ due to the high Nb concentration here. Considering the low diffusion rate of Nb atoms, the Fe_2Nb should be less and dispersedly distributed in the SS FZ (will also be verified by hardness analysis later). It has been investigated that the hardness and elastic modulus of Nb-Fe_7Nb_6 eutectics are much lower than those of Fe_2Nb [143]. Furthermore, dispersed Nb-BCC phases also provided good toughness for the TZ. Therefore, both Nb/NiTi interface and Nb/SS interface are composed of Nb-containing eutectics with the low brittleness.

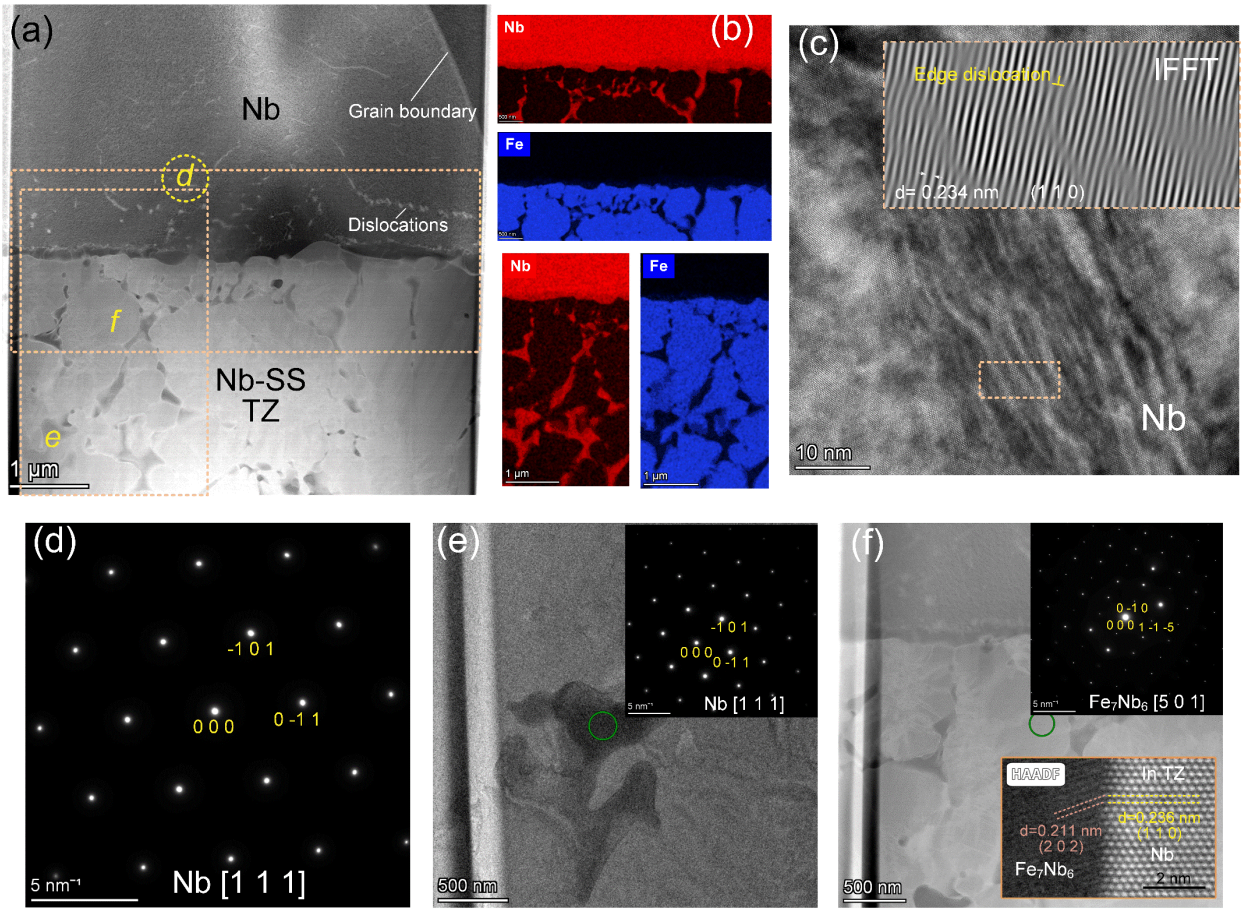


Fig. 4.5 (a) HAADF image of the Nb/SS interface region; (b) EDS mappings of square regions marked in Fig. 4.5a; (c) HRTEM image of a dislocation pile-up region in Nb; (d) SAD pattern from the region marked in Fig. 4.5a at Nb; (e) TEM image and SAD pattern from the marked Nb-rich region, as also marked in Fig. 4.5a; (f) HAADF image and SAD pattern from the marked Nb-Fe mixed region, as also marked in Fig. 4.5a (the insert shows the HRSTEM image of a interface between eutectic phases).

In Fig. 4.6a, an ultrathin interfacial layer (~100-200 nm) was observed between Nb and TZ, and the EDS analysis suggested that it was Nb-based (88.2 at%) with segregated Mo (1.5 at%). SAD proved that this interfacial layer was also Nb-BCC structure (Fig. 4.6c). The diffusion of Mo from SS into the interfacial layer might be attributed to the similarities of both atomic size and crystal structure between Nb and Mo. The detailed atomic joining mechanisms of the interface were characterized by HRTEM. Firstly, the interface between the Nb and the interfacial layer was completely continuous in atomic arrangement and ideally coherent (as marked by a (1 1 0) plane in Fig. 4.6d). Secondly, the interface between the interfacial layer and the Nb-SS TZ (i.e., Fe_7Nb_6) was a semi-coherent interface or a coherent interface with misfit strain (~10% mismatch of lattice parameters between Fe_7Nb_6 (2 0 2) and Nb (1 1 0)

in Fig. 4.6e), suggesting a relatively good match-up between dissimilar phases. A similar interface between the eutectic phases was also found in the TZ (Fig. 4.5f). Overall, metallurgical bonding could be realized based on elemental diffusions and the resultant interfacial layer/eutectics.

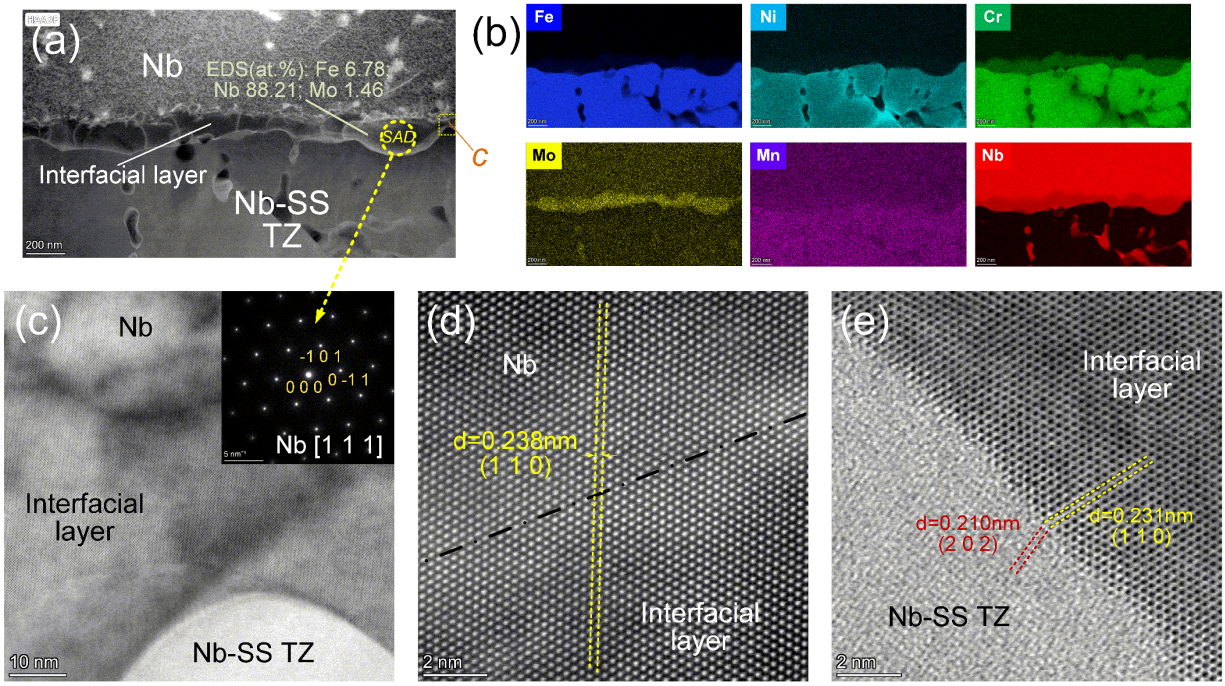


Fig. 4.6 (a) HAADF image of the detailed Nb/SS interface showing an interfacial layer between Nb and Nb-SS TZ; (b) EDS mappings the region of Fig. 4.6a; (c) HRSTEM image (with averaging filter) of the interfacial region and the SAD pattern from the interfacial layer marked in Fig. 4.6a. (d) HRSTEM image of the interfacial layer/Nb interface; (e) HRSTEM image (with averaging filter) of the interfacial layer/Nb-SS TZ interface.

4.4 Effect of Ni interlayer on the microstructure

The Ni-interlayered joint showed similar features as the directly welded joint, thus the microstructure of the directly welded joint was analyzed first in this section. Fig. 4.7a-c present the overall weld morphologies of the directly welded joint. An obvious weld nugget formed between SS and NiTi, where cracks crossed the whole nugget due to the FZ brittleness. The microstructure in this weld nugget was the typical IMCs network with many microcracks (Fig. 4.7d) [18,144]. The interfaces between SS and the weld nugget or between the weld nugget and NiTi exhibited the chemical segregation at the semi-fusion zone (Fig. 4.7e and f), which could result in the cellular-dendritic growth of brittle $(Fe,Cr)_2Ti$ in the SS side interface [16]. EDS line scanning revealed similar atomic fractions among Ni, Ti and Fe in the weld nugget region, as shown in Fig. 4.7g. The Ni-Ti peak and Fe peak near the weld nugget/NiTi interface corresponded to the chemical or microstructural segregations.

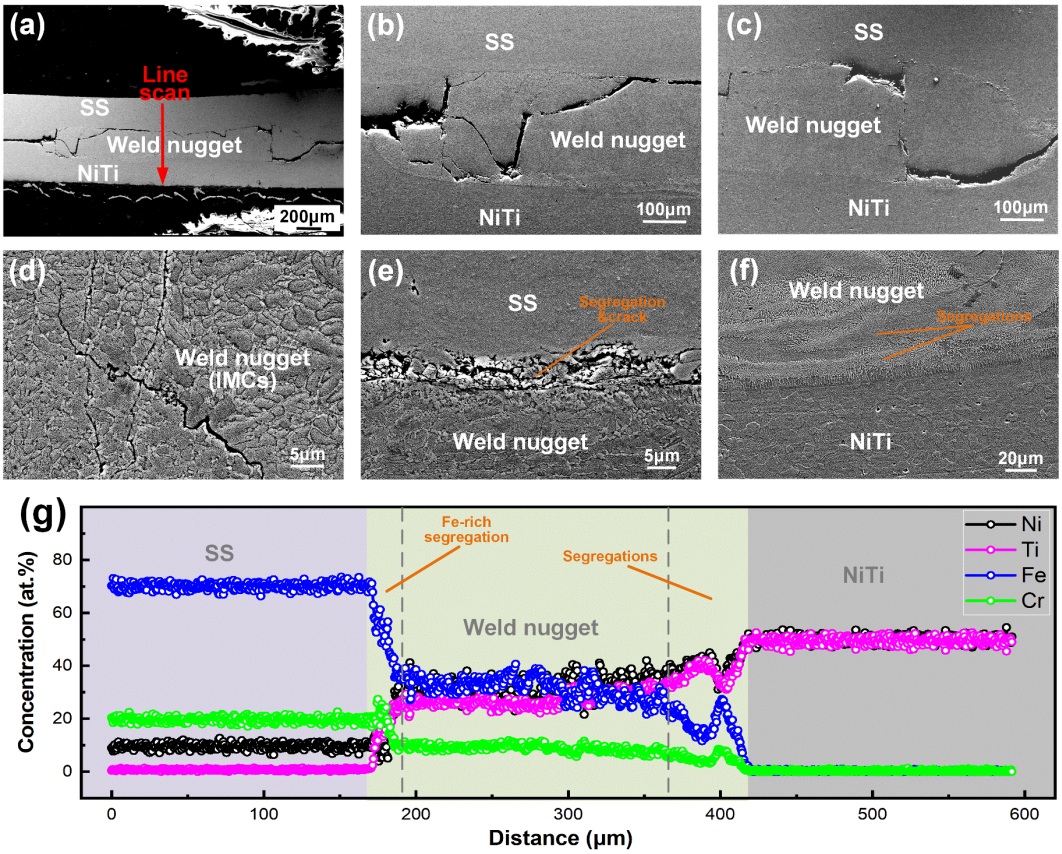


Fig. 4.7 (a-c) SEM images of different regions from the cross section of a directly welded sample; (d) microstructure in weld nugget center; (e, f) morphologies of SS/weld nugget interface and weld nugget/NiTi interface, respectively; (g) EDS line scanning result according to the direction marked in Fig. 4.7a.

The melting point, resistivity and thermal conductivity of pure Ni are similar to those of NiTi and SS (Fig. 4.1d also indicates similarity of the dynamic resistance), thus a typical weld nugget also formed in the Ni-interlayered joint based on the mixing of molten NiTi, SS and Ni. On the other hand, Ni has a significantly higher equilibrium vapor pressure and was more likely to be vaporized in a Ni-Ti-Fe-Cr system [137,145]. The vaporization-induced porosity has been observed in other RSW research [146]. Although Ni-vaporization pores were normally dispersed and in a small size due to the limited Ni vapor content, as observed during laser welding in Chapter 3; pores in this work were likely to further grow into large ones due to the higher Ni concentration in FZ. Besides, the original gaps between interlayer and BMs might also contribute to the formation of porosity in the weld zone. These pores then moved and aggregated towards the weld nugget border under the electrode pressure (Fig. 4.8a). No transition zone (TZ) was found in the SS/weld nugget interface (Fig. 4.8b). The weld nugget microstructure (Fig. 4.8c and d) differed from that in directly welded joint, suggesting different phases caused by the high Ni content.

A TZ could be observed between the weld nugget and the NiTi BM (Fig. 4.8e). Shrinkage cavities existed in the weld center region originated from the last stage of solidification due to the loss of alloying element loss (mainly via Ni vaporization). Cracks across the whole thickness of the weld nugget were found in the weld center (Fig. 4.8g). The crack gap (Fig. 4.8h, over 5 μm) was much larger than that in the IMCs network of a directly welded joint (Fig. 4.8d). It was speculated that this large-gap crack was induced by shrinkage cavities and electrode pressure, differing from the microcrack caused by brittleness and residual stress [18,75,85]. The weld nugget microstructure transformed from equiaxed grains at the NiTi or the SS border into columnar dendrites at the weld center, as observed from Fig. 4.8c or d to Fig. 4.8i. In brief of the classical supercooling theory [65,118], during solidification an equiaxed grain morphology is more likely to transfer into columnar grain with the increase of G/R (G is the temperature gradient and R is the growth rate); hence it is understandable that the transition from equiaxed grains to columnar grains, when moving towards the center considering the water-cooled electrodes at both sides. Fig. 4.8j shows that Ni dominated (around 50 at.%) in the weld nugget. A region of NiTi-rich to Fe-rich transformation (i.e., chemical or microstructural segregations) near NiTi was also observed in this joint, corresponding to the formation of a TZ.

Mixing of dissimilar molten metals and the nonequilibrium solidification resulted in complex IMCs structures being formed. Phases with similar crystal structures, such as Fe_2Ti, Cr_2Ti, Ni_3Ti, etc. are tricky to be identified by regular techniques [18,72]. Therefore, thermodynamic calculation regarding a Ni-Ti-Fe-Cr melt was carried out using *Thermo-Calc*. Both TCFE10 Fe-based database and SSOL6 alloy solution database were adopted to gain a comprehensive understanding of the microstructural evolution. Besides of equilibrium phase fraction calculation, the Scheil calculations were also performed to describe the solidification path during a nonequilibrium solidification [147,148]. The calculation for a typical composition in the FZ of the directly welded joint (29.1 at.% Ni, 32.4 at. Ti, 30.8 at.% Fe, 7.7 at.% Cr, detected by EDS) suggested that C14_Laves (namely Fe_2Ti or Cr_2Ti) phase was the highest content (50%-60%), while the rest was mainly Ni_3Ti+B2 (~20% for each) and Ni_3Ti (over 30%) for TCFE10 and SSOL6, respectively (Fig. 4.9a and b). Scheil simulations also indicated the C14_Laves was the first precipitated phase with high fraction in the solid (Fig. 4.9c and d). The IMCs network of Fe_2Ti and Ni_3Ti would form in the weld nugget in directly welded joint, which agrees with other works [17,18,50]. The formation of a Ni_3Ti-dominated (~70%) weld nugget was verified by the calculation of a typical composition (51.2 at.% Ni, 19.7 at. Ti, 23.4 at.% Fe, 5.7 at.% Cr, detected by EDS) in Ni-interlayered FZ (Fig. 4.9 e-h). The

microstructure and cracking origin in the Ni-interlayered joint could be verified again, as Ni_3Ti phase was a relatively ductile phase [11,149].

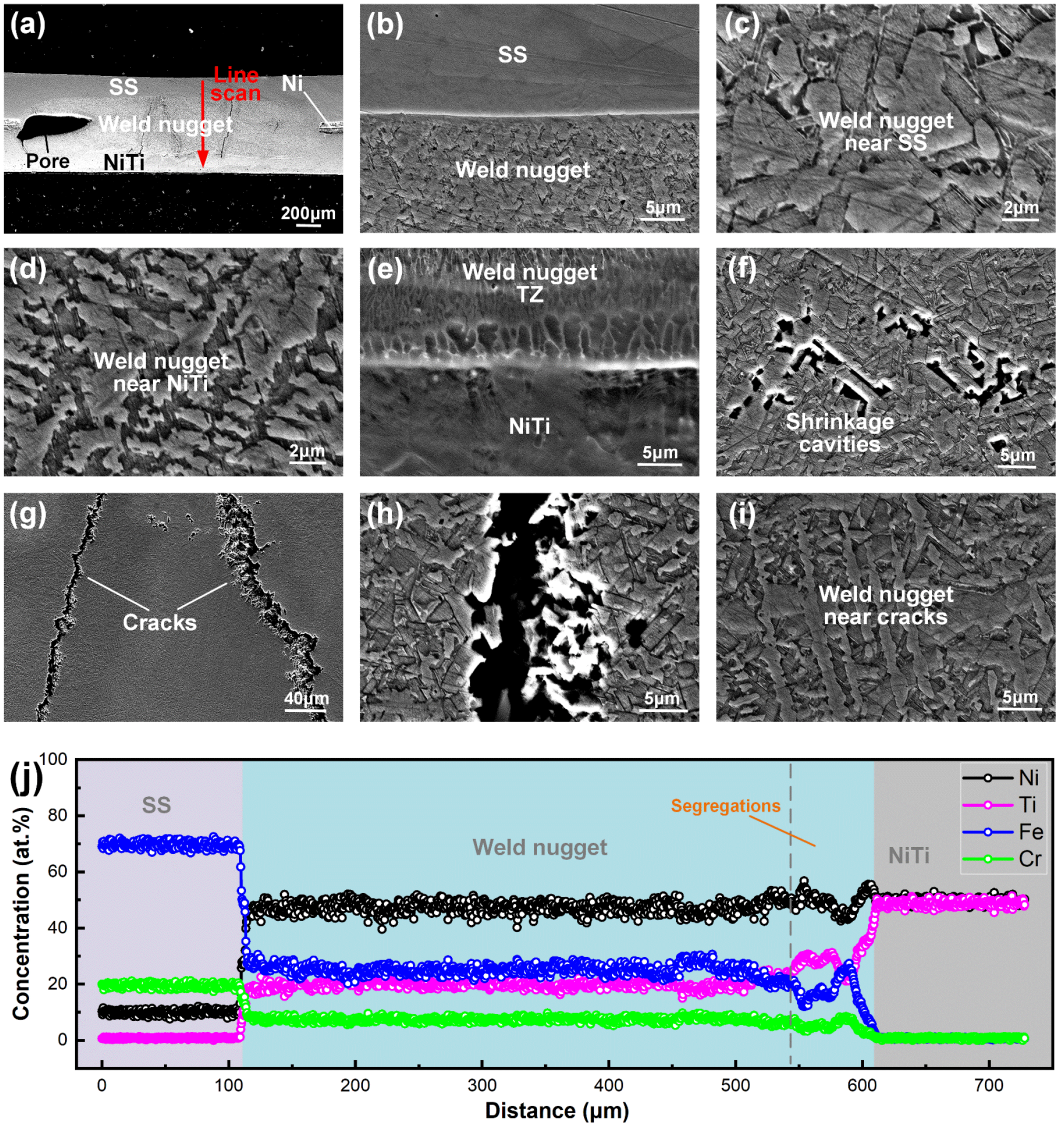


Fig. 4.8 (a) SEM image of the cross section of Ni-interlayered joint; (b) morphology of the SS/weld nugget interface; (c) weld nugget microstructure near SS side; (d) weld nugget microstructure near the NiTi side; (e) morphology of the weld nugget/NiTi interface; (f) shrinkage cavities in the weld nugget; (g, h) morphologies of cracks in the weld nugget; (i) microstructure near cracks in the weld nugget center region; (j) EDS line scanning result according to the direction marked in Fig. 4.8a.

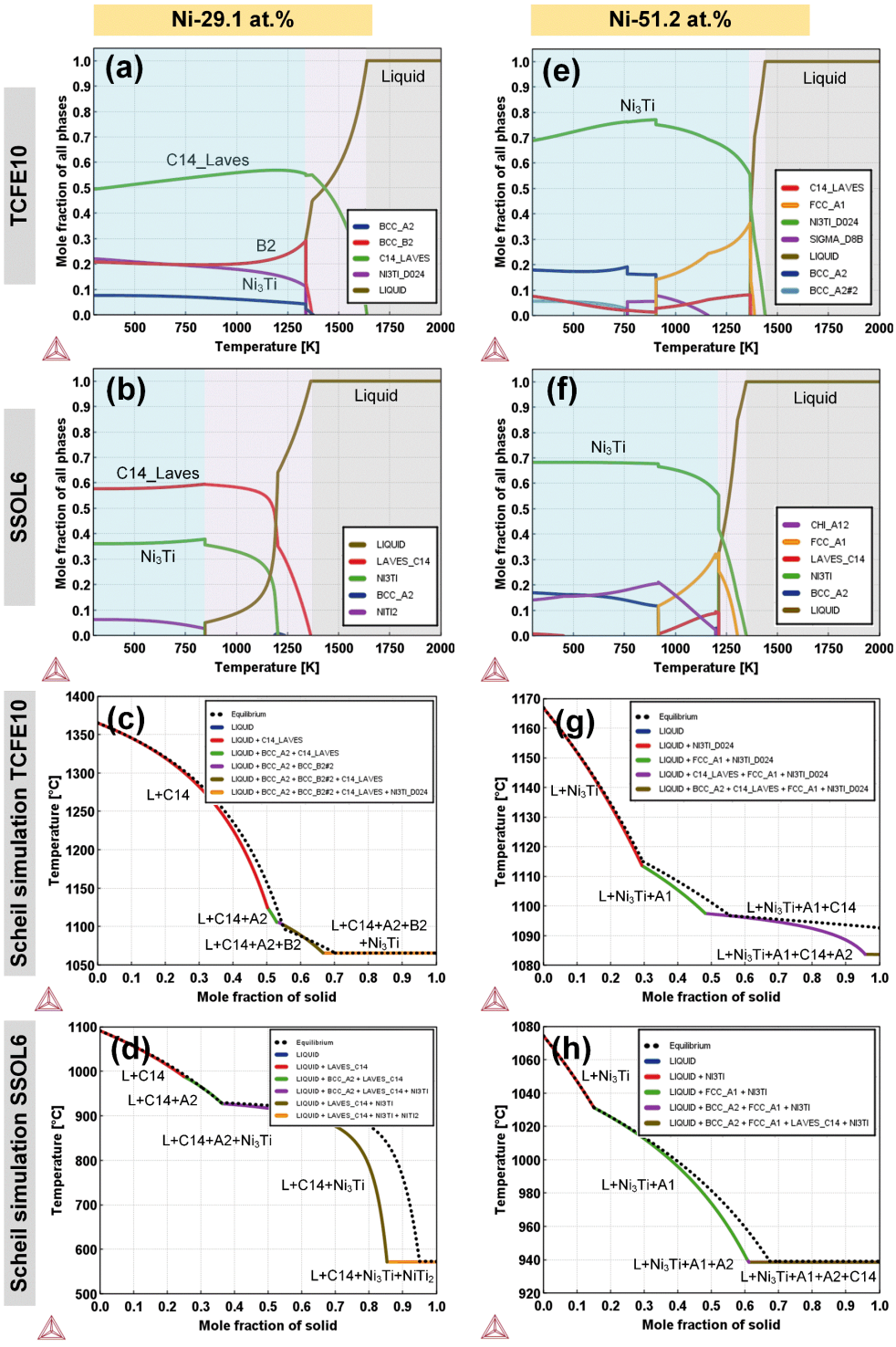


Fig. 4.9 For the composition of 29.1 at.% Ni, 32.4 at. Ti, 30.8 at.% Fe, 7.7 at.% Cr: the calculated equilibrium phase fractions with (a) TCFE10 database and (b) SSOL6 database, respectively; Scheil calculation results with (c) TCFE10 database and (d) SSOL6 database, respectively. For the composition of 51.2 at.% Ni, 19.7 at. Ti, 23.4 at.% Fe, 5.7 at.% Cr: the calculated equilibrium phase fractions with (e) TCFE10 database and (f) SSOL6 database, respectively; Scheil calculation results with (g) TCFE10 database and (h) SSOL6 database, respectively.

4.5 Mechanical properties and fractography

Microhardness was measured according to the schematic insert in Fig. 4.10a. With the IMCs network, the weld nugget of directly welded joint exhibited an extremely high hardness over 750 HV, due to the presence of brittle Fe_2Ti [149]. Melting of the Ni interlayer into the mixed FZ effectively reduced the hardness to 500-600 HV by replacing Fe_2Ti with more ductile Ni_3Ti. The hardness profile in Nb-interlayered joint showed more variations, but the whole weld zone is significantly softer. The unmolten Nb had lowest hardness, with a slightly increased value (by ~10 HV) compared to its as-received state (*Appendix B*) due to the deformation during RSW process. SS FZ was relatively hard (but still lower than 450 HV), which should be due to the precipitation of small amount of Fe_2Nb, as analyzed before. The low hardness also indicated decreased IMCs in the Nb-interlayered joint.

Fig. 4.10b illustrates that Nb interlayer could improve the joint tensile-shear load to over 1.2 kN from ~0.9 kN in the case of Ni-interlayered or direct welded joints (increase by ~38%). This improvement was more significant when looking at energy absorption during the testing (increase by ~460%), suggesting an enhancement in toughness. The Nb-interlayered joint fractured during the plastic deformation with higher elongation as shown in Fig. 4.10c; while the directly welded and Ni-interlayered joints fractured right after the elastic stage, highlighting their brittle-like behavior. Both Ni-interlayered and Nb-interlayered joints fractured with a NiTi BM failure (BF) mode. Only directly welded joints fractured with an interfacial failure (IF) mode. Therefore, in Fig. 4.10d, the shear stress and tensile stress for the directly welded joint and Ni/Nb interlayered joint are calculated, respectively. The strength of the Nb-interlayered joint was higher than the yield strength of SS (*Appendix B*). The requirement for the whole-thickness NiTi BF should be around 250 MPa as verified from the results of Nb-interlayered joint, but the low-strength NiTi BF occurred in the Ni-interlayered joint. The inconsistency between joint strength and failure mode will be discussed through fractographic analysis. As seen from Fig. 4.11, micro-scale indentation test was performed on NiTi BM and NiTi FZ to evaluate the influence of RSW process on superelasticity. Test was also performed on the SS BM as a reference. Compared to SS with a large residual strain around 4.5 μm, both NiTi BM and NiTi FZ exhibited typical superelastic curves with lower residual strains. B2 phase transformed into B19’ phase during loading, and the inverse martensitic transformation occurred during unloading. However, the welding process degraded the superelastic performance of NiTi, as the residual strain increased from ~0.5 μm to ~2 μm. This degradation was always observed in NiTi welds, and it might originate from the grain coarsening and the deviation of B2 orientation [150].

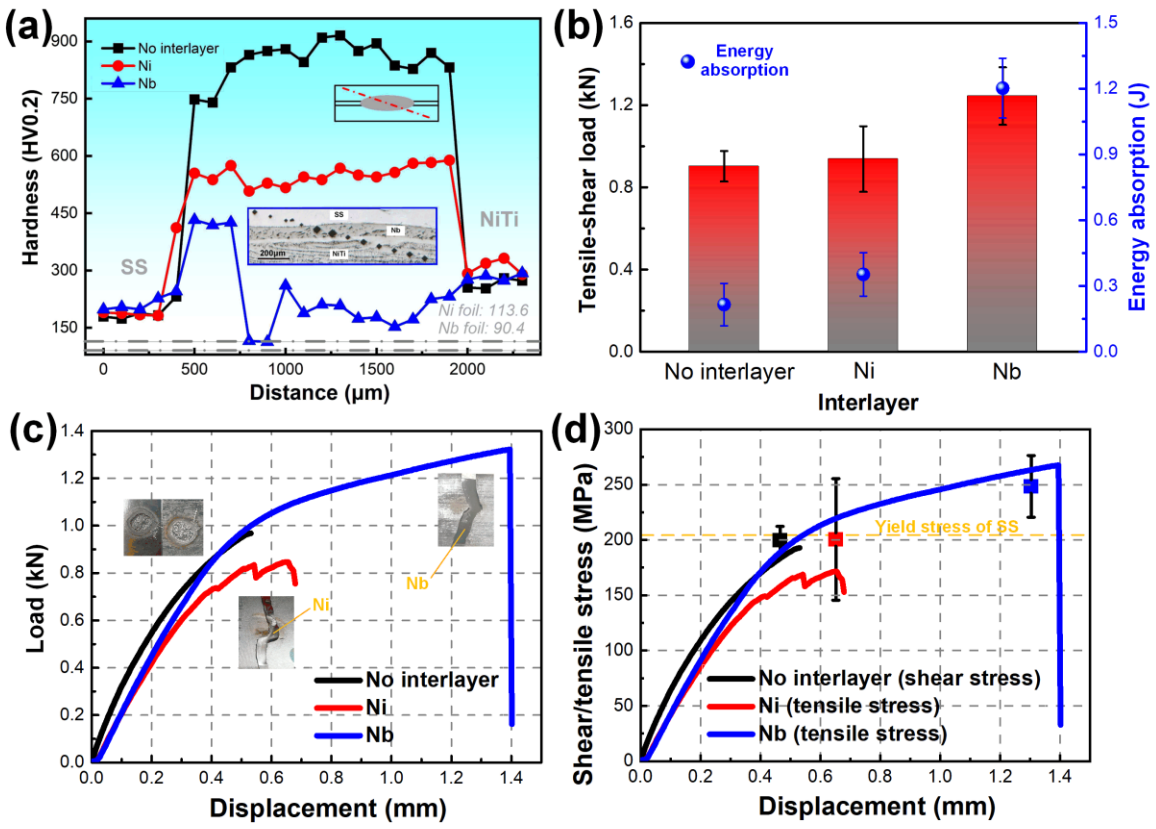


Fig. 4.10 (a) Microhardness distributions, (b) tensile-shear strength and energy absorption, (c) load-displacement curves and (d) shear/tensile stress-displacement curves of the RSWed joints without interlayer, with Ni interlayer and with Nb interlayer, respectively.

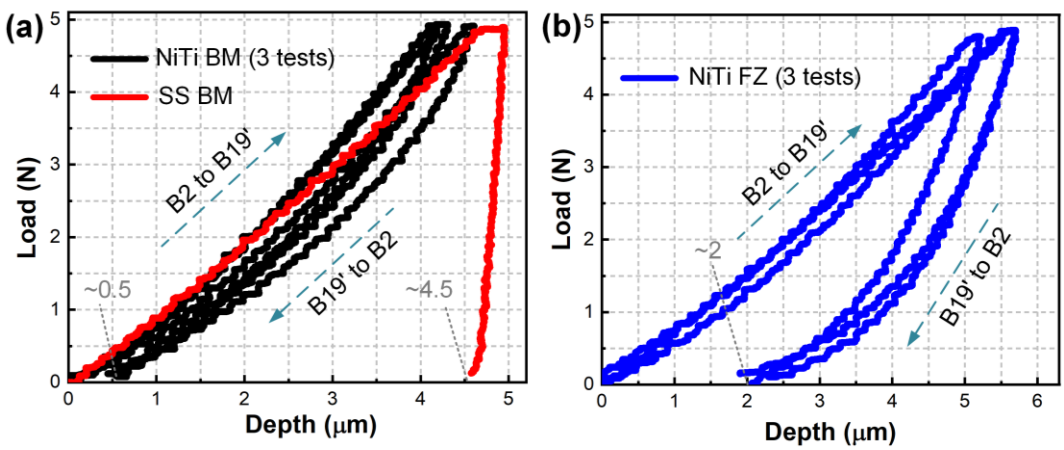


Fig. 4.11 Micro-scale indentation results of (a) the BMs and (b) NiTi FZ.

The fracture surfaces and related EDS analysis are depicted in Fig. 4.12 and Table 4.1, respectively. With an IF mode in the directly welded joint, the height of the weld nugget zone at SS side was lower than

BM (Fig. 4.12a1), in agreement with the crack observation in Fig. 4.6a. The fracture surface exhibited typical brittle features with many cleavage facets (Fig. 4.12a3 and a4) [16,77,145,151], which were identified as mainly Fe_2Ti+Ni_3Ti IMCs. The traversed cracks at the weld nugget led to an IF with low fracture strength. The NiTi BF occurring in the Ni-interlayered joint (Fig. 4.12b1-b4) was mainly due to the large pore at the weld border (as seen in Fig. 4.2b). Other factors, including lower brittleness and crack direction, also contributed to a BF in NiTi in this type of joints. The significant reduction of joining area caused by the large pore and cracks resulted in low strength of the Ni-interlayered joint. Differently, NiTi BF in the Nb-interlayered joint implied a good interfacial joining. As seen in Fig. 4.12c1 and c2, the crack mostly propagated inside the NiTi BM, and a small Nb tear zone was observed at the weld zone border. This tear zone (Fig. 4.12c3 and c4) exhibited a ductile fracture mode with obvious dimples [144,152]. The considerable elongation of the Nb-interlayered joint during tensile-shear testing was linked to the plastic deformation of both SS and Nb.

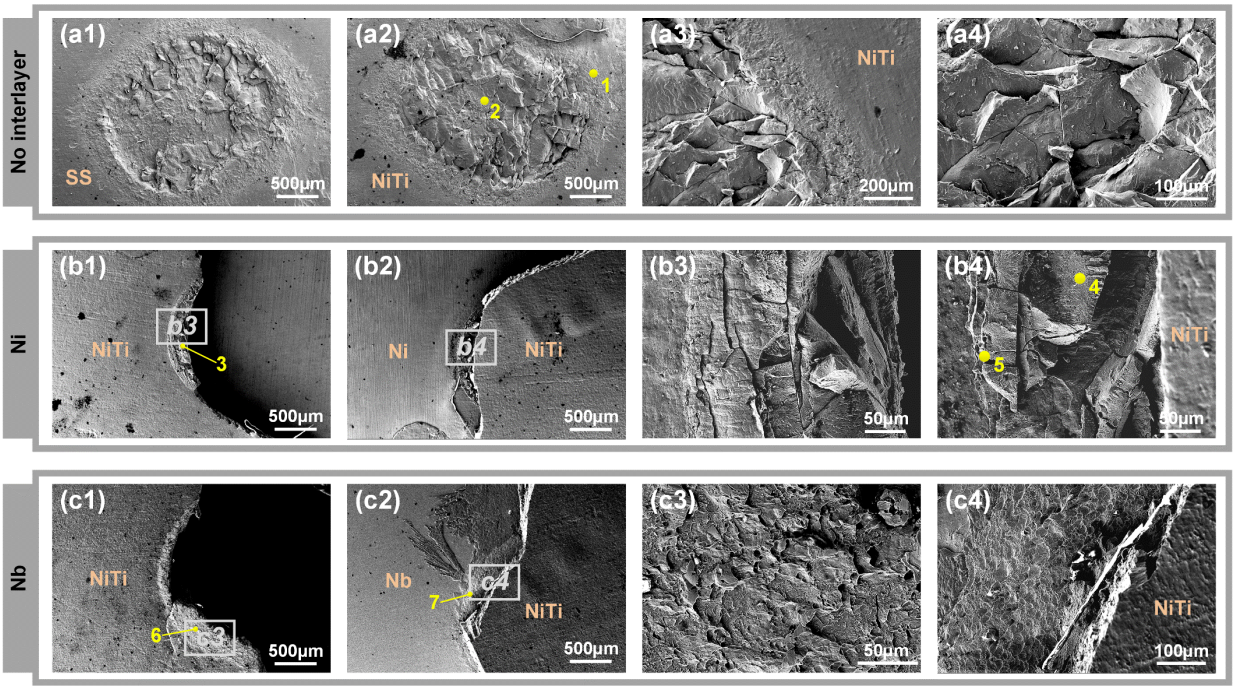


Fig. 4.12 SEM images of fracture surfaces from (a1-a4) directly welded joint, (b1-b4) Ni-interlayered joint and (c1-c4) Nb-interlayered joint.

Table 4.1 EDS analysis (at.%) of different positions marked in Fig. 4.12.

Position	Ni	Ti	Fe	Cr	Nb	Possible phase
1	23.8	32.8	34.8	Bal.	--	Fe_2Ti+Ni_3Ti
2	34.4	32.3	26.0	Bal.	--	Fe_2Ti+Ni_3Ti
3	43.4	22.8	26.2	Bal.	--	Fe_2Ti+Ni_3Ti (Ni_3Ti-rich)
4	41.2	23.6	27.4	Bal.	--	Fe_2Ti+Ni_3Ti (Ni_3Ti-rich)
5	62.3	37.4	0.3	Bal.	--	Ni_3Ti+NiTi
6	2.1	0.6	1.2	Bal.	95.5	Nb
7	--	0.6	--	--	99.4	Nb

4.6 Joining and failure mechanisms

The dynamics of the weld zone of the Nb-interlayered joint was further revealed by EBSD analysis. The different regions could be divided based on the combination of inverse pole figure (IPF) and kernel average misorientation (KAM) maps (Fig. 4.13a and b). The SS BM was unmolten but deformed due to the pressure from the electrode, as indexed by a relatively high KAM value. SS FZ underwent a melting-solidification process and presented equiaxed grains with low KAM value. It is worth noting that Nb interlayer had dominantly <111> type grain orientation (see IPF map) with the highest KAM value, supporting the severe deformation. Obvious columnar grains were observed at the NiTi FZ from the IPF map, as already analyzed in previous Sections. Compared to that in SS FZ, the KAM value in NiTi FZ was higher. The higher misorientation in the NiTi FZ might be caused by the resilient stress from superelastic NiTi BM. Fine equiaxed grains and lower KAM value were found in NiTi BM, due to its original annealed state. An unindexed line between NiTi FZ and BM also existed in NiTi-NiTi RSWed joint [150], because of the compositional segregation, high lattice strain, fine grain size or/and complex phase mixing. The pole figure (PF) maps in Fig. 4.13c indicate that Nb had strong deformation fiber texture along <111> direction as a pole lied on the center of the {111} figure [153]. This deformation texture originated from both the fabrication of the Nb thin foil (i.e., cold rolling) and the further deformation during RSW. However, relatively random textures were observed in SS FZ and NiTi FZ. Therefore, the joining mechanism is schematically presented in Fig. 4.13d. Unmolten Nb interlayer

suppressed the mixing of molten NiTi and SS during RSW. The Nb-Fe_7Nb_6 eutectics and Nb-NiTi eutectics at the interfaces led to good interfacial bonding and high joint strength.

The joining mechanisms of the directly welded and Ni-interlayered joints were essentially similar as a regular RSW process. For the direct welding (Fig. 4.13e), simultaneous melting and mixing of NiTi and SS contributed to the formation of a weld nugget composed of IMCs network (mainly Fe_2Ti and Ni_3Ti) with many microcracks due to the overall brittleness. By inserting a Ni interlayer (Fig. 4.13f), higher Ni content caused a Ni_3Ti-dominated weld nugget with reduced brittleness. However, enhanced Ni vaporization led to pore formation, shrinkage cavities, and consequently shrinkage-induced cracks in the weld nugget. Considering the traversed crack/brittleness and large pore/reduced joining area from direct welding and Ni-interlayered welding respectively, both joints were low-strength.

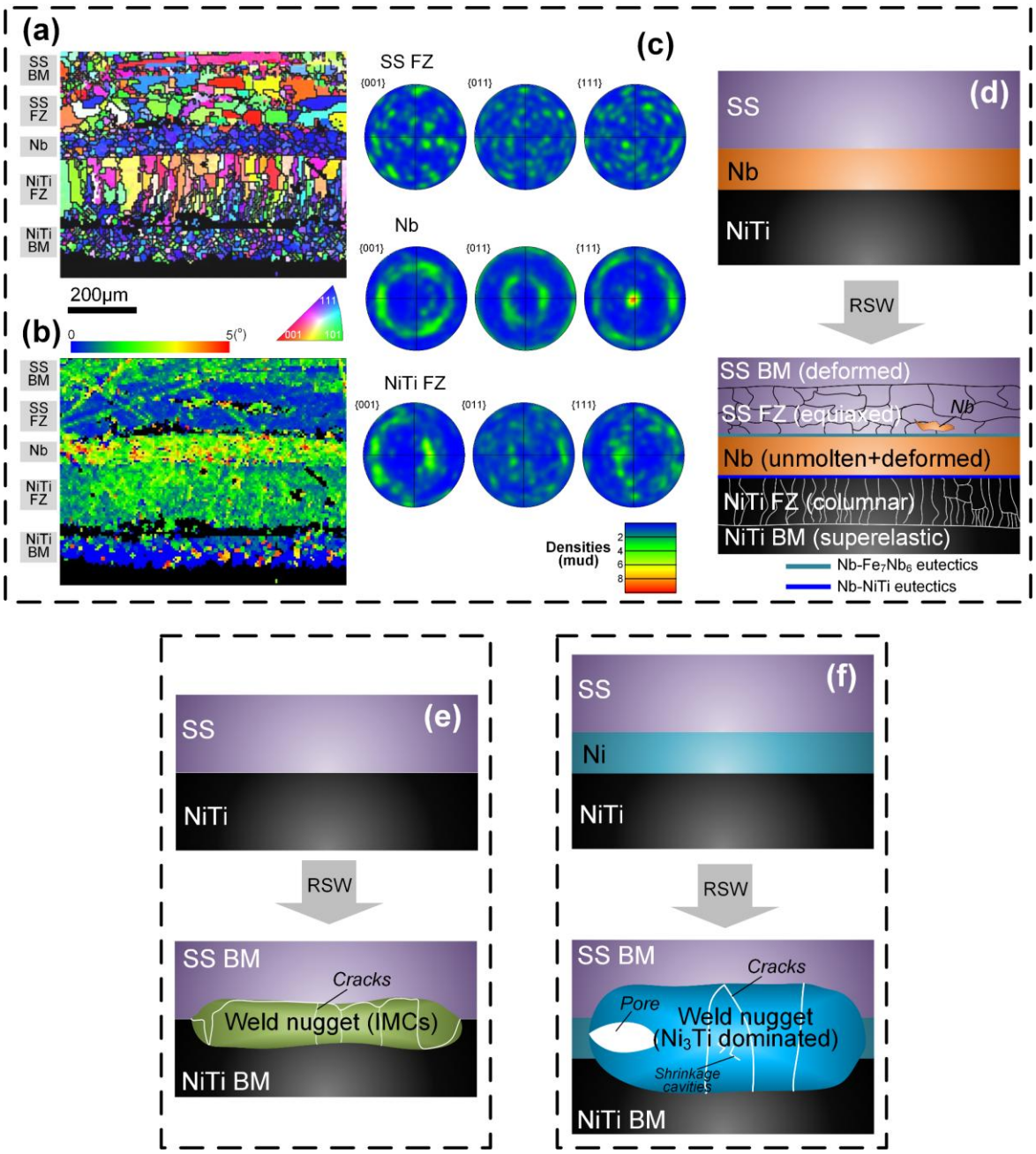


Fig. 4.13 EBSD results of the Nb-interlayered joint characterized by (a) IPF map (with grain boundaries), (b) KAM map, and (c) PF maps; (d-f) the joint formation mechanisms of Nb-interlayered joint, directly welded joint and Ni-interlayered joint, respectively.

Nb-interlayered joint exhibited an unconventional sandwich structure that contributed to the enhanced joint properties. To figure out the weak position of this Nb-interlayered joint (i.e. the reason for fracture at NiTi BM side), FEM simulation on the residual stress field was carried out (von Mises stress was used to evaluate the average stress level [154]; idealized modeling conditions in this model might cause

relatively higher stress than for the actual situation). Overall, the NiTi FZ showed higher stress than Nb interlayer or SS FZ (Fig. 4.14a and b). The stress in the NiTi FZ/Nb interface was higher than that in the SS FZ/Nb interface (Fig. 4.14a and c). It is worth noting that the edge of NiTi FZ/Nb interface exhibited elevated residual stress, which was in good agreement with the SXRD results and the observed fracture location. Fig. 4.14d illustrates the evolution of stress distribution during the cooling process. The residual stress in the RSWed joint gradually accumulated, due to the difference of thermophysical properties among different materials, but the NiTi FZ, especially the interface edge, always showed the highest stress value. High residual stress and large columnar grains (Fig. 4.3h) made the NiTi/Nb interface edge a weak position, resulting in the BF of NiTi.

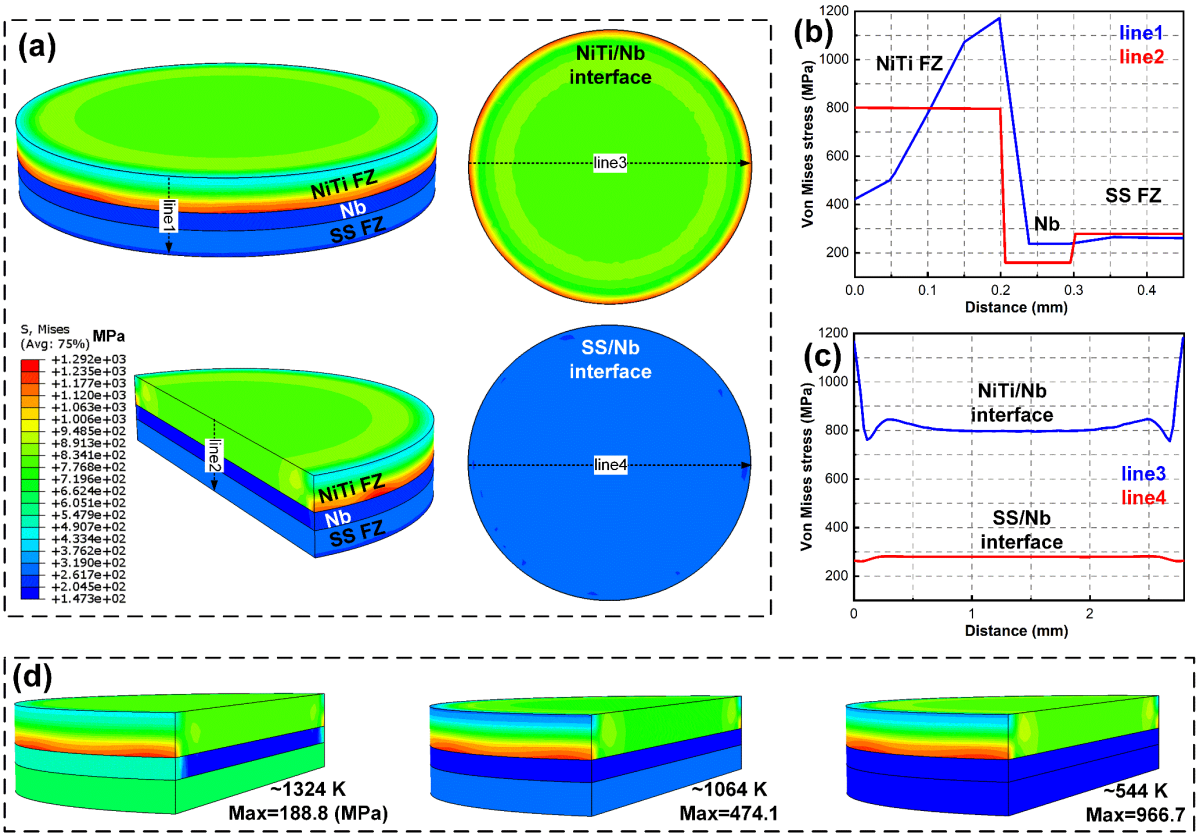


Fig. 4.14 (a) Simulated residual stress distribution in the weld zone of Nb-interlayered joint; (b, c) corresponding residual stress along the line directions marked in Fig. 4.14a; (d) the dynamic residual stress distributions at different temperatures during the cooling.

4.7 Summary

This chapter focuses on microstructure, mechanical properties, and weld formation of NiTi-SS RSWed joints welded with Nb interlayer or Ni interlayer. By applying Nb interlayer, the joint strength was significantly enhanced by 38% on fracture load and 460% on energy absorption, due to the restriction of molten metal mixing and IMCs formation. Separated NiTi FZ and SS FZ formed at each side of the unmolten but deformed Nb interlayer during RSW. Nb-containing eutectics formed at the interfaces, contributing to a good metallurgical bonding between the interlayer and BMs. The joint fractured at NiTi BM side at plastic stage during tensile-shear testing, indicating good interfacial joining. These findings highlight the potential of a high-melting-point interlayer for achieving reliable NiTi-SS RSWed joints

In the directly RSWed NiTi-SS joint, a weld nugget with the presence of Fe_2Ti+Ni_3Ti IMCs network formed, based on the mixing of molten NiTi and SS. Numerous cracks were present throughout the weld nugget. The overall brittleness and traversed crack caused low joint strength with an interfacial failure mode. A Ni interlayer was introduced to evaluate the feasibility of replacing the brittle Fe_2Ti phase with ductile Ni_3Ti in RSW. Microstructure, thermodynamic calculation and hardness results revealed a Ni_3Ti-dominated weld nugget with better ductileness. However, increase of Ni concentration in RSW could lead to large pore, shrinkage cavities, and induced cracks. The joint exhibited low strength because of the reduced effective joining area.

Chapter 5 Interfacial liquid control and the reaction layer of resistance microwelded NiTi-SS joints

5.1 Overview

The previous chapters have indicated that the control of mixing and interface during NiTi-SS welding is the key to limit the IMCs and to enhance the joining strength. However, both fusion welding and solid-state welding methods have limitations, as summarized in Section 2.4. To more effectively control brittle IMCs and preserve the NiTi functional properties in the joint, this chapter proposes a novel approach that achieves a solid-state joined interface during a fusion welding process. The method combines the advantages of both fusion and solid-state welding techniques. Specifically, a FZ containing mixed Ni-Ti-Fe-Cr liquid will be removed from the interface to create a solid-state joined interface, during the fusion welding process. This interfacial liquid control is realized by applying pressure during resistance microwelding (RMW), meanwhile Joule heating ensures a strong metallurgical bonding at the interface and minimizes deformation and work hardening on NiTi side to preserve its functional properties. In this work, the process window on interfacial liquid control was investigated, followed by analysis of microstructural evolution and joining mechanisms. The mechanical and functional properties of the welded joints were evaluated. Since the interface-controlled joints could possess excellent strength and superelasticity, their corrosion or biocompatibility characterizations (hydrogen embrittlement, Ni ion release, and electrochemical corrosion) were further conducted. This work not only provides a comprehensive study on RMW of NiTi and SS wires but also proposes an effective approach on the control of interfacial molten metals and IMCs behavior during the welding process, which can shed a light on the dissimilar-metal joining.

5.2 Methodology

400-μm Ni-rich superelastic NiTi and annealed 316L SS wires were selected as BMs in this work. Micro X-ray diffraction (μXRD, Bruker D8 Discover, 300-μm collimator and 0.15406-nm X-ray wavelength) results (Fig. 5.1a and b) showed that the NiTi wire consisted of B2 phase, while γ-Fe austenite was the parent phase of 316L wire. Fig. 5.1c depicts the SEM image of nanocrystalline NiTi wire where particle void assemblies (PVAs) were found. The particle was identified as Ti_2NiO_x (as shown from the EDS result), a common inclusion formed during NiTi fabrication. The voids typically result from the

deformation mismatch between particle and matrix during the wire drawing. EBSD IPF and PF maps of SS showed large equiaxed grains with annealing twins and a <111> fiber texture on drawing direction (Fig. 5.1d). Prior to welding, all wires were ultrasonically cleaned in acetone for 15 min to remove grease and contaminants. Based on the design of a biomedical multifunctional prototype, NiTi and SS were crossly assembled (Fig. 5.1e). A welding system composed of a Miyachi Unitek HF2 high frequency inverter welding controller and an Amada Miyachi America Thin-Line Series 80 Weld Head was adopted for RMW. A pair of Cu-Cr electrodes with the 1-mm flat tip was used. Based on preliminary experiments, the welding time was fixed as 1 ms, while the welding current and electrode force were selected as variables within the range of 0.3-0.7 kA and 0.5-6.9 kg respectively.

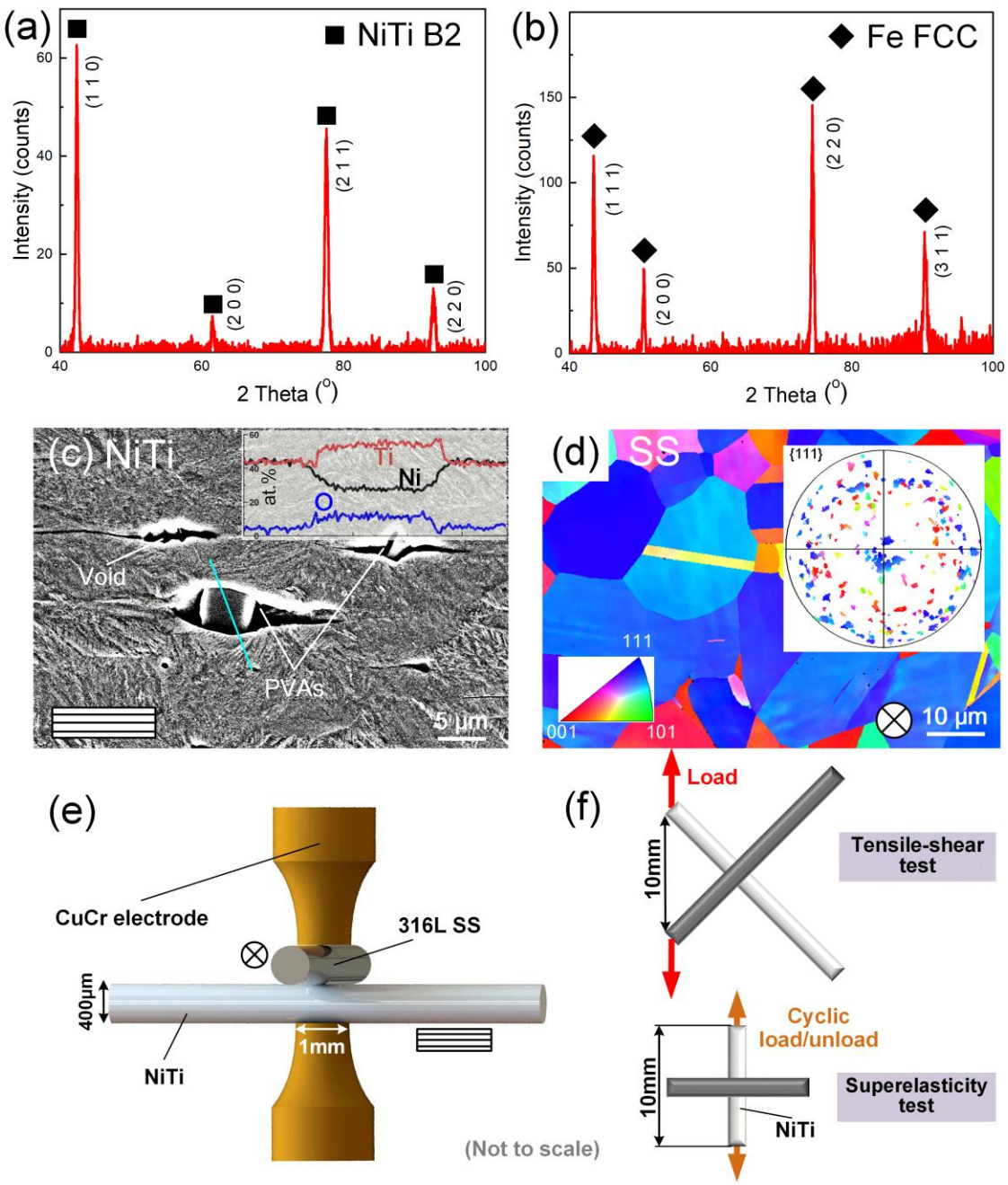


Fig. 5.1 (a, b) μXRD of NiTi and 316L SS BMs, respectively; (c) SEM image of NiTi BM (the inserted EDS line scanning result is according to the region labelled by the blue arrow); (d) EBSD IPF and PF maps of SS; (e) schematic of RMW configuration; (f) schematics of tensile-shear test and superelasticity test for the NiTi-SS joint. (the inserted schematics in Fig. 5.1c, d and e represent observing directions for NiTi and SS cross sections, respectively)

As illustrated in Fig. 5.1f, through an Instron 5548 micro tester, at least three as-welded specimens were tensile-shear tested to evaluate the process window of NiTi-SS joining, and the cyclic loading-

unloading test (strain control) on the NiTi wire direction was applied to characterize the preservation of macroscopic superelasticity after welding. The gauge length and crosshead speed were set as 10 mm and 1 mm/min, respectively. Metallographic samples were prepared according to the standard procedure. Microhardness was measured by a CMT Clemex hardness tester with 200-gf force and 10-s dwell time. Joint appearance and microstructure were characterized by OM (Olympus BX51M) and field-emission SEMs (Zeiss Ultra Plus; JEOL 7000F) equipped with EDS and EBSD detectors. The joint interface was characterized through TEM (ThermoFisher Scientific Spectra Ultra) under the accelerating volage of 300 kV. The TEM foil was prepared by FIB with a plan-view lift-up method on the cross-sectional sample (Fig. C1). EBSD and TEM data were post-processed by software *HKL Channel 5* and *DigitalMicrograph*, respectively. Fractography was carried out by SEM, EDS and laser scanning confocal microscope (LSCM, Keyence VK-X250K). To investigate NiTi localized superelasticity, load-control nanoindentation was conducted on the Anton Paar NHT3 platform, with 20-μm-radius spherical indent tip, 50-mN maximum load, 60-mN/min loading rate and 10-s dwell time. The thermodynamic calculations based on computer coupling of phase diagrams and thermochemistry (CALPHAD) were conducted by *Thermo-Calc ver. 2024b SSOL6* alloy solutions database.

A hydrogen charging experiment was performed by using the 0.9% NaCl solution (Sigma-Aldrich) and a Keithley 2620A ultra-sensitive current source. The hydrogen embrittlement was evaluated by tensile-shear tester and SEM. Ni ion release was in-vitro simulated, in which the Newport Green DCF was employed as the fluorescent indicator to precisely observe the quantitative distribution of nickel ions in the working solution by a fluorescence microscope (Nikon Ti-E), and the detailed setup is given later. Electrochemical corrosion tests were performed in 0.9% NaCl solution at room temperature, through an electrochemical workstation (Gamry Interface 1010E) and a standard three-electrode cell with NiTi BM or welded NiTi as the working electrode, silver/silver chloride (Ag/AgCl, Koslow 1004G) as the reference electrode and Pt foil as the counter electrode. Cleaning of the electrodes was conducted to reduce the surface films [87]. SS was mostly cut off from the NiTi-SS joint (still with a remained but small piece to keep the weld zone), and hot glue was used to seal the sharp edges and to control a consistent immersion length (4 mm). The open circuit potential (OCP) was measured for 2 hours to realize a steady state, then the potentiodynamic polarization tests were carried out from -0.25 V to 1.2 V (vs Ag/AgCl) with a scan rate of 1 mV/s. The corroded samples were further characterized by SEM and EDS, and the *ImageJ* program was used to quantify the pitting void density.

5.3 Process window for the interfacial liquid control

In this work of NiTi-SS setup, Joule heat was primarily generated at NiTi side and was dissipated through SS side. Despite the similar dynamic thermal conductivities of NiTi and SS, several factors contributed to the difference in heating and dissipation. Firstly, NiTi martensitic transformations (stress-induced B2-to-B19' transformation at early low-temperature stage and the B19'-to-B2 transformation at high-temperature stage) during RMW process (Fig. 5.1e) could cause significant uprush of resistance on NiTi, especially considering R phase as the intermediate [2,155]. Secondly, the annealed SS was more deformable than superelastic NiTi to form a larger contact area with electrode for less contact resistance but better heat dispassion.

The process window is presented in Fig. 5.2a, with the step size of 0.1 kA for welding current and of 1.6 kgf for electrode force, respectively. In general, welding current had a more significant influence. The tensile-shear load of joints initially increased and then decreased as current increased, accompanying a transition of interfacial failure (IF) to NiTi base-metal failure (BF). An IF/BF mixed mode, where both IF and BF randomly occurred in one tested group, was observed between IF and BF. BF suggested unaccepted damage to NiTi BM and the dramatic drop in joining strength. The optimized welding current from Fig. 5.2a was located between 0.5 kA and 0.6 kA, thus 0.55 kA was further tested with varied electrode forces as shown in Fig. 5.2b.

Low electrode force could result in some residual IMCs at the interface and over-burning of NiTi BM due to the inefficient heat dissipation (cross section in Fig. 5.2b; detailed microstructure in Fig. 5.2d; EDS mapping in Fig. C2). The joints were therefore fractured with an IF/BF mixed mode. Larger electrode force significantly increased SS/NiTi contact area and heat dispassion rate, successfully squeezing out the interfacial liquid. Accordingly, the joining strength was improved to the optimized value of over 25 N (welded at 0.55 kA and 5.3 kgf) with an IF mode, notably higher than the NiTi-NiTi RMWed joints in published work [156] and tested in our work. The detailed influence of welding current (with 5.3-kgf electrode force) in Fig. 5.2c showed that the joint failure mode changed from low-strength IF to high-strength IF and then to low-strength BF, with the increase of current. Low welding current could not generate enough heat for interfacial bonding despite a sufficient NiTi-SS contact area. Increasing the current gradually promoted the joining, but elevated currents caused overheating and resulted in damaged NiTi BM with IMCs penetration (Fig. 5.2d and Fig. C3). In short, balancing welding current and electrode force is important to achieve IMCs-free interfacial joining and minimize damage to the NiTi BM in RMW.

In comparison with the hardness in BMs (SS: ~150 HV, NiTi: ~350 HV), the weld zone exhibited increased hardness for SS but decreased hardness for NiTi (Fig. 5.2e and f), which indicated plastic deformation in SS and dynamic recrystallization in NiTi during the welding process. As suggested in Fig. 5.2e, the electrode force led to SS work hardening especially at the SS/electrode interface. The heat effect reduced this SS hardening at the SS/NiTi interface, although a higher electrode force could enhance SS interfacial hardness. On the other hand, the change of welding current (Fig. 5.2f) showed significant influence on NiTi recrystallization. Higher currents resulted in lower hardness (i.e., higher degree of recrystallization) in NiTi heat affected zone (HAZ). It is noted that the two extremely high-hardness points corresponded to the interfacial residual IMCs and penetrated IMCs respectively, as shown in Fig. 5.2d.

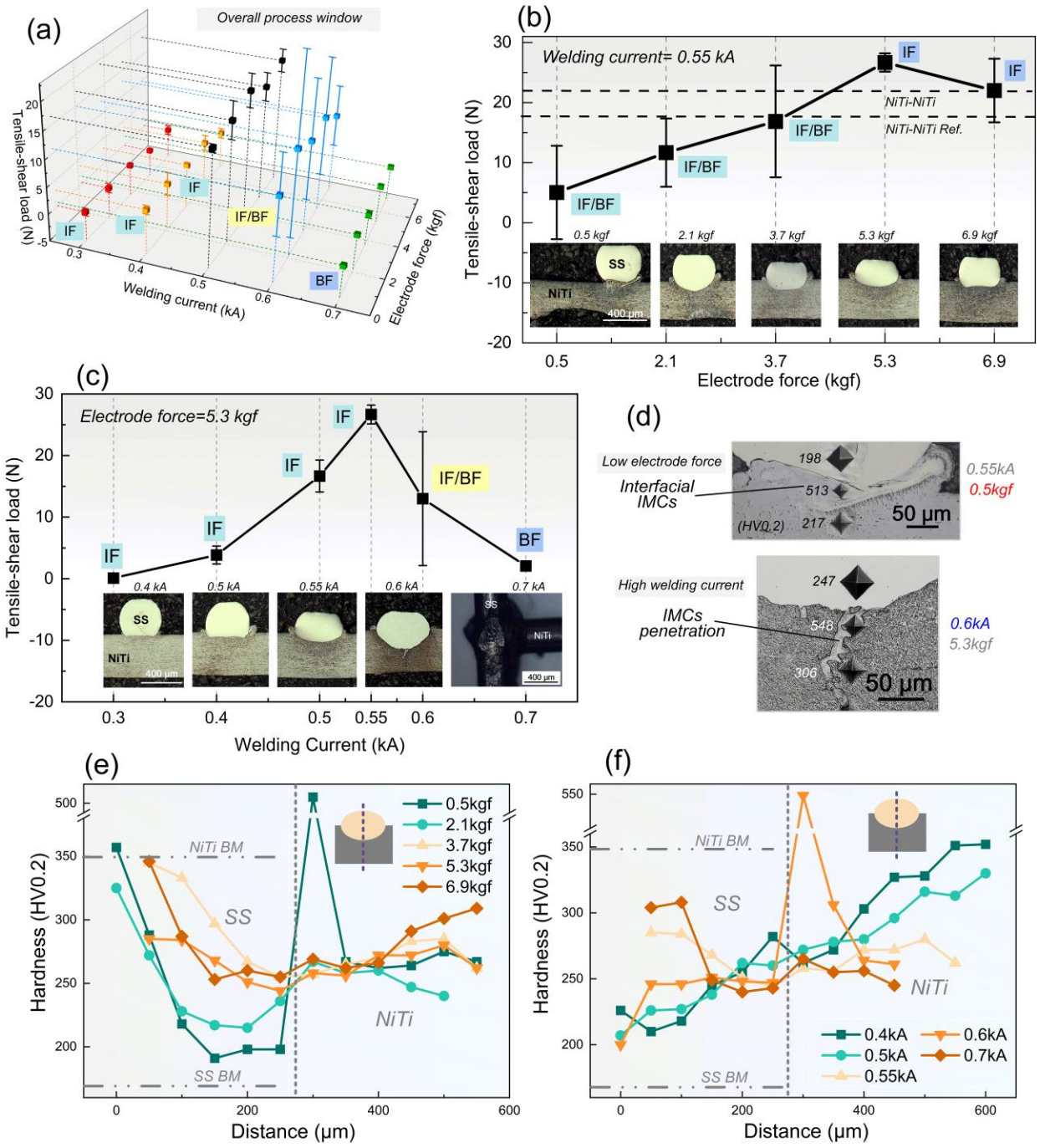


Fig. 5.2 (a) Welding current-electrode force process window, (b) the curve of tensile-shear load versus electrode force with the fixed welding current of 0.55 kA; (c) the curve of tensile-shear load versus welding current with the fixed electrode force of 5.3 kgf (corresponding cross sections are inserted); (d) OM images showing the microstructure and interfacial hardness of low-electrode-force and high-welding-current samples; influence of (e) electrode force and (f) welding current on the joint hardness distribution, respectively.

5.4 Microstructure and mechanical properties of joints

The optimized joint was further analyzed to reveal its microstructure and joining mechanism. The squeezing-out events were observed on both the NiTi and SS sides of the welded joint, and there was no overall chemical mixing at the whole joined interface (Fig. 5.3a and Fig. C4). SS top-surface was flattened compared to the unchanged NiTi geometry because of different deformability. As mentioned, heat was dominantly generated in NiTi but dissipated through SS, resulting in SS deformation and NiTi recrystallization during the welding process. Hardness mapping in Fig. 5.3b reflected the regions for SS work hardening and NiTi recrystallization, respectively. As seen in the EBSD IPF map in Fig. 5.3c, SS grains were plastically extruded along the electrode force direction, while the equiaxed B2 recrystallized phase was formed at the NiTi HAZ. The difference of BM behaviors was also validated by the lower geometrically necessary dislocation (GND) density and its more concentrated distribution frequency in NiTi HAZ, compared to those in SS (Fig. 5.3d). The PF maps in Fig. 5.3e revealed the strong preserved <111> texture in SS and the <111> recrystallization preference texture in NiTi HAZ.

Microstructural segregation, pores and cracks were found in the squeezed-out zone of Fig. 5.4a, and EDS mapping results (Fig. 5.4b and Fig. C4) indicated the Ni-Ti-based composition with mixed Fe and Cr in this squeezed-out zone. Elemental line analysis in Fig. 5.4c suggested the formation of extremely hard and brittle IMCs (over 600 HV in Fig. 5.3b) due to the Ni-Ti-Fe-Cr mixing. The thermodynamic calculation (details in Fig. C4, Table C1 and Table C2) suggested phase formations at different regions in Fig. 5.4a: Laves phase (mainly Fe_2Ti) and Ni_3Ti formed at the Fe-rich region; Laves phase, B2 and Ni_3Ti formed at the highly mixed region; B2 matrix with some Ni_3Ti and Laves phase formed at the NiTi-rich region (Fig. 5.4d-f). Scheil simulation is closer to the welding nonequilibrium solidification process, and the results revealed that the brittle C14 Laves was the first precipitated phase with a high fraction at both Fe-rich and mixed regions, causing the formation of microcracks (Fig. 5.4d-f). It should be mentioned that all these brittle phases and defects were found in squeezed-out zone but were outside of the NiTi-SS interface (Fig. 5.3a). By the interfacial liquid control during welding process, mixed liquid and surficial contaminations/oxides could be removed from the interface, ensuring a clean contact and solid-state joining between SS and NiTi, as depicted in Fig. 5.3f.

An ultrathin reaction layer (submicron thickness in Fig. 5.3g) formed at the joining interface (EBSD and EDS mapping results are shown in Fig. C5), indicating metallurgical bonding without overall brittleness. Since the NiTi functional properties in the joint are of particular interest, the microstructural evolution of NiTi HAZ was further analyzed in Fig. 5.3h. Compared to the nanocrystalline NiTi BM with

PVAs (Fig. 5.1c or yellow arrows in Fig. 5.3i), grown equiaxed grains were observed in the HAZ. The voids from PVA were eliminated, but the original particles remained embedded in NiTi matrix (labelled by yellow arrows in Fig. 5.3h).

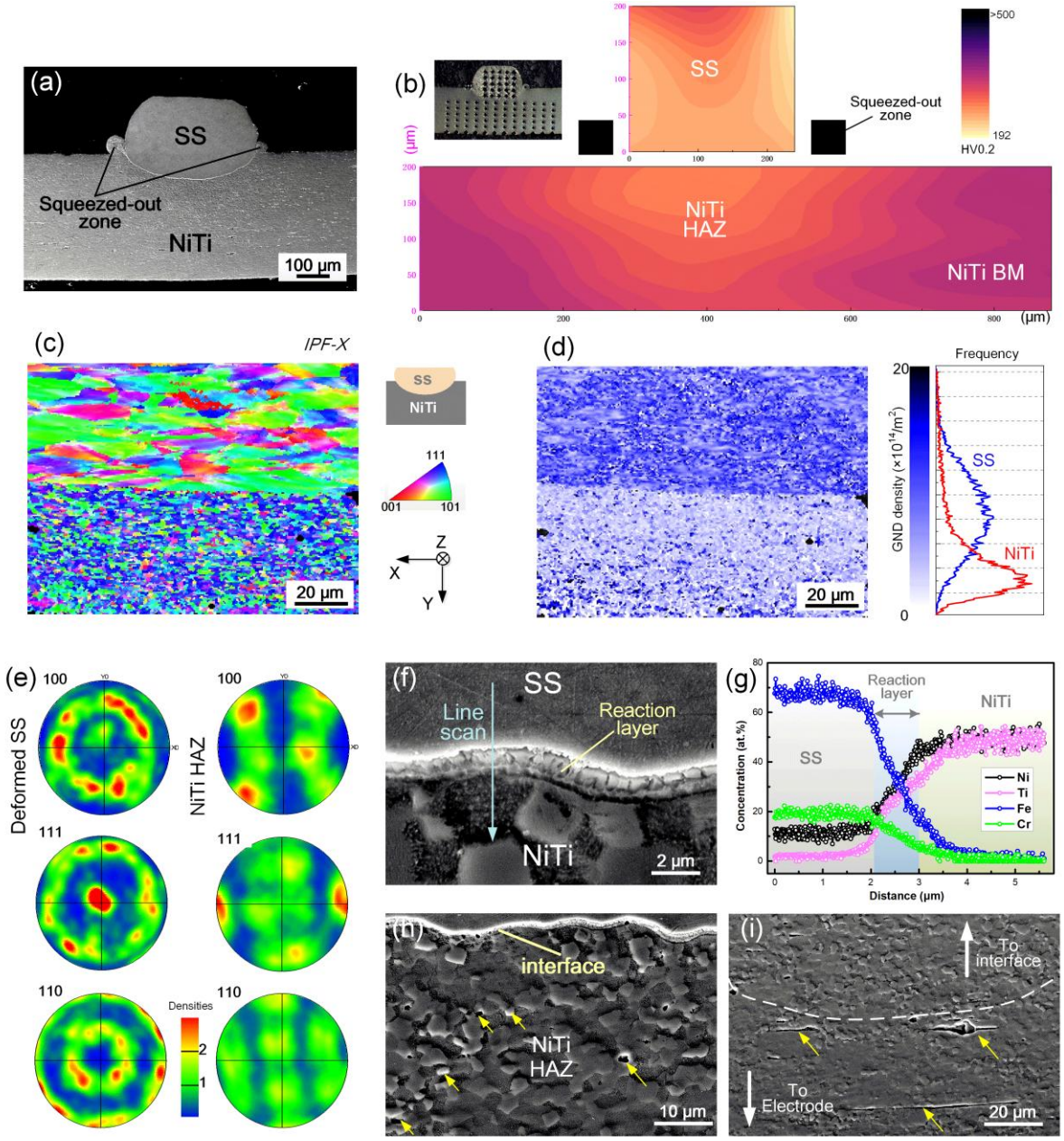


Fig. 5.3 (a) Cross-sectional SEM image and (b) the hardness mapping of the optimized joint; (c) EBSD IPF-X map of the interface; (d) EBSD GND density map and its distribution frequency of the interface; (e) EBSD PF maps of interfacial SS and NiTi, respectively; (f) SEM image of the interface between SS and NiTi; (g) EDS line scanning result for the region labelled in Fig. 5.3f; (h) SEM image of NiTi HAZ; (i) SEM image of NiTi HAZ/BM boundary.

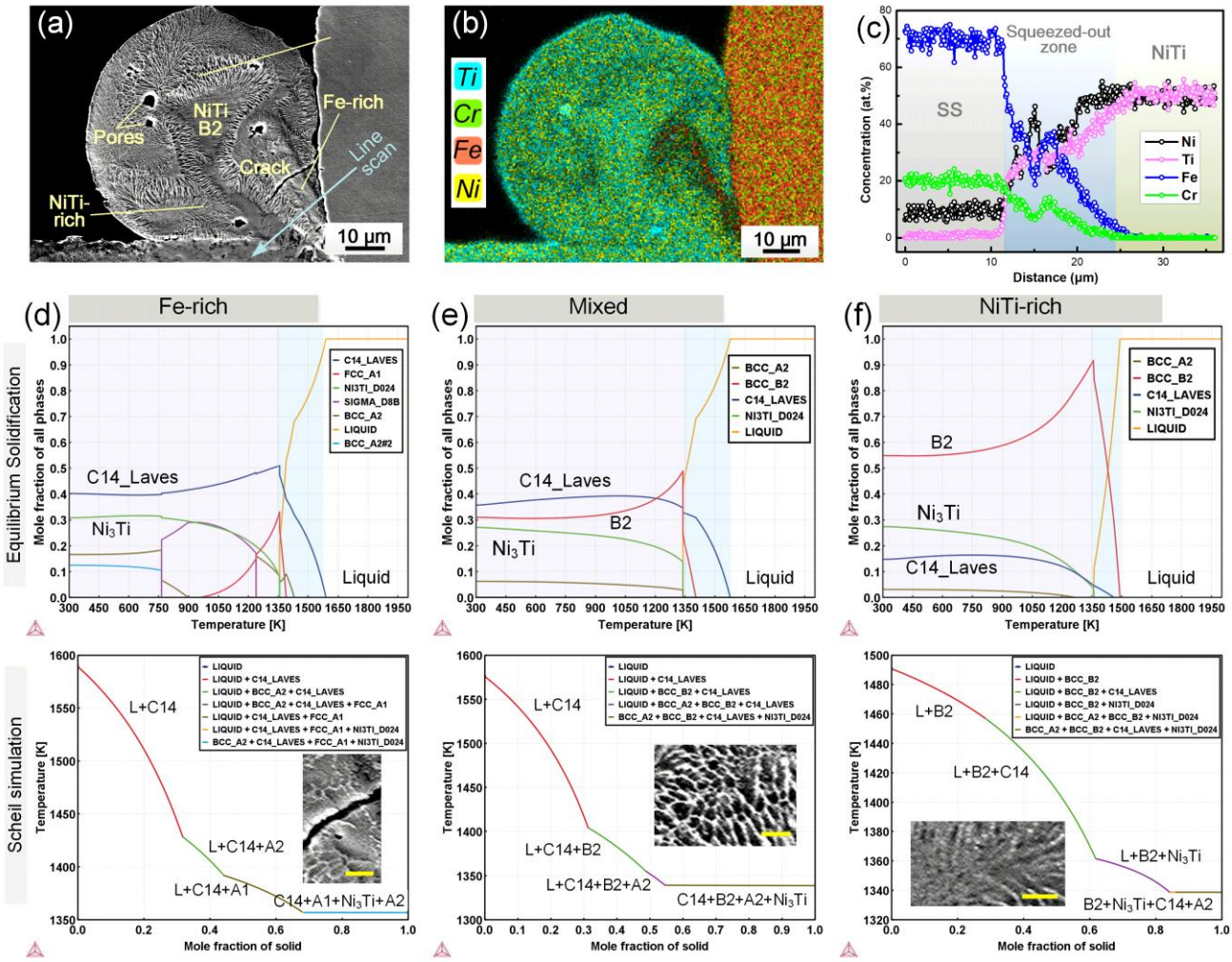


Fig. 5.4 (a) SEM image and (b) EDS mapping of the squeezed-out zone; (c) EDS line scanning result for the region labelled in Fig. 5.4a; the thermodynamic calculation results of phase formation at (d) Fe-rich region, (e) mixed region and (f) NiTi-rich region considering both equilibrium solidification and Scheil simulation (atomic percentages of Fe and Ti are labelled; microstructural images are inserted in the Scheil simulation figures, with the 2-μm scale bar).

Detailed interfacial material behaviors and reaction layer were characterized via TEM. High-density deformation twins were found at SS side, while the recrystallized NiTi equiaxed grains were formed at NiTi HAZ (Fig. 5.5a). High-resolution TEM (HRTEM) images and the related Fourier fast transform (FFT) of the SS deformation twins revealed the $(1\bar{1}\mathbf{1})$ twin plane and the <110> twinning direction. The stacking fault inside twin domain indicated the origin of secondary twinning to accommodate the applied strain. Considering the <111> texture on of SS BM drawing direction and slip systems of {111} <1$\bar{\mathbf{1}}$0> of Fe FCC on the electrode force direction, the slip can be activated by the pressure, resulting in both

dislocation pile-ups and deformation twins in SS (see Fig. 5.5d). A reaction layer with the thickness of around 850 nm formed between SS and NiTi based on the interfacial mixing/diffusion of alloying elements, in which the main phase was identified as the Laves $(Fe,Cr,Ni)_2Ti$ with the TEM zone axis (ZA) of $[\bar{1}100]$ in Fig. 5.5e. Such a thin IMCs layer is also observed in other dissimilar solid-stated joints after thermo-mechanical process [157]. It is worth mentioning that the Laves Fe_2Ti, with a topological close-packed (TCP) structure, is usually considered as one of the most harmful phases in NiTi-steel fusion welded joint; however, the present solid-stated joined interface only formed a Laves phase layer with highly limited thickness and brittleness, which in turn promoted the bonding strength between BMs. Detailed analysis of this reaction layer can be found in Section 5.6. NiTi is usually functionally damaged (e.g., dislocation density increase and martensitic phase transformation) by the large deformation and work hardening during the solid-state welding process. Benefit from the Joule heating in this work, the NiTi was recrystallized without any phase transformation and work-hardening defects (Fig. 5.5f), contributing to the preservation of superelasticity after welding.

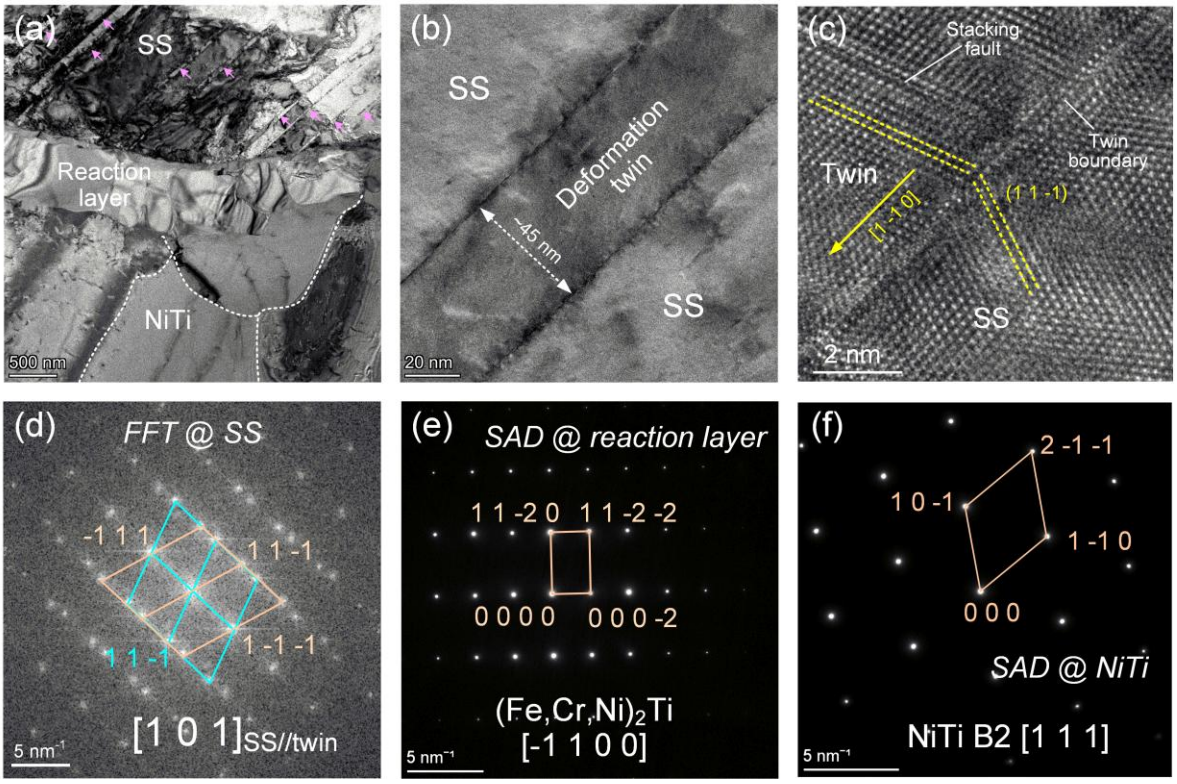


Fig. 5.5 (a) TEM image of NiTi-SS interface; (b) deformation twin in the SS side; (c) HRTEM image of the deformation twin boundary; (d) FFT pattern obtained from SS deformation twin boundary; (e) SAD pattern obtained from the main phase of the reaction layer; (f) SAD pattern obtained within one grain of the recrystallized NiTi HAZ.

The load-displacement curves of the tensile-shear testing are plotted in Fig. 5.6a to show the deformation behavior and multifunctional performance of NiTi-SS cross joint. The damage of NiTi (i.e., the NiTi overburning at low electrode force and the IMCs-penetration at high welding current in Fig. 5.2) caused the fracture happening at NiTi side with a very low strength (less than 0.6 N) at the early testing stage. For the IF sample with low joining strength (welded with low current), a low-stress deformation stage existed until ~8-mm displacement, during which the NiTi and SS wires rotated around the welded point. Subsequently, the applied load increased dramatically and the low-strength IF occurred due to the weak interfacial bonding. The optimized sample exhibited a similar low-stress deformation behavior during the early stage. However, at the final stage, it is notable that the NiTi/SS wire angle could reach 180 degrees, and the joint possessed much higher tensile-shear strength. After fracture, the superelastic NiTi wire recovered back to its original straight shape, while the annealed SS wire retained its plastic deformation. This clearly demonstrated the different deformation characteristics in different directions within one joint. The sufficient interfacial joining strength enabled the joint to demonstrate potential for multifunctional biomedical device applications, highlighted by the flexible deformation capacity at SS direction and the superelasticity at NiTi direction, as shown in Fig. 5.6b.

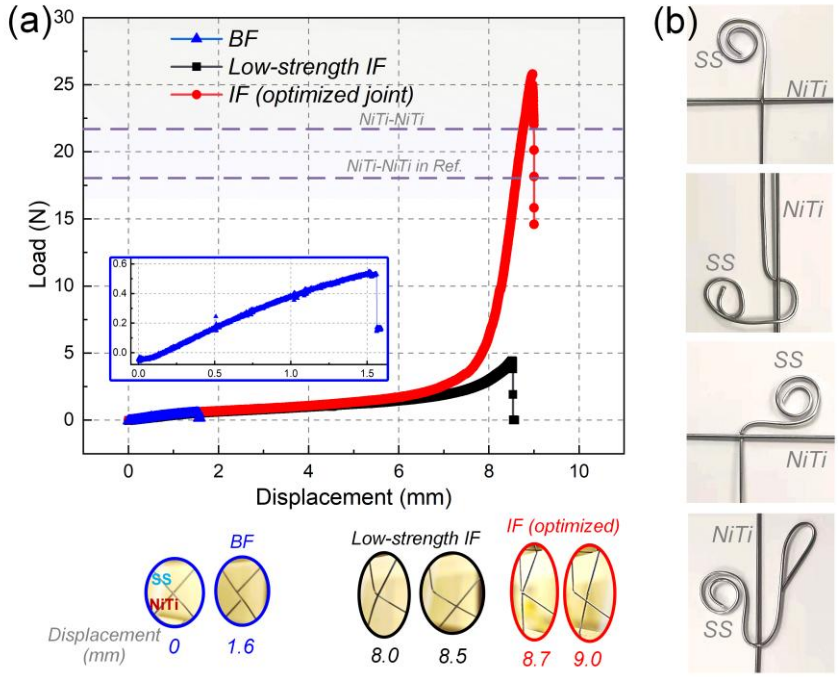


Fig. 5.6 (a) Three typical load-displacement curves and the related deformation images of RMWed NiTi-SS joints during tensile-shear testing (BF sample and low-strength IF sample were welded with 0.55 kA-0.5 kgf and 0.4 kA-5.3 kgf, respectively); (b) simple demos showing the deformation and superelasticity capacities from NiTi-SS RMWed joints.

Two cases of BF samples, namely the NiTi overburnt sample welded with low electrode force and the IMCs-penetrated sample welded with high welding current, were selected for fractographic analysis. In the first case, the overburning of NiTi on the electrode side (Fig. 5.7a) reduced the effective load-bearing area, resulting in NiTi base material (BM) fracture with distinct regions—a ductile fracture surface (Fig. 5.7a2) and a rapid-propagation surface (Fig. 5.7a3). In the second BF case, cracks initiated from the penetrated IMCs (Fig. 5.7b3) and propagated into the NiTi matrix (Fig. 5.7b1), with the fracture surface transitioning from brittle to ductile behavior. Fig. 5.7c shows the fracture surfaces of a typical low-strength IF sample welded with low current. Despite some squeezing, the joining area was relatively small. Both NiTi and SS sides have relatively flat fracture surfaces, and EDS results (Table C3) indicated separated NiTi-based and SS-based compositions suggesting the inefficient interfacial reaction. Voids from NiTi PVAs were also observed on the NiTi side. Fig. 5.7d presents the fracture morphologies of the optimized joint, where four squeezed-out zones remained attached to NiTi wire side after fracture. The joining area was significantly increased compared to the low-strength IF sample. The height profile (Fig. 5.7d1) indicated an indentation depth of ~60 μm, or 15% of the NiTi wire diameter. The detailed effect of this BM reduction on NiTi wire mechanical and functional properties will be analyzed later. The fracture surface observed from SS side indicated two possible crack propagation paths (Table C3): either γ Fe from original SS or $(Ni,Fe)_3Ti$ phase (formed between the Laves phase and the NiTi BM in the interface). This verified again that the Laves $(Fe,Cr,Ni)_2Ti$ was no longer a harmful phase in such a ultrathin interfacial reaction layer.

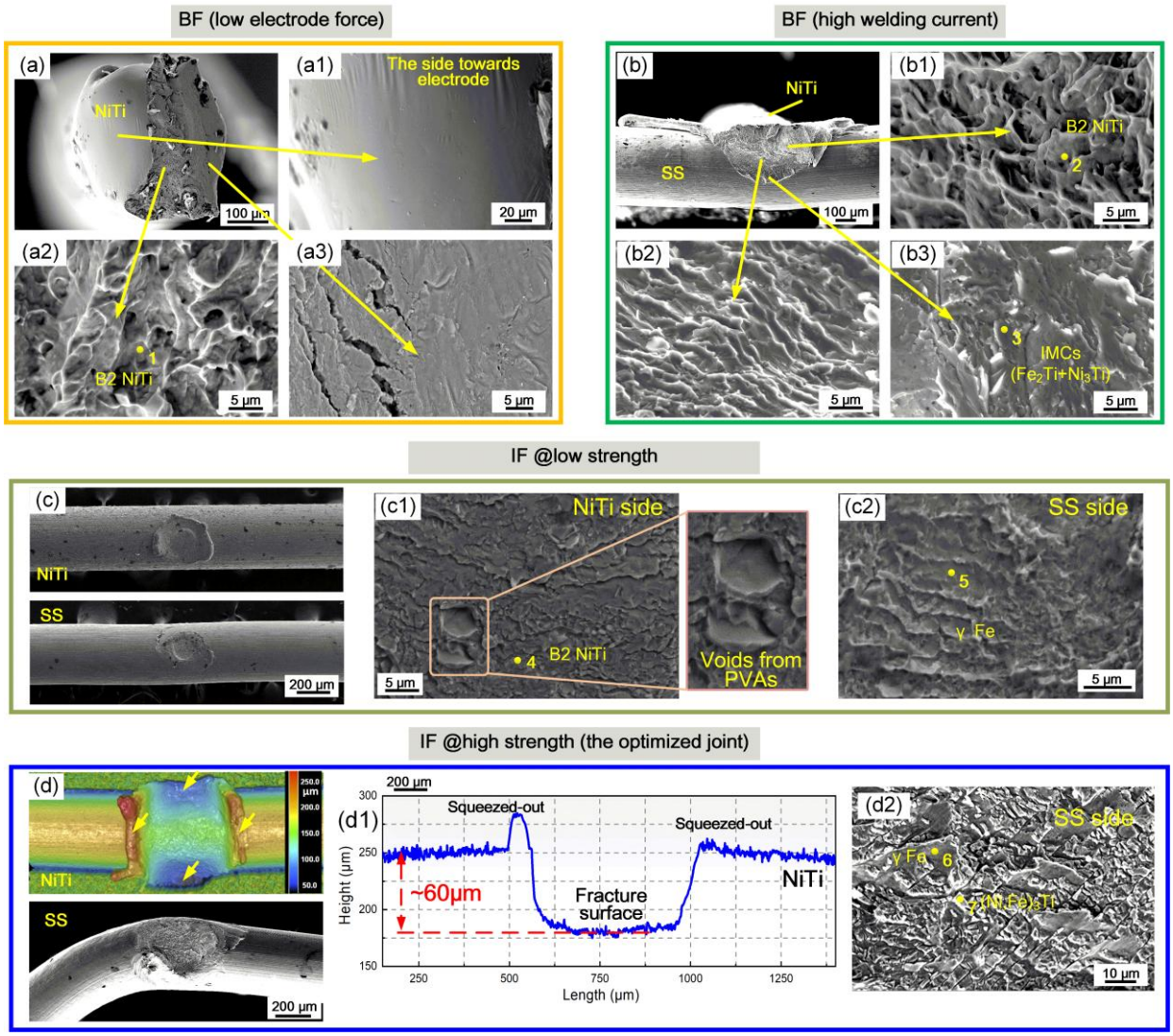


Fig. 5.7 SEM images of fracture surfaces of BF samples welded with (a) low electrode force and (b) high welding current, respectively; (c) SEM images of fracture surfaces of the typical IF sample welded with low welding current; (d) fracture surfaces of the optimized sample (LSCM image of NiTi side with height value; SEM images of SS side); (d1) height profile along a line across NiTi-side fracture surface; (d2) SEM image of SS-side fracture surface (EDS results of all marked positions in Table C3).

5.5 Superelasticity and corrosion resistance of joints

The interface-controlled joint showed excellent strength and multifunctional behaviors, making it essential to evaluate the NiTi superelasticity after welding. The preservation of NiTi superelasticity in the welded joint is important as it ensures the realization of unique properties (like providing corrective force or mimicking bone deformation) in biomaterial devices. Cyclic testing was performed according to Fig.

5.1f for both welded joint and NiTi BM to characterize the overall superelasticity. As seen from Fig. 5.8a and b, NiTi in the welded joint still possessed the typical superelastic curves based on stress induced martensitic transformation (SIMT) upon loading and the reversible transformation upon unloading, despite the decrease of final fracture load from 165 N to 100 N due to the NiTi wire diameter reduction. The existence of kinks during the B2-B19' transformation (labelled by arrows in Fig. 5.8a) originated from the inconsistency of SIMT (nucleation of different martensite bands [158]) or residual stress release [140] due to the formation of NiTi HAZ. In general, it was remarkable that in this work, the welded NiTi demonstrated cyclic superelastic curves quite similar to those of NiTi BM.

Residual strain (RS) is usually used to evaluate superelastic performance and functional fatigue, which originates from the dislocation slip and residual martensite during reversible SIMT. Interestingly, the welded NiTi even showed less RS (by 0.058% in overall, or by 6.5 % compared to NiTi BM after 50 cycles) as presented in Fig. 5.8c, suggesting that the welding process did not degrade but instead improved the macroscopic superelasticity at NiTi direction. Ni:Ti ratio change can alter the martensitic transformation temperature, the critical stress for SIMT and the possible RS [159], which is a common issue during NiTi fusion welding because of the Ni vaporization loss. Nevertheless, in this work all the melted materials were squeezed out, and the NiTi HAZ should possess a similar composition as NiTi BM. Another piece of evidence was from the comparison on superelasticity plateau level (Fig. 5.8d), which can reflect the SIMT critical stress. There were no obvious aberrations of superelasticity plateau level of welded NiTi compared to NiTi BM, indicating again the negligible effect on Ni:Ti ratio change of the HAZ. Moreover, their similar trends of superelasticity plateau reduction at high cyclic numbers suggested similar localized-slip-assisted SIMT in the weld and BM [160].

The microstructural change during welding process could affect the RS. The total RS in polycrystalline NiTi during the cyclic testing can be divided into two types: 1) RS^{first} after the first cycle due to the dislocation slip and residual martensite mainly from the initial microstructure (grain size, defects, and precipitates); 2) RS^{rest} due to the accumulated slip and residual martensite during the rest of the cycles. As seen in Fig. 5.8c, RS^{first} difference (0.070%) was higher than the finial RS difference (0.058%) between welded NiTi and NiTi BM, indicating the RS reduction in welded NiTi was attributed to initial microstructural change caused by the welding process. NiTi recrystallization occurred at the HAZ, resulting in dislocation annihilation that could decrease the slip during cyclic testing. Another important result was the elimination of voids from PVAs (Fig. 5.3h and i) in NiTi HAZ, which reduced the stress concentration and the consequent slip activity at these regions [161]. However, HAZ recrystallization also

caused NiTi grain coarsening, and the overall grain coarsening could in turn increase the RS [162]. The nanoindentation results in Fig. 5.8e also revealed the dispersed distribution of residual depths owing to the anisotropy of superelasticity of large grains in NiTi HAZ [163,164], as a result, the localized superelasticity was degraded. On the other hand, the <111> recrystallization (Fig. 5.3e) texture is expected to have a good superelastic response; in this case the intergranular constraint is not considered to play a strong role in macroscopic SIMT performance [137,165]. It should be mentioned that interfacial high-modulus IMCs layer might provide a “rigid bracing” for NiTi that could also reduce RS. To sum up, localized superelasticity and macroscopic superelasticity cannot be conflated in such a welded joint.

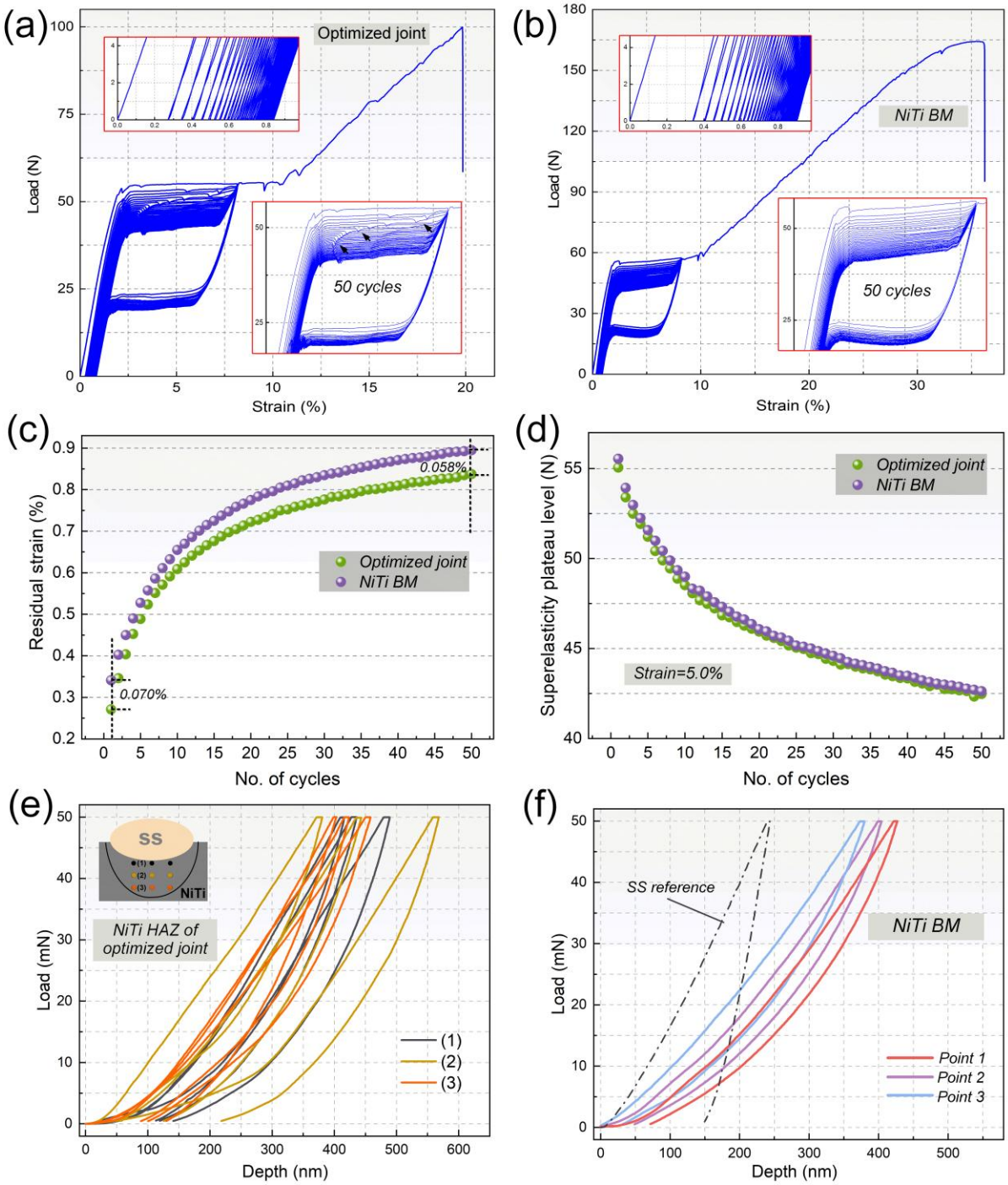


Fig. 5.8 Load-strain curves obtained from the cyclic loading-unloading test of (a) welded NiTi and (b) NiTi BM, respectively; evolution of (c) residual strain and (d) superelasticity plateau level (at 5.0% strain) during the cyclic test, respectively; nanoindentation load-depth curves of (e) NiTi HAZ of welded joint and (f) NiTi BM, respectively (different colors represent different height in HAZ, while they represent random test points in BM; dashed curve in Fig. 5.8f was from the test on SS showing a typical elastoplastic behavior as a reference).

Hydrogen embrittlement is regarded as one of the biocompatibility/corrosion issues when using NiTi or SS implants [104,166] because of the formation of the in-situ currents and the fretting corrosion, however, the hydrogen embrittlement of NiTi-SS joint has rarely been investigated yet. Given that the optimized joints in this work showed excellent mechanical and functional properties, electrolysis hydrogen charging [104] and immediate tensile-shear test were further performed (Fig. 5.9a) to assist if the weld zone will be more susceptive to hydrogen embrittlement. From the tensile-shear test results in Fig. 5.9b and c, with a relatively low current density of $1A/m^2$, the increase of charging duration (12 hours to 72 hours) did not significantly affect the joint strength (over 20N with IF mode).

On the contrary, the joints were more sensitive to the change of current density with a fixed charging duration of 24 hours. There appears to be a threshold value between 1 A/m^2 and $5A/m^2$ that could cause the occurrence of prominent hydrogen embrittlement at NiTi wire of joints. The NiTi wire was even plastically deformed after charging at 5 A/m^2 or higher (Fig. 5.9d), suggesting the absorption of abundant hydrogen and the formation of hydride in the NiTi wire [167]. In this case, the joint fractured at the junction between the tensile tester fixture and NiTi wire (Fig. 5.9b) with a dramatically reduced strength (less than 5 N). Corrosion pits and cracks were observed at the NiTi surface of the joint after 5-A/m^2 and 24-hour charging and tensile-shear testing (Fig. 5.9e). The fracture surface showed typical hydrogen embrittlement features [168], namely the brittle fracture zone at the peripheral part and the shallow dimple area at the center of the cross section. Note that at the high charging current densities, the hydrogen embrittlement-induced brittleness happened at NiTi BM of the joint instead of the weld zone. The new phases at the interface and recrystallization accompanying voids elimination at NiTi HAZ were regarded to be contributed to the improvement of the resistance to hydrogen embrittlement.

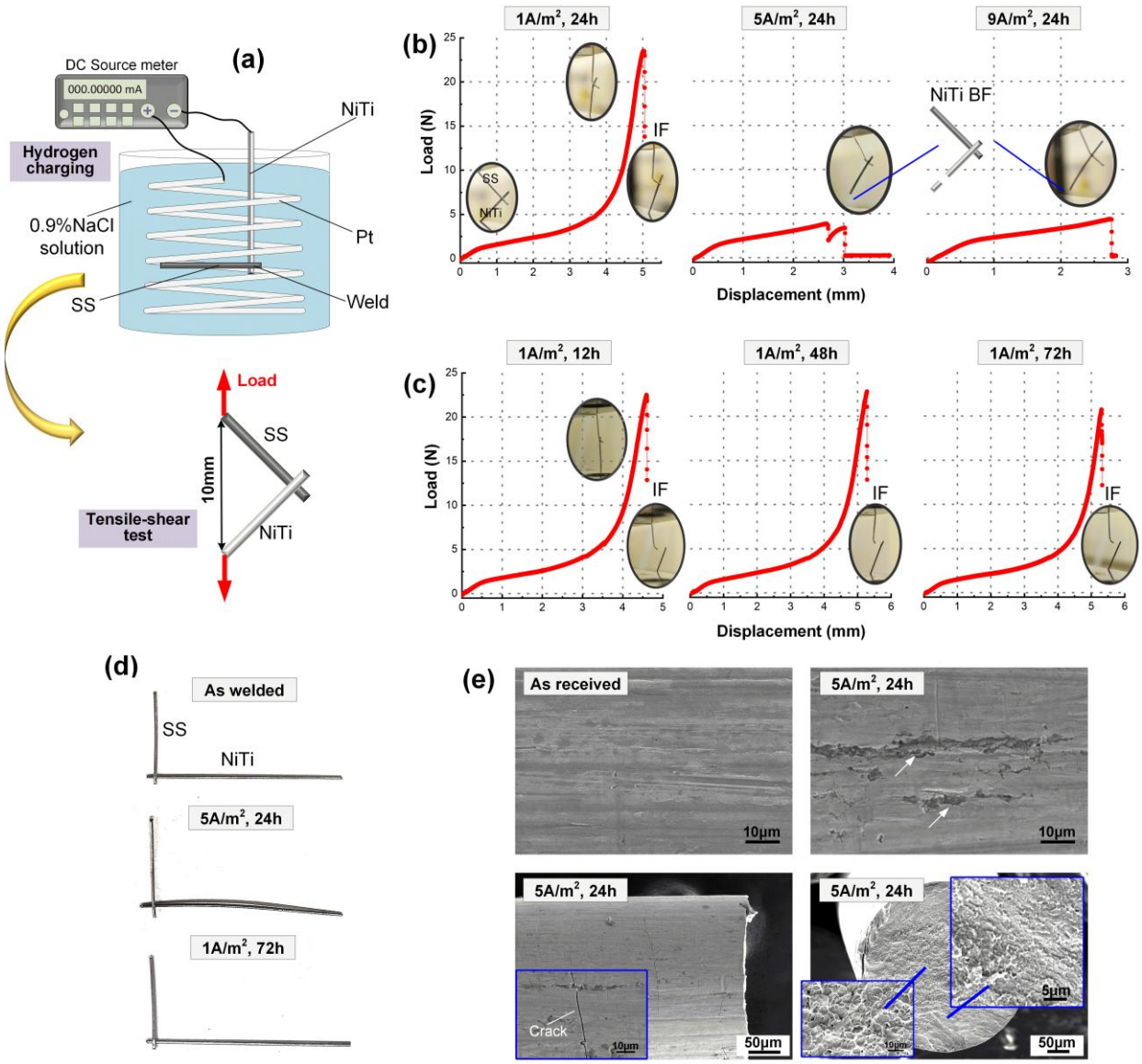


Fig. 5.9 (a) Schematics of hydrogen charging and the subsequent tensile-shear test of NiTi-SS RMWed joints (not to scale); (b,c) load-displacement curves of joints hydrogen charged with different current densities and durations, respectively; (d) joint appearances after hydrogen charging; (e) morphologies of as-received NiTi BM surface and NiTi surfaces/fracture surfaces from welded joint after hydrogen charging and tensile-shear testing.

Ni ion release is another concern for NiTi biomedical devices or implants, as Ni is usually considered as harmful to the human body and typically has a higher release concentration than Ti from NiTi [169,170]. Therefore, the Ni ion release experiment was conducted (Fig. 5.10a). A 10 μM working solution was prepared by dissolving Newport Green DCF (Ni ion fluorescent indicator) into dimethyl sulfoxide followed by a dilution process using deionized water and NaCl (0.9%). The nickel ion release circuit was built up by reversing the circuit for hydrogen charging to keep a consistent current [171], considering the

complex bioenvironment like oral cavity where the galvanic current exists in NiTi/SS orthodontic wires [104,172], and percutaneous transseptal puncture where the electrification is applied on NiTi/SS guidewires [173,174]. After cutting SS BM off to reduce the influence from SS, the welded NiTi (still with a remained SS piece at the weld zone) and Pt electrodes were immersed in 200-μL working solution for variable durations. NiTi BM was also tested as a reference, and all samples/Pt electrodes were immersed into the same depth of the solution. Quantitative characterization was performed by extracting 20-μL working solution for fluorescent microscopy with 1-second exposure time, thus the higher normalized fluorescent intensity, the higher released Ni ion concentration. As seen in Fig. 5.10b, both NiTi BM and welded NiTi showed an increase in Ni ion release with longer immersion time. Notably, welded NiTi exhibited a lower capacity to release Ni ions compared to NiTi BM, indicating good corrosion resistance of the weld zone. The welding process eliminated PVA voids in NiTi HAZ, which could reduce the contact reaction of NiTi/solution and the corrosion of NiTi. Welding also introduced Cr-Ti-containing phases in the weld zone (both squeezed-out zone and interfacial layer), and the combined effect of Cr and Ti in forming a protective oxide could enhance passivation [102].

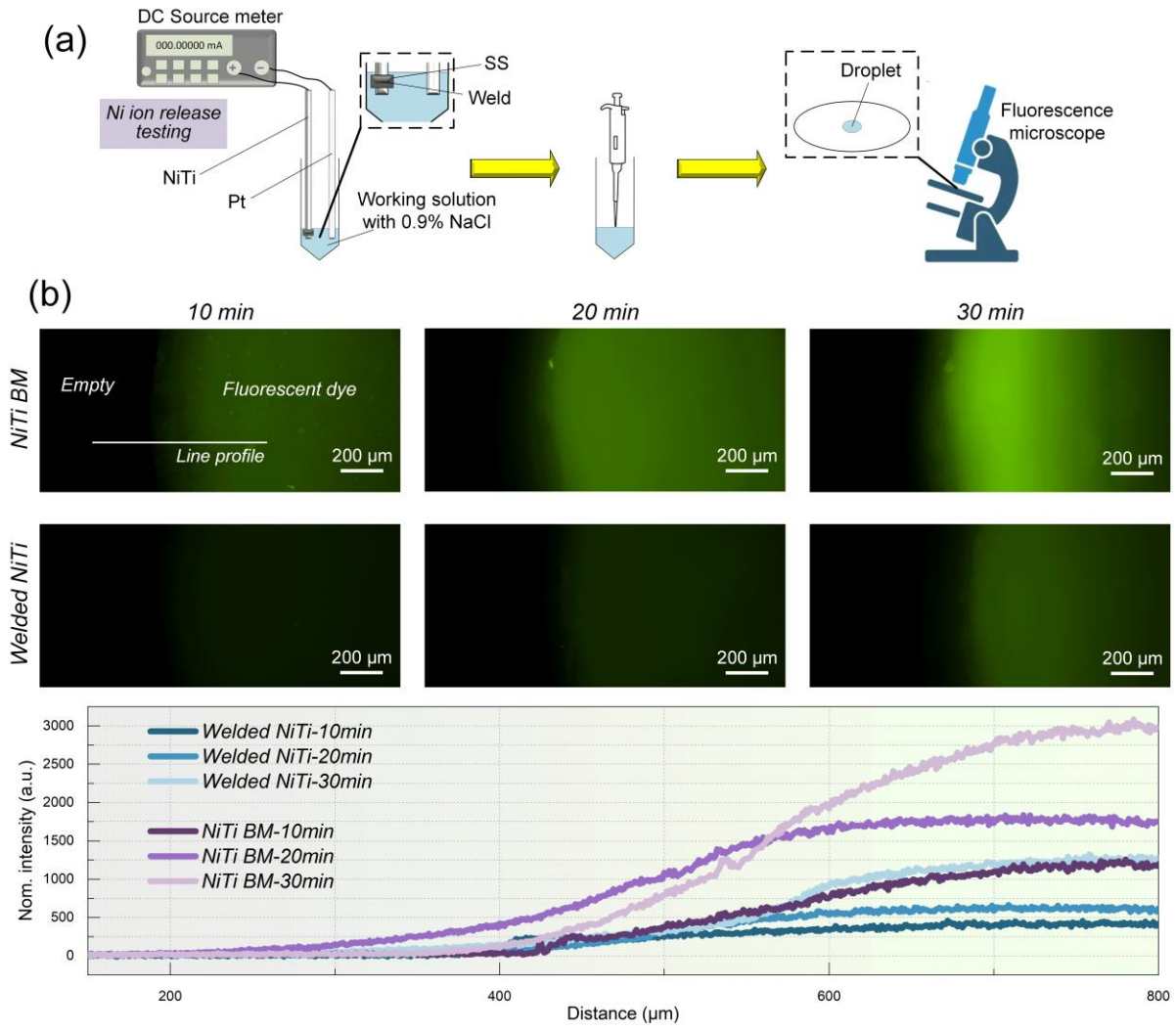


Fig. 5.10 (a) Schematics of Ni ion release experiment and fluorescent characterization (not to scale); (b) fluorescent images and intensity line distributions of the extracted solutions from the Ni ion release test of NiTi BM and welded NiTi with different current application durations.

Electrochemical corrosion of NiTi and SS could occur in bioenvironment, and it is highly associated with the Ni ion release from NiTi. In Fig. 5.11a, The open circuit potential (OCP) of welded NiTi was significantly higher than that of NiTi BM (0.028 vs -0.048 at 7200 s), indicating an enhanced capacity for forming the protective oxide film and a higher corrosion resistance in the welded NiTi sample [87]. The OCP of welded NiTi showed an ennoblement at the beginning after which it dropped and stabilized (0-1500 s). This phenomenon was attributed to the passivity and the crevice corrosion onset of SS and squeezed-out zone, with the existence of a Fe-Cr-Ni-Ti system [175,176], as evidenced by the observation of micro-crevice in squeezed-out zone (Fig. 5.11k). Both potentiodynamic polarization (PDP) curves (Fig.

5.11b) revealed the absence of a typical passive region up to pitting potentials, suggesting the lower corrosion resistance of NiTi compared to other passive materials, consistent with previous findings [87,177]. Based on Tafel extrapolation (Fig. C7), the calculated electrochemical parameters are shown in Fig. 5.11b and Table C4. Notably, the welded NiTi exhibited higher corrosion potential (E_{corr}) and pitting potential (E_{pit}) than NiTi BM, further confirming its superior corrosion resistance.

Fig. 5.11c depicts the high density of deep pits (19.1%) on NiTi BM surface after polarization. Particles (marked by arrows in Fig. 5.11d and e; additional images in Fig. C9) were observed at the edge or inside of the initial pits. They were identified as the salt-coated Ti-O-rich particles originating from PVAs of NiTi BM (Fig. 5.1c). The schematic in Fig. 5.11 illustrates how these PVAs created favorable conditions for pitting with localized cathode and anode, leading to the rapid Ni ion release and corrosion damage of NiTi [178]. The welding Joule heating eliminated the PVA voids (Fig. 5.3 h and i) at HAZ, reducing the pitting spots. This heat effect on NiTi worked for both interfaces with SS and electrode (Fig. 5.2f). As a result, the density of deep pits in NiTi weld zone significantly decreased to 6.0% (Fig. 5.11f). The corrosive morphology in the weld zone shifted to a more uniform pattern, characterized by a relatively flat surface with smaller and lighter pits (Fig. 5.11g and h). Besides of the NiTi weld zone, both SS and squeezed-out zone in the NiTi-SS joint exhibited less corrosion damages (Fig. 5.11 i-k), compared to NiTi BM. The welding process introduced the coexistence of Cr and Ti in NiTi/SS interface and squeezed-out zone, and the Cr-Ti joint action contributed to the better passivation and the higher E_{corr}/E_{pit} [102]. It should be mentioned that Cr is known to increase the corrosion current density (i_{corr}) after breakdown, which explains the higher i_{corr} in the welded NiTi in this study (Table C4). However, in bioenvironments with "zero toxicity" requirements, E_{corr} and E_{pit} are generally considered as more critical indicators of corrosion performance. These electrochemical results are in good agreement with the observation of Ni ion release in Fig. 5.10. In short, NiTi-SS RMWed joint could even show better corrosion resistance than NiTi BM in terms of hydrogen embrittlement, Ni ion release and electrochemical corrosion. This improvement was attributed to the Joule heating that eliminated PVA voids in NiTi HAZ, as well as interfacial reactions that introduced new alloying elements and phases in the interface and squeezed-out zone.

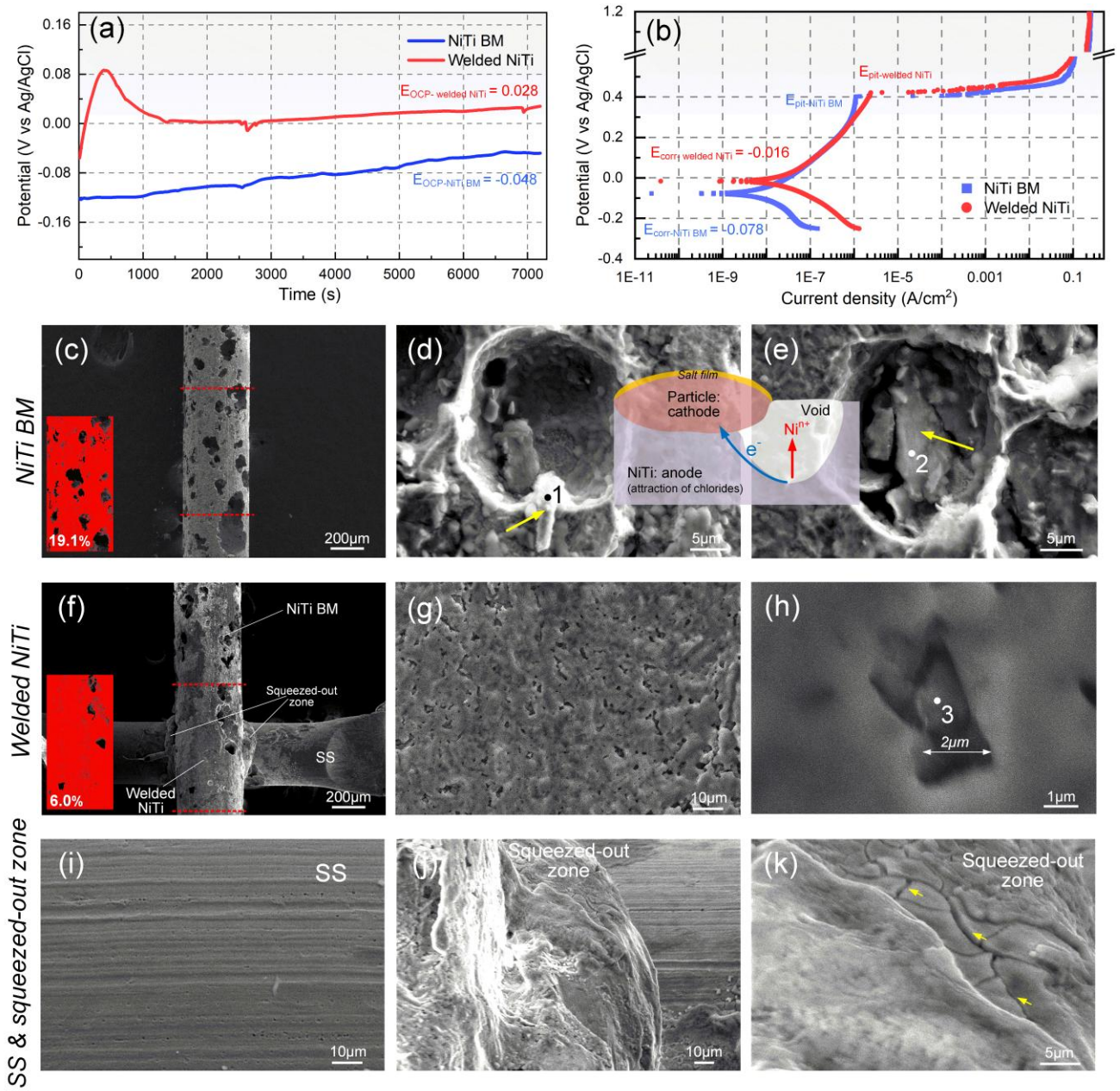


Fig. 5.11 (a) OCP curves of NiTi BM and welded NiTi; (b) PDP curves of NiTi BM and welded NiTi; (c-e) SEM images of NiTi BM after polarization; (f-h) SEM images of welded NiTi after polarization; (i) SS surface morphology after polarization; (j,k) morphologies of squeezed-out zone after polarization (the inserts in Fig. 5.11 c and f were processed by contrast threshold control to indicate the pit densities; EDS results of spots 1, 2 and 3 are shown in Fig. C8).

5.6 Ultrathin multi-phase reaction layer at the RMWed NiTi-SS interface

It has been widely recognized that an ultrathin reaction layer (usually <5μm; generally the thinner the better) at the dissimilar-metal interface usually does not exhibit extreme brittleness and is conducive to metallurgical bonding [157], which aligns well with the observations in the previous sections of this Chapter. This empirical principle not only applies to solid-state joined interfaces but also proves effective for interfaces in some weld-brazing and even fusion welding [115,179,180] of dissimilar metals. Many studies have thus been carried out focusing on the thickness control of the interfacial layer to obtain the optimized joint properties [181,182]. The dominant phase of the interfacial layer is identified and used to represent the overall properties of the interface in a general manner [183]. However, detailed information within such an ultrathin reaction layer, especially concerning the secondary interfaces and the microstructural behavior under the thermomechanical processing, remains unclear, which clouds the further efforts to further enhance dissimilar joint properties. Therefore, in this section, the study of the such an ultrathin reaction layer obtained from RMWed NiTi-SS interface was conducted.

The formation of the reaction layer originated from the diffusion under thermomechanical processing. The STEM HAADF image and the associated EDS mappings of the interface in Fig. C11 unveiled four sub-layers, suggesting the complexity in the submicron scale. This complexity arose from the combination of short cooling duration and electrode pressure during the solid-state joining process, resulting in diverse phases within a narrow zone. Phases in different layers were identified by SAD, FFT, STEM contrast and composition analysis (EDS), as shown in Fig. 5.12. From SS side to NiTi side, four layers are labelled as layer I, II, III and transition zone (TZ), respectively. The summarized results are shown in Table 5.1. Layer I was identified as a cubic τ-$(Cr,Ni)_8Ti_5(Fe,Ni)_{16}$ [184] (α-Mn structure). From Fig. 5.12d the HAADF image, fine inclusions were found inside layer I and layer II. They were identified as Fe-Cr-rich or Ti-rich oxide particles, as seen in the FFT superlattice pattern showing a good coherence between these particles and layer I matrix. The formation of these oxides should be associated with the dissolution of the initial Ti-rich oxides from NiTi PVAs. Layer II was thick enough to be characterized by SAD, showing a C14-Laves $(Fe,Ni,Cr)_2Ti$ Laves phase structure under [$\bar{1}$100] ZA in Fig. 5.12e, namely the primary phase as identified in Fig. 5.5 earlier. Note that in Fig. 5.12b, layer III was marked by the high Ni segregation with a concentration higher than that in both BMs; the FFT in Fig. 5.12f revealed a $(Ni,Fe)_3Ti$ phase forming in this layer. Ni diffused along the $(Fe,Ni,Cr)_2Ti$ grain boundary (GB), thus it extended the $(Ni,Fe)_3Ti$ to

SS surface, as seen in Ni EDS mapping. Atomic-scale element distribution in the TZ confirmed the presence of ordered BCC structure (B2) by comparing Ni/Ti and Fe/Ti overlapped EDS mappings or line scanning (Fig. 5.12g-j). Therefore, TZ was composed of B2 (Ni,Fe)Ti phase forming through Fe atom diffusion and subsequent substitution of Ni sites in the original NiTi B2. The phase evaluation crossing the interface is SS→τ→$(Fe,Ni,Cr)_2Ti$→$(Ni,Fe)_3Ti$→(Ni,Fe)Ti→NiTi.

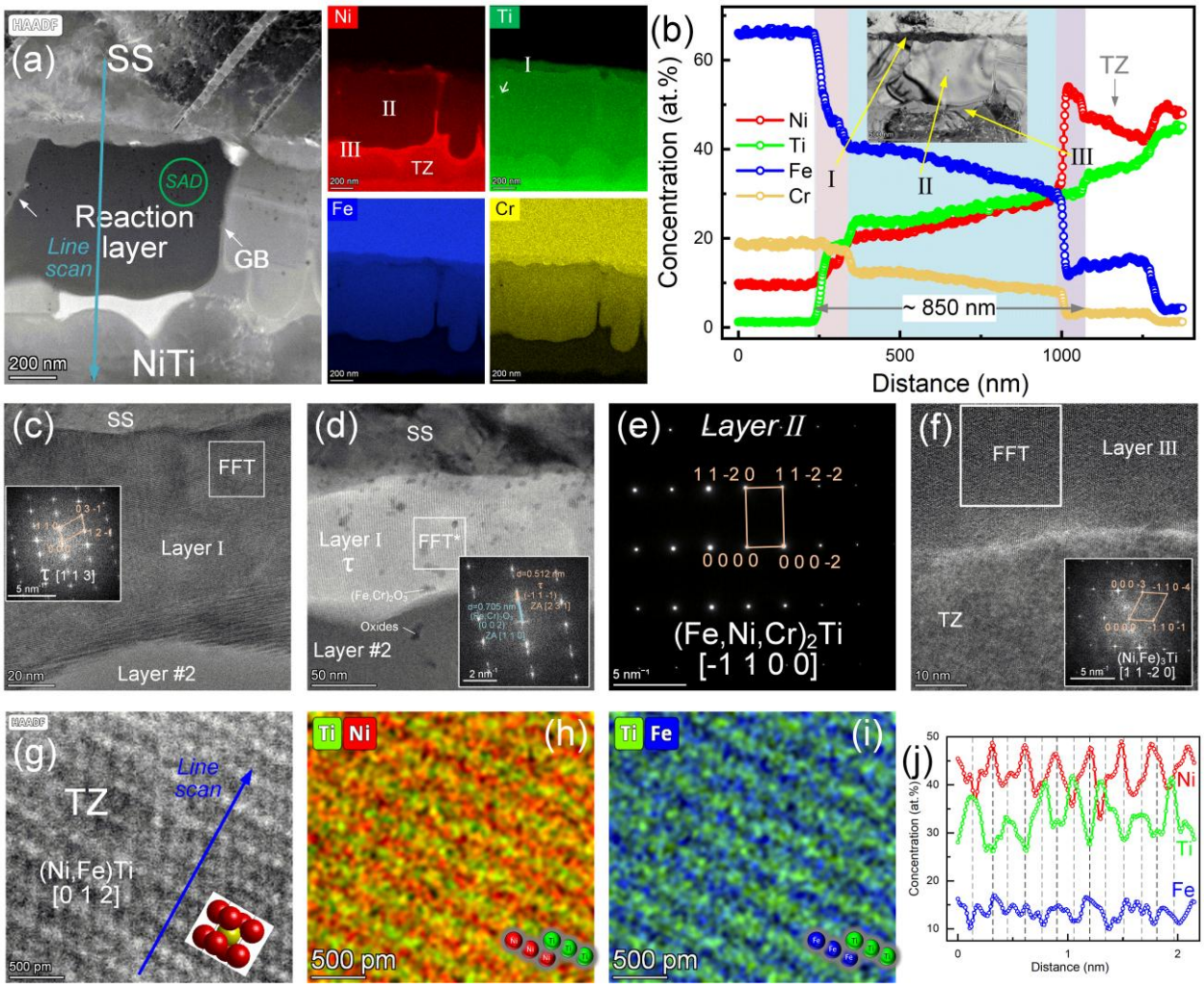


Fig. 5.12 (a) STEM HAADF image of the reaction layer and the related EDS mappings; (b) EDS line scanning according to the direction marked in Fig. 5.12a; (c) HRTEM image and the related FFT pattern of layer I; (d) HAADF image and the FFT pattern from layer I and inclusions (FFT was obtained from the same region but in a TEM image); (e) SAD pattern from layer II, as marked in Fig. 5.12a; (f) HRTEM image of layer III and TZ, with FFT pattern from layer III; (g-j) HRTEM image and the related atomic-scale EDS mappings or line scanning.

Table 5.1 Interfacial phases from SS to NiTi

Layer#	Thickness (nm)	Phase	Prototype; Space group	Lattice constants (nm)	Ref.
SS	Base metal	γ-Fe	Cu; $Fm\bar{3}m$	a=0.3591	[185]
I	77	τ-$(Cr,Ni)_8Ti_5(Fe,Ni)_{16}$	Mn; $I\bar{4}3m$	a=0.8922	[184]
II	650	$(Fe,Ni,Cr)_2Ti$	$MgZn_2$; $P6_3/mmc$	a=0.4757, c=0.7829	[186]
III	81	$(Ni,Fe)_3Ti$	Ni_3Ti; $P6_3/mmc$	a=0.5096, c=0.8304	[187]
TZ	244	B2-(Ni,Fe)Ti	ClCs; $Pm\bar{3}m$	a=0.3008	[185]
NiTi	Base metal	B2-NiTi	ClCs; $Pm\bar{3}m$	a=0.3015	[188]

Section 5.4 indicated that the original SS surface was the crack path, instead of $(Fe,Ni,Cr)_2Ti$ phase, suggesting a shift from the conventional notion that the more brittle phase poses greater risk in dissimilar-metal welds. Fig. 5.13 a-e display HRTEM images and corresponding FFT patterns of SS/τ interface with ZA aligned to [113] of τ phase. Interestingly, a reorientated layer (ROL) with the thickness of around 2 nm, comprising a few atomic layers, was observed between SS and τ, as evidenced by the atomic-resolution image in Fig. 5.13e. The image contrast indicated that the ROL did not possess a τ phase structure but instead exhibited a Fe-FCC crystal structure. The presence of this ROL was further confirmed by the FFT analysis from Fig. 5.13b to d. Especially, the localized FFT on the narrow ROL in Fig. 5.13d extracted its FCC pattern with a ZA on [101], and it indicated the crystallographic relationship (CR) of $(1\,\overline{\mathbf{1}}\,\overline{\mathbf{1}})_{ROL}//(1\,\overline{\mathbf{4}}\,1)_{\tau}$, $(0\,\overline{\mathbf{2}}\,0)_{ROL}//(33\,\overline{\mathbf{2}}\,)_{\tau}$ and $[101]_{ROL}//[113]_{\tau}$. Overall, the ROL exhibited a good crystallographic match with τ, as illustrated by the schematics in Fig. 5.13e (the unit cell of τ was simplified for better visualization). The ZA was then adjusted to observe the CR between SS and ROL ($[211]_{ROL}//[\overline{\mathbf{1}}10]_{\tau}$), whereas in this case τ phase would not be aligned by a good ZA (Fig. 5.13h). Moiré fringes in SS in Fig. 5.13f resulted from the local orientation variation due to the heavy deformation [189], which was also evidenced by the astigmatic FFT pattern in Fig. 5.13g. By superposing SS lattice planes on ROL FFT pattern (Fig. 5.13i) and observing atomic configurations at SS/ROL interface (Fig. 5.13j), an obvious mismatch could be found, characterized by the grouped but non-parallel $(0\overline{\mathbf{2}}2)_{ROL}$-$(220)_{SS}$ and $(1\overline{\mathbf{1}}\overline{\mathbf{1}})_{ROL}$-$(002)_{SS}$, especially considering the large interplanar spacing difference between $(1\overline{\mathbf{1}}\overline{\mathbf{1}})_{ROL}$ and $(002)_{SS}$.

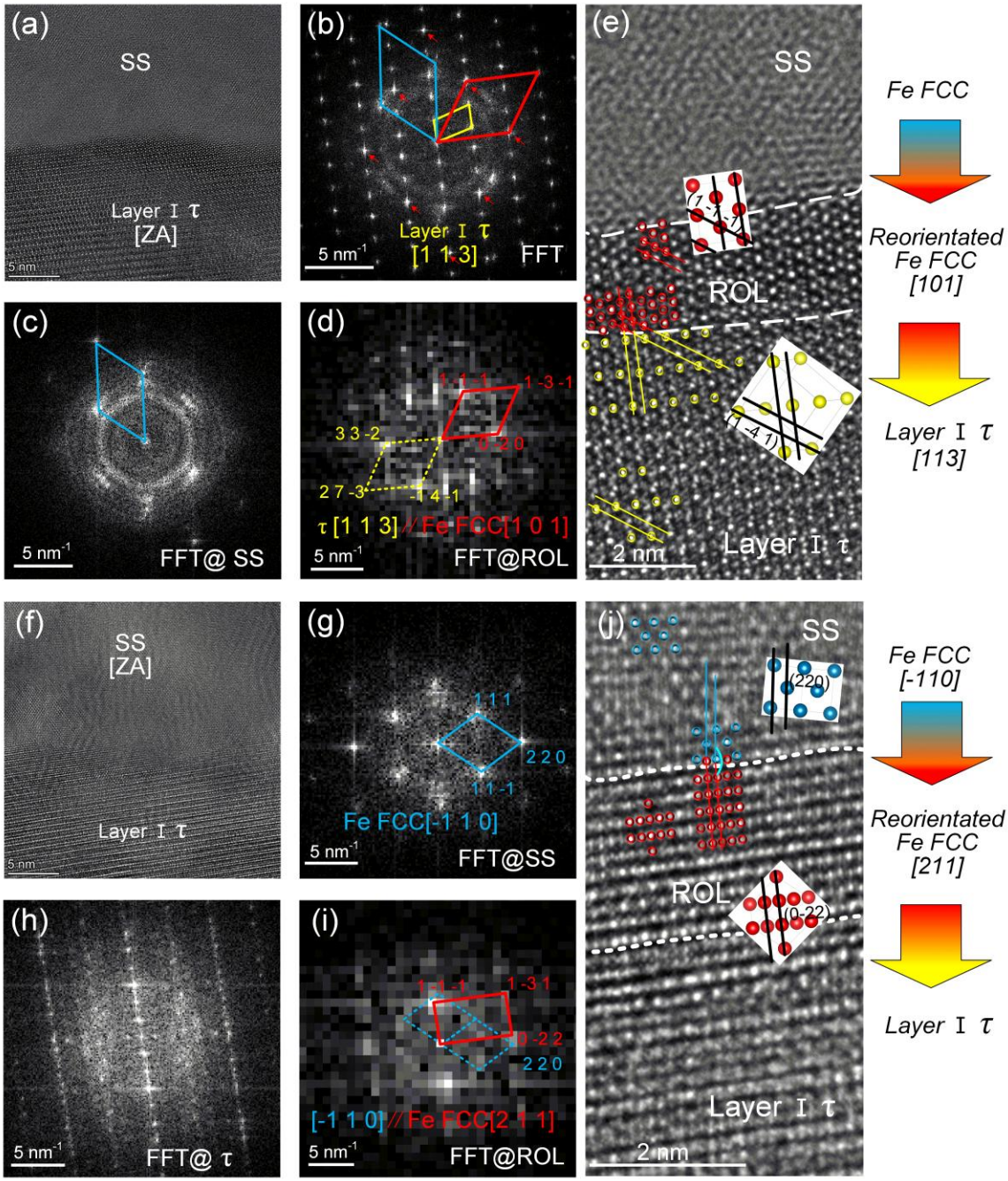


Fig. 5.13 (a) HRTEM image of SS/τ interface with ZA aligned for τ phase; (b-c) FFT patterns obtained from the whole region, the SS side, and the ROL, respectively; (e) HRTEM image of SS/τ interface showing the CR between ROL and τ; (f) HRTEM image of SS/τ interface with ZA aligned for SS; (g-i) FFT patterns obtained from the SS side, τ, and the ROL, respectively; (j) HRTEM image of SS/τ interface showing the CR between ROL and SS.

The identification of the ROL at the SS BM/τ interface represents a new finding at such a solid-state joined interface. An epitaxial growth model was applied to explain the ROL formation, considering the heat transfer direction from NiTi to SS (i.e., from τ to SS), as well as the thermophysical properties of τ and Fe-FCC. As an IMC, τ phase has higher modulus and forms at a high temperature during RMW, which can be regarded as a potent substrate for Fe-FCC growth, like many classical heterogeneous epitaxy couples: Al/Al_2O_3 [190], Al/TiB_2 [191] and Fe/GaN [192]. Once τ phase forms at the interface, it would heat and activate several SS atomic layers for recrystallization and re-growth based on τ orientation (Fig. 5.14a). Stemming from the study of Frank and Van der Merwe [193] on mathematical exposition of misfitting monolayers and oriented overgrowth involving the interfacial sinusoidal force, strain and dislocation formation, it has been accepted that in a low-misfit epitaxial couple (<9 pct.), the coherent but strained layer forms within a critical thickness (h_c). The further growth of such an epitaxial layer relies on the energy release by forming dislocations at the heterogeneous interface. The relationship between lattice misfit (f) and critical thickness (h_c) is governed by an implicit equation $F(f, h_c)=0$ [194–196]:

$$Bf^2h_c = 2Dbfln\left(\frac{h_c}{b}+1\right) \tag{5.1}$$

Here, b is the Burger's vector; B and D are temperature-dependent constants for the epitaxial layer (i.e., ROL) calculated by the parameters in Table C5:

$$B = \frac{2\mu(1+\upsilon)}{1-\upsilon} \tag{5.2}$$

$$D = \frac{\mu}{4\pi(1-\upsilon)} \tag{5.3}$$

Considering the ultrafast cooling rate during RMW, one obtains $B=2.76*10^{11}$ or $2.26*10^{11}$ (N/m^2) while $D=8.48*10^9$ or $6.77*10^9$ (N/m^2) at room temperature or at recrystallization temperature, respectively. f is the natural lattice misfit calculated by [194]:

$$f = \frac{d_{[uvw]ROL} - d_{[uvw]\tau}}{d_{[uvw]ROL}} \tag{5.4}$$

Here, $d_{[uvw]ROL}$ and $d_{[uvw]\tau}$ are atomic spacings along the close packed direction on the close packed plane for matched epitaxial layer and substrate, respectively. According to the HRTEM/FFT results, zigzag atom-matching model [197] and the edge-to-edge matching model [198], these spacings could be confirmed. The f is therefore calculated as 1.575 pct, and the h_c-f relationship is plotted in Fig. 5.14b. f_c (~6 pct) was the threshold for nucleation of a strained layer, hence the nucleation of ROL on τ substrate

is possible because of f=1.575 pct < f_c. The calculated h_c is ~2.25 nm, which is similar but slightly higher than the measured ROL average thickness (1.89 nm). These calculations indicate that ROL should be a strained layer with a coherent relationship with τ (i.e., no interfacial dislocations). IFFT is therefore performed on two matched plane groups, $(1\bar{1}\bar{1})_{ROL}//(1\bar{4}1)_{\tau}$ and $(0\bar{2}0)_{ROL}//(33\bar{2})_{\tau}$, and no dislocations were found in ROL/τ interface (Fig. 5.14c and d). At the last stage of the epitaxial growth, the ROL created a "hard" contact with the original SS orientation, forming a three-layer structure with interfacial energies ($\gamma_{ss/ROL}$ and $\gamma_{\tau/ROL}$) and ROL strain energy (E_s), as illustrated in Fig. 5.14a. Due to the large misfit at the ROL/SS interface, high-density dislocations should be introduced, as observed in Fig. 5.14e and f.

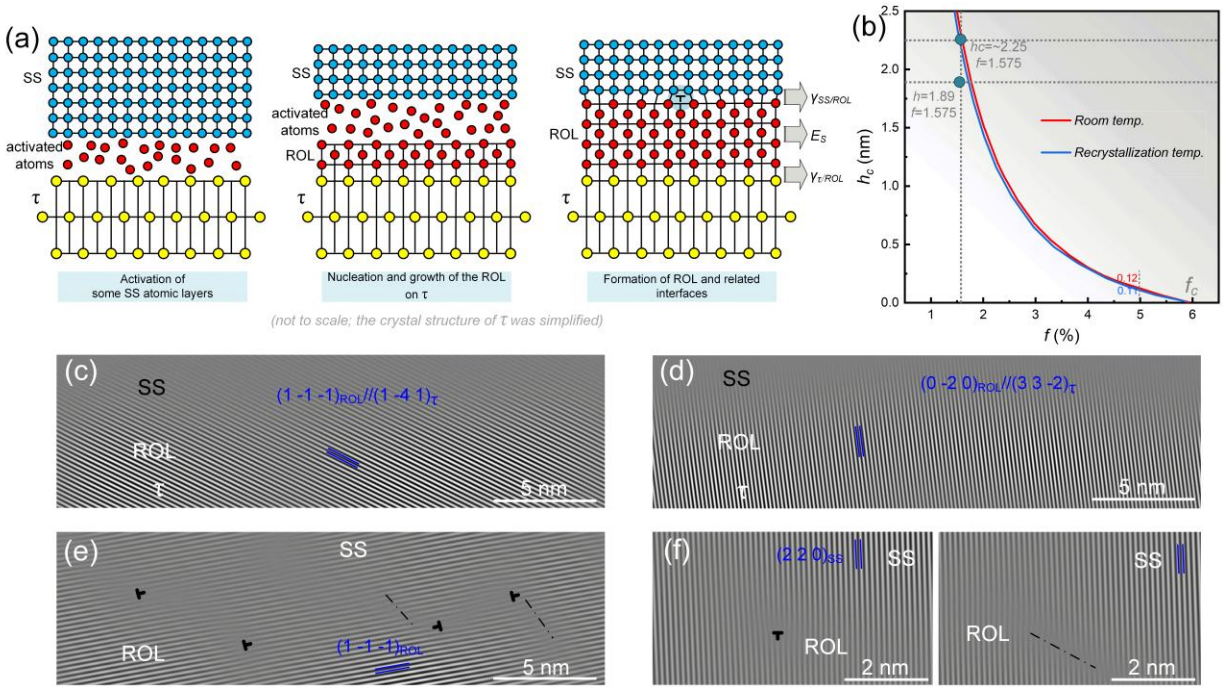


Fig. 5.14 (a) Schematics of epitaxial growth of ROL on τ substrate; (b) h_c-f curves plotted from equation (5.1); (c,d) HRTEM IFFT of the SS/ROL/τ interfaces with masks on $(1\bar{1}\bar{1})_{ROL}//(1\bar{4}1)_{\tau}$ and $(0\bar{2}0)_{ROL}//(33\bar{2})_{\tau}$, respectively; (e, f) HRTEM IFFT of the SS/ROL/τ interfaces with masks on $(1\bar{1}\bar{1})_{ROL}$-$(002)_{SS}$ and $(0\bar{2}2)_{ROL}$-$(220)_{SS}$, respectively.

The "precursor" of ROL is the original textured SS, which undergoes heavy deformation due to the welding process, as analyzed in previous Sections. The epitaxial growth of ROL can therefore be also regarded as the extremely localized recrystallization of SS, with τ serving as a nucleation site. The driving force of this recrystallization is determined by the energy difference ΔE between the deformed SS and recrystallized ROL [199]:

$$\Delta E \approx \rho G b^2 \approx 3\frac{\gamma_s}{d_s} \tag{5.5}$$

ΔE increases with the increase in dislocation density ρ or sub-grain boundaries γ_s, whereas decreases with the increase in sub-grain size d_s. In other words, the higher the deformation or work hardening degree of SS, the easier and faster the ROL nucleation [200]. The deformation of SS results in deformation twins with high-density twin boundaries (i.e., increase in γ_s but decrease in d_s), as well as high dislocation density (i.e., increase of ρ), as shown in Fig. 5.5. Therefore, severely deformed SS at the SS/τ interface provides high driving force for ROL epitaxial growth on τ surface, even though with rapid heating and cooling.

5.7 Summary

To overcome the limitations of both fusion welding and solid-state welding techniques for NiTi-SS joining, this chapter proposes a novel approach that achieves a solid-state joined interface in RMW process by interfacial liquid control. The interface-controlled joint demonstrated superior strength, superelasticity, and corrosion resistance compared to NiTi joints or BM. The good NiTi-SS RMWed joint relied on the precise control of welding current and electrode force to squeeze interfacial mixed liquid out and to reduce the NiTi BM damage. During the welding process, SS was deformed while NiTi was recrystallized. A squeezed-out zone, composed of a Ni-Ti-Fe-Cr mixture, formed out of the interface. The reliable interfacial joining is achieved by the formation of the ultrathin interfacial reaction layer (~850 nm). The optimized joint exhibited an excellent strength that was even higher than NiTi-NiTi joints, highlighting its potential for multifunctional biomedical device fabrication, with superelasticity on the NiTi side and flexible deformation capacity on the SS side. The welded NiTi demonstrated superelastic curves similar to those of NiTi BM. The RMW process reduced the residual strain by eliminating dislocations and PVA voids in the NiTi HAZ and forming a high-modulus interfacial layer. The weld zone did not exhibit susceptibility to hydrogen embrittlement, Ni ion release, or electrochemical corrosion, thanks to the Joule heating effect on NiTi and interfacial reactions. Moreover, the FCC reorientated layer (ROL) was found between SS and IMC layer at the ultrathin interface. The formation of this ROL was uncovered based on the epitaxial growth model, which caused a strong mismatch with the textured SS, resulting in fracture at the SS/ROL interface.

Chapter 6 Conclusions and future work

6.1 Conclusions

This thesis was motivated by the high demand on dissimilar welding between NiTi and SS. The brittleness caused by IMCs is a key issue in NiTi-SS welding. The work focuses on the microstructure control to enhance the NiTi-SS joint properties. It deepens the understanding of the metallurgy of a Ni-Ti-Fe-Cr system, proposes novel approaches to realize a reliable NiTi-SS joints, and provides some new insights into the FZ and the interface of dissimilar-material welds. The detailed findings in this thesis are as follows:

(1) The combination of laser defocus and large beam offset enabled the laser weld-brazing for NiTi and SS wire, which eliminated the IMCs network in FZ. This achievement improved the joint strength and shifted the complex FZ brittleness issues to the focus on the brazed interface control. Additionally, laser welding modes significantly influenced the FZ macrosegregation and porosity of NiTi-SS joints. Low laser power density and long welding time mitigated the macrosegregation and porosity by weakening the laser keyhole effect and extending the molten pool duration. In NiTi-SS FZ, large pores were caused by the instability or collapse of the laser keyhole, while small pores initiated from the Ni vaporization.

(2) Both strategies of mixing restriction and harmful phase replacement were investigated in the RSW of NiTi and SS for the first time. The unique thermomechanical processing characteristics in RSW led to some new findings. The use of a Nb interlayer resulted in a fundamentally different sandwich-structured joint, where FZs on NiTi and SS sides, separated by the unmolten Nb, suppressed the mixing of dissimilar molten metals. Nb-containing eutectics formed at the interfaces, contributing to a significant enhancement in joint strength (with a 38% increase in fracture load and a 460% increase in energy absorption). In this case, the NiTi side experienced grain coarsening, degradation of superelasticity, and concentration of residual stresses, which made it the failure site in the joint. Adding Ni concentration in the FZ effectively replaced the Laves Fe_2Ti phase with the ductile Ni_3Ti phase. However, excessive Ni content could lead to large pores and cracks, reducing the effective joining area.

(3) To overcome the limitations from both fusion welding and solid-state welding techniques for NiTi-SS joining, a novel approach was proposed that achieves a solid-state joined interface in RMW process by interfacial liquid control. The interface-controlled joint exhibited superior strength, superelasticity, and corrosion resistance compared to NiTi joints or NiTi BM. Reliable interfacial joining was achieved

through the formation of an ultrathin interfacial reaction layer (~850 nm). The optimized joint demonstrated excellent strength, even higher than NiTi-NiTi joints, highlighting its potential for multifunctional biomedical device fabrication by emphasizing superelasticity on the NiTi side and flexible deformation capacity on the SS side. The RMW process reduced the NiTi residual strain because of the elimination of dislocations and PVA voids in NiTi HAZ and the formation of high-modulus interfacial layer. The weld zone did not exhibit susceptibility to hydrogen embrittlement, Ni ion release, or electrochemical corrosion, thanks to the Joule heating effect on NiTi and interfacial reactions. The FCC reorientated layer (ROL) was found between SS and IMC layer at the ultrathin interface. The formation of this ROL was uncovered based on an epitaxial growth model. This ROL introduced a strong mismatch with the textured SS, resulting in fracture at this interface.

6.2 Future work

(1) The precipitation mechanisms of IMCs in the FZ or the solid-state joined interface:

While the current study has provided a comprehensive and detailed understanding on the control of microstructure of NiTi-SS welded joints, the work on the nature of IMCs-filled FZ or solid-sate joined interface needs to be further conducted. Specifically, the precipitation mechanisms of various IMCs in the Ni-Ti-Fe-Cr system, involving their precipitation order, percentages, spatial distribution forms and interfaces should be uncovered. Due to the non-equilibrium solidification and thermomechanical processing of welding, it is extremely challenging to directly characterize the evolution of these IMCs. Some thermodynamic calculation software could provide useful information on the phase precipitation order and phase percentage. However, it should be noticed that the selection of database and modelling methods may influence the calculation results (as seen in Fig. 4.9 and Fig. 5.4). Most of the available databases are designed based on those common alloys. The development into a particular thermodynamic calculation methodology regarding the Ni-Ti-Fe-Cr system should be therefore carried out. In addition to the high-resolution and atomic-scale characterizations, phase field simulation could be another good approach to predict the microstructural evolution; density functional theory (DFT) and molecular dynamics (MD) simulations might be helpful for the insights into distributions and interfaces of IMCs.

(2) Phase transformations and functional properties of NiTi-SS joints:

NiTi-SS dissimilar welding is crucial for expanding the applications of NiTi alloys. To preserve or even enhance the functional properties of NiTi (e.g., SME or SE) in the welded joint, it is essential to investigate the NiTi phase transformations that occur during welding. These transformations involve changes in chemical composition, grain size, secondary phase precipitation, and more. However, as summarized in Chapter 2, there are limited studies that provide a detailed analysis of NiTi phase transformations and functional properties in NiTi-SS joints, particularly regarding the evolution of NiTi dislocations, texture, and grain orientation resulting from either fusion or solid-state welding processes. Furthermore, the deformation mechanisms of NiTi-SS joints under different loading conditions need to be explored, and the fatigue life of NiTi-SS joints should also be studied.

(3) Processing and applications of NiTi-SS joints:

The welding process needs further optimization to address the brittleness issue of NiTi-SS joints, and several coupling strategies can be implemented to achieve this. Welding flexibility is also a concern depending on the specific application scenarios. In general, solid-state welded NiTi-SS joints exhibit higher strength; however, their joint configurations are often limited to a lapped form, and micro-scale solid-state welding remains challenging. The welding process alters the appearance and geometry of the NiTi and SS raw materials, making post-processing (e.g., centerless grinding) necessary. Therefore, achieving a one-step welding process that results in a well-formed joint is highly desirable. Given the diverse applications of NiTi-SS joints, particularly in the biomedical field, assessing their corrosion resistance and biocompatibility is crucial. Additionally, the standards and production cost-efficiency of NiTi-SS joints need to be developed and evaluated.

References

[1] Medical Device Contract Manufacturing Market by Device Type (IVD (Equipment, Consumable), Cardiovascular, Diabetes Care, Drug Delivery, Orthopedic, Ophthalmic, Endoscopy Devices), Class of Device (Class I, II, III), & Services (2022-2026), 2021. https://www.marketsandmarkets.com/Market-Reports/medical-device-contract-manufacturing-market-170622851.html.

[2] K. Otsuka, X. Ren, Prog. Mater. Sci. 50 (2005) 511–678.

[3] K. Safaei, H. Abedi, M. Nematollahi, F. Kordizadeh, H. Dabbaghi, P. Bayati, R. Javanbakht, A. Jahadakbar, M. Elahinia, B. Poorganji, Jom. 73 (2021) 3771–3786.

[4] M.H. Elahinia, M. Hashemi, M. Tabesh, S.B. Bhaduri, Prog. Mater. Sci. 57 (2012) 911–946.

[5] L. Petrini, F. Migliavacca, J. Metall. 2011 (2011) 1–15.

[6] S. Alipour, F. Taromian, E.R. Ghomi, M. Zare, S. Singh, S. Ramakrishna, Proc. Inst. Mech. Eng. Part H J. Eng. Med. 236 (2022) 1595–1612.

[7] M.R. Hosseini, M. Ahangari, M.H. Johar, S.R. Allahkaram, Mater. Lett. 285 (2021) 129097.

[8] L. Patnaik, S. Ranjan Maity, S. Kumar, Mater. Today Proc. 26 (2020) 638–643.

[9] A. Bekmurzayeva, W.J. Duncanson, H.S. Azevedo, D. Kanayeva, Mater. Sci. Eng. C. 93 (2018) 1073–1089.

[10] H. Zeng, J. Zhou, Y. Zhang, Adv. Mater. 11 (2022) 14.

[11] S. Asadi, T. Saeid, A. Valanezhad, I. Watanabe, J. Khalil-Allafi, J. Manuf. Process. 55 (2020) 13–21.

[12] Y. Haga, T. Mineta, M. Esashi, Sensors Updat. 8 (2000) 147–186.

[13] E. Ayvali, C.P. Liang, M. Ho, Y. Chen, J.P. Desai, Int. J. Rob. Res. 31 (2012) 588–603.

[14] J. Mohd Jani, M. Leary, A. Subic, M.A. Gibson, Mater. Des. 56 (2014) 1078–1113.

[15] M.M. Kheirikhah, S. Rabiee, M.E. Edalat, A Review of Shape Memory Alloy Actuators in Robotics BT - RoboCup 2010: Robot Soccer World Cup XIV, in: J. Ruiz-del-Solar, E. Chown, P.G. Plöger (Eds.), Springer Berlin Heidelberg, Berlin, Heidelberg, 2011: pp. 206–217.

[16] A. Shamsolhodaei, J.P. Oliveira, N. Schell, E. Maawad, B. Panton, Y.N. Zhou, Intermetallics. 116 (2020) 106656.

[17] P. Burdet, J. Vannod, A. Hessler-Wyser, M. Rappaz, M. Cantoni, Acta Mater. 61 (2013) 3090–3098.

[18] H. Niu, H.C. Jiang, M.J. Zhao, L.J. Rong, J. Mater. Sci. Technol. 61 (2021) 16–24.

[19] Q. Li, Y. Zhu, J. Guo, J. Mater. Process. Technol. 249 (2017) 538–548.

[20] S.S. Ao, M.P. Cheng, W. Zhang, J.P. Oliveira, S.M. Manladan, Z. Zeng, Z. Luo, Ultrasonics. 121 (2022) 106684.

[21] M.B. Lezaack, A. Simar, Y. Marchal, M. Steinmetz, K. Faes, J.P. de Almeida, J. Pacheco de Almeida, J.P. de Almeida, J. Pacheco de Almeida, J.P. de Almeida, J. Pacheco de Almeida, Sci. Technol. Weld. Join. 27 (2022) 418–428.

[22] L.C. Chang, T.A. Read, JOM. 3 (1951) 47–52.

[23] Z. S. Basinski, J.W. Christian, Acta Metall. 2 (1954) 101–116.

[24] W.J. Buehler, J. V. Gilfrich, R.C. Wiley, J. Appl. Phys. 34 (1963) 1475–1477.

[25] R. Hang, F. Zhao, X. Yao, B. Tang, P.K. Chu, Appl. Surf. Sci. 517 (2020) 146118.

[26] S. Rodinò, C. Maletta, Prog. Eng. Sci. 1 (2024) 100021.

[27] X. Wang, W. Xia, X. Wu, Y. Wei, C. Huang, Mater. Sci. Eng. A. 578 (2013) 1–5.

[28] P. Šittner, L. Heller, P. Sedlák, Y. Chen, O. Tyc, O. Molnárová, L. Kadeřávek, H. Seiner, Shape Mem. Superelasticity. 5 (2019) 383–396.

[29] M. Losertová, M. Štencek, D. Matýsek, O. Štefek, J. Drápala, IOP Conf. Ser. Mater. Sci. Eng. 266 (2017).
[30] X. Kong, Y. Yang, Z. Sun, H. Yang, Y. Liu, Y. Ren, L. Cui, C. Chen, S. Hao, Appl. Mater. Today. 22 (2021) 100904.
[31] N. Gangil, A.N. Siddiquee, S. Maheshwari, J. Manuf. Process. 59 (2020) 205–222.
[32] J. Seo, Y.C. Kim, J.W. Hu, Appl. Sci. 5 (2015) 187–208.
[33] W. Tang, Metall. Mater. Trans. A Phys. Metall. Mater. Sci. 28 A (1997) 537–544.
[34] K. Otsuka, K. Shimizu, Int. Met. Rev. 31 (1986) 93–114.
[35] S. Miyazaki, K. Otsuka, Y. Suzuki, Scr. Metall. 15 (1981) 287–292.
[36] J. Chen, L. Xing, G. Fang, L. Lei, W. Liu, Acta Mater. 208 (2021) 116741.
[37] K.H. Lo, C.H. Shek, J.K.L. Lai, Mater. Sci. Eng. R Reports. 65 (2009) 39–104.
[38] C. Morsiya, Aust. J. Mech. Eng. 20 (2022) 803–813.
[39] L. Liu, C. Fan, H. Sun, F. Chen, J. Guo, T. Huang, Materials (Basel). 15 (2022) 1–31.
[40] D. Grabco, O. Shikimaka, C. Pyrtsac, A. Prisacaru, Z. Barbos, M. Bivol, S. Alexandrov, D. Vilotic, M. Vilotic, Mater. Sci. Eng. A. 805 (2021) 140597.
[41] Y. Aghayar, A.R. Naghashzadeh, M. Atapour, Vacuum. 184 (2021) 109970.
[42] M. Hathesh, Int. Res. J. Eng. Technol. 07 (2020) 5166–5174.
[43] H. Wang, K. Wang, W. Wang, L. Huang, P. Peng, H. Yu, Mater. Charact. 155 (2019) 109803.
[44] S. Soleymani, O.A. Ojo, N. Richards, J. Mater. Eng. Perform. 24 (2015) 499–504.
[45] S. Hossein Nedjad, M. Yildiz, A. Saboori, Sci. Technol. Weld. Join. 28 (2023) 1–17.
[46] J.A. Brooks, A.W. Thompson, Int. Mater. Rev. 36 (1991) 16–44.
[47] S. Jin, L. Guo, F. Luo, Z. Yao, S. Ma, R. Tang, Scr. Mater. 68 (2013) 138–141.
[48] R. Zhang, J. He, S. Xu, F. Zhang, Y. Ma, X. Wang, J. He, F. Zhang, Y. Ma, X. Wang, J. Mater. Res. Technol. 21 (2022) 1248–1255.
[49] L. Chang, M.G. Burke, K. Mukahiwa, J. Duff, Y.L. Wang, F. Scenini, Corros. Sci. 189 (2021) 109600.
[50] J.P. Oliveira, R.M. Miranda, F.M. Braz Fernandes, Prog. Mater. Sci. 88 (2017) 412–466.
[51] M.M. Quazi, M. Ishak, M.A. Fazal, A. Arslan, S. Rubaiee, M.H. Aiman, A. Qaban, F. Yusof, T. Sultan, M.M. Ali, S.M. Manladan, Crit. Rev. Solid State Mater. Sci. 46 (2021) 109–151.
[52] T. Deepan Bharathi Kannan, T. Ramesh, P. Sathiya, Jom. 68 (2016) 1227–1245.
[53] J.E. Gould, Weld. J. 91 (2012) 23–34.
[54] C. Schmal, G. Meschut, Weld. World. 64 (2020) 1471–1480.
[55] L. Liu, L. Xiao, J. Feng, L. Li, S. Esmaeili, Y. Zhou, Scr. Mater. 65 (2011) 982–985.
[56] R. Cao, J.H. Chang, Q. Huang, X.B. Zhang, Y.J. Yan, J.H. Chen, J. Manuf. Process. 31 (2018) 674–688.
[57] S.M. Manladan, Y. Zhang, S. Ramesh, Y. Cai, Z. Luo, S. Ao, A. Arslan, J. Manuf. Process. 48 (2019) 12–30.
[58] C. Zang, J. Liu, C. Tan, K. Zhang, X. Song, B.B. Chen, L. Li, J. Feng, J. Manuf. Process. 32 (2018) 595–605.
[59] C. Tan, J. Yang, X. Zhao, K. Zhang, X. Song, B.B. Chen, L. Li, J. Feng, J. Alloys Compd. 764 (2018) 186–201.
[60] J. Yang, J.P. Oliveira, Y. Li, C. Tan, C. Gao, Y. Zhao, Z. Yu, J. Mater. Process. Technol. 301 (2022) 117443.
[61] P. Wang, X. Chen, Q. Pan, B. Madigan, J. Long, Int. J. Adv. Manuf. Technol. 87 (2016) 3081–3090.
[62] C. Tan, F. Liu, Y. Sun, B. Chen, X. Song, L. Li, H. Zhao, J. Feng, J. Mater. Eng. Perform. 27 (2018)

3521–3531.
[63] N. Kumar, C. Pandey, P. Kumar, J. Press. Vessel Technol. 145 (2022) 1–25.
[64] Y. Jin, S. Jiahao, G. Chenkai, Z. Yixuan, L. Hongbing, J.P. Ovliera, T. Caiwang, Y. Zhishui, Opt. Laser Technol. 142 (2021) 107218.
[65] K. Zhang, L. Wu, C. Tan, Y. Sun, B.B. Chen, X. Song, J. Mater. Process. Technol. 271 (2019) 23–35.
[66] F.S. Shieu, M.J. Deng, K.C. Lin, J.C. Wong, J.Y. Wu, J. Mater. Sci. 34 (1999) 5265–5272.
[67] A. Safdel, M.A. Elbestawi, J. Alloys Compd. 885 (2021) 160971.
[68] M.N.A. Nasr, E.G. Ng, M.A. Elbestawi, Int. J. Mach. Tools Manuf. 47 (2007) 401–411.
[69] Z. Chen, J. Mater. Sci. 42 (2007) 5756–5765.
[70] V. Novák, P. Šittner, G.N. Dayananda, F.M. Braz-Fernandes, K.K. Mahesh, Mater. Sci. Eng. A. 481–482 (2008) 127–133.
[71] B. Cheng, L. Loeber, H. Willeck, U. Hartel, C. Tuffile, J. Mater. Eng. Perform. 28 (2019) 6565–6578.
[72] S. Asadi, T. Saeid, F. Habibi, Y. Kim, A. Valanezhad, N. Park, J. Mater. Res. Technol. 16 (2022) 25–38.
[73] S. Asadi, T. Saeid, A. Valanezhad, I. Watanabe, J. Khalil-Allafi, J. Mech. Behav. Biomed. Mater. 109 (2020) 103818.
[74] J. Pouquet, R.M. Miranda, L. Quintino, S. Williams, Int. J. Adv. Manuf. Technol. 61 (2012) 205–212.
[75] J. Vannod, M. Bornert, J.E. Bidaux, L. Bataillard, A. Karimi, J.M. Drezet, M. Rappaz, A. Hessler-Wyser, Acta Mater. 59 (2011) 6538–6546.
[76] M.J.C. Oliveira, R.H.F. Melo, T.M. Maciel, C.J. de Araújo, Mater. Chem. Phys. 224 (2019) 137–147.
[77] G.R. Mirshekari, A. Saatchi, A. Kermanpur, S.K. Sadrnezhaad, Opt. Laser Technol. 54 (2013) 151–158.
[78] C.H. Ng, E.S.H.H. Mok, H.C. Man, J. Mater. Process. Technol. 226 (2015) 69–77.
[79] Y. Chen, S. Sun, T. Zhang, X. Zhou, S. Li, Mater. Sci. Eng. A. 771 (2020) 138545.
[80] H. Gugel, A. Schuermann, W. Theisen, Mater. Sci. Eng. A. 481–482 (2008) 668–671.
[81] H.J. Kim, S. Asadi, F. Habibi, T. Saeid, A. Valanezhad, N. Park, U. Lee, J. Mater. Res. Technol. 20 (2022) 4197–4212.
[82] H.M. Li, D.Q. Sun, X.L. Cai, P. Dong, W.Q. Wang, Mater. Des. 39 (2012) 285–293.
[83] H. Li, D. Sun, X. Gu, P. Dong, Z. Lv, Mater. Des. 50 (2013) 342–350.
[84] A. Shojaei Zoeram, A. Rahmani, S.A.A. Akbari Mousavi, J. Manuf. Process. 26 (2017) 355–363.
[85] H. Li, D. Sun, X. Cai, P. Dong, X. Gu, Opt. Laser Technol. 45 (2013) 453–460.
[86] H. Wang, J. Xie, Y. Chen, W. Liu, W. Zhong, J. Mater. Res. Technol. 18 (2022) 1028–1037.
[87] G.R. Mirshekari, A. Saatchi, A. Kermanpur, S.K. Sadrnezhaad, J. Mater. Eng. Perform. 25 (2016) 2395–2402.
[88] H. Gugel, W. Theisen, Microstructural investigations of laser welded dissimilar Nickel-Titanium-steel joints, in: Eur. Symp. Martensitic Transform., EDP Sciences, 2009: p. 05009.
[89] G. Brandal, G. Satoh, Y.L. Yao, S. Naveed, J. Manuf. Sci. Eng. 135 (2013) 1–10.
[90] X.L. Gao, X.Q. Wang, J. Liu, L. kun Li, Mater. Lett. 268 (2020) 127573.
[91] P. West, V.C. Shunmugasamy, C.A. Usman, I. Karaman, B. Mansoor, J. Adv. Join. Process. 4 (2021) 100072.
[92] J. Li, B. Panton, S. Liang, A. Vivek, G. Daehn, Mater. Today Commun. 25 (2020) 101306.
[93] Q. Li, Y. Zhu, J. Mater. Process. Technol. 255 (2018) 434–442.

[94] J. Li, B. Panton, Y. Mao, A. Vivek, G. Daehn, Smart Mater. Struct. 29 (2020) 105023.
[95] K. Zhang, A. Shamsolhodaei, A. Ghatei-Kalashami, J.P. Oliveira, C. Zang, N. Schell, J. Li, A.R.H.H. Midawi, J.G. Lopes, J. Yan, P.E.J.J. Rivera-Díaz-del-Castillo, P. Peng, Y.N. Zhou, J. Mater. Sci. Technol. 180 (2024) 160–173.
[96] A. Bansiddhi, T.D. Sargeant, S.I. Stupp, D.C. Dunand, Acta Biomater. 4 (2008) 773–782.
[97] M. Cioffi, D. Gilliland, G. Ceccone, R. Chiesa, A. Cigada, Acta Biomater. 1 (2005) 717–724.
[98] J. Vannod, Laser Welding of Nickel-Titanium and Stainless Steel Wires : Processing , Metallurgy and Properties, ÉCOLE POLYTECHNIQUE FÉDÉRALE DE LAUSANNE, 2011.
[99] C. Van Der Eijk, H. Fostervoll, Z.K. Sallom, O.M. Akselsen, ASM Conf. Proc. Join. Adv. Spec. Mater. (2004) 125–129.
[100] A. Shamsolhodaei, M.H. Razmpoosh, C. Maletta, P. Magaro, Y.N. Zhou, Mater. Lett. 287 (2021) 129310.
[101] E. Kassab, J.A. da C.P. Gomes, J. Mech. Behav. Biomed. Mater. 116 (2021) 104323.
[102] D. Ruhlig, H. Gugel, A. Schulte, W. Theisenb, W. Schuhmann, Analyst. 133 (2008) 1700–1706.
[103] C. Zhang, S. Zhao, X.X. Sun, D. Sun, X.X. Sun, Corros. Sci. 82 (2014) 404–409.
[104] K. Yokoyama, K. Hamada, K. Moriyama, K. Asaoka, Biomaterials. 22 (2001) 2257–2262.
[105] H. Naujokat, A.I. Gökkaya, Y. Açil, K. Loger, T. Klüter, S. Fuchs, J. Wiltfang, J. Mater. Sci. Mater. Med. 33 (2022) 13.
[106] M. Li, Y.B. Wang, X. Zhang, Q.H. Li, Q. Liu, Y. Cheng, Y.F. Zheng, T.F. Xi, S.C. Wei, Mater. Sci. Eng. C. 33 (2013) 15–20.
[107] S.M. Toker, D. Canadinc, Mater. Sci. Eng. C. 40 (2014) 142–147.
[108] P. Vondrous, L. Kolarik, M. Kolarikova, Plasma arc welding of NiTi and 304 steel, in: Ann. DAAAM, 2012: pp. 1039–1042.
[109] S. Fukumoto, T. Inoue, S. Mizuno, K. Okita, T. Tomita, A. Yamamoto, Sci. Technol. Weld. Join. 15 (2010) 124–130.
[110] C. Tan, B.B. Chen, S. Meng, K. Zhang, X. Song, L.L. Zhou, J. Feng, Mater. Des. 99 (2016) 127–134.
[111] L. Li, C. Tan, Y. Chen, W. Guo, F. Song, Mater. Des. 43 (2013) 59–65.
[112] J. Singh, K.S. Arora, D.K. Shukla, J. Alloys Compd. 783 (2019) 753–764.
[113] W. Huang, H. Wang, T. Rinker, W. Tan, Mater. Des. 195 (2020) 109056.
[114] Z. Liu, P. Zhang, M. Yan, Z. Yu, Y. Tian, D. Wu, J. Mater. Process. Technol. 303 (2022) 117490.
[115] T. Soysal, S. Kou, D. Tat, T. Pasang, Acta Mater. 110 (2016) 149–160.
[116] R.M. Miranda, E. Assunção, R.J.C. Silva, J.P. Oliveira, L. Quintino, Int. J. Adv. Manuf. Technol. 81 (2015) 1533–1538.
[117] L. Quintino, E. Assunção, 6 - Conduction laser welding, in: S. Katayama (Ed.), Handb. Laser Weld. Technol., Woodhead Publishing, 2013: pp. 139–162.
[118] W. Xu, D.L. Chen, L. Liu, H. Mori, Y. Zhou, Mater. Sci. Eng. A. 537 (2012) 11–24.
[119] J. Yan, M. Gao, X. Zeng, Opt. Lasers Eng. 48 (2010) 512–517.
[120] N. Guo, Y. Fu, X. Xing, Y. Liu, S. Zhao, J. Feng, J. Mater. Process. Technol. 260 (2018) 146–155.
[121] W. Gao, S. Zhao, F. Liu, Y. Wang, C. Zhou, X. Lin, Surf. Coatings Technol. 248 (2014) 54–62.
[122] J. Metelkova, Y. Kinds, K. Kempen, C. de Formanoir, A. Witvrouw, B. Van Hooreweder, Addit. Manuf. 23 (2018) 161–169.
[123] J. Xu, Y. Rong, Y. Huang, P. Wang, C. Wang, J. Mater. Process. Technol. 252 (2018) 720–727.
[124] X. Zhang, S. Bian, P. Zhao, X. Ding, Y. Li, Z. Cao, Opt. Laser Technol. 149 (2022) 107894.
[125] L. Cui, Z. Peng, Y. Chang, D. He, Q. Cao, X. Guo, Y. Zeng, Opt. Laser Technol. 150 (2022) 107952.
[126] J. Norris, M. Perricone, R.A. Roach, K. Faraone, C. Ellison, 26th Int. Congr. Appl. Lasers Electro-

Optics, ICALEO 2007 - Congr. Proc. 804 (2007).
[127] X. Xiao, Y. Fu, X. Ye, M. Cheng, L. Song, Infrared Phys. Technol. 120 (2022) 103996.
[128] W.L. Daugherty, G.R. Cannell, Pract. Fail. Anal. 3 (2003) 56–62.
[129] M. Rezanezhad, S.A. Lajevardi, S. Karimpouli, Eng. Fract. Mech. 253 (2021) 107882.
[130] M. Mazar Atabaki, J. Ma, W. Liu, R. Kovacevic, Mater. Des. 67 (2015) 509–521.
[131] X. Chen, Z. Lei, Y. Chen, Y. Han, M. Jiang, Z. Tian, J. Bi, S. Lin, J. Manuf. Process. 56 (2020) 19–27.
[132] J. Li, Y. Cai, F. Yan, C. Wang, Z. Zhu, C. Hu, Opt. Laser Technol. 122 (2020) 105881.
[133] A.J. Castellanos S., J. Toro-Mendoza, M. Garcia-Sucre, J. Phys. Chem. B. 113 (2009) 5891–5896.
[134] J.L. Huang, N. Warnken, J.C. Gebelin, M. Strangwood, R.C. Reed, Acta Mater. 60 (2012) 3215–3225.
[135] F. Fetzer, M. Sommer, R. Weber, J.P. Weberpals, T. Graf, Opt. Lasers Eng. 108 (2018) 68–77.
[136] S.M.H. Hojjatzadeh, N.D. Parab, Q. Guo, M. Qu, L. Xiong, C. Zhao, L.I. Escano, K. Fezzaa, W. Everhart, T. Sun, L. Chen, Int. J. Mach. Tools Manuf. 153 (2020) 103555.
[137] A. Shamsolhodaei, Y.N. Zhou, A. Michael, Sci. Technol. Weld. Join. 24 (2019) 706–712.
[138] E. Mohammad Sharifi, A. Kermanpur, F. Karimzadeh, A. Esmaili, J. Mater. Eng. Perform. 23 (2014) 1408–1414.
[139] Q. Sun, J. Chen, X. Wang, F. Gu, C. Tan, A. Shamsolhodaei, L. Sun, Y.N. Zhou, Opt. Laser Technol. 140 (2021) 107071.
[140] J.P. Oliveira, F.M.B. Fernandes, R.M. Miranda, N. Schell, J.L. Ocaña, Mater. Des. 100 (2016) 180–187.
[141] J.P. Oliveira, B. Panton, Z. Zeng, C.M. Andrei, Y. Zhou, R.M. Miranda, F.M.B.B. Fernandes, Acta Mater. 105 (2016) 9–15.
[142] J. Li, A. Vivek, G. Daehn, J. Mater. Sci. Technol. 79 (2021) 191–204.
[143] Q. Chu, L. Zhang, T. Xia, P. Cheng, J. Zheng, M. Zhang, J. Li, F. Yan, C. Yan, Metals (Basel). 11 (2021) 1–9.
[144] K. Zhang, P. Peng, Y.N. Zhou, Mater. Sci. Eng. A. 835 (2022) 142660.
[145] K. Zhang, F. Liu, C. Tan, Y.N. Zhou, P. Peng, Mater. Sci. Eng. A. 848 (2022) 143426.
[146] V. Onar, Trans. Indian Inst. Met. 75 (2022) 1731–1739.
[147] B. Bocklund, L.D. Bobbio, R.A. Otis, A.M. Beese, Z. Liu, Materialia. 11 (2020) 100689.
[148] J. Eiken, E. Subasic, J. Lacaze, Materialia. 9 (2020) 100538.
[149] V. Hoppe, A. Gibas, W. Grzegorczyk, Interdiscip. J. Eng. Sci. 1 (2019) 1–9.
[150] A. Shamsolhodaei, A. GhateiKalashami, A. Safdel, A.R.H.H. Midawi, M.A. Elbestawi, P. Peng, Y.N. Zhou, J. Manuf. Process. 81 (2022) 467–475.
[151] H. Xia, L. Li, C. Tan, J. Yang, H. Li, W. Song, K. Zhang, Q. Wang, N. Ma, Mater. Des. 224 (2022) 111320.
[152] J. Xue, W. Guo, J. Yang, M. Xia, G. Zhao, C. Tan, Z. Wan, J. Chi, H. Zhang, J. Mater. Sci. Technol. 148 (2023) 138–149.
[153] V. Nikoli, J. Riesch, R. Pippan, Mater. Sci. Eng. A. 737 (2018) 422–433.
[154] X. Wang, X. Si, M. Li, Q. Zhou, J. Gao, C. Li, J. Qi, J. Cao, Compos. Part B Eng. 242 (2022) 110108.
[155] H. Kato, K. Sasaki, J. Mater. Sci. 47 (2012) 1399–1410.
[156] B. Tam, A. Pequegnat, M.I. Khan, Y. Zhou, Metall. Mater. Trans. A Phys. Metall. Mater. Sci. 43 (2012) 2969–2978.
[157] W. Cai, G. Daehn, A. Vivek, J. Li, H. Khan, R.S. Mishra, M. Komarasamy, J. Manuf. Sci. Eng. Trans. ASME. 141 (2019) 1–35.

[158] N. Zotov, M. Pfund, E. Polatidis, A.F. Mark, E.J. Mittemeijer, Mater. Sci. Eng. A. 682 (2017) 178–191.
[159] G. Li, T. Yu, N. Zhang, M. Chen, Comput. Mater. Sci. 215 (2022) 111804.
[160] O.E. Ozbulut, S. Hurlebaus, R. Desroches, J. Intell. Mater. Syst. Struct. 22 (2011) 1531–1549.
[161] B. Reinholz, S. Brinckmann, Int. J. Fatigue. 41 (2012) 72–82.
[162] O. Tyc, O. Molnárová, P. Šittner, Int. J. Fatigue. 152 (2021) 106400.
[163] J. Pfetzing-Micklich, C. Somsen, A. Dlouhy, C. Begau, A. Hartmaier, M.F.X. Wagner, G. Eggeler, Acta Mater. 61 (2013) 602–616.
[164] G. Laplanche, J. Pfetzing-Micklich, G. Eggeler, Acta Mater. 68 (2014) 19–31.
[165] K. Gall, H. Sehitoglu, Y.I. Chumlyakov, I. V. Kireeva, Acta Mater. 47 (1999) 1203–1217.
[166] H.S. Yun, S.K. Jeon, Y.K. Lee, J.S. Park, S.H. Nahm, Int. J. Hydrogen Energy. 50 (2024) 175–188.
[167] K. Yokoyama, M. Tomita, J. Sakai, Acta Mater. 57 (2009) 1875–1885.
[168] K. Yokoyama, K. Kaneko, T. Ogawa, K. Moriyama, K. Asaoka, J. Sakai, Biomaterials. 26 (2005) 101–108.
[169] J. Ševčíková, D. Bártková, M. Goldbergová, M. Kuběnová, J. Čermák, J. Frenzel, A. Weiser, A. Dlouhý, Appl. Surf. Sci. 427 (2018) 434–443.
[170] A. Azizi, A. Jamilian, F. Nucci, Z. Kamali, N. Hosseinikhoo, L. Perillo, Prog. Orthod. 17 (2016) 1–4.
[171] Y.S. Hedberg, I. Odnevall Wallinder, Biointerphases. 11 (2016) 018901.
[172] X. Li, J. Wang, E. hou Han, W. Ke, Acta Biomater. 3 (2007) 807–815.
[173] J.M. Khan, T. Rogers, M.H. Eng, R.J. Lederman, A.B. Greenbaum, Catheter. Cardiovasc. Interv. 91 (2018) 1164–1170.
[174] V. Wadehra, A.E. Buxton, A.P. Antoniadis, J.W. McCready, C.J. Redpath, O.R. Segal, E. Rowland, M.D. Lowe, P.D. Lambiase, A.W.C. Chow, EP Eur. 13 (2011) 1401–1405.
[175] P. Jakupi, J.J. Noel, D.W. Shoesmith, Corros. Sci. 53 (2011) 3122–3130.
[176] M.A. Rodríguez, R.M. Carranza, R.B. Rebak, Crevice corrosion of alloy 22 at open circuit potential in chloride solutions at 90 °c, in: NACE - Int. Corros. Conf. Ser., 2009: p. NACE-09424.
[177] C.L. Chu, T. Hu, S.L. Wu, Y.S. Dong, L.H. Yin, Y.P. Pu, P.H. Lin, C.Y. Chung, K.W.K. Yeung, P.K. Chu, Acta Biomater. 3 (2007) 795–806.
[178] F. Sun, L. Jordan, V. Albin, V. Lair, A. Ringuedé, F. Prima, ACS Omega. 5 (2020) 3073–3079.
[179] N. Li, Q. Lang, H. Wang, G. Song, L. Liu, Scr. Mater. 227 (2023) 115278.
[180] D. Wang, H. Wang, H. Cui, G. He, J. Mater. Process. Technol. 237 (2016) 277–285.
[181] H. Xia, B. Yang, Y. Han, L. Xu, C. Tan, L. Li, H. Li, X. Zhao, K. Zhang, X. Su, P. Geng, N. Ma, J. Mater. Process. Technol. 325 (2024) 118294.
[182] Y. Mao, D. Qin, X. Xiao, X. Wang, L. Fu, Mater. Sci. Eng. A. 865 (2023) 144164.
[183] T. Zhang, Z. Hao, K. Wang, K. Qiao, K. Xue, Q. Liu, P. Han, W. Wang, P. Zheng, Int. J. Fatigue. 180 (2024) 108096.
[184] L. Zeng, L. Liu, S. Huang, L. Zhang, Calphad Comput. Coupling Phase Diagrams Thermochem. 58 (2017) 58–69.
[185] G. Cacciamani, J. De Keyzer, R. Ferro, U.E. Klotz, J. Lacaze, P. Wollants, Intermetallics. 14 (2006) 1312–1325.
[186] A.M. Van der Kraan, K.H.J. Buschow, Phys. B+C. 138 (1986) 55–62.
[187] F. Laves, H.J. Wallbaum, Zeitschrift Für Krist. - Cryst. Mater. 101 (1939) 78–93.
[188] T. V Philip, P.A. Beck, JOM. 9 (1957) 1269–1271.
[189] C. Zhao, R. Xin, F. Ren, Metall. Mater. Trans. A Phys. Metall. Mater. Sci. 50 (2019) 5640–5649.
[190] S.H. Oh, Y. Kauffmann, C. Scheu, W.D. Kaplan, M. Rühle, Science (80-.). 310 (2005) 661–663.

[191] M. Easton, D. Stjohn, Metall. Mater. Trans. A Phys. Metall. Mater. Sci. 30 (1999) 1613–1623.
[192] C. Gao, O. Brandt, S.C. Erwin, J. Lähnemann, U. Jahn, B. Jenichen, H.P. Schönherr, Phys. Rev. B - Condens. Matter Mater. Phys. 82 (2010) 1–5.
[193] F.C. Frank, J.H. Van Der Merwe, Proc. R. Soc. London. Ser. A. (1947) 216–225.
[194] Z. Fan, Metall. Mater. Trans. A Phys. Metall. Mater. Sci. 44 (2013) 1409–1418.
[195] J.W. Cahn, Acta Metall. 10 (1962) 179–183.
[196] D. Hull, D.J. Bacon, Introduction to dislocations, 3rd ed., Pergamon Press, Oxford [Oxfordshire] ;, 1984.
[197] M.X. Zhang, P.M. Kelly, M. Qian, J.A. Taylor, Acta Mater. 53 (2005) 3261–3270.
[198] P.M. Kelly, M.-X. Zhang, Metall. Mater. Trans. A. 37 (2006) 833–839.
[199] R.D. Doherty, D.A. Hughes, F.J. Humphreys, J.J. Jonas, D. Juul Jensen, M.E. Kassner, W.E. King, T.R. McNelley, H.J. McQueen, A.D. Rollett, Mater. Sci. Eng. A. 238 (1997) 219–274.
[200] R.L. Barto, L.J. Ebert, Metall. Trans. 2 (1971) 1643–1649.
[201] F. Liu, X. Zhou, X. Chen, X. Gong, L. Wu, B. Chen, K. Chen, C. Tan, Opt. Laser Technol. 151 (2022) 108024.
[202] S. Geng, P. Jiang, X. Shao, L. Guo, X. Gao, J. Mater. Sci. Technol. 46 (2020) 50–63.
[203] F. Cheng, L. Hu, J.N. Reddy, I. Karaman, E. Hoffman, M. Radovic, Acta Mater. 68 (2014) 267–278.
[204] P. Ternik, M. Zadravec, R. Rudolf, Sci. Sinter. 49 (2017) 39–49.
[205] C. Zanotti, P. Giuliani, P. Bassani, Z. Zhang, A. Chrysanthou, Intermetallics. 18 (2010) 14–21.
[206] C. Zanotti, P. Giuliani, A. Chrysanthou, Intermetallics. 24 (2012) 106–114.
[207] J.B. Haskins, J.W. Lawson, J. Appl. Phys. 121 (2017) 205103.
[208] F. Yu, Y. Liu, Computation. 7 (2019) 57.
[209] S. Gao, F. Weng, O.P. Bodunde, M. Qin, W.H. Liao, P. Guo, J. Manuf. Process. 71 (2021) 417–428.
[210] Y.F. Li, S.L. Tang, Y.M. Gao, S.Q. Ma, Q.L. Zheng, Y.H. Cheng, Int. J. Mod. Phys. B. 31 (2017) 1–14.
[211] X. Huang, J. Nohava, B. Zhang, A.G. Ramirez, Int. J. Smart Nano Mater. 2 (2011) 39–49.
[212] M. Morakabati, M. Aboutalebi, S. Kheirandish, A. Karimi Taheri, S.M. Abbasi, Intermetallics. 19 (2011) 1399–1404.
[213] S.Y. Jiang, Y.Q. Zhang, Y.N. Zhao, Trans. Nonferrous Met. Soc. China (English Ed. 23 (2013) 140–147.
[214] S. Singaravelu, J.M. Klopf, G. Krafft, M.J. Kelley, J. Vac. Sci. Technol. B, Nanotechnol. Microelectron. Mater. Process. Meas. Phenom. 29 (2011) 061803.
[215] H.-J.J. Lunk, H. Hartl, ChemTexts. 5 (2019) 15.
[216] M.S. Dias, J.R.L. de Mattos, URANIUM-ZIRCONIUM BASED ALLOYS Part I: Reference Points for Thermophysical Properties, in: 2015 Int. Nucl. Atl. Conf. - Ina. 2015, São Paulo, SP, Brazil, 2015. https://inis.iaea.org/records/fc5e3-9da04.
[217] D. Wang, X. Zhang, Z. Li, R. Bai, F. Wang, Procedia Eng. 27 (2012) 1233–1240.
[218] X. Ficquet, D.J. Smith, C.E. Truman, E.J. Kingston, R.J. Dennis, Int. J. Press. Vessel. Pip. 86 (2009) 20–30.
[219] A. Kiran, J. Hodek, J. Vavřík, M. Urbánek, J. Džugan, Materials (Basel). 13 (2020) 2666.
[220] P. Li, H. Dong, Y. Xia, X. Hao, S. Wang, L. Pan, J. Zhou, J. Manuf. Process. 33 (2018) 54–63.
[221] P. Lindström, Improved CWM platform for modelling welding procedures and their effects on structural behaviour, University West, 2015.
[222] S. Fukumoto, K. Fujiwara, S. Toji, A. Yamamoto, Mater. Sci. Eng. A. 492 (2008) 243–249.

[223] D. Pfoertsch, C. Ruud, CDD Grant-in-Aid, ICDD index No 33-0397, Pennsylvania, USA, 1982.
[224] P. Villars, K. Cenzual, eds., (n.d.). https://materials.springer.com/isp/crystallographic/docs/sd_1215974.
[225] P. Villars, K. Cenzual, eds., (n.d.). https://materials.springer.com/isp/crystallographic/docs/sd_0530352.
[226] H.M. Ledbetter, J. Appl. Phys. 52 (1981) 1587–1589.
[227] M. Fukuhara, A. Sanpei, Isij Int. 33 (1993) 508–512.
[228] H.M. Ledbetter, Met. Sci. 14 (1980) 595–596.

Appendix A: FVM simulation setup of NiTi-SS laser welding in Chapter 3

The FVM simulation setup in Chapter 3 is given as follows. The related governing equations can be found in the published paper [201]. The heat input from laser irradiation was achieved by adopting a cone-shaped volumetric heat source model, as seen in equation A-1, which could be adjusted to change the defocused distance and power density and has been used in the laser welding simulation [202].

$$q(r,z) = \frac{3\partial P ln(\gamma)}{\pi(1-e^{-3})(zi-ze)\left\{r_e^2-r_i^2\gamma-2\frac{ri-re}{\ln(\gamma)}\left[re-ri*\gamma-\frac{ri-re}{\ln(\gamma)}(1-\gamma)\right]\right\}}\exp\left(\frac{\ln(\gamma)}{zi-ze}(z-ze)\right)\exp\left(\frac{-3r^2}{r_0^2(z)}\right) \quad \text{(A-1)}$$

Where P is laser power, ∂ is the effective absorption coefficient, γ is a scaling factor, ze and re are the height coordinate and radius at the cone top surface respectively, zi and ri are the height coordinate and radius at the cone bottom surface respectively. In this work double cones with the vertex inside of metals were used for negative defocus while the single cone with vertex above metals surface was adopted for positive defocus. Fig. A1 shows the mesh generation with the dimension of 4×2×2 mm. Totally 607441 tetrahedral cells were generated in the solution domain. The region of NiTi-SS wires was 1 mm in diameter and 4 mm in length, which was surrounded by the air domain with room temperature and ambient pressure. The boundary condition of air domain was pressure outlet while the molten metals-air free surface were wall boundaries, except that the bottom side of metals were set as a fixed shape considering the fixture and stronger gas flow (pressure inlet) in actual situation.

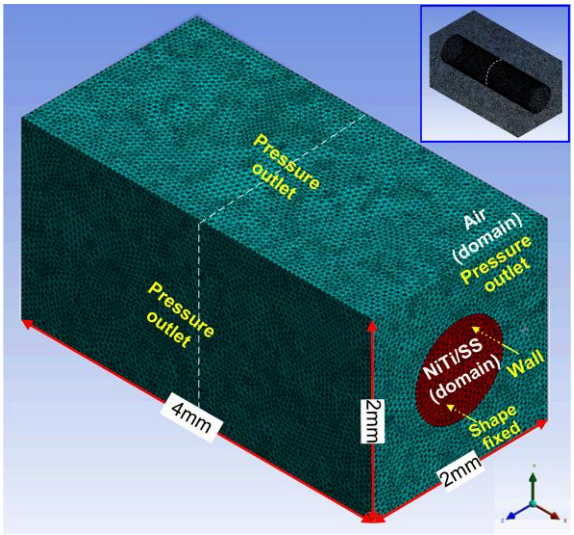


Fig. A1 The mesh for FVM simulation of NiTi-SS wires laser welding.

Appendix B: Supporting information of NiTi-SS RSW in Chapter 4

The FIB was performed by a Helios 5 DualBeam system (ThermoFisher Scientific). Fig. B1 shows the selected region of the Nb-SS TZ/Nb interface and the FIB thinning process.

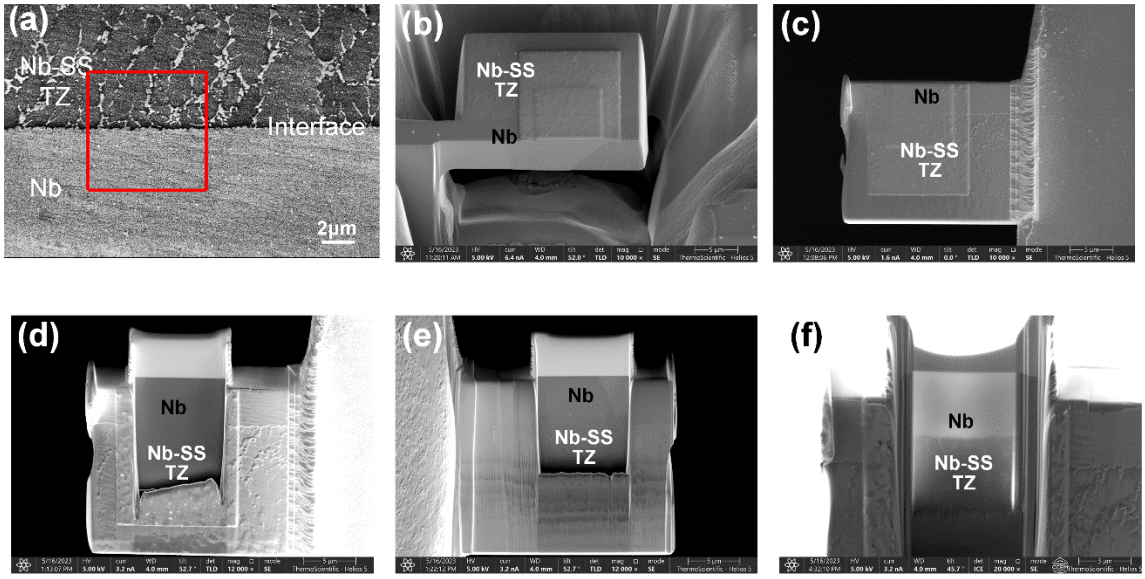


Fig. B1 (a) Selected region for the FIB and TEM (SEM high current mode, corresponding to the region in Fig. 4.3e); (b-f) FIB thinning process.

The FEM simulation was run in the weld zone of the Nb-interlayered joint, and the diameter of weld nugget and thicknesses of NiTi FZ and SS FZ were measured from OM/SEM/EBSD results. The detailed meshing and dimensions of simulated region are shown in Fig. B2. C3D8R-type hexahedral element was used. In total, 73788 nodes and 56454 elements were created in this model.

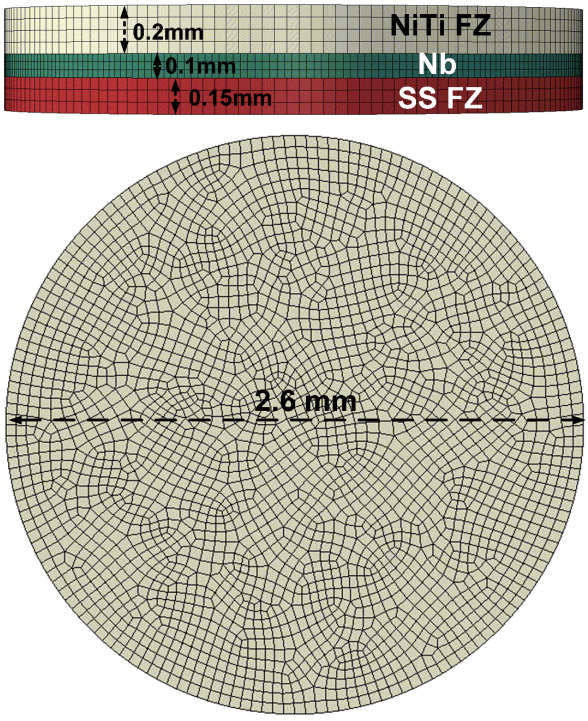


Fig. B2 Meshing and dimensions for the simulated region.

Temperature-dependent thermal conductivity, elastic property, thermal expansion coefficient and superelasticity/plasticity of NiTi were obtained or estimated from [203–206], [207–209] [207,210] and [150,211–213], respectively. Temperature-dependent thermal conductivity, elastic property, thermal expansion coefficient and plasticity of Nb were obtained or estimated from [214], [215], [216] and [217], respectively. Temperature-dependent thermal conductivity, elastic property, thermal expansion coefficient and plasticity of 316L SS were obtained or estimated from published papers [218–221]. The strain hardening of the materials was also considered.

As shown in Fig. B3, the NiTi FZ/Nb and Nb/SS FZ interfaces were treated with the tie constraints since they are welded. Considering the lower temperature and higher stiffness of the solid-state surrounding (especially considering the extremely high cooling rate of the RSW), the boundary conditions of all the outer surfaces of the simulated region were set as fixed. Based on the origin of weld residual stress, the simulation was run from ~ NiTi melting point (~1584 K) to ~room temperature, namely along the cooling process of the solid state [154]. A typical cooling rate ($2*10^5$K/s) of RSW of thin metallic sheets was used in this model [222].

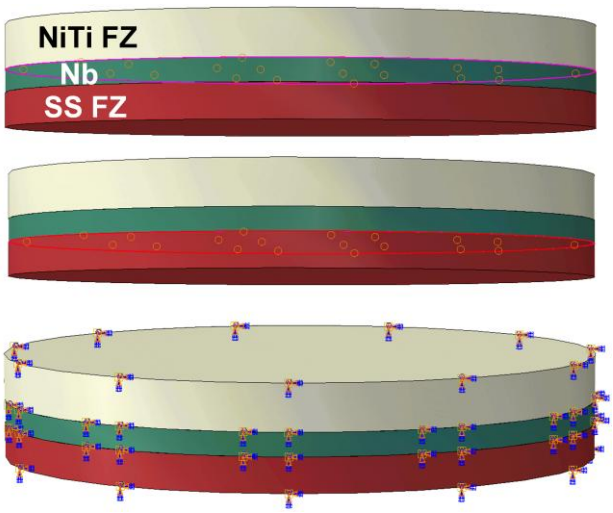


Fig. B3 Interface constraint and boundary conditions used in the modeling.

High energy SXRD allows us to infer on the stress state on non-destructive manner. The materials in the joint were mainly composed of three different phases, namely Fe-FCC, Nb-BCC and NiTi-B2. The diffraction peaks that were used for microstrain calculation corresponded to the (311) plane in the Fe-FCC case, and the (211) plane in the Nb-BCC and NiTi-B2 cases, due to their insensitivities to intergranular strains within the corresponding crystal structures, allowing them to represent the overall behavior of each phase. For the calculation of the lattice parameters in each analyzed position, fittings of the corresponding diffraction peaks were performed using a *Voight* profile via python-based scripts. It should be mentioned that the modeling of the data was only performed where peak intensity was sufficient to accurately perform the fitting process. Therefore, diffraction angle (θ_{hkl}) corresponding to the peak center could be determined. Based on the Bragg's law (equation B-1) and equation B-2, the lattice parameter a of the cubic crystal structure of each analyzed peak could be obtained. Then the microstrain could be calculated by equation B-3 [140].

$$\lambda = 2 \cdot d_{hkl} \cdot \sin(\theta_{hkl}) \tag{B-1}$$

$$\frac{1}{d^2_{hkl}} = \frac{h^2 + k^2 + l^2}{a^2} \tag{B-2}$$

$$\varepsilon = \frac{a - a_0}{a_0} \tag{B-3}$$

Where, λ is the X-ray beam wavelength; d is the interplanar spacing; h, k, l correspond to the miller indices of the analyzed peaks; a_0 corresponds to the lattice parameter in a stress-free condition, which was obtained from [223–225].

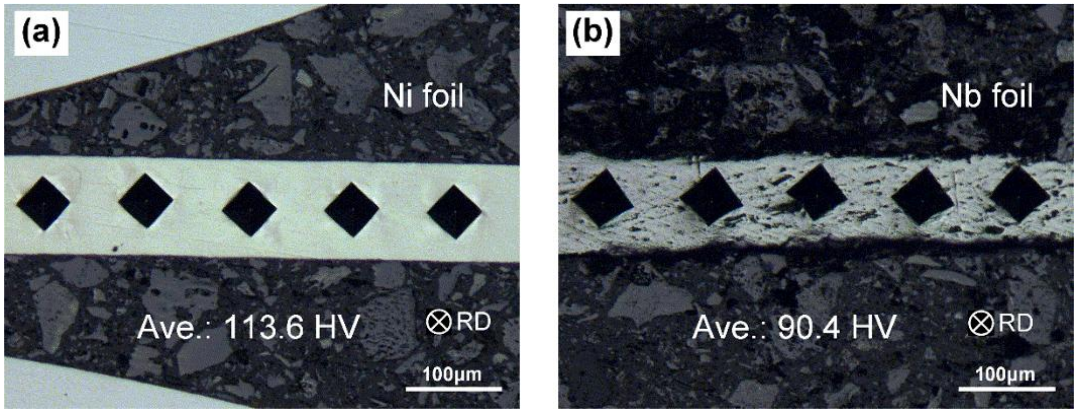


Fig. B4 OM morphologies of the hardness indents and the related average hardness for (a) Ni foil and (b) Nb foil, respectively.

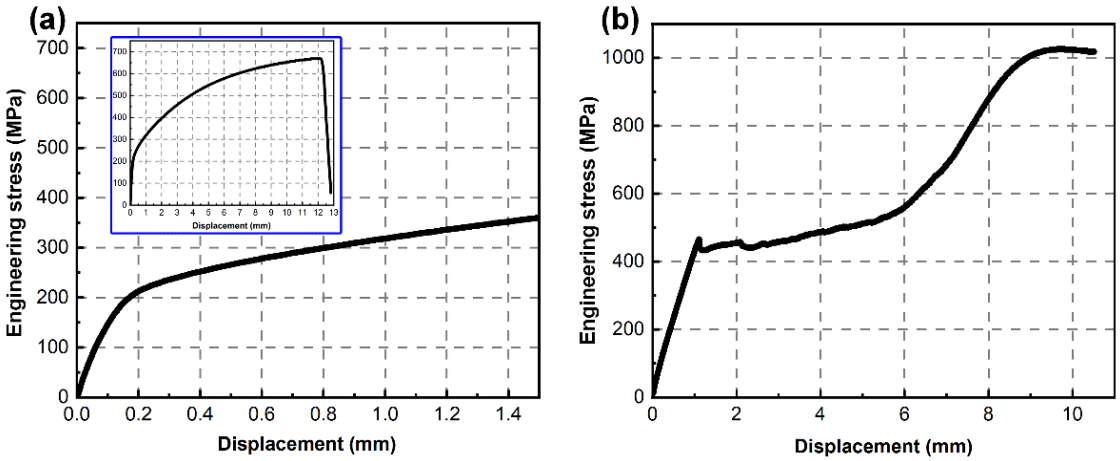


Fig. B5 Tensile curves of (a) SS BM and (b) NiTi BM.

Appendix C: Supporting information of NiTi-SS RMW in Chapter 5

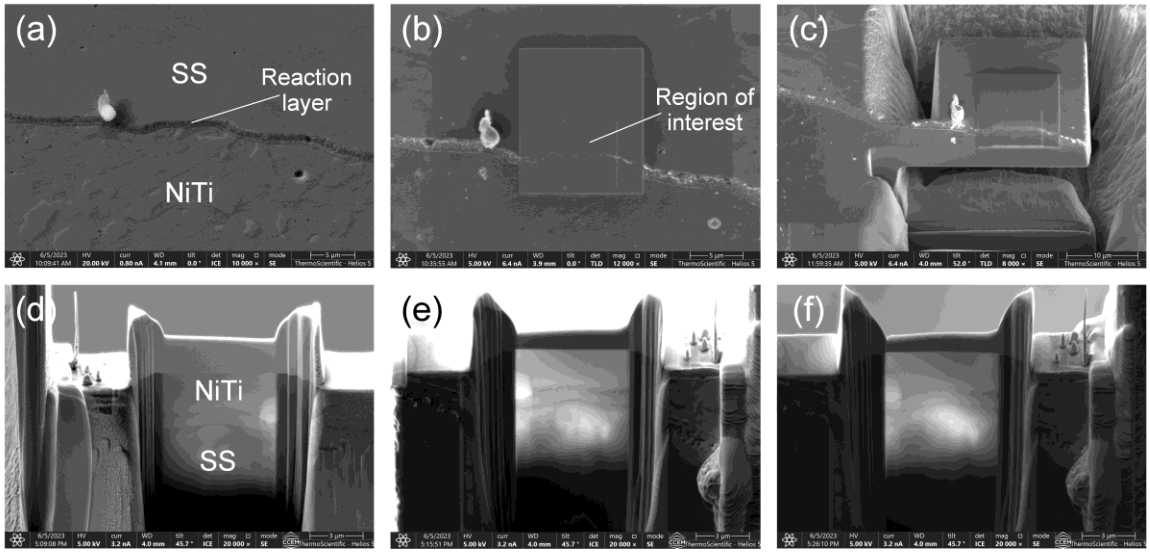


Fig. C1 (a) SEM image of the optimized NiTi-SS interface; (b) the region of interest for FIB TEM sample preparation; (c-f) FIB sample thinning process.

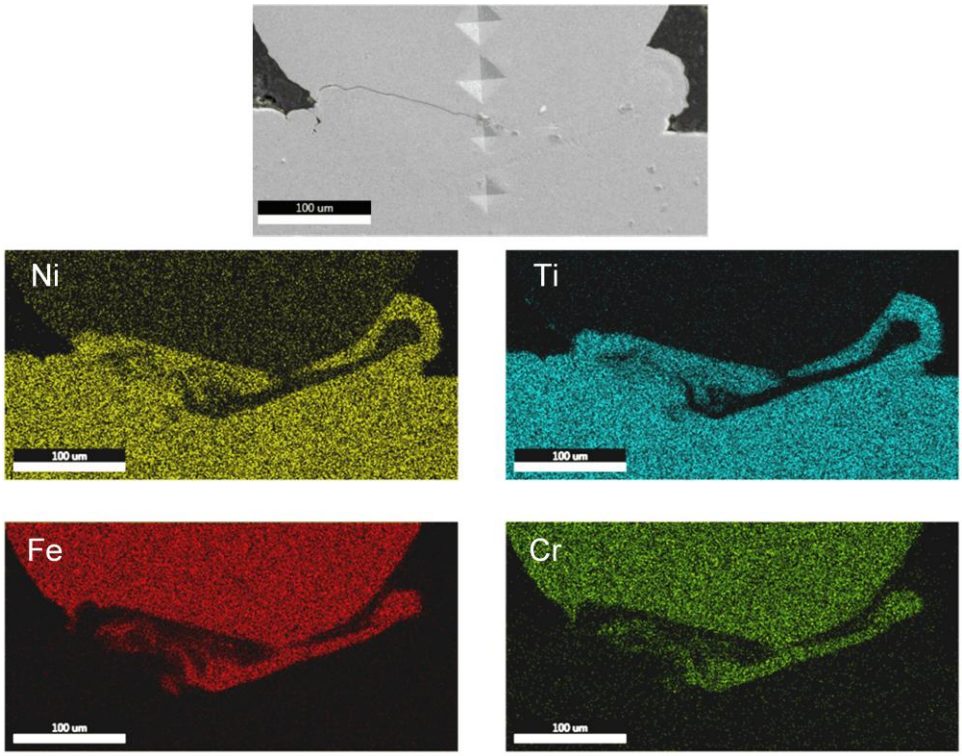


Fig. C2 SEM image of interfacial residual IMCs and the related EDS mapping results.

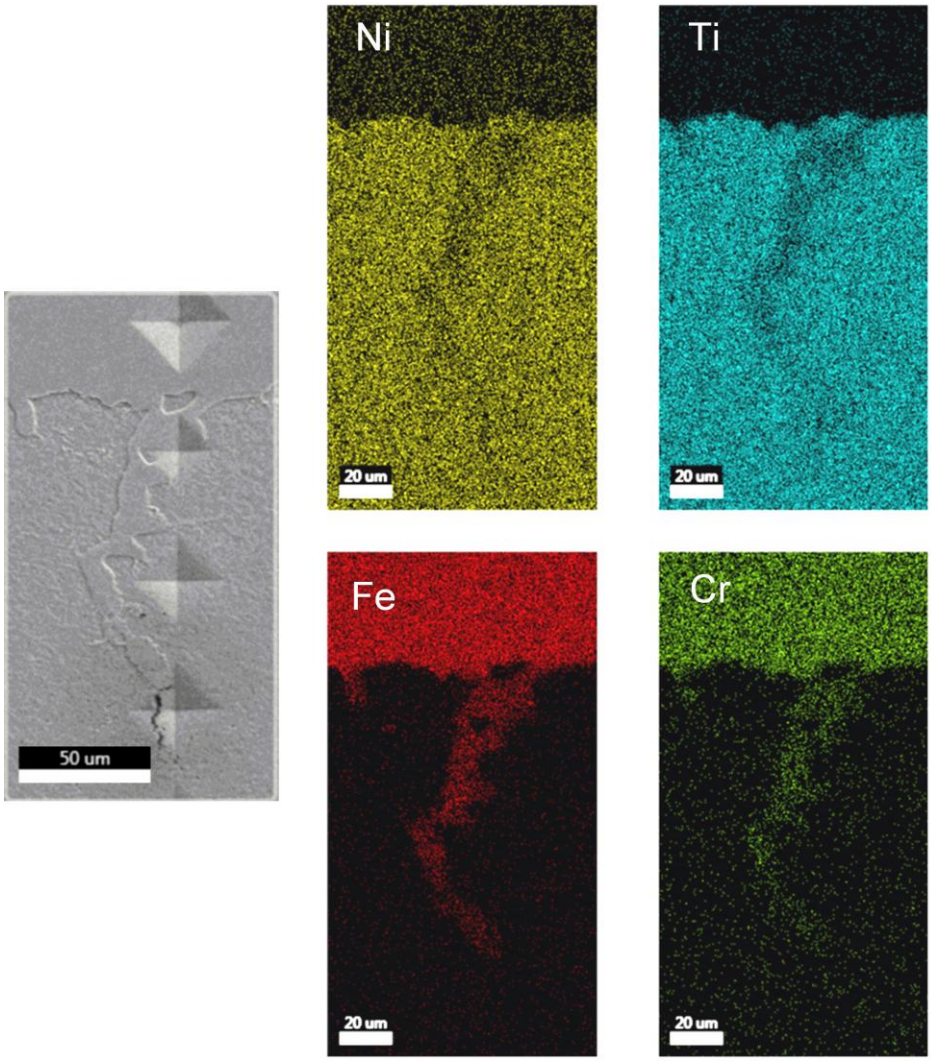


Fig. C3 SEM image of IMCs penetration and the related EDS mapping results.

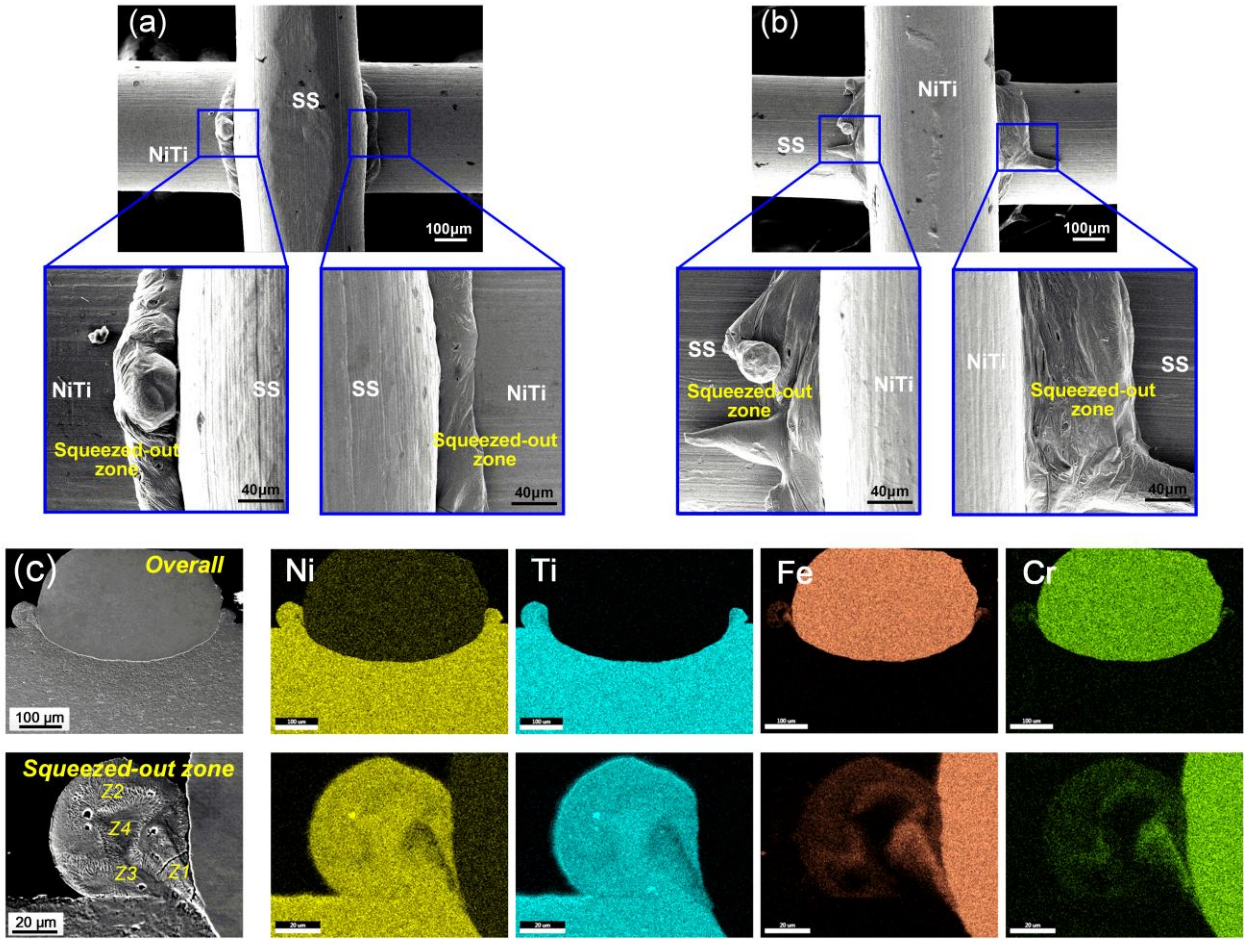


Fig. C4 SEM images of the optimized joint observed by placing (a) SS and (b) NiTi on the top, respectively; (c) SEM images and EDS mappings for the overall cross section and squeezed-out zone, respectively.

Table C1 EDS analysis (at.%) of different positions (Z1-Z4) marked in Fig. C4.

Position	Ni	Ti	Fe	Cr	Possible phase
Z1	25.3	21.1	41.2	Bal.	Thermodynamic calculation
Z2	36.6	33.3	23.5	Bal.	Thermodynamic calculation
Z3	44.2	38.1	14.4	Bal.	Thermodynamic calculation
Z4	48.4	49.0	1.3	Bal.	NiTi B2

Table C2 Phase mole fraction (%) of squeezed-out zone from thermodynamic calculation (300 K).

Region	C14_Laves	Ni_3Ti	B2	BCC_A2	BCC_A2#2
Fe-rich	40.20	30.53	--	16.28	12.21
Mixed	35.58	27.12	31.08	6.22	--
NiTi-rich	14.70	27.42	54.83	3.31	--

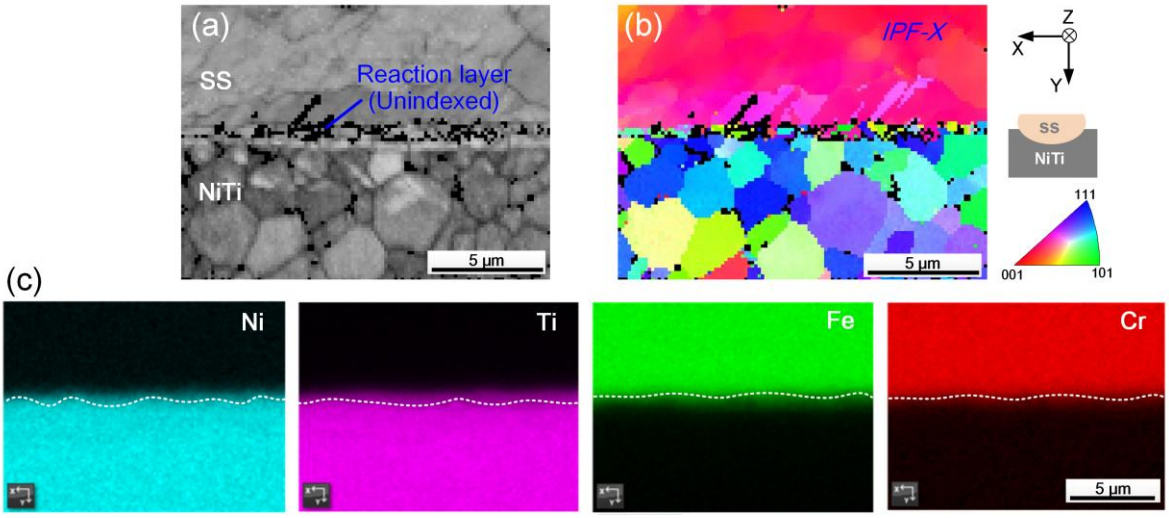


Fig. C5 (a) EBSD band contrast map, (b) EBSD IPF-X map and (c) EDS mapping results of the NiTi-SS RMWed interface (the reaction layer was difficult to be indexed by EBSD, due to its ultrafine thickness and grain size that are beyond the capacity of SEM).

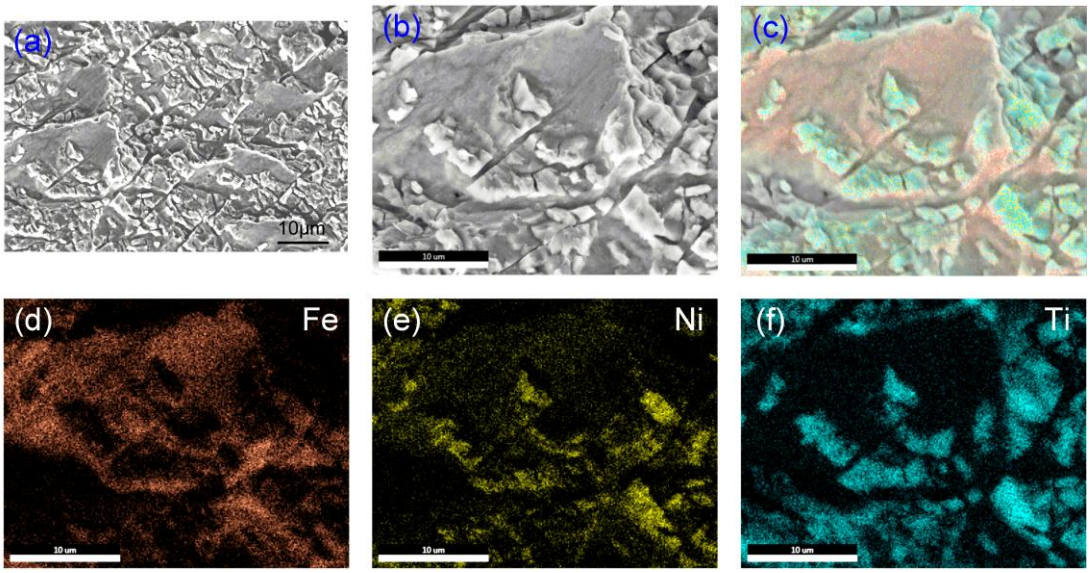


Fig. C6 (a,b) SEM images of fracture surface observed from SS side; (c-f) EDS mapping results.

Table C3 EDS analysis (at.%) of different positions marked in Fig. 5.7.

Position	Ni	Ti	Fe	Cr	Possible phase
1	51.9	47.7	0.3	Bal.	B2 NiTi
2	51.1	48.1	0.5	Bal.	B2 NiTi
3	23.0	22.7	43.6	Bal.	IMCs (Fe_2Ti+Ni_3Ti)
4	46.6	47.1	4.9	Bal.	B2 NiTi
5	14.0	7.9	60.6	Bal.	γ Fe
6	9.8	0.5	71.5	Bal.	γ Fe
7	48.2	29.7	17.5	Bal.	$(Ni,Fe)_3Ti$

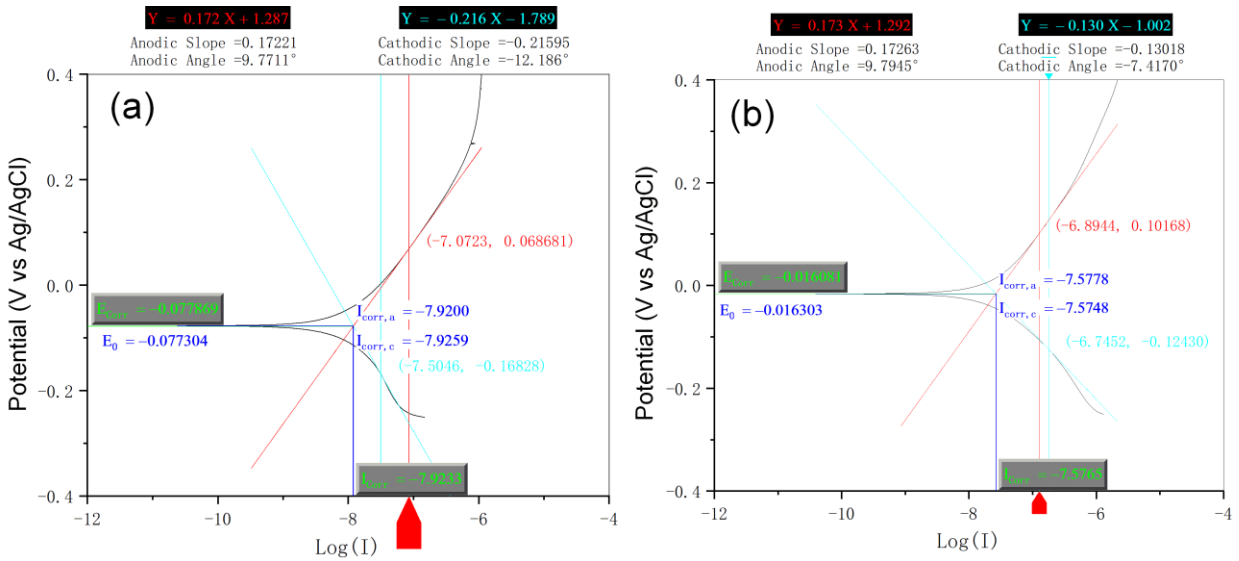


Fig. C7 Fitting results of PDP curves of (a) NiTi BM and (b) welded NiTi using Tafel extrapolation tool in Origin software.

Table C4 Data of NiTi BM and welded NiTi from OCP (Fig. 5.11a) and PDP curves (Fig. 5.11b) using Tafel extrapolation method.

Sample	OCP (V vs Ag/Ag/Cl)	E_{corr} (V vs Ag/Ag/Cl)	i_{corr} ($\mu A/cm^2$)	E_{pit} (V vs Ag/Ag/Cl)	Tafel slopes (cathode/anode) (V/dec)
NiTi BM	-0.048	-0.078	0.012	0.421	-0.216/0.172
Welded NiTi	0.028	-0.016	0.027	0.396	-0.130/0.173

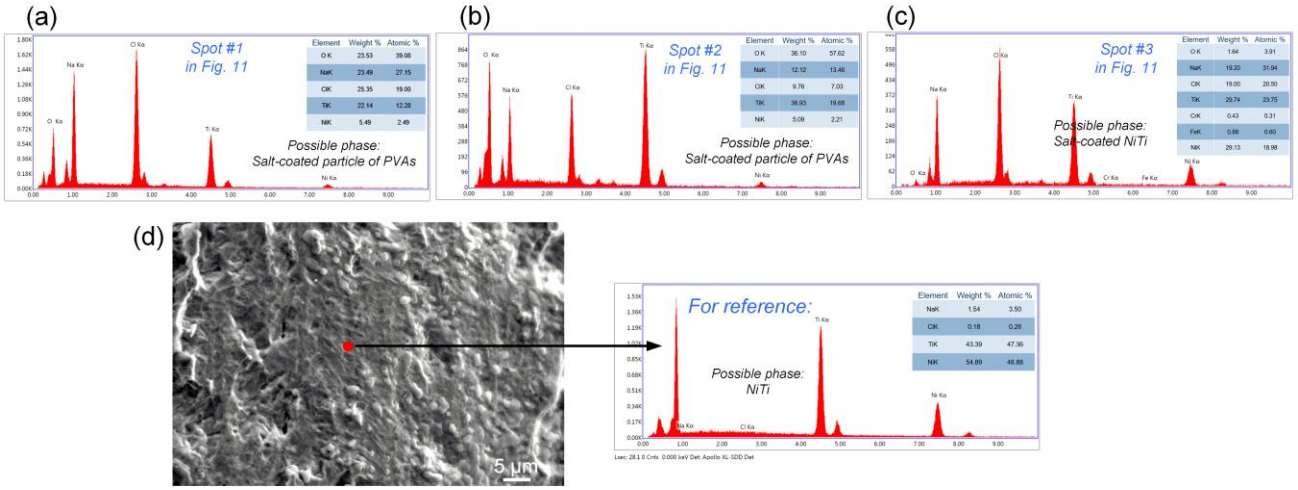


Fig. C8 (a-c) EDS results for spot 1, 2 and 3 as marked in Fig. 5.11d, e and h, respectively; (d) SEM image and EDS results of the selected NiTi area without deep pits after polarization.

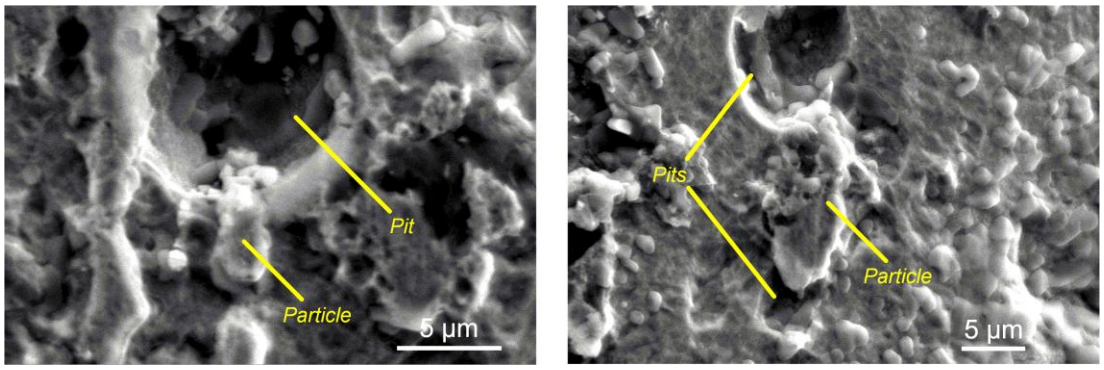


Fig. C9 Some other typical SEM images of particles with pits in NiTi BM after polarization.

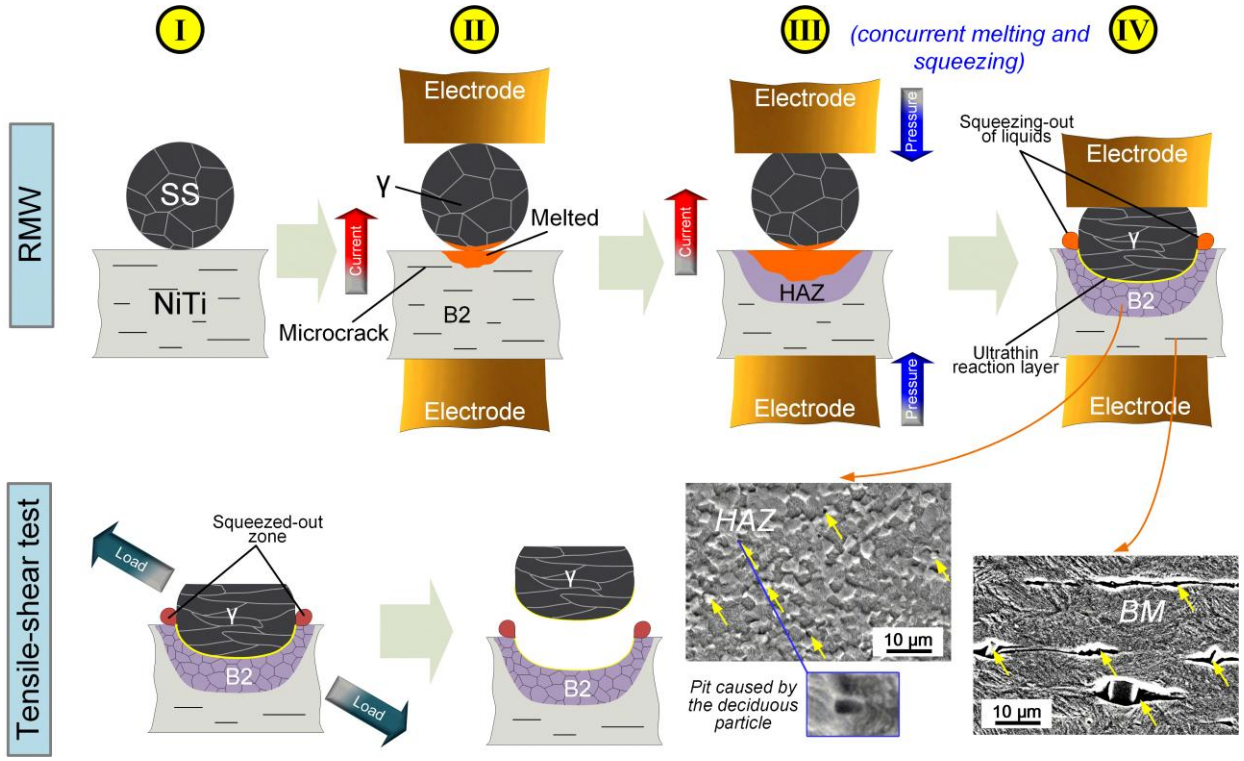


Fig. C10 Schematics showing joining formation of NiTi-SS during RMW and tensile-shear test of the joint, with SEM images showing NiTi HAZ and BM microstructures.

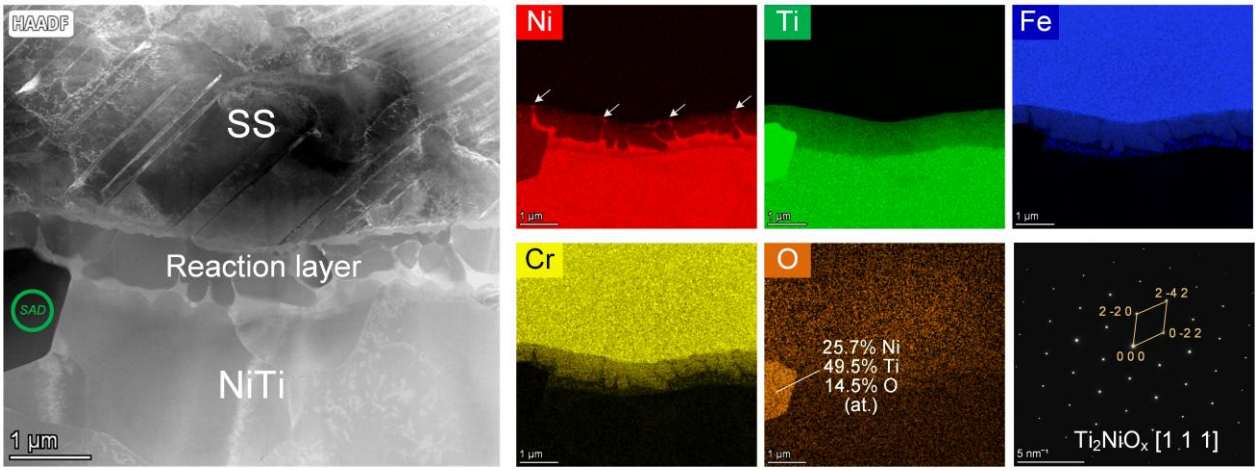


Fig. C11 STEM HAADF image of the NiTi-SS RMWed interface, with EDS mapping and SAD results.

Table C5 Related physical properties of the ROL layer for the h_c-f equation.

Symbol	Definition	Value	Unit	Ref.
μ	Shear modulus at room temperature	$7.52*10^{10}$	N/m^2	[226]
μ	Shear modulus at recrystallization temperature	$5.70*10^{10}$	N/m^2	[227]
G	Bulk modulus at room temperature	$1.58*10^{11}$	N/m^2	[228]
υ	Poisson's ratio at room temperature	0.294	--	[226]
υ	Poisson's ratio at recrystallization temperature	0.330	--	[227]
b	Burger's vector	$2.54*10^{-10}$	m	a

a. the Burger's vector along the close packed direction on the close packed plane (i.e., $b = a/\sqrt{2}$)

Appendix D: List of copyright permissions

Permissions to reuse the published figures or the author's articles in this thesis have been obtained. A copy of the first two pages of each permission letter is listed. A copy of the entire document will be provided upon request.

SAGE PUBLICATIONS LICENSE
TERMS AND CONDITIONS

Mar 09, 2025

This Agreement between Kaiping Zhang ("You") and Sage Publications ("Sage Publications") consists of your license details and the terms and conditions provided by Sage Publications and Copyright Clearance Center.

License Number	5984930292801
License date	Mar 09, 2025
Licensed Content Publisher	Sage Publications
Licensed Content Publication	Proceedings of the Institution of Mechanical Engineers, Part H: Journal of Engineering in Medicine
Licensed Content Title	Nitinol: From historical milestones to functional properties and biomedical applications
Licensed Content Author	Saeid Alipour, Farzaneh Taromian, Erfan Rezvani Ghomi, Mina Zare, et al.
Licensed Content Date	Nov 1, 2022
Licensed Content Volume	236
Licensed Content Issue	11
Licensed Content Pages	18
Type of Use	Dissertation/Thesis

Requestor type	I am NOT the author of the requested article
Format	Print and electronic
Portion	Figure/table
Number of figures/tables	1
Will you be translating?	No, only English
Circulation	1
Title of new work	Microstructure control and property enhancement of NiTi-stainless steel dissimilar joints
Institution name	University of Waterloo
Expected presentation date	Feb 2026
Portions	Fig. 1
The Requesting Person / Organization to Appear on the License	Kaiping Zhang
Requestor Location	Dr. Kaiping Zhang 706-4, 254 Phillip St Waterloo, ON N2L 0E1 Canada
Publisher Tax ID	12978 6448 RT
Billing Type	Invoice
Billing Address	University of Waterloo 706-4, 254 Phillip St

ELSEVIER LICENSE
TERMS AND CONDITIONS

Mar 09, 2025

This Agreement between Kaiping Zhang ("You") and Elsevier ("Elsevier") consists of your license details and the terms and conditions provided by Elsevier and Copyright Clearance Center.

License Number	5984930449722
License date	Mar 09, 2025
Licensed Content Publisher	Elsevier
Licensed Content Publication	Applied Surface Science
Licensed Content Title	Self-assembled anodization of NiTi alloys for biomedical applications
Licensed Content Author	Ruiqiang Hang,Feilong Zhao,Xiaohong Yao,Bin Tang,Paul K. Chu
Licensed Content Date	Jul 1, 2020
Licensed Content Volume	517
Licensed Content Issue	n/a
Licensed Content Pages	1
Start Page	146118
End Page	0

Type of Use	reuse in a thesis/dissertation
Portion	figures/tables/illustrations
Number of figures/tables/illustrations	1
Format	both print and electronic
Are you the author of this Elsevier article?	No
Will you be translating?	No
Title of new work	Microstructure control and property enhancement of NiTi-stainless steel dissimilar joints
Institution name	University of Waterloo
Expected presentation date	Feb 2026
Portions	Fig. 1
The Requesting Person / Organization to Appear on the License	Kaiping Zhang
Requestor Location	Dr. Kaiping Zhang 706-4, 254 Phillip St Waterloo, ON N2L 0E1 Canada
Publisher Tax ID	GB 494 6272 12
Total	0.00 USD
Terms and Conditions	

ELSEVIER LICENSE
TERMS AND CONDITIONS

Mar 09, 2025

This Agreement between Kaiping Zhang ("You") and Elsevier ("Elsevier") consists of your license details and the terms and conditions provided by Elsevier and Copyright Clearance Center.

License Number	5984930539648
License date	Mar 09, 2025
Licensed Content Publisher	Elsevier
Licensed Content Publication	Progress in Materials Science
Licensed Content Title	Physical metallurgy of Ti–Ni-based shape memory alloys
Licensed Content Author	K. Otsuka,X. Ren
Licensed Content Date	Jul 1, 2005
Licensed Content Volume	50
Licensed Content Issue	5
Licensed Content Pages	168
Start Page	511
End Page	678

Type of Use	reuse in a thesis/dissertation
Portion	figures/tables/illustrations
Number of figures/tables/illustrations	1
Format	both print and electronic
Are you the author of this Elsevier article?	No
Will you be translating?	No
Title of new work	Microstructure control and property enhancement of NiTi-stainless steel dissimilar joints
Institution name	University of Waterloo
Expected presentation date	Feb 2026
Portions	Fig. 2
The Requesting Person / Organization to Appear on the License	Kaiping Zhang
Requestor Location	Dr. Kaiping Zhang 706-4, 254 Phillip St Waterloo, ON N2L 0E1 Canada
Publisher Tax ID	GB 494 6272 12
Total	0.00 USD
Terms and Conditions	

ELSEVIER LICENSE
TERMS AND CONDITIONS

Mar 09, 2025

This Agreement between Kaiping Zhang ("You") and Elsevier ("Elsevier") consists of your license details and the terms and conditions provided by Elsevier and Copyright Clearance Center.

License Number	5984930682201
License date	Mar 09, 2025
Licensed Content Publisher	Elsevier
Licensed Content Publication	Materials Science and Engineering: A
Licensed Content Title	Microstructure and mechanical properties of an austenite NiTi shape memory alloy treated with laser induced shock
Licensed Content Author	Xi Wang,Weiguang Xia,Xianqian Wu,Yanpeng Wei,Chenguang Huang
Licensed Content Date	Aug 20, 2013
Licensed Content Volume	578
Licensed Content Issue	n/a
Licensed Content Pages	5
Start Page	1
End Page	5

Type of Use	reuse in a thesis/dissertation
Portion	figures/tables/illustrations
Number of figures/tables/illustrations	1
Format	both print and electronic
Are you the author of this Elsevier article?	No
Will you be translating?	No
Title of new work	Microstructure control and property enhancement of NiTi-stainless steel dissimilar joints
Institution name	University of Waterloo
Expected presentation date	Feb 2026
Portions	Fig. 1a
The Requesting Person / Organization to Appear on the License	Kaiping Zhang
Requestor Location	Dr. Kaiping Zhang 706-4, 254 Phillip St Waterloo, ON N2L 0E1 Canada
Publisher Tax ID	GB 494 6272 12
Total	0.00 USD
Terms and Conditions	

SPRINGER NATURE LICENSE
TERMS AND CONDITIONS

Mar 09, 2025

This Agreement between Kaiping Zhang ("You") and Springer Nature ("Springer Nature") consists of your license details and the terms and conditions provided by Springer Nature and Copyright Clearance Center.

License Number	5984930776131
License date	Mar 09, 2025
Licensed Content Publisher	Springer Nature
Licensed Content Publication	Shape Memory and Superelasticity
Licensed Content Title	B2 ⇒ B19′ ⇒ B2T Martensitic Transformation as a Mechanism of Plastic Deformation of NiTi
Licensed Content Author	P. Šittner et al
Licensed Content Date	Nov 27, 2019
Type of Use	Thesis/Dissertation
Requestor type	academic/university or research institute
Format	print and electronic
Portion	figures/tables/illustrations
Number of figures/tables/illustrations	1

Will you be translating?	no
Circulation/distribution	1 - 29
Author of this Springer Nature content	no
Title of new work	Microstructure control and property enhancement of NiTi-stainless steel dissimilar joints
Institution name	University of Waterloo
Expected presentation date	Feb 2026
Portions	Fig. 3a
The Requesting Person / Organization to Appear on the License	Kaiping Zhang
Requestor Location	Dr. Kaiping Zhang 706-4, 254 Phillip St Waterloo, ON N2L 0E1 Canada
Billing Type	Invoice
Billing Address	University of Waterloo 706-4, 254 Phillip St Waterloo, ON N2L 0E1 Canada
Total	0.00 USD
Terms and Conditions	

Springer Nature Customer Service Centre GmbH Terms and Conditions

ELSEVIER LICENSE
TERMS AND CONDITIONS

Mar 09, 2025

This Agreement between Kaiping Zhang ("You") and Elsevier ("Elsevier") consists of your license details and the terms and conditions provided by Elsevier and Copyright Clearance Center.

License Number	5984930901904
License date	Mar 09, 2025
Licensed Content Publisher	Elsevier
Licensed Content Publication	Applied Materials Today
Licensed Content Title	In-situ high energy X-ray diffraction study of microscopic deformation behavior of martensite variant reorientation in NiTi wire
Licensed Content Author	Xiangguang Kong,Ying Yang,Zhen Sun,Hong Yang,Yinong Liu,Yang Ren,Lishan Cui,Changfeng Chen,Shijie Hao
Licensed Content Date	Mar 1, 2021
Licensed Content Volume	22
Licensed Content Issue	n/a
Licensed Content Pages	1
Start Page	100904

End Page	0
Type of Use	reuse in a thesis/dissertation
Portion	figures/tables/illustrations
Number of figures/tables/illustrations	1
Format	both print and electronic
Are you the author of this Elsevier article?	No
Will you be translating?	No
Title of new work	Microstructure control and property enhancement of NiTi-stainless steel dissimilar joints
Institution name	University of Waterloo
Expected presentation date	Feb 2026
Portions	Fig. 3c
The Requesting Person / Organization to Appear on the License	Kaiping Zhang
Requestor Location	Dr. Kaiping Zhang 706-4, 254 Phillip St Waterloo, ON N2L 0E1 Canada
Publisher Tax ID	GB 494 6272 12
Total	0.00 USD

ELSEVIER LICENSE
TERMS AND CONDITIONS

Mar 09, 2025

This Agreement between Kaiping Zhang ("You") and Elsevier ("Elsevier") consists of your license details and the terms and conditions provided by Elsevier and Copyright Clearance Center.

License Number	5984930991784
License date	Mar 09, 2025
Licensed Content Publisher	Elsevier
Licensed Content Publication	Journal of Manufacturing Processes
Licensed Content Title	Towards applications, processing and advancements in shape memory alloy and its composites
Licensed Content Author	Namrata Gangil,Arshad Noor Siddiquee,Sachin Maheshwari
Licensed Content Date	Nov 1, 2020
Licensed Content Volume	59
Licensed Content Issue	n/a
Licensed Content Pages	18
Start Page	205
End Page	222

Type of Use	reuse in a thesis/dissertation
Portion	figures/tables/illustrations
Number of figures/tables/illustrations	1
Format	both print and electronic
Are you the author of this Elsevier article?	No
Will you be translating?	No
Title of new work	Microstructure control and property enhancement of NiTi-stainless steel dissimilar joints
Institution name	University of Waterloo
Expected presentation date	Feb 2026
Portions	Fig. 3
The Requesting Person / Organization to Appear on the License	Kaiping Zhang
Requestor Location	Dr. Kaiping Zhang 706-4, 254 Phillip St Waterloo, ON N2L 0E1 Canada
Publisher Tax ID	GB 494 6272 12
Total	0.00 USD
Terms and Conditions	

ELSEVIER LICENSE
TERMS AND CONDITIONS

Mar 09, 2025

This Agreement between Kaiping Zhang ("You") and Elsevier ("Elsevier") consists of your license details and the terms and conditions provided by Elsevier and Copyright Clearance Center.

License Number	5984931071048
License date	Mar 09, 2025
Licensed Content Publisher	Elsevier
Licensed Content Publication	Scripta Metallurgica
Licensed Content Title	Transformation pseudoelasticity and deformation behavior in a Ti-50.6at%Ni alloy
Licensed Content Author	S. Miyazaki,K. Otsuka,Y. Suzuki
Licensed Content Date	Mar 1, 1981
Licensed Content Volume	15
Licensed Content Issue	3
Licensed Content Pages	6
Start Page	287
End Page	292

Type of Use	reuse in a thesis/dissertation
Portion	figures/tables/illustrations
Number of figures/tables/illustrations	1
Format	both print and electronic
Are you the author of this Elsevier article?	No
Will you be translating?	No
Title of new work	Microstructure control and property enhancement of NiTi-stainless steel dissimilar joints
Institution name	University of Waterloo
Expected presentation date	Feb 2026
Portions	Fig. 1
The Requesting Person / Organization to Appear on the License	Kaiping Zhang
Requestor Location	Dr. Kaiping Zhang 706-4, 254 Phillip St Waterloo, ON N2L 0E1 Canada
Publisher Tax ID	GB 494 6272 12
Total	0.00 USD
Terms and Conditions	

ELSEVIER LICENSE
TERMS AND CONDITIONS

Mar 09, 2025

This Agreement between Kaiping Zhang ("You") and Elsevier ("Elsevier") consists of your license details and the terms and conditions provided by Elsevier and Copyright Clearance Center.

License Number	5984931155205
License date	Mar 09, 2025
Licensed Content Publisher	Elsevier
Licensed Content Publication	Acta Materialia
Licensed Content Title	Improved elastocaloric cooling performance in gradient-structured NiTi alloy processed by localized laser surface annealing
Licensed Content Author	Junyu Chen,Leilei Xing,Gang Fang,Liping Lei,Wei Liu
Licensed Content Date	Apr 15, 2021
Licensed Content Volume	208
Licensed Content Issue	n/a
Licensed Content Pages	1
Start Page	116741
End Page	0

Type of Use	reuse in a thesis/dissertation
Portion	figures/tables/illustrations
Number of figures/tables/illustrations	3
Format	both print and electronic
Are you the author of this Elsevier article?	No
Will you be translating?	No
Title of new work	Microstructure control and property enhancement of NiTi-stainless steel dissimilar joints
Institution name	University of Waterloo
Expected presentation date	Feb 2026
Portions	Fig. 4 a and d, Fig. 5b
The Requesting Person / Organization to Appear on the License	Kaiping Zhang
Requestor Location	Dr. Kaiping Zhang 706-4, 254 Phillip St Waterloo, ON N2L 0E1 Canada
Publisher Tax ID	GB 494 6272 12
Total	0.00 USD
Terms and Conditions	

ELSEVIER LICENSE
TERMS AND CONDITIONS

Mar 09, 2025

This Agreement between Kaiping Zhang ("You") and Elsevier ("Elsevier") consists of your license details and the terms and conditions provided by Elsevier and Copyright Clearance Center.

License Number	5984931228556
License date	Mar 09, 2025
Licensed Content Publisher	Elsevier
Licensed Content Publication	Materials Science and Engineering: A
Licensed Content Title	Microstructures generated in AISI 316L stainless steel by Vickers and Berkovich indentations
Licensed Content Author	Daria Grabco,Olga Shikimaka,Constantin Pyrtsac,Andrian Prisacaru,Zinaida Barbos,Mihaela Bivol,Sergei Alexandrov,Dragisha Vilotic,Marko Vilotic
Licensed Content Date	Feb 23, 2021
Licensed Content Volume	805
Licensed Content Issue	n/a
Licensed Content Pages	1
Start Page	140597

End Page	0
Type of Use	reuse in a thesis/dissertation
Portion	figures/tables/illustrations
Number of figures/tables/illustrations	2
Format	both print and electronic
Are you the author of this Elsevier article?	No
Will you be translating?	No
Title of new work	Microstructure control and property enhancement of NiTi-stainless steel dissimilar joints
Institution name	University of Waterloo
Expected presentation date	Feb 2026
Portions	Fig. 1 and Fig. 2
The Requesting Person / Organization to Appear on the License	Kaiping Zhang
Requestor Location	Dr. Kaiping Zhang 706-4, 254 Phillip St Waterloo, ON N2L 0E1 Canada
Publisher Tax ID	GB 494 6272 12
Total	0.00 USD

ELSEVIER LICENSE
TERMS AND CONDITIONS

Mar 09, 2025

This Agreement between Kaiping Zhang ("You") and Elsevier ("Elsevier") consists of your license details and the terms and conditions provided by Elsevier and Copyright Clearance Center.

License Number	5984931337924
License date	Mar 09, 2025
Licensed Content Publisher	Elsevier
Licensed Content Publication	Vacuum
Licensed Content Title	An assessment of microstructure and mechanical properties of inconel 601/ 304 stainless steel dissimilar weld
Licensed Content Author	Yahya Aghayar,AmirReza Naghashzadeh,Masoud Atapour
Licensed Content Date	Feb 1, 2021
Licensed Content Volume	184
Licensed Content Issue	n/a
Licensed Content Pages	1
Start Page	109970
End Page	0

Type of Use	reuse in a thesis/dissertation
Portion	figures/tables/illustrations
Number of figures/tables/illustrations	1
Format	both print and electronic
Are you the author of this Elsevier article?	No
Will you be translating?	No
Title of new work	Microstructure control and property enhancement of NiTi-stainless steel dissimilar joints
Institution name	University of Waterloo
Expected presentation date	Feb 2026
Portions	Fig. 2a
The Requesting Person / Organization to Appear on the License	Kaiping Zhang
Requestor Location	Dr. Kaiping Zhang 706-4, 254 Phillip St Waterloo, ON N2L 0E1 Canada
Publisher Tax ID	GB 494 6272 12
Total	0.00 USD
Terms and Conditions	

SAGE PUBLICATIONS LICENSE
TERMS AND CONDITIONS

Mar 09, 2025

This Agreement between Kaiping Zhang ("You") and Sage Publications ("Sage Publications") consists of your license details and the terms and conditions provided by Sage Publications and Copyright Clearance Center.

License Number	5984931420484
License date	Mar 09, 2025
Licensed Content Publisher	Sage Publications
Licensed Content Publication	Science and Technology of Welding and Joining
Licensed Content Title	Solidification behaviour of austenitic stainless steels during welding and directed energy deposition
Licensed Content Author	Syamak Hossein Nedjad, Mehmet Yildiz, Abdollah Saboori
Licensed Content Date	Jan 1, 2023
Licensed Content Volume	28
Licensed Content Issue	1
Licensed Content Pages	17
Type of Use	Dissertation/Thesis
Requestor type	I am NOT the author of the requested article

Format	Print and electronic
Portion	Figure/table
Number of figures/tables	1
Will you be translating?	No, only English
Circulation	1
Title of new work	Microstructure control and property enhancement of NiTi-stainless steel dissimilar joints
Institution name	University of Waterloo
Expected presentation date	Feb 2026
Portions	Fig.2
The Requesting Person / Organization to Appear on the License	Kaiping Zhang
Requestor Location	Dr. Kaiping Zhang 706-4, 254 Phillip St Waterloo, ON N2L 0E1 Canada
Publisher Tax ID	12978 6448 RT
Billing Type	Invoice

ELSEVIER LICENSE
TERMS AND CONDITIONS

Mar 09, 2025

This Agreement between Kaiping Zhang ("You") and Elsevier ("Elsevier") consists of your license details and the terms and conditions provided by Elsevier and Copyright Clearance Center.

License Number	5984940009837
License date	Mar 09, 2025
Licensed Content Publisher	Elsevier
Licensed Content Publication	Scripta Materialia
Licensed Content Title	Ion irradiation-induced precipitation of Cr23C6 at dislocation loops in austenitic steel
Licensed Content Author	Shuoxue Jin,Liping Guo,Fengfeng Luo,Zhongwen Yao,Shuli Ma,Rui Tang
Licensed Content Date	Jan 1, 2013
Licensed Content Volume	68
Licensed Content Issue	2
Licensed Content Pages	4
Start Page	138
End Page	141

Type of Use	reuse in a thesis/dissertation
Portion	figures/tables/illustrations
Number of figures/tables/illustrations	2
Format	both print and electronic
Are you the author of this Elsevier article?	No
Will you be translating?	No
Title of new work	Microstructure control and property enhancement of NiTi-stainless steel dissimilar joints
Institution name	University of Waterloo
Expected presentation date	Feb 2026
Portions	Fig. 2c and d
The Requesting Person / Organization to Appear on the License	Kaiping Zhang
Requestor Location	Dr. Kaiping Zhang 706-4, 254 Phillip St Waterloo, ON N2L 0E1 Canada
Publisher Tax ID	GB 494 6272 12
Total	0.00 USD
Terms and Conditions	

ELSEVIER LICENSE
TERMS AND CONDITIONS

Mar 09, 2025

This Agreement between Kaiping Zhang ("You") and Elsevier ("Elsevier") consists of your license details and the terms and conditions provided by Elsevier and Copyright Clearance Center.

License Number	5984940125831
License date	Mar 09, 2025
Licensed Content Publisher	Elsevier
Licensed Content Publication	Optics & Laser Technology
Licensed Content Title	Effect of heat input on interfacial microstructure, tensile and bending properties of dissimilar Al/steel lap joints by laser Welding-brazing
Licensed Content Author	Yang Jin,Su Jiahao,Gao Chenkai,Zhao Yixuan,Liu Hongbing,Joao Pedro Oliveira,Tan Caiwang,Yu Zhishui
Licensed Content Date	Oct 1, 2021
Licensed Content Volume	142
Licensed Content Issue	n/a
Licensed Content Pages	1
Start Page	107218

End Page	0
Type of Use	reuse in a thesis/dissertation
Portion	figures/tables/illustrations
Number of figures/tables/illustrations	4
Format	both print and electronic
Are you the author of this Elsevier article?	No
Will you be translating?	No
Title of new work	Microstructure control and property enhancement of NiTi-stainless steel dissimilar joints
Institution name	University of Waterloo
Expected presentation date	Feb 2026
Portions	Figs. 5f, 6b, 12d and 13d
The Requesting Person / Organization to Appear on the License	Kaiping Zhang
Requestor Location	Dr. Kaiping Zhang 706-4, 254 Phillip St Waterloo, ON N2L 0E1 Canada
Publisher Tax ID	GB 494 6272 12
Total	0.00 USD

ELSEVIER LICENSE
TERMS AND CONDITIONS

Mar 09, 2025

This Agreement between Kaiping Zhang ("You") and Elsevier ("Elsevier") consists of your license details and the terms and conditions provided by Elsevier and Copyright Clearance Center.

License Number	5984940207550
License date	Mar 09, 2025
Licensed Content Publisher	Elsevier
Licensed Content Publication	Acta Materialia
Licensed Content Title	Three-dimensional chemical analysis of laser-welded NiTi–stainless steel wires using a dual-beam FIB
Licensed Content Author	P. Burdet,J. Vannod,A. Hessler-Wyser,M. Rappaz,M. Cantoni
Licensed Content Date	May 1, 2013
Licensed Content Volume	61
Licensed Content Issue	8
Licensed Content Pages	9
Start Page	3090
End Page	3098

Type of Use	reuse in a thesis/dissertation
Portion	figures/tables/illustrations
Number of figures/tables/illustrations	3
Format	both print and electronic
Are you the author of this Elsevier article?	No
Will you be translating?	No
Title of new work	Microstructure control and property enhancement of NiTi-stainless steel dissimilar joints
Institution name	University of Waterloo
Expected presentation date	Feb 2026
Portions	Figs. 3, 8b and 12
The Requesting Person / Organization to Appear on the License	Kaiping Zhang
Requestor Location	Dr. Kaiping Zhang 706-4, 254 Phillip St Waterloo, ON N2L 0E1 Canada
Publisher Tax ID	GB 494 6272 12
Total	0.00 USD

Terms and Conditions

ELSEVIER LICENSE
TERMS AND CONDITIONS

Mar 10, 2025

This Agreement between Kaiping Zhang ("You") and Elsevier ("Elsevier") consists of your license details and the terms and conditions provided by Elsevier and Copyright Clearance Center.

License Number	5985470747730
License date	Mar 10, 2025
Licensed Content Publisher	Elsevier
Licensed Content Publication	Intermetallics
Licensed Content Title	Controlling intermetallic compounds formation during laser welding of NiTi to 316L stainless steel
Licensed Content Author	A. Shamsolhodaei,J.P. Oliveira,N. Schell,E. Maawad,B. Panton,Y.N. Zhou
Licensed Content Date	Jan 1, 2020
Licensed Content Volume	116
Licensed Content Issue	n/a
Licensed Content Pages	1
Start Page	106656
End Page	0

Type of Use	reuse in a thesis/dissertation
Portion	figures/tables/illustrations
Number of figures/tables/illustrations	10
Format	both print and electronic
Are you the author of this Elsevier article?	No
Will you be translating?	No
Title of new work	Microstructure control and property enhancement of NiTi-stainless steel dissimilar joints
Institution name	University of Waterloo
Expected presentation date	Feb 2026
Portions	Figs. 5a-c and g-i, 6a and c, 7a, and 9a
The Requesting Person / Organization to Appear on the License	Kaiping Zhang
Requestor Location	Dr. Kaiping Zhang 706-4, 254 Phillip St Waterloo, ON N2L 0E1 Canada
Publisher Tax ID	GB 494 6272 12
Total	0.00 USD

Terms and Conditions

ELSEVIER LICENSE
TERMS AND CONDITIONS

Mar 09, 2025

This Agreement between Kaiping Zhang ("You") and Elsevier ("Elsevier") consists of your license details and the terms and conditions provided by Elsevier and Copyright Clearance Center.

License Number	5984940382100
License date	Mar 09, 2025
Licensed Content Publisher	Elsevier
Licensed Content Publication	Journal of Materials Science & Technology
Licensed Content Title	Effect of interlayer addition on microstructure and mechanical properties of NiTi/stainless steel joint by electron beam welding
Licensed Content Author	H. Niu,H.C. Jiang,M.J. Zhao,L.J. Rong
Licensed Content Date	Jan 20, 2021
Licensed Content Volume	61
Licensed Content Issue	n/a
Licensed Content Pages	9
Start Page	16
End Page	24

Type of Use	reuse in a thesis/dissertation
Portion	figures/tables/illustrations
Number of figures/tables/illustrations	12
Format	both print and electronic
Are you the author of this Elsevier article?	No
Will you be translating?	No
Title of new work	Microstructure control and property enhancement of NiTi-stainless steel dissimilar joints
Institution name	University of Waterloo
Expected presentation date	Feb 2026
Portions	Fig.4, Fig. 5a, Fig. 11a and d-f, Fig. 6, Fig. 7
The Requesting Person / Organization to Appear on the License	Kaiping Zhang
Requestor Location	Dr. Kaiping Zhang 706-4, 254 Phillip St Waterloo, ON N2L 0E1 Canada
Publisher Tax ID	GB 494 6272 12
Total	0.00 USD

Terms and Conditions

ELSEVIER LICENSE
TERMS AND CONDITIONS

Mar 09, 2025

This Agreement between Kaiping Zhang ("You") and Elsevier ("Elsevier") consists of your license details and the terms and conditions provided by Elsevier and Copyright Clearance Center.

License Number	5984940468299
License date	Mar 09, 2025
Licensed Content Publisher	Elsevier
Licensed Content Publication	Journal of the Mechanical Behavior of Biomedical Materials
Licensed Content Title	The effect of annealing temperature on microstructure and mechanical properties of dissimilar laser welded superelastic NiTi to austenitic stainless steels orthodontic archwires
Licensed Content Author	Saeed Asadi,Tohid Saeid,Alireza Valanezhad,Ikuya Watanabe,Jafar Khalil-Allafi
Licensed Content Date	Sep 1, 2020
Licensed Content Volume	109
Licensed Content Issue	n/a
Licensed Content Pages	1
Start Page	103818

End Page	0
Type of Use	reuse in a thesis/dissertation
Portion	figures/tables/illustrations
Number of figures/tables/illustrations	2
Format	both print and electronic
Are you the author of this Elsevier article?	No
Will you be translating?	No
Title of new work	Microstructure control and property enhancement of NiTi-stainless steel dissimilar joints
Institution name	University of Waterloo
Expected presentation date	Feb 2026
Portions	Figs. 3and 11
The Requesting Person / Organization to Appear on the License	Kaiping Zhang
Requestor Location	Dr. Kaiping Zhang 706-4, 254 Phillip St Waterloo, ON N2L 0E1 Canada
Publisher Tax ID	GB 494 6272 12

SPRINGER NATURE LICENSE
TERMS AND CONDITIONS

Mar 09, 2025

This Agreement between Kaiping Zhang ("You") and Springer Nature ("Springer Nature") consists of your license details and the terms and conditions provided by Springer Nature and Copyright Clearance Center.

License Number	5984940544771
License date	Mar 09, 2025
Licensed Content Publisher	Springer Nature
Licensed Content Publication	The International Journal of Advanced Manufacturing Technology
Licensed Content Title	Dissimilar laser welding of NiTi to stainless steel
Licensed Content Author	J. Pouquet et al
Licensed Content Date	Oct 26, 2011
Type of Use	Thesis/Dissertation
Requestor type	academic/university or research institute
Format	print and electronic
Portion	figures/tables/illustrations
Number of figures/tables/illustrations	1

Will you be translating?	no
Circulation/distribution	1 - 29
Author of this Springer Nature content	no
Title of new work	Microstructure control and property enhancement of NiTi-stainless steel dissimilar joints
Institution name	University of Waterloo
Expected presentation date	Feb 2026
Portions	Fig. 4a
The Requesting Person / Organization to Appear on the License	Kaiping Zhang
Requestor Location	Dr. Kaiping Zhang 706-4, 254 Phillip St Waterloo, ON N2L 0E1 Canada
Billing Type	Invoice
Billing Address	University of Waterloo 706-4, 254 Phillip St Waterloo, ON N2L 0E1 Canada
Total	0.00 USD

Terms and Conditions

Springer Nature Customer Service Centre GmbH Terms and Conditions

ELSEVIER LICENSE
TERMS AND CONDITIONS

Mar 09, 2025

This Agreement between Kaiping Zhang ("You") and Elsevier ("Elsevier") consists of your license details and the terms and conditions provided by Elsevier and Copyright Clearance Center.

License Number	5984940633990
License date	Mar 09, 2025
Licensed Content Publisher	Elsevier
Licensed Content Publication	Acta Materialia
Licensed Content Title	Mechanical and microstructural integrity of nickel–titanium and stainless steel laser joined wires
Licensed Content Author	J. Vannod,M. Bornert,J.-E. Bidaux,L. Bataillard,A. Karimi,J.-M. Drezet,M. Rappaz,A. Hessler-Wyser
Licensed Content Date	Oct 1, 2011
Licensed Content Volume	59
Licensed Content Issue	17
Licensed Content Pages	9
Start Page	6538

End Page	6546
Type of Use	reuse in a thesis/dissertation
Portion	figures/tables/illustrations
Number of figures/tables/illustrations	6
Format	both print and electronic
Are you the author of this Elsevier article?	No
Will you be translating?	No
Title of new work	Microstructure control and property enhancement of NiTi-stainless steel dissimilar joints
Institution name	University of Waterloo
Expected presentation date	Feb 2026
Portions	Figs. 3a-d, 4 and 8
The Requesting Person / Organization to Appear on the License	Kaiping Zhang
Requestor Location	Dr. Kaiping Zhang 706-4, 254 Phillip St Waterloo, ON N2L 0E1 Canada
Publisher Tax ID	GB 494 6272 12
Total	0.00 USD

ELSEVIER LICENSE
TERMS AND CONDITIONS

Mar 09, 2025

This Agreement between Kaiping Zhang ("You") and Elsevier ("Elsevier") consists of your license details and the terms and conditions provided by Elsevier and Copyright Clearance Center.

License Number	5984940717244
License date	Mar 09, 2025
Licensed Content Publisher	Elsevier
Licensed Content Publication	Materials Chemistry and Physics
Licensed Content Title	Microstructural evaluation and mechanical behaviour of dissimilar niti-stainless steel joints welded by micro gas tungsten arc welding
Licensed Content Author	M.J.C. Oliveira,R.H.F. Melo,T.M. Maciel,C.J. de Araújo
Licensed Content Date	Feb 15, 2019
Licensed Content Volume	224
Licensed Content Issue	n/a
Licensed Content Pages	11
Start Page	137
End Page	147

Type of Use	reuse in a thesis/dissertation
Portion	figures/tables/illustrations
Number of figures/tables/illustrations	1
Format	both print and electronic
Are you the author of this Elsevier article?	No
Will you be translating?	No
Title of new work	Microstructure control and property enhancement of NiTi-stainless steel dissimilar joints
Institution name	University of Waterloo
Expected presentation date	Feb 2026
Portions	Fig. 8
The Requesting Person / Organization to Appear on the License	Kaiping Zhang
Requestor Location	Dr. Kaiping Zhang 706-4, 254 Phillip St Waterloo, ON N2L 0E1 Canada
Publisher Tax ID	GB 494 6272 12
Total	0.00 USD
Terms and Conditions	

ELSEVIER LICENSE
TERMS AND CONDITIONS

Mar 09, 2025

This Agreement between Kaiping Zhang ("You") and Elsevier ("Elsevier") consists of your license details and the terms and conditions provided by Elsevier and Copyright Clearance Center.

License Number	5984940794671
License date	Mar 09, 2025
Licensed Content Publisher	Elsevier
Licensed Content Publication	Optics & Laser Technology
Licensed Content Title	Laser welding of NiTi shape memory alloy: Comparison of the similar and dissimilar joints to AISI 304 stainless steel
Licensed Content Author	G.R. Mirshekari,A. Saatchi,A. Kermanpur,S.K. Sadrnezhaad
Licensed Content Date	Dec 30, 2013
Licensed Content Volume	54
Licensed Content Issue	n/a
Licensed Content Pages	8
Start Page	151
End Page	158

Type of Use	reuse in a thesis/dissertation
Portion	figures/tables/illustrations
Number of figures/tables/illustrations	2
Format	both print and electronic
Are you the author of this Elsevier article?	No
Will you be translating?	No
Title of new work	Microstructure control and property enhancement of NiTi-stainless steel dissimilar joints
Institution name	University of Waterloo
Expected presentation date	Feb 2026
Portions	Figs. 7b and 8b
The Requesting Person / Organization to Appear on the License	Kaiping Zhang
Requestor Location	Dr. Kaiping Zhang 706-4, 254 Phillip St Waterloo, ON N2L 0E1 Canada
Publisher Tax ID	GB 494 6272 12
Total	0.00 USD
Terms and Conditions	

ELSEVIER LICENSE
TERMS AND CONDITIONS

Mar 09, 2025

This Agreement between Kaiping Zhang ("You") and Elsevier ("Elsevier") consists of your license details and the terms and conditions provided by Elsevier and Copyright Clearance Center.

License Number	5984940869774
License date	Mar 09, 2025
Licensed Content Publisher	Elsevier
Licensed Content Publication	Journal of Materials Processing Technology
Licensed Content Title	Effect of Ta interlayer on laser welding of NiTi to AISI 316L stainless steel
Licensed Content Author	C.H. Ng,Edwin S.H. Mok,H.C. Man
Licensed Content Date	Dec 1, 2015
Licensed Content Volume	226
Licensed Content Issue	n/a
Licensed Content Pages	9
Start Page	69
End Page	77

Type of Use	reuse in a thesis/dissertation
Portion	figures/tables/illustrations
Number of figures/tables/illustrations	3
Format	both print and electronic
Are you the author of this Elsevier article?	No
Will you be translating?	No
Title of new work	Microstructure control and property enhancement of NiTi-stainless steel dissimilar joints
Institution name	University of Waterloo
Expected presentation date	Feb 2026
Portions	Figs. 6e, 7 and 9a
The Requesting Person / Organization to Appear on the License	Kaiping Zhang
Requestor Location	Dr. Kaiping Zhang 706-4, 254 Phillip St Waterloo, ON N2L 0E1 Canada
Publisher Tax ID	GB 494 6272 12
Total	0.00 USD
Terms and Conditions	

ELSEVIER LICENSE
TERMS AND CONDITIONS

Mar 09, 2025

This Agreement between Kaiping Zhang ("You") and Elsevier ("Elsevier") consists of your license details and the terms and conditions provided by Elsevier and Copyright Clearance Center.

License Number	5984940948031
License date	Mar 09, 2025
Licensed Content Publisher	Elsevier
Licensed Content Publication	Materials Science and Engineering: A
Licensed Content Title	Effects of post-weld heat treatment on the microstructure and mechanical properties of laser-welded NiTi/304SS joint with Ni filler
Licensed Content Author	Yuhua Chen,Songwei Sun,Timing Zhang,Xingwen Zhou,Shuhan Li
Licensed Content Date	Jan 13, 2020
Licensed Content Volume	771
Licensed Content Issue	n/a
Licensed Content Pages	1
Start Page	138545
End Page	0

Type of Use	reuse in a thesis/dissertation
Portion	figures/tables/illustrations
Number of figures/tables/illustrations	6
Format	both print and electronic
Are you the author of this Elsevier article?	No
Will you be translating?	No
Title of new work	Microstructure control and property enhancement of NiTi-stainless steel dissimilar joints
Institution name	University of Waterloo
Expected presentation date	Feb 2026
Portions	Figs. 5a-d, 7 and 8a
The Requesting Person / Organization to Appear on the License	Kaiping Zhang
Requestor Location	Dr. Kaiping Zhang 706-4, 254 Phillip St Waterloo, ON N2L 0E1 Canada
Publisher Tax ID	GB 494 6272 12
Total	0.00 USD
Terms and Conditions	

ELSEVIER LICENSE
TERMS AND CONDITIONS

Mar 09, 2025

This Agreement between Kaiping Zhang ("You") and Elsevier ("Elsevier") consists of your license details and the terms and conditions provided by Elsevier and Copyright Clearance Center.

License Number	5984941107957
License date	Mar 09, 2025
Licensed Content Publisher	Elsevier
Licensed Content Publication	Journal of Manufacturing Processes
Licensed Content Title	Microstructure and properties analysis of laser-welded Ni–Ti and 316l sheets using copper interlayer
Licensed Content Author	A. Shojaei Zoeram,A. Rahmani,S.A.A. Akbari Mousavi
Licensed Content Date	Apr 1, 2017
Licensed Content Volume	26
Licensed Content Issue	n/a
Licensed Content Pages	9
Start Page	355
End Page	363

Type of Use	reuse in a thesis/dissertation
Portion	figures/tables/illustrations
Number of figures/tables/illustrations	1
Format	both print and electronic
Are you the author of this Elsevier article?	No
Will you be translating?	No
Title of new work	Microstructure control and property enhancement of NiTi-stainless steel dissimilar joints
Institution name	University of Waterloo
Expected presentation date	Feb 2026
Portions	Fig. 8
The Requesting Person / Organization to Appear on the License	Kaiping Zhang
Requestor Location	Dr. Kaiping Zhang 706-4, 254 Phillip St Waterloo, ON N2L 0E1 Canada
Publisher Tax ID	GB 494 6272 12
Total	0.00 USD
Terms and Conditions	

ELSEVIER LICENSE
TERMS AND CONDITIONS

Mar 09, 2025

This Agreement between Kaiping Zhang ("You") and Elsevier ("Elsevier") consists of your license details and the terms and conditions provided by Elsevier and Copyright Clearance Center.

License Number	5984941184763
License date	Mar 09, 2025
Licensed Content Publisher	Elsevier
Licensed Content Publication	Optics & Laser Technology
Licensed Content Title	Laser welding of TiNi shape memory alloy and stainless steel using Co filler metal
Licensed Content Author	Hongmei Li,Daqian Sun,Xiaolong Cai,Peng Dong,Xiaoyan Gu
Licensed Content Date	Feb 1, 2013
Licensed Content Volume	45
Licensed Content Issue	n/a
Licensed Content Pages	8
Start Page	453
End Page	460

Type of Use	reuse in a thesis/dissertation
Portion	figures/tables/illustrations
Number of figures/tables/illustrations	1
Format	both print and electronic
Are you the author of this Elsevier article?	No
Will you be translating?	No
Title of new work	Microstructure control and property enhancement of NiTi-stainless steel dissimilar joints
Institution name	University of Waterloo
Expected presentation date	Feb 2026
Portions	Fig.5
The Requesting Person / Organization to Appear on the License	Kaiping Zhang
Requestor Location	Dr. Kaiping Zhang 706-4, 254 Phillip St Waterloo, ON N2L 0E1 Canada
Publisher Tax ID	GB 494 6272 12
Total	0.00 USD
Terms and Conditions	

SPRINGER NATURE LICENSE
TERMS AND CONDITIONS

Mar 09, 2025

This Agreement between Kaiping Zhang ("You") and Springer Nature ("Springer Nature") consists of your license details and the terms and conditions provided by Springer Nature and Copyright Clearance Center.

License Number	5984941266980
License date	Mar 09, 2025
Licensed Content Publisher	Springer Nature
Licensed Content Publication	Journal of Materials Engineering and Performance
Licensed Content Title	Effect of Post Weld Heat Treatment on Mechanical and Corrosion Behaviors of NiTi and Stainless Steel Laser-Welded Wires
Licensed Content Author	G. R. Mirshekari et al
Licensed Content Date	Apr 21, 2016
Type of Use	Thesis/Dissertation
Requestor type	academic/university or research institute
Format	print and electronic
Portion	figures/tables/illustrations
Number of figures/tables/illustrations	1

Will you be translating?	no
Circulation/distribution	1 - 29
Author of this Springer Nature content	no
Title of new work	Microstructure control and property enhancement of NiTi-stainless steel dissimilar joints
Institution name	University of Waterloo
Expected presentation date	Feb 2026
Portions	Fig. 9
The Requesting Person / Organization to Appear on the License	Kaiping Zhang
Requestor Location	Dr. Kaiping Zhang 706-4, 254 Phillip St Waterloo, ON N2L 0E1 Canada
Billing Type	Invoice
Billing Address	University of Waterloo 706-4, 254 Phillip St Waterloo, ON N2L 0E1 Canada
Total	0.00 USD
Terms and Conditions	

Springer Nature Customer Service Centre GmbH Terms and Conditions

ELSEVIER LICENSE
TERMS AND CONDITIONS

Mar 09, 2025

This Agreement between Kaiping Zhang ("You") and Elsevier ("Elsevier") consists of your license details and the terms and conditions provided by Elsevier and Copyright Clearance Center.

License Number	5984941335622
License date	Mar 09, 2025
Licensed Content Publisher	Elsevier
Licensed Content Publication	Materials Letters
Licensed Content Title	A novel laser welding method for the reliable joining of NiTi/301SS
Licensed Content Author	Xiao-Long Gao,Xiao-Qiang Wang,Jing Liu,Lun-kun Li
Licensed Content Date	Jun 1, 2020
Licensed Content Volume	268
Licensed Content Issue	n/a
Licensed Content Pages	1
Start Page	127573
End Page	0

Type of Use	reuse in a thesis/dissertation
Portion	figures/tables/illustrations
Number of figures/tables/illustrations	3
Format	both print and electronic
Are you the author of this Elsevier article?	No
Will you be translating?	No
Title of new work	Microstructure control and property enhancement of NiTi-stainless steel dissimilar joints
Institution name	University of Waterloo
Expected presentation date	Feb 2026
Portions	Fig.1a and b and Fig.3a
The Requesting Person / Organization to Appear on the License	Kaiping Zhang
Requestor Location	Dr. Kaiping Zhang 706-4, 254 Phillip St Waterloo, ON N2L 0E1 Canada
Publisher Tax ID	GB 494 6272 12
Total	0.00 USD
Terms and Conditions	

CCC Marketplace

Order Confirmation

Thank you, your order has been placed. An email confirmation has been sent to you. Your order license details and printable licenses will be available within 24 hours. Please access Manage Account for final order details.

This is not an invoice. Please go to manage account to access your order history and invoices.

CUSTOMER INFORMATION

Payment by invoice: You can cancel your order until the invoice is generated by contacting customer service.

Billing Address

Dr. Kaiping Zhang
University of Waterloo
706-4, 254 Phillip St
Waterloo, ON N2L 0E1
Canada

+1 (226) 581-3691
kaiping.zhang@uwaterloo.ca

Customer Location

Dr. Kaiping Zhang
University of Waterloo
706-4, 254 Phillip St
Waterloo, ON N2L 0E1
Canada

PO Number (optional)

N/A

Payment options

Invoice

PENDING ORDER CONFIRMATION

Confirmation Number: Pending

Order Date: 09-Mar-2025

1. Smart Materials and Structures

0.00 USD

Order License ID	Pending	Publisher	IOP Publishing
ISSN	0964-1726	Portion	Chart/graph/table/figure
Type of Use	Republish in a thesis/dissertation		

LICENSED CONTENT

Publication Title	Smart Materials and Structures	Country	United Kingdom of Great Britain and Northern Ireland
Author / Editor	Institute of Physics (Great Britain), Society of Photo-optical Instrumentation Engineers.	Rightsholder	IOP Publishing, Ltd
		Publication Type	Journal
Date	01/01/1992		
Language	English		

REQUEST DETAILS

Portion Type	Chart/graph/table/figure	Distribution	Worldwide
Number of Charts / Graphs / Tables / Figures Requested	2	Translation	Original language of publication
Format (select all that apply)	Print, Electronic	Copies for the Disabled?	No
Who Will Republish the Content?	Academic institution	Minor Editing Privileges?	Yes
Duration of Use	Life of current and all future editions	Incidental Promotional Use?	No
Lifetime Unit Quantity	Up to 499	Currency	USD
Rights Requested	Main product and any product related to main product		

NEW WORK DETAILS

Title	Microstructure control and property enhancement of NiTi-stainless steel dissimilar joints	Institution Name	University of Waterloo
		Expected Presentation Date	2026-02-27
Instructor Name	Kaiping Zhang		

ADDITIONAL DETAILS

Order Reference Number	N/A	The Requesting Person / Organization to Appear on the License	Kaiping Zhang

REQUESTED CONTENT DETAILS

Title, Description or Numeric Reference of the Portion(s)	Fig.4 and 8c	Title of the Article / Chapter the Portion Is From	High strength impact welding of NiTi and stainless steel wires
Editor of Portion(s)	N/A	Author of Portion(s)	Jianxiong Li, Boyd Panton, Yu Mao, Anupam Vivek and Glenn Daehn
Volume / Edition	N/A		
Page or Page Range of Portion	page 4 and 8	Issue, if Republishing an Article From a Serial	N/A
		Publication Date of Portion	2020-09-07

RIGHTSHOLDER TERMS AND CONDITIONS

These special terms and conditions are in addition to the standard terms and conditions for CCC's Republication Service and, together with those standard terms and conditions, govern the use of the Works. As the User you will make all reasonable efforts to contact the author(s) of the article which the Work is to be reused from, to seek consent for your intended use. Contacting one author who is acting expressly as authorised agent for their co-author(s) is acceptable. User will reproduce the following wording prominently alongside the Work: the source of the Work, including author, article title, title of journal, volume number, issue number (if relevant), page range (or first page if this is the only information available) and date of first publication; and a link back to the article (via DOI); and if practicable, and IN ALL CASES for new works published under any of the Creative Commons licences, the words "© IOP Publishing. Reproduced with permission. All rights reserved" Without the express permission of the author(s) and the Rightsholder of the article from which the Work is to be reused, User shall not use it in any way which, in the opinion of the Rightsholder, could: (i) distort or alter the author(s)' original intention(s) and meaning; (ii) be prejudicial to the honour or reputation of the author(s) and/or (iii) imply endorsement by the author(s) and/or the Rightsholder. This licence does not apply to any article which is credited to another source and which does not have the copyright line "© IOP Publishing Ltd". User must check the copyright line of the article from which the Work is to be reused to check that IOP Publishing Ltd has all the necessary rights to be able to grant permission. User is solely responsible for identifying and obtaining separate licences and permissions from the copyright owner for reuse of any such third party material/figures which the Rightsholder is not the copyright owner of. The Rightsholder shall not reimburse any fees which User pays for a republication license for such third party content. This licence does not apply to any material/figure which is credited to another source in the Rightsholder's publication or has been obtained from a third party. User must check the Version of Record of the article from which the Work is to be reused, to check whether any of the material in the Work is third party material. Third party citations and/or copyright notices and/or permissions statements may not be included in any other version of the article from which the Work is to be reused and so cannot be relied upon by the User. User is solely responsible for identifying and obtaining separate licences and permissions from the copyright owner for reuse of any such third party material/figures where the Rightsholder is not the copyright owner. The Rightsholder shall not reimburse any fees which User pays for a republication license for such third party content. User and CCC acknowledge that the Rightsholder may, from time to time, make changes or additions to these special terms and conditions without express notification, provided that these shall not

SAGE PUBLICATIONS LICENSE
TERMS AND CONDITIONS

Mar 09, 2025

This Agreement between Kaiping Zhang ("You") and Sage Publications ("Sage Publications") consists of your license details and the terms and conditions provided by Sage Publications and Copyright Clearance Center.

License Number	5984950263559
License date	Mar 09, 2025
Licensed Content Publisher	Sage Publications
Licensed Content Publication	Science and Technology of Welding and Joining
Licensed Content Title	Dissimilar friction welding of NiTi shape memory alloy and steel reinforcing bars for seismic performance
Licensed Content Author	Matthieu B. Lezaack, Aude Simar, Yannick Marchal, Martin Steinmetz, et al.
Licensed Content Date	Aug 1, 2022
Licensed Content Volume	27
Licensed Content Issue	6
Licensed Content Pages	11
Type of Use	Dissertation/Thesis
Requestor type	I am NOT the author of the requested article

Format	Print and electronic
Portion	Figure/table
Number of figures/tables	2
Will you be translating?	No, only English
Circulation	1
Title of new work	Microstructure control and property enhancement of NiTi-stainless steel dissimilar joints
Institution name	University of Waterloo
Expected presentation date	Feb 2026
Portions	Figs. 5a and 6
The Requesting Person / Organization to Appear on the License	Kaiping Zhang
Requestor Location	Dr. Kaiping Zhang 706-4, 254 Phillip St Waterloo, ON N2L 0E1 Canada
Publisher Tax ID	12978 6448 RT
Billing Type	Invoice

ELSEVIER LICENSE
TERMS AND CONDITIONS

Mar 09, 2025

This Agreement between Kaiping Zhang ("You") and Elsevier ("Elsevier") consists of your license details and the terms and conditions provided by Elsevier and Copyright Clearance Center.

License Number	5984950347482
License date	Mar 09, 2025
Licensed Content Publisher	Elsevier
Licensed Content Publication	Journal of Materials Processing Technology
Licensed Content Title	Microstructure and mechanical properties of resistance-welded NiTi/stainless steel joints
Licensed Content Author	Qiao Li,Yuanxiang Zhu,Jialin Guo
Licensed Content Date	Nov 1, 2017
Licensed Content Volume	249
Licensed Content Issue	n/a
Licensed Content Pages	11
Start Page	538
End Page	548

Type of Use	reuse in a thesis/dissertation
Portion	figures/tables/illustrations
Number of figures/tables/illustrations	3
Format	both print and electronic
Are you the author of this Elsevier article?	No
Will you be translating?	No
Title of new work	Microstructure control and property enhancement of NiTi-stainless steel dissimilar joints
Institution name	University of Waterloo
Expected presentation date	Feb 2026
Portions	Figs. 1, 3d and 11
The Requesting Person / Organization to Appear on the License	Kaiping Zhang
Requestor Location	Dr. Kaiping Zhang 706-4, 254 Phillip St Waterloo, ON N2L 0E1 Canada
Publisher Tax ID	GB 494 6272 12
Total	0.00 USD

Terms and Conditions

ELSEVIER LICENSE
TERMS AND CONDITIONS

Mar 09, 2025

This Agreement between Kaiping Zhang ("You") and Elsevier ("Elsevier") consists of your license details and the terms and conditions provided by Elsevier and Copyright Clearance Center.

License Number	5984950421238
License date	Mar 09, 2025
Licensed Content Publisher	Elsevier
Licensed Content Publication	Materials & Design (1980-2015)
Licensed Content Title	Laser welding of TiNi shape memory alloy and stainless steel using Ni interlayer
Licensed Content Author	H.M. Li,D.Q. Sun,X.L. Cai,P. Dong,W.Q. Wang
Licensed Content Date	Aug 1, 2012
Licensed Content Volume	39
Licensed Content Issue	n/a
Licensed Content Pages	9
Start Page	285
End Page	293

Type of Use	reuse in a thesis/dissertation
Portion	figures/tables/illustrations
Number of figures/tables/illustrations	2
Format	both print and electronic
Are you the author of this Elsevier article?	No
Will you be translating?	No
Title of new work	Microstructure control and property enhancement of NiTi-stainless steel dissimilar joints
Institution name	University of Waterloo
Expected presentation date	Feb 2026
Portions	Figs. 2e and 8c
The Requesting Person / Organization to Appear on the License	Kaiping Zhang
Requestor Location	Dr. Kaiping Zhang 706-4, 254 Phillip St Waterloo, ON N2L 0E1 Canada
Publisher Tax ID	GB 494 6272 12
Total	0.00 USD
Terms and Conditions	

ELSEVIER LICENSE
TERMS AND CONDITIONS

Mar 09, 2025

This Agreement between Kaiping Zhang ("You") and Elsevier ("Elsevier") consists of your license details and the terms and conditions provided by Elsevier and Copyright Clearance Center.

License Number	5984950488495
License date	Mar 09, 2025
Licensed Content Publisher	Elsevier
Licensed Content Publication	Materials Letters
Licensed Content Title	A comprehensive insight into the superelasticity measurement of laser welded NiTi shape memory alloys
Licensed Content Author	A. Shamsolhodaei,M.H. Razmpoosh,C. Maletta,P. Magaro,Y.N. Zhou
Licensed Content Date	Mar 15, 2021
Licensed Content Volume	287
Licensed Content Issue	n/a
Licensed Content Pages	1
Start Page	129310
End Page	0

Type of Use	reuse in a thesis/dissertation
Portion	figures/tables/illustrations
Number of figures/tables/illustrations	1
Format	both print and electronic
Are you the author of this Elsevier article?	No
Will you be translating?	No
Title of new work	Microstructure control and property enhancement of NiTi-stainless steel dissimilar joints
Institution name	University of Waterloo
Expected presentation date	Feb 2026
Portions	Fig. 1b
The Requesting Person / Organization to Appear on the License	Kaiping Zhang
Requestor Location	Dr. Kaiping Zhang 706-4, 254 Phillip St Waterloo, ON N2L 0E1 Canada
Publisher Tax ID	GB 494 6272 12
Total	0.00 USD
Terms and Conditions	

ELSEVIER LICENSE
TERMS AND CONDITIONS

Mar 09, 2025

This Agreement between Kaiping Zhang ("You") and Elsevier ("Elsevier") consists of your license details and the terms and conditions provided by Elsevier and Copyright Clearance Center.

License Number	5984950610186
License date	Mar 09, 2025
Licensed Content Publisher	Elsevier
Licensed Content Publication	Journal of the Mechanical Behavior of Biomedical Materials
Licensed Content Title	Corrosion induced fracture of NiTi wires in simulated oral environments
Licensed Content Author	Elisa Kassab,José Antônio da Cunha Ponciano Gomes
Licensed Content Date	Apr 1, 2021
Licensed Content Volume	116
Licensed Content Issue	n/a
Licensed Content Pages	1
Start Page	104323
End Page	0

Type of Use	reuse in a thesis/dissertation
Portion	figures/tables/illustrations
Number of figures/tables/illustrations	1
Format	both print and electronic
Are you the author of this Elsevier article?	No
Will you be translating?	No
Title of new work	Microstructure control and property enhancement of NiTi-stainless steel dissimilar joints
Institution name	University of Waterloo
Expected presentation date	Feb 2026
Portions	Fig. 5
The Requesting Person / Organization to Appear on the License	Kaiping Zhang
Requestor Location	Dr. Kaiping Zhang 706-4, 254 Phillip St Waterloo, ON N2L 0E1 Canada
Publisher Tax ID	GB 494 6272 12
Total	0.00 USD
Terms and Conditions	

CCC Marketplace

Order Confirmation

Thank you, your order has been placed. An email confirmation has been sent to you. Your order license details and printable licenses will be available within 24 hours. Please access Manage Account for final order details.

This is not an invoice. Please go to manage account to access your order history and invoices.

CUSTOMER INFORMATION

Payment by Invoice: You can cancel your order until the invoice is generated by contacting customer service.

Billing Address
Dr. Kaiping Zhang
University of Waterloo
706-4, 254 Phillip St
Waterloo, ON N2L 0E1
Canada

+1 (226) 581-3691
kaiping.zhang@uwaterloo.ca

Customer Location
Dr. Kaiping Zhang
University of Waterloo
706-4, 254 Phillip St
Waterloo, ON N2L 0E1
Canada

PO Number (optional)
N/A

Payment options
Invoice

PENDING ORDER CONFIRMATION

Confirmation Number: Pending

Order Date: 09-Mar-2025

1. The analyst online — 0.00 USD

Article: Visualization of local electrochemical activity and local nickel ion release on laser-welded NiTi/steel joints using combined alternating current mode and stripping mode SECM.

Order License ID	Pending	Publisher	Royal Society of Chemistry
ISSN	1364-5528	Portion	Chart/graph/table/figure
Type of Use	Republish in a thesis/dissertation		

LICENSED CONTENT

Publication Title	The analyst online	Rightsholder	Royal Society of Chemistry
Article Title	Visualization of local electrochemical activity and local nickel ion release on laser-welded NiTi/steel joints using combined alternating current mode and stripping mode SECM.	Publication Type	e-Journal
		Start Page	1700
		Issue	12
		Volume	133
		URL	http://www.rsc.org/is/journals/current/analyst/analcon.htm

Author / Editor	Royal Society of Chemistry (Great Britain), Society of Public Analysts (Great Britain), Society for Analytical Chemistry, Chemical Society (Great Britain), Society of Public Analysts (Great Britain)
Date	01/01/1876
Language	English
Country	United Kingdom of Great Britain and Northern Ireland

REQUEST DETAILS

Portion Type	Chart/graph/table/figure	Distribution	Worldwide
Number of Charts / Graphs / Tables / Figures Requested	1	Translation	Original language of publication
Format (select all that apply)	Print, Electronic	Copies for the Disabled?	No
Who Will Republish the Content?	Academic institution	Minor Editing Privileges?	Yes
Duration of Use	Life of current edition	Incidental Promotional Use?	No
Lifetime Unit Quantity	Up to 499	Currency	USD
Rights Requested	Main product, any product related to main product, and other compilations/derivative products		

NEW WORK DETAILS

Title	Microstructure control and property enhancement of NiTi-stainless steel dissimilar joints	Institution Name	University of Waterloo
		Expected Presentation Date	2026-02-27
Instructor Name	Kaiping Zhang		

ADDITIONAL DETAILS

Order Reference Number	N/A	The Requesting Person / Organization to Appear on the License	Kaiping Zhang

REQUESTED CONTENT DETAILS

Title, Description or Numeric Reference of the Portion(s)	Fig.3e	Title of the Article / Chapter the Portion Is From	Visualization of local electrochemical activity and local nickel ion release on laser-welded NiTi/steel joints using combined alternating current mode and stripping mode SECM.
Editor of Portion(s)	Ruhlig, D.; Gugel, H.; Schulte, A.; Theisen, W.; Schuhmann, W.		
Volume / Edition	133		
Page or Page Range of Portion	1700	Author of Portion(s)	Ruhlig, D.; Gugel, H.; Schulte, A.; Theisen, W.; Schuhmann, W.
		Issue, if Republishing an Article From a Serial	12
		Publication Date of Portion	2008-12-01

Total Items: 1 — **Total Due: 0.00 USD**

ELSEVIER LICENSE
TERMS AND CONDITIONS

Mar 09, 2025

This Agreement between Kaiping Zhang ("You") and Elsevier ("Elsevier") consists of your license details and the terms and conditions provided by Elsevier and Copyright Clearance Center.

License Number	5984950973270
License date	Mar 09, 2025
Licensed Content Publisher	Elsevier
Licensed Content Publication	Biomaterials
Licensed Content Title	Degradation and fracture of Ni–Ti superelastic wire in an oral cavity
Licensed Content Author	Ken'ichi Yokoyama,Kenichi Hamada,Keiji Moriyama,Kenzo Asaoka
Licensed Content Date	Aug 15, 2001
Licensed Content Volume	22
Licensed Content Issue	16
Licensed Content Pages	6
Start Page	2257
End Page	2262

Type of Use	reuse in a thesis/dissertation
Portion	figures/tables/illustrations
Number of figures/tables/illustrations	3
Format	both print and electronic
Are you the author of this Elsevier article?	No
Will you be translating?	No
Title of new work	Microstructure control and property enhancement of NiTi-stainless steel dissimilar joints
Institution name	University of Waterloo
Expected presentation date	Feb 2026
Portions	Fig. 3 and 7c and e
The Requesting Person / Organization to Appear on the License	Kaiping Zhang
Requestor Location	Dr. Kaiping Zhang 706-4, 254 Phillip St Waterloo, ON N2L 0E1 Canada
Publisher Tax ID	GB 494 6272 12
Total	0.00 USD
Terms and Conditions	



Laser welding-brazing of NiTi/304 stainless steel wires with beam defocus and large offset

Author: Kaiping Zhang,Peng Peng,Y. Norman Zhou
Publication: Materials Science and Engineering: A
Publisher: Elsevier
Date: 17 February 2022

© 2022 Elsevier B.V. All rights reserved.

Journal Author Rights

Please note that, as the author of this Elsevier article, you retain the right to include it in a thesis or dissertation, provided it is not published commercially. Permission is not required, but please ensure that you reference the journal as the original source. For more information on this and on your other retained rights, please visit: https://www.elsevier.com/about/our-business/policies/copyright#Author-rights

BACK CLOSE WINDOW



Effect of heat input modes on microstructure, mechanical properties and porosity of laser welded NiTi-316L joints: A comparative study

Author: Kaiping Zhang,Fuyun Liu,Caiwang Tan,Y. Norman Zhou,Peng Peng
Publication: Materials Science and Engineering: A
Publisher: Elsevier
Date: 19 July 2022

© 2022 Elsevier B.V. All rights reserved.

Journal Author Rights

Please note that, as the author of this Elsevier article, you retain the right to include it in a thesis or dissertation, provided it is not published commercially. Permission is not required, but please ensure that you reference the journal as the original source. For more information on this and on your other retained rights, please visit: https://www.elsevier.com/about/our-business/policies/copyright#Author-rights

BACK CLOSE WINDOW

Revealing microstructural evolution and mechanical properties of resistance spot welded NiTi-stainless steel with Ni or Nb interlayer
Author: K. Zhang,A. Shamsolhodaei,A. Ghatei-Kalashami,J.P. Oliveira,C. Zang,N. Schell,J. Li,A.R.H. Midawi,J.G. Lopes,J. Yan,P.E.J. Rivera-Díaz-del-Castillo,P. Peng,Y.N. Zhou
Publication: Journal of Materials Science & Technology
Publisher: Elsevier
Date: 1 May 2024
© 2024 Published by Elsevier Ltd on behalf of The editorial office of Journal of Materials Science & Technology.

Journal Author Rights

Please note that, as the author of this Elsevier article, you retain the right to include it in a thesis or dissertation, provided it is not published commercially. Permission is not required, but please ensure that you reference the journal as the original source. For more information on this and on your other retained rights, please visit: https://www.elsevier.com/about/our-business/policies/copyright#Author-rights

BACK CLOSE WINDOW

IOP Conference Series: Materials Science and Engineering

PAPER • OPEN ACCESS

Microstructure evolution of heat treated NiTi alloys

M Losertová, M Štencek, D Matýsek, O Štefek and J Drápala

Published under licence by IOP Publishing Ltd

IOP Conference Series: Materials Science and Engineering, Volume 266, 27th Joint Seminar Development of Materials Science in Research and Education 4–8 September 2017, Kežmarské Žlaby, High Tatras, Slovakia

Citation M Losertová *et al* 2017 *IOP Conf. Ser.: Mater. Sci. Eng.* **266** 012008

DOI 10.1088/1757-899X/266/1/012008

Article PDF

Authors References

Hide article information

Buy this article in print

Open Access Article

Pilot Study for Investigating the Cyclic Behavior of Slit Damper Systems with Recentering Shape Memory Alloy (SMA) Bending Bars Used for Seismic Restrainers

by **Junwon Seo** [1], **Young Chan Kim** [2] and **Jong Wan Hu** [2,3,*]

[1] Department of Civil and Environmental Engineering, South Dakota State University, Brookings, SD 57007, USA
[2] Department of Civil and Environmental Engineering, Incheon National University, 12-1 Songdo-dong, Yeonsu-gu, Incheon 406-772, Korea
[3] Incheon Disaster Prevention Research Center, Incheon National University, 12-1 Songdo-dong, Yeonsu-gu, Incheon 406-772, Korea
[*] Author to whom correspondence should be addressed.

Appl. Sci. **2015**, *5*(3), 187-208; **https://doi.org/10.3390/app5030187**

Submission received: 29 May 2015 / Revised: 17 July 2015 / Accepted: 22 July 2015 / Published: 30 July 2015

RightsLink



Design considerations and applications of shape memory alloy-based actuation in morphing structures: A systematic review

Author: Stefano Rodinò,Carmine Maletta
Publication: Progress in Engineering Science
Publisher: Elsevier
Date: December 2024

© 2024 The Author(s). Published by Elsevier B.V.

Creative Commons

This is an open access article distributed under the terms of the Creative Commons CC-BY license, which permits unrestricted use, distribution, and reproduction in any medium, provided the original work is properly cited.

You are not required to obtain permission to reuse this article.

To request permission for a type of use not listed, please contact Elsevier Global Rights Department.

Are you the author of this Elsevier journal article?

RightsLink

KZ

Microstructural development and solidification cracking susceptibility of austenitic stainless steel welds

Author: A. W. Thompson, J. A. Brooks
Publication: International Materials Reviews
Publisher: Taylor & Francis
Date: Nov 29, 2013

Rights managed by Taylor & Francis

Thesis/Dissertation Reuse Request

Taylor & Francis is pleased to offer reuses of its content for a thesis or dissertation free of charge contingent on resubmission of permission request if work is published.

BACK CLOSE

RightsLink



A σ phase-γ phase orientation relationship observed in solidification of the 7Mo super-austenitic stainless steel

Author: Runze Zhang,Jinshan He,Shiguang Xu,Fucheng Zhang,Yizhan Ma,Xitao Wang
Publication: Journal of Materials Research and Technology
Publisher: Elsevier
Date: November–December 2022

© 2022 The Authors. Published by Elsevier B.V.

Creative Commons

This is an open access article distributed under the terms of the Creative Commons CC-BY license, which permits unrestricted use, distribution, and reproduction in any medium, provided the original work is properly cited.

You are not required to obtain permission to reuse this article.

To request permission for a type of use not listed, please contact Elsevier Global Rights Department.

Are you the author of this Elsevier journal article?

RightsLink



The effect of martensite on stress corrosion crack initiation of austenitic stainless steels in high-temperature hydrogenated water

Author: Litao Chang,M. Grace Burke,Kudzanai Mukahiwa,Jonathan Duff,YongLiang Wang,Fabio Scenini
Publication: Corrosion Science
Publisher: Elsevier
Date: 15 August 2021

© 2021 The Authors. Published by Elsevier Ltd.

Creative Commons

This is an open access article distributed under the terms of the Creative Commons CC-BY license, which permits unrestricted use, distribution, and reproduction in any medium, provided the original work is properly cited.

You are not required to obtain permission to reuse this article.

To request permission for a type of use not listed, please contact Elsevier Global Rights Department.

Are you the author of this Elsevier journal article?

RightsLink

Sign in/Register

A comprehensive assessment of laser welding of biomedical devices and implant materials: recent research, development and applications

Author: M. M. Quazi, M. Ishak, M. A. Fazal, et al
Publication: Critical Reviews in Solid State & Materials Sciences
Publisher: Taylor & Francis
Date: Jan 3, 2020

Rights managed by Taylor & Francis

Thesis/Dissertation Reuse Request

Taylor & Francis is pleased to offer reuses of its content for a thesis or dissertation free of charge contingent on resubmission of permission request if work is published.

BACK CLOSE

RightsLink

Refill friction stir spot and resistance spot welding of aluminium joints with large total sheet thicknesses (III-1965-19)

Author: Christopher Schmal et al
Publication: Welding in the World
Publisher: Springer Nature
Date: May 30, 2020

Copyright © 2020, The Author(s)

Creative Commons

This is an open access article distributed under the terms of the Creative Commons CC BY license, which permits unrestricted use, distribution, and reproduction in any medium, provided the original work is properly cited.

You are not required to obtain permission to reuse this article.
To request permission for a type of use not listed, please contact Springer Nature

RightsLink

Influence of Al-Si coating on resistance spot welding of Mg to 22MnB5 boron steel

Author: Kaiping Zhang,Laijun Wu,Caiwang Tan,Yiming Sun,Bo Chen,Xiaoguo Song
Publication: Journal of Materials Processing Technology
Publisher: Elsevier
Date: September 2019

© 2019 Elsevier B.V. All rights reserved.

Journal Author Rights

Please note that, as the author of this Elsevier article, you retain the right to include it in a thesis or dissertation, provided it is not published commercially. Permission is not required, but please ensure that you reference the journal as the original source. For more information on this and on your other retained rights, please visit: https://www.elsevier.com/about/our-business/policies/copyright#Author-rights

BACK CLOSE WINDOW

RightsLink

Phase identification and thermodynamic modeling of a quaternary system in dissimilar laser-welded NiTi/ASS

Author: Saeed Asadi,Tohid Saeid,Farzad Habibi,Yejin Kim,Alireza Valanezhad,Nokeun Park
Publication: Journal of Materials Research and Technology
Publisher: Elsevier
Date: January–February 2022

© 2021 Published by Elsevier B.V.

Creative Commons Attribution-NonCommercial-No Derivatives License (CC BY NC ND)

This article is published under the terms of the Creative Commons Attribution-NonCommercial-No Derivatives License (CC BY NC ND).
For non-commercial purposes you may copy and distribute the article, use portions or extracts from the article in other works, and text or data mine the article, provided you do not alter or modify the article without permission from Elsevier. You may also create adaptations of the article for your own personal use only, but not distribute these to others. You must give appropriate credit to the original work, together with a link to the formal publication through the relevant DOI, and a link to the Creative Commons user license above. If changes are permitted, you must indicate if any changes are made but not in any way that suggests the licensor endorses you or your use of the work.

Permission is not required for this non-commercial use. For commercial use please continue to request permission via RightsLink.

BACK CLOSE WINDOW

RightsLink

Process optimization and thermodynamic modeling of weld zone in nickel powder-added dissimilar pulsed-laser NiTi/ASS joint

Author: Hyung Jun Kim,Saeed Asadi,Farzad Habibi,Tohid Saeid,Alireza Valanezhad,Nokeun Park,Unhea Lee
Publication: Journal of Materials Research and Technology
Publisher: Elsevier
Date: September–October 2022

© 2022 The Author(s). Published by Elsevier B.V.

Creative Commons Attribution-NonCommercial-No Derivatives License (CC BY NC ND)

This article is published under the terms of the Creative Commons Attribution-NonCommercial-No Derivatives License (CC BY NC ND).
For non-commercial purposes you may copy and distribute the article, use portions or extracts from the article in other works, and text or data mine the article, provided you do not alter or modify the article without permission from Elsevier. You may also create adaptations of the article for your own personal use only, but not distribute these to others. You must give appropriate credit to the original work, together with a link to the formal publication through the relevant DOI, and a link to the Creative Commons user license above. If changes are permitted, you must indicate if any changes are made but not in any way that suggests the licensor endorses you or your use of the work.

Permission is not required for this non-commercial use. For commercial use please continue to request permission via RightsLink.

BACK CLOSE WINDOW

RightsLink

Effect of CoCrFeNiMn high entropy alloy interlayer on microstructure and mechanical properties of laser-welded NiTi/304 SS joint

Author: Hongwei Wang,Jilin Xie,Yuhua Chen,Wenkuo Liu,Wenbin Zhong
Publication: Journal of Materials Research and Technology
Publisher: Elsevier
Date: May–June 2022

© 2022 The Authors. Published by Elsevier B.V.

Creative Commons

This is an open access article distributed under the terms of the Creative Commons CC-BY license, which permits unrestricted use, distribution, and reproduction in any medium, provided the original work is properly cited.

You are not required to obtain permission to reuse this article.

To request permission for a type of use not listed, please contact Elsevier Global Rights Department.

Are you the author of this Elsevier journal article?

RightsLink



Microstructure and mechanical properties of dissimilar NiTi and 304 stainless steel joints produced by ultrasonic welding

Author: S.S. Ao,M.P. Cheng,W. Zhang,J.P. Oliveira,S.M. Manladan,Z. Zeng,Z. Luo
Publication: Ultrasonics
Publisher: Elsevier
Date: April 2022

© 2022 The Authors. Published by Elsevier B.V.

Creative Commons

This is an open access article distributed under the terms of the Creative Commons CC-BY license, which permits unrestricted use, distribution, and reproduction in any medium, provided the original work is properly cited.

You are not required to obtain permission to reuse this article.

To request permission for a type of use not listed, please contact Elsevier Global Rights Department.

Are you the author of this Elsevier journal article?

RightsLink

Part II.: Dissimilar friction stir welding of nickel titanium shape memory alloy to stainless steel – microstructure, mechanical and corrosion behavior

Author: Parker West,Vasanth C. Shunmugasamy,Chaudhry A. Usman,Ibrahim Karaman,Bilal Mansoor
Publication: Journal of Advanced Joining Processes
Publisher: Elsevier
Date: November 2021

© 2021 The Authors. Published by Elsevier B.V.

Creative Commons

This is an open access article distributed under the terms of the Creative Commons CC-BY license, which permits unrestricted use, distribution, and reproduction in any medium, provided the original work is properly cited.

You are not required to obtain permission to reuse this article.

To request permission for a type of use not listed, please contact Elsevier Global Rights Department.

Are you the author of this Elsevier journal article?

CCC | RightsLink

SPRINGER NATURE

In vivo biocompatibility evaluation of 3D-printed nickel–titanium fabricated by selective laser melting

Author: Hendrik Naujokat et al
Publication: Journal of Materials Science: Materials in Medicine
Publisher: Springer Nature
Date: Jan 21, 2022

Copyright © 2022, The Author(s)

Creative Commons

This is an open access article distributed under the terms of the Creative Commons CC BY license, which permits unrestricted use, distribution, and reproduction in any medium, provided the original work is properly cited.

You are not required to obtain permission to reuse this article.
To request permission for a type of use not listed, please contact Springer Nature